N^0 d'ordre : 41233

Mémoire

présenté à

l'Université de Lille 1, Sciences et Technologies

en vue d'obtenir

l'Habilitation à diriger des recherches

PAR

Emmanuel Courtade

DYNAMIQUE DU STRESS EN CELLULE VIVANTE

Soutenue le 15 novembre 2013 devant le jury composé de :

Francesco Lenci	Université de Pise	Rapporteur
Valérie Mezger	Université de Paris Diderot	Rapporteur
Pierre François Lenne	Université Aix Marseille	Rapporteur
Evelyne Sage	Institut Curie	Examinatrice
Marc Douay	Université de Lille I	Examinateur
Stéphane Randoux	Université de Lille I	Examinateur

Table des matières

Introduction

Après une thèse en physique atomique sur le "Pompage optique de l'hélium en condition non standard" en vue de comprendre les mécanismes de production d'hélium-3 gazeux très polarisé et dense pour une exploration de la fonction des voies respiratoires chez l'homme par IRM, j'ai décidé de faire un post-doctorat dans le domaine des atomes froids dans le groupe d'E. Arimondo à Pise. Durant cette période, je me suis intéressé à différents sujets comme le refroidissement sympathique dans un mélange atomique ou à la dynamique d'un condensat de Bose Einstein dans un réseau optique. Je ne rappellerai que brièvement dans cette introduction mes activités dans le domaine des atomes froids pour présenter l'émergence d'une nouvelle activité à l'interface entre physique, chimie et biologie au sein du laboratoire PhLAM.

Le refroidissement sympathique dans un mélange est une voie très prometteuse pour atteindre le régime de dégénérescence pour des espèces atomiques qui ne peuvent être efficacement refroidies par évaporation directe, ou encore pour la production des molécules hétéronucléaires possédant un dipôle important qui peut être mis à profit dans des réalisations de portes logiques quantiques. Pour que le refroidissement sympathique soit efficace, il faut s'assurer que le taux de collisions élastiques entre espèces soit plus important que celui des collisions inélastiques qui peuvent introduire de fortes pertes dans le processus de thermalisation. Dans un mélange ultrafroid, l'interaction entre les espèces est principalement décrite en terme d'un paramètre clef, la longueur de diffusion a_s en onde s, qui détermine l'efficacité du refroidissement sympathique. L'étude des propriétés collisionnelles d'un mélange ultrafroid de Rb-Cs en vue d'une condensation par refroidissement sympathique du ^{133}Cs par le ^{87}Rb, a montré qu'il est possible de refroidir les deux espèces jusqu'à des températures de quelques dizaines de μK. Des simulations des collisions ont montré qu'avec la longueur de diffusion a_s mesurée, on pouvait atteindre ce régime pour la condensation du ^{133}Cs mais que les densités d'atomes de ^{87}Rb accessibles dans l'expérience étaient trop faibles. En 2011, l'équipe d'atomes froids de S. L. Cornish a réussi à refroidir sympathiquement le ^{133}Cs avec du ^{87}Rb et atteindre le régime de dégénérescence suffisant pour obtenir un double condensat de Bose.

L'effet tunnel Landau Zener est un exemple d'un problème tunnel dans lequel des particules quantiques peuvent franchir une barrière de potentiel par croisement entre deux niveaux d'énergie du système. Ce phénomène est décrit par la solution d'une équation de Schrödinger avec un Hamiltonien du système dépendant du temps. L'étude de cet effet tunnel Landau Zener peut être menée avec l'accélération de condensats de Bose-Einstein dans des réseaux optiques. En effet, les potentiels

lumineux permettent un contrôle du transport dans les bandes d'énergie de systèmes quantiques périodiques : la profondeur du réseau optique contrôle la barrière tunnel alors que l'accélération du réseau contrôle la dépendance en temps de l'hamiltonien qui gère l'effet tunnel. La dynamique d'un condensat de Bose, quand le potentiel périodique obtenu par le réseau optique est accéléré, conduit à des oscillations de Bloch dans la bande fondamentale et à des effets tunnels Landau-Zener assymétriques qui dépendent du sens de passage entre les différentes bandes d'énergie. Au-delà d'un déplacement critique, le condensat subit une réflexion de Bragg et pour des densités d'atomes élevées (typiquement $\sim 10^{14}\ cm^{-3}$), la première réflexion de Bragg génère des solitons et des vortex qui déstabilisent la cohérence du condensat.

La spectroscopie pompe-sonde permet de préparer les atomes piégés dans des états internes bien choisis qui peuvent être la base binaire de calcul quantique. Les réseaux optiques 3D traditionnels présentent une forte densité de sites, de périodicité de l'ordre de $\lambda/2$ (λ est la longueur d'onde de la lumière). Cette propriété est un inconvénient lorsque ces réseaux sont chargés à partir d'un piège magnéto-optique (PMO), car elle mène à un taux de remplissage du réseau largement inférieur à l'unité (typiquement, un site sur cent sera occupé par un atome). J'ai été recruté en 2005 dans l'équipe atomes froids du PhLAM (P. Verkerk et D. Hennequin) pour étudier la dynamique d'atomes froids dans un réseau optique de pièges annulaires. Un tel réseau, réalisé sur le bleu de la transition atomique, permet, tout en conservant un grand volume de capture, de confiner étroitement des atomes froids dans les directions radiale et longitudinale. Ce réseau optique de pièges annulaires est obtenu expérimentalement en faisant interférer un faisceau cylindrique creux avec un faisceau gaussien contra-propageant obtenu à l'aide une paire de lentilles coniques (axicons). L'interaction des atomes d'un même site ou de deux sites voisins, et leur dynamique dans un tel réseau donne alors lieu à des effets nouveaux. On peut par exemple envisager l'observation de la transition entre un régime de grande diffusion des atomes dans le réseau et un régime de localisation des atomes dans les sites, analogue à la transition conducteur-isolant de Mott, en physique du solide. L'occupation régulière de tous les sites du réseau est aussi une condition nécessaire pour réaliser une porte logique quantique par le contrôle de l'interaction entre atomes de sites adjacents. D'autres applications liées au fort taux d'occupation sont envisageables comme, par exemple, la condensation de Bose-Einstein dans un réseau.

En 2007, j'ai démarré une nouvelle activité à l'interface entre physique, chimie et biologie avec le dépôt d'un brevet de deux collègues du laboratoire PhLAM, J. Zemmouri et I. Razdobreev, concernant la possibilité d'induire de la mort cellulaire par excitation directe de l'oxygène singulet. L'oxygène dans son premier état électronique excité (oxygène singulet) est une espèce chimique très réactive qui joue un rôle majeur dans de nombreux processus de photo-oxydation tant en chimie qu'en biologie. L'oxygène singulet est généralement produit par réactions chimiques ou photochimiques. Les photosensibilisants, sous l'action d'une lumière laser visible, sont amenés de l'état fondamental à un état excité puis relaxent en présence de l'oxygène qui capte l'excès énergétique et passe à l'état singulet. La forte réactivité de l'oxygène singulet peut induire un stress oxydant conduisant à la mort cellulaire. Nous avons montré que l'excitation laser directe de l'oxygène singulet à 1270 nm,

sans utilisation de substance photosensibilisante, peut induire la mort cellulaire. En raison de sa simplicité, cette nouvelle approche de photothérapie laser, peut potentiellement surmonter des problèmes associés à l'administration systémique de photosensibilisants en thérapie (photosensibilité du patient, évacuation du photosensibilisant de l'organisme). Par ailleurs, ces travaux ont conduit à des études photochimiques pour caractériser la cinétique de l'oxygène singulet créé à 1270 *nm* afin d'évaluer quantitativement sa production ainsi que sa réactivité. A terme ces études pourraient conduire à développer des rapporteurs biologiques utilisables *in vitro* qui renseignent sur les réponses physiologiques des cellules au stress oxydant.

L'expérience acquise dans le domaine du stress oxydant a permis d'étendre les activités de l'équipe à l'étude de la réponse à un stress thermique (par laser), ce qui permet d'étudier non seulement une autre voie de signalisation cellulaire, mais également la cinétique d'activation de gènes en réponse au stress. La réponse au choc thermique est caractérisée par l'activation de l'expression de protéines de choc thermique, sous le contrôle de facteurs de transcription appelés Heat Shock Factors (HSFs) pour les cellules humaines. En réponse à une élévation de température, des modifications profondes d'expression des protéines se produisent au sein de la cellule. Les mécanismes de réponse au stress sont contrôlés par des régulations complexes avec de multiples partenaires. La cinétique temporelle du recrutement du facteur de transcription (HSF1) est étudié dans des expériences de vidéo-microscopie. L'originalité de cette étude est d'induire un stress par laser, ce qui permet de contrôler les amplitudes et cinétiques du choc thermique. Nous avons aussi décrit un modèle minimal de la réponse au choc thermique avec les données expérimentales. Le modèle décrivant le réseau de régulation moléculaire de réponse au choc thermique permet de i) prédire des mécanismes de réponse suivant différents types de stress ii) d'évaluer les contributions des principales réactions impliquées dans le mécanisme de stress thermique.

Le projet "Oxygène singulet" a démarré avec une question d'interaction lumière-cellule vivante sur la possibilité d'exciter directement l'oxygène dans son état singulet. Très vite, cette activité expérimentale s'est projetée dans le fait d'intégrer une salle de culture cellulaire au sein d'un laboratoire de physique ainsi que d'acquérir une culture sur les questions biologiques associées à la mort cellulaire. Une première étape importante des activités a consisté à de nombreux développement expérimentaux avec mes collègues P. Suret et S. Randoux pour la partie optique (développement de nouvelles sources laser Raman), I. El-Yazidi Belkoura du laboratoire de Glycobiologie Glycobiologie Structurale et Fonctionnelle pour la partie biologie, et le travail de fond de la thèse de F. Anquez (2007-2010). Fort de ces résultats, une deuxième étape a consisté à introduire des mesures quantitatives sur la production de l'oxygène singulet avec notamment des collaborations avec des chimistes (C. Pierlot, J. M. Aubry du laboratoire de Chimie Moléculaire et Formulation de l'Université Lille 1, A. Barras et R. Boukherroub de l'équipe "Nanobiointerfaces" de l'Institut de Recherche Interdisciplinaire de Lille). Une autre dimension importante des activités est liée aujourd'hui aux voies de signalisation et de régulation au niveau cellulaire du stress thermique dans le cadre de la thèse d'A. Sivéry (2010-2014) et une collaboration avec Q. Thommen du groupe de "Dynamique des réseaux biologiques". Toutes ces

collaborations entre physiciens, chimistes et biologistes nourrissent aujourd'hui une activité importante de l'équipe avec une vision intégrative de questions biologiques. Je ne présenterai dans ce manuscrit que les travaux concernant les activités liées à la dynamique du stress en cellules vivantes avec dans une première partie, les études du stress oxydant avec la création d'oxygène singulet sans photosensibilisant et dans une seconde partie les études cinétiques liées aux mécanismes mis en jeu lors d'un stress thermique au niveau cellulaire.

Chapitre 1

Stress oxydant et mort cellulaire

1.1 Stress oxydant et production d'oxygène singulet photosensibilisée

Le stress cellulaire peut-être de nature variée (mécanique, chimique, thermique...) et le déséquilibre homéostasique associé peut générer plusieurs types de réponses allant de la réparation et/ou à la mort cellulaire. Le stress oxydant est caractérisé par la présence d'Espèces Réactives de l'Oxygène (ERO) qui, lorsqu'elles sont en excès, dépassent les capacités de barrière antioxydante de la cellule. Les ERO comprennent des radicaux libres de l'oxygène ($^{\cdot}OH$, $O_2^{\cdot -}$...) et des dérivés non radicalaire (H_2O_2) qui sont formés dans les cellules. Ces ERO, par leur nature instable, sont particulièrement réactives et sont capables de provoquer des dégâts cellulaires importants comme des cassures et des mutations de l'ADN, l'inactivation de protéines et enzymes, l'oxydation de pigments ou de sucres. Les ERO peuvent aussi induire de processus de peroxydation lipidique au sein des acides gras polyinsaturés des lipoprotéines ou de la membrane cellulaire [Favier 03].

Dans cette famille des ERO, l'oxygène singulet ($^1O_2$) qui est le premier état électronique excité de la molécule de dioxygène joue un rôle particulier : sa conformation électronique lui confère une très grande réactivité chimique [Derosa et Crutchley 02, Maisch *et al.* 07]. Il est en général produit quand un photosensibilisant exogène ou endogène absorbe une radiation visible ou UV en présence de dioxygène alors que les autres ERO sont en général produites durant des processus physiologiques dans la cellule par des enzymes de type NADPH oxydase. En biologie, l'oxygène singulet peut être activé chimiquement par exemple dans la décomposition de péroxydes d'hydrogène comme dans des mécanismes de réponse par « bursts » oxydatifs chez les neutrophiles, ou physiquement par l'activation d'un photosensibilisant (PS) comme dans la photosynthèse de la chlorophylle chez les plantes ou chez les humains.

Les premières observations de mort cellulaire induite par activation d'un PS pour produire de l'$^1O_2$ datent du début du XXe siècle. O. Raab et H. Von Tappeiner ont montré que l'action de l'acridine (PS), activée par la lumière pouvait induire la mort cellulaire de paramécies [Raab 00, Tappeiner et Jodlbauer 04, Tappeiner 09]. C'est grâce aux travaux de R. S. Mulliken [Mulliken 28] qui décrira les niveaux d'énergie du dioxygène que C. S. Foote proposera les mécanismes d'oxidation photosensibilisée

avec l'oxygène singulet [Foote 68] (voir figure 1.1).

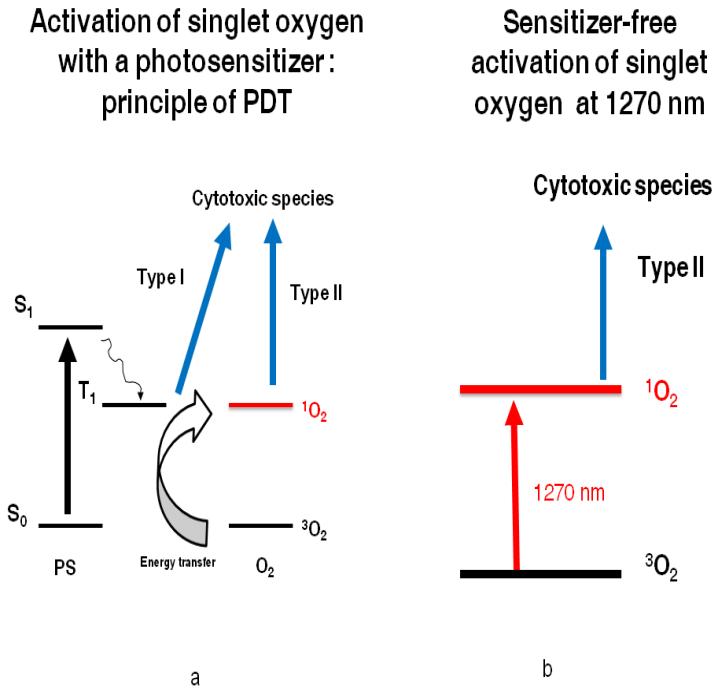

FIGURE 1.1 – Mécanismes photophysiques de production d'oxygène singulet. La création photosensibilisée d'$^1O_2$ requiert trois éléments : la lumière, un photosensibilisant (PS) et le dioxygène (O_2) (schéma a). Le PS, dans son état excité triplet(T1) peut produire deux types de réactions. Dans la réaction de type I, il peut directement réagir avec la membrane cellulaire ou avec une molécule pour former un radical de type anion ou cation. Dans les réaction de type II, l'état triplet du PS peut transférer son énergie à l'état fondamental du dioxygène ($^3O_2$) pour former l'$^1O_2$. Le ratio entre les réaction de type I et II dépend de la nature du PS et de la concentration locale d'O_2. A l'échelle moléculaire, la création photosensibilisée d'$^1O_2$ est un processus intrinséquement complexe (photoblanchiment du PS, réaction avec l'oxygène singulet produit), ce qui rend difficile une dosimétrie prédictive et quantitative en PDT. Le projet "Oxygène Singulet" consiste à créer directement de l'$^1O_2$ sans PS, en excitant la transition $O_2[^3\Sigma_g^-] \longrightarrow O_2[^1\Delta_g]$ à 1270 nm (schéma b) pour induire la mort cellulaire.

La très grande réactivité de l'oxygène singulet peut être mise à profit pour le traitement de certaines maladies. Les réactions d'$^1O_2$ avec des molécules au niveau cellulaire peuvent générer des réponses de stress en photobiologie et en photothérapie médicale [Dougherty *et al.* 76, Dougherty *et al.* 98]. L'application la plus répandue de création d'$^1O_2$ avec des photosensibilisants est la photothérapie dynamique (ou Photodynamic Therapy, PDT) qui est utilisée en médecine pour traiter certains types de cancers [Dougherty 02] ou des dégénérescences maculaires liées à l'âge [SE 00]. La PDT cible des cellules ou des tissus spécifiques en délivrant de façon sélective des photosensibilisants exogènes et une irradiation lumineuse localisée.

La génération d'$^1O_2$ *via* un photosensibilisant peut présenter de nombreux inconvénients. D'un point de vue du clinique, le PS qui est une substance invasive, se répand dans tout le corps et peut rendre le patient photosensible pendant plusieurs jours. De plus la biodistribution, le franchissement de barrière membranaire et la reconnaissance spécifique de la cellule tumorale dépend de la nature même du PS utilisé. Concernant la sélectivité vis à vis de la cellule cible, des PS dits de $2^{ème}$ et $3^{ème}$ génération, vont être fonctionnalisés avec des molécules de reconnaissance comme des sucres (PS glycoconjugués avec du mannose [Ballut *et al.* 12]), des peptides [Bechet *et al.* 10] ou des anticorps monoclonaux. D'un point de vue fondamental, le rendement quantique de production d'$^1O_2$ avec le PS, qui dépend fortement de l'environnement, rend difficile l'interprétation des doses léthales en thérapie. Le temps de vie d'$^1O_2$ est d'environ de 3 μs dans l'eau, si on estime le cas d'une diffusion libre, il parcourt environ 100 nm sur sa durée de vie. La distribution spatiale du PS définit donc précisément où $^1O_2$ est généré et définit une réponse cellulaire spatiale du stress oxydatif [Redmond et Kochevar 06]. Il faut noter par ailleurs que la localisation du PS dans les compartiments cellulaires déterminés (mitochondrie, membrane...) dépend de la nature du PS lui-même et du type cellulaire [Castanoa *et al.* 04,Castanoa *et al.* 05]. Cette localisation rend donc difficile les études qualitatives et quantitatives dans le toxicité de $^1O_2$ dans la mort cellulaire.

En PDT, l'un des axes de recherche actuel est de pouvoir estimer la quantité d'$^1O_2$ généré afin d'optimiser la dosimétrie du traitement (concentration du PS, quantité de lumière et temps d'irradiation, vectorisation intracellulaire du PS...) afin de pouvoir optimiser l'efficacité de cette thérapie du cancer [Dysart *et al.* 05]. Le complexe PS-$^1O_2$ constitue donc un système dynamique complexe qui rend non triviale une estimation quantitative et prédictive de la dose d'oxygène singulet intracellulaire.

1.2 Contexte et motivations

C'est dans ce contexte que nous avons démarré le projet "Oxygène Singulet" avec P. Suret, S. Randoux pour la partie optique, I. El-Yazidi Belkoura du laboratoire de Glycobiologie Glycobiologie Structurale et Fonctionnelle pour la partie biologie, et la thèse de F. Anquez (2007-2010). Ces études proposent une alternative à la PDT "standard" en produisant directement, sans photosensibilisant, de l'$^1O_2$ *via* la transition $O_2[^3\Sigma_g^-] \longrightarrow O_2[^1\Delta_g]$ à 1270 nm afin de pouvoir induire un stress oxydant pouvant conduire à la mort cellulaire. D'un pont de vue fondamental, cette approche permet de mieux appréhender les mécanismes fonctionnels mis en jeu lors de l'activation d'un stress oxydant au niveau cellulaire.

Contrairement à beaucoup d'autres molécules, l'état fondamental du dioxygène ($O_2[^3\Sigma_g^-]$) est un triplet de spin. D'un point de vue des règles de transition, si on considère cette molécule isolée (cas d'un gaz), la transition de l'état fondamental à l'état $^1O_2$ est "interdite" à l'ordre dipolaire électrique [Mulliken 28, Schweitzer et Schmidt 03]. En solution (*i. e.* en phase dense), la probabilité d'absorption augmente : le temps de vie de $^1O_2$ passe de 72 minutes dans un gaz à 3.5 μs dans l'eau. Si on compare la section efficace d'absorption dans l'eau d'un PS $\sim 10^{-18}$ cm^2 à

celle de l'absorption directe de du dioxygène à 1270 $nm \sim 10^{-23}$ cm^2, on a une probabilité de production d'$^1O_2$ qui est 5 ordres de grandeur plus faible à 1270 nm que celle d'un PS [Jr. *et al.* 08, Sivery *et al.* 13a].

En conséquence de cette faible efficacité de production d'$^1O_2$ sans PS, seules quelques travaux ont été entrepris dans les systèmes biologiques. Nous pouvons citer les études sur des effet de transitions structurales réversibles dans la biomembrane et sur le traitement de tumeurs chez le rat [Zakharov et Ivanov 99]. Récemment, des résultats préliminaires sur le traitement de basaliomes avec des irradiations à 1260 nm indiquent une réduction du tissu tumoral [Yusupov *et al.* 10]. Ces études ne montrent pas de façon claire l'implication directe de l'oxygène singulet et de son caractère cytotoxique avec entre autre la possibilité d'induire aussi à 1270 nm un stress thermique pendant l'irradiation laser.

1.3 Mort cellulaire induite *in vitro* par activation directe à 1270 nm de l'oxygène singulet

Au démarrage de ce projet, les sources lasers commerciales à 1270 nm ne permettaient pas d'obtenir de grandes puissances ($\sim 100\ mW$) ni d'accordabilité autour de 1270 nm. Nous avons donc réalisé au sein du laboratoire PhLAM, avec P. Suret et S. Randoux, un laser de puissance basé sur une technologie de laser Raman à fibre pour pouvoir sonder la transition $O_2[^3\Sigma_g^-] \longrightarrow O_2[^1\Delta_g]$ avec une résolution spectrale de l'ordre du nm. Cette source peut fournir jusqu'à 2.5 W dans la gamme 1239-1297 nm [Anquez *et al.* 10].

Les cellules choisies dans le cadre de ces expériences *in vitro*, sont des cellules épithéliales humaines du cancer (adénocarcinome) du sein chez la femme MCF-7 (Michigan Cancer Fundation). Elles constituent une référence en recherche sur le cancer et sont bien caractérisées notamment dans les voies de signalisation de mort cellulaire. Dans les premiers essais, les cellules étaient préparées par I. El-Yazidi Belkoura au laboratoire de signalisation des facteurs de croissance dans le cancer du sein de l'université Lille 1, et irradiées au PhLAM. Assez rapidement, nous avons choisi de réaliser une salle de culture au sein du laboratoire pour pouvoir travailler dans des conditions permettant de limiter des transports (et d'éventuelles contaminations) et de mieux synchroniser les expériences.

Afin de pouvoir simplifier l'environnement de la tumeur, ces études *in vitro* ont été menées en microscopie optique afin de pouvoir visualiser la mort des cellules irradiées par laser sur une population de cellules. Le développement d'un incubateur régulé en gaz et en température a permis d'observer jusqu'à trois jours les cinétiques de mort cellulaire.

Lorsque les cellules sont irradiées à 1270 nm ($\sim 100\ W.cm^2$-3 h), on observe à partir d'une quinzaine d'heures post-irradiation, un changement morphologique de ces dernières. 27 heures post-irradiation, les cellules sont toutes mortes dans un diamètre de 200 μm centré sur le spot laser. Ces changements morphologiques ont été corrélés avec un test d'exclusion au bleu Trypan associé à la mort cellulaire (Fig. 1.2) ainsi que des marqueurs AnnexinV et iodure de propidium pour marquer

respectivement l'apoptose et la nécrose. L'apoptose des cellules observées 15h post irradiation est corrélée à une morphologie plus arrondie des cellules. Les cellules passent alors en nécrose secondaire environ 20 heures post-irradiation.

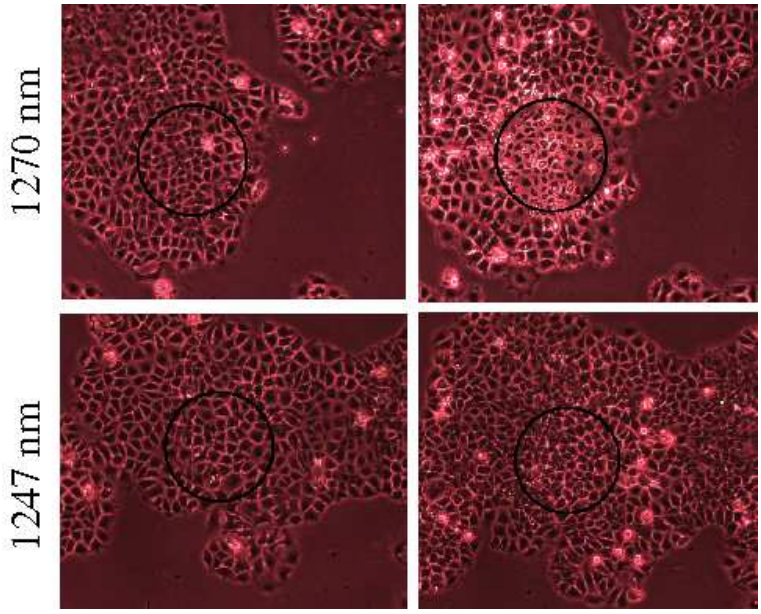

FIGURE 1.2 – Images de cellules MCF-7 irradiées ($\sim$ 100 $W.cm^2$-3 h) à différentes longueurs d'onde (images du haut à 1270 nm et en bas à 1247 nm). La taille des images est de 407 $\times$ 435 μm^2. A gauche et droite, on observe respectivement les cellules avant et 27h post irradiation. La zone d'irradiation par laser (FWHM= 300 μm, P$\sim$100mW) est représentée par un cercle noir. A 1270 nm, les cellules sont toutes mortes dans un diamètre de 200 μm centré sur le spot laser. Aucune mort cellulaire n'est observée à 1247 nm. La viabilité cellulaire est déterminée par le changement de critères morphologiques corrélés à un test d'exclusion au bleu Trypan.

La première vérification de l'effet direct de la génération d'$^1O_2$ à 1270 nm est la construction du spectre d'action de la mort des cellules en fonction de l'absorption de la transition $O_2[^3\Sigma_g^-] \longrightarrow O_2[^1\Delta_g]$ (Fig. 1.4). Ce résultat est assez remarquable car il permet pour la première fois de montrer qu'il est possible de générer directement (sans PS) une quantité d'oxygène singulet permettant d'induire de la mort cellulaire.

Afin de confirmer ce résultat, des expériences mettant les cellules soit en hypoxie (saturation en N_2) ou en hyperoxie (saturation en O_2) ont permis d'observer une dépendance du dioxygène sur la mort cellulaire. Après avoir saturé le milieu de culture pendant 2h30 et, pendant l'irradiation, aucune mort cellulaire est observée en hypoxie tandis qu'en hyperoxie, la mort cellulaire est plus importante et rapide qu'en condition standard (Fig. 1.5).

1.4 Effets thermiques

Vu les intensités d'irradiation de ces expériences ($\sim$ 100 W/cm^2), il est légitime de s'intéresser aux effets thermiques sur les cellules. En effet, l'absorption de la

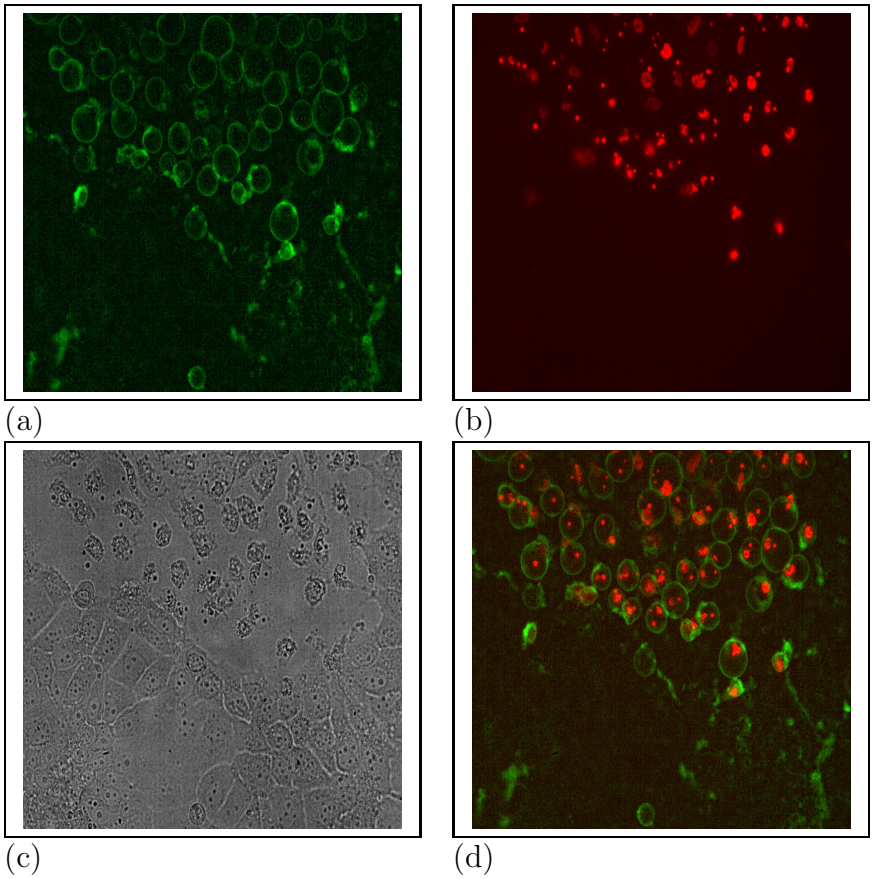

FIGURE 1.3 – Cellules MCF-7 irradiées à 1270 nm($\sim$ 70 $W.cm^2$- 1h30) et observées 24h post irradiation. Afin d'évaluer le type de mort induit, un marquage fluorescent AnnexinV et PI (Iodure de Propidium) permet d'observer respectivement les résidus de phosphatidylsérine et l'ADN. L'AnnexinV marque la perte d'assymétrie membranaire, qui peut être associée à l'apoptose précoce [Vitale *et al.* 93, Honda *et al.* 00, Lecoeur *et al.* 01]. Le PI, qui est un intercalant de l'ADN, lors de la perte d'intégrité membranaire, est associé aux premières étapes de une nécrose [Elmore 07]. (a) Les cellules irradiées sont bien marquées Annexin V (a) et au PI (b). En sommant les images (a) et (b), on observe sur les cellules un co-marquage associé à la nécrose. Sur une image en lumière blanche par transmission (c), la morphologie des cellules irradiées est très différente des cellules témoin avec notamment une forte altération de la membrane.

lumière à 1270 nm par l'eau est d'environ 0,5 cm^{-1} [Hale et Querry 73]. Une mesure de température optique *in situ*, basée sur des changements de fluorescence de la rhodamine [Sakakibara et Adrian 99, SS *et al.* 05], a permis d'évaluer l'augmentation de la température à 1270 nm dans des conditions expérimentales standard (100 mW sur 200 μm). Le rhodamine B présente une fluorescence sensible à la température (vers 550 nm) : sa fluorescence diminue lorsque l'élévation de la température avec une pente de $2\%.K^{-1}$. La Rhodamine 110 a des caractéristiques spectrales similaires, mais ne dépend pas tant de la température ($0.1\%.K^{-1}$) : c'est donc un bon colorant à prendre en compte pour évaluer un possible effet de lentille thermique du laser à 1270 nm. Le rapport rhodamine B / Rhodamine 110 est d'abord calibré avec un

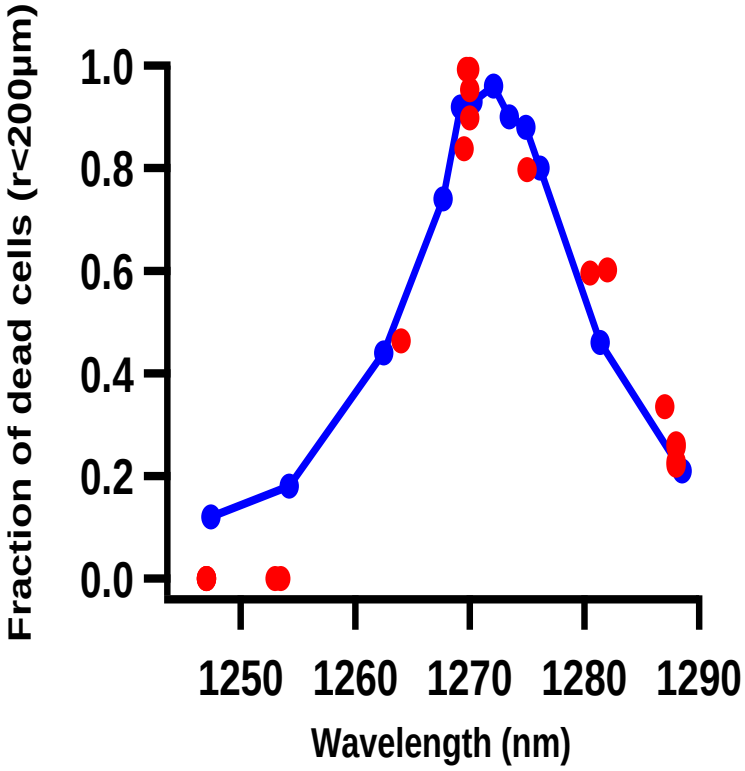

FIGURE 1.4 – Spectre d'action de la lumière (points rouges) montrant la fraction de cellules mortes dans un rayon de 200 μm centré sur le spot laser. Le spectre d'action est fortement corrélé avec celui de la bande d'absorption de la transition $O_2[^3\Sigma_g^-] \longrightarrow O_2[^1\Delta_g]$ dans l'éthanol (en bleu) [Anquez *et al.* 10].

contrôle de la température de l'incubateur et ensuite l'élévation du laser à 1270 nm est ainsi évaluée $\sim 60K.W^{-1}$ dans les conditions d'irradiation. Un bon accord de ces mesures de température de fluorescence a été trouvé avec une simulation numérique de l'équation de la chaleur par une méthode d'éléments finis. Expérimentalement, il est facile de compenser cette élévation de température due à l'absorption à 1270 nm en diminuant la température de l'incubateur de contrôle lors de l'irradiation des cellules afin de minimiser les effets thermiques.

La largeur FWHM de 15 nm du spectre d'action doit être comparée à la largeur de 100 nm de la bande d'absorption autour de 1210 nm dans H_2O [Bayly *et al.* 63, Singh *et al.* 84]. Il n'y a pas de formation possible d'$^1O_2$ par transfert d'énergie dans l'eau excitée vibrationnellement pour induire de la mort cellulaire dans ces expériences. Par ailleurs, on peut remarquer qu'à 1247 nm, l'absorption du milieu de culture cellulaire est le même qu'à 1270 nm : cette longueur d'onde est donc un bon témoin thermique.

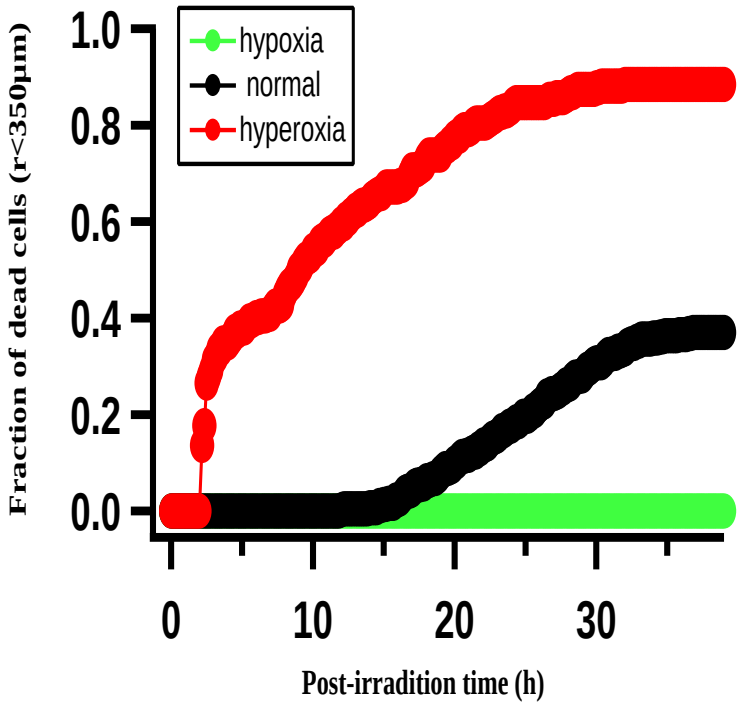

FIGURE 1.5 – Influence de la concentration en dioxygène dissout sur la mort cellulaire induite par une irradiation à 1270 nm ($200W.cm^{-2}$-1h30). Les expériences sont menées soit en conditions "normales" pour le milieu de culture (courbe noire, 80% N_2, 20% O_2, 5% CO_2), soit en hypoxie (points verts) ou hyperoxie (points rouges). Aucune mort cellulaire n'est observée en hypoxie alors que la population de cellules mortes est fortement augmentée en hyperoxie.

1.5 Production, réactivité de l'oxygène singulet et dosimétrie

1.5.1 Production et réactivité de l'oxygène singulet

Prédire un résultat thérapeutique en PDT nécessite entre autre la connaissance de la quantité d'espèces cytotoxiques générés. Dans ce contexte, une dosimétrie précise est nécessaire pour assurer un traitement complet avec des résultats cohérents et reproductibles pour les patients. Lorsque l'oxyène singulet est généré avec un PS, la dosimétrie implique un ensemble de complexes interactions dynamiques qui incluent le PS lui-même, la lumière, l'oxygène et les différentes cibles biologiques dans le tissu. On peut souligner des mécanismes différents, comme le photoblanchiment du PS, ou le bleaching de son état triplet par $^1O_2$ [Georgakoudi *et al.* 97, Dysart *et al.* 05] qui établissent une relation non triviale entre la lumière laser et de l' $^1O_2$ produit. Avec la génération directe d'$^1O_2$, la définition de la dose est directement liée avec la fluence de la lumière à 1270 nm.

Dans la littérature, il y a peu de données quantitatives quant à l'évaluation des sections efficaces d'absorption de la transition $O_2[^3\Sigma_g^-] \longrightarrow O_2[^1\Delta_g]$ à 1270 nm et

donc de la production d'$^1O_2$. Les premiers travaux sont ceux de Krasnovsky *et al.* dans des solvants organiques saturés en air [Jr. *et al.* 03, Jr. et Ambartzumian 04].

Une première étape à la détermination de mesures de production et de réactivités d'$^1O_2$ en cellule vivante a consisté à développer des expériences nouvelles pour étudier des cinétiques photochimiques en solution. Les résultats de ces études sont détaillés dans [Anquez *et al.* 10, Sivery *et al.* 13b, Sivery *et al.* 13a]. A terme ces études devraient conduire à développer des rapporteurs biologiques utilisables *in vitro* qui renseignent sur les réponses physiologiques des cellules au stress oxydant.

La production d'$^1O_2$ à 1270 nm est évaluée par la cinétique de réaction avec un piège chimique, que ce soit le 1,3-diphenylisobenzofuran (DPIBF) ou le rubrène qui sont connus pour réagir fortement avec $^1O_2$ en conduisant à la formation de produits oxydés selon ce schéma réactionnel :

$$^3O_2 + h\nu_{1270} \longrightarrow {}^1O_2 \tag{1.1}$$

$$^1O_2 \xrightarrow{k_d} {}^3O_2 + T \tag{1.2}$$

$$^1O_2 + T \xrightarrow{k_q} {}^3O_2 \tag{1.3}$$

$$^1O_2 + T \xrightarrow{k_r} TO_2 \tag{1.4}$$

L'oxygène singulet est ici produit *via* la transition $O_2[^3\Sigma_g^-] \longrightarrow O_2[^1\Delta_g]$ à 1270 *nm* [Anquez *et al.* 10] (réaction 1.1). k_d est la constante de pseudo vitesse de premier ordre de la cinétique de désactivation dans le solvant de l'oxygène singulet, définie comme suit : $k_d = 1/\tau_{^1O_2}$ où $\tau_{^1O_2}$ est la durée de vie de l'oxygène singulet en l'absence de piège chimique. T est le piège chimique, k_r est la constante de vitesse de réaction de d'$^1O_2$ avec T conduisant à la formation du produit oxydé TO_2. k_q est la constante de vitesse de désexcitation d'$^1O_2$ avec T par quenching physique. Les pièges chimiques utilisés sont très réactifs avec l'oxygène singulet : on a donc $k_q << k_r$ (limite de diffusion) [Ogilby 10].

Le produit oxydé étant incolore, on peut en mesurant sa variation d'absorbance, en déduire la quantité d'oxygène singulet ayant réagi. Pour suivre cette cinétique, une nouveau dispositif expérimental a permis de mesurer en temps réel la concentration du piège chimique et d'en tirer une expression analytique simple pour son taux de consommation. Cette vitesse de réaction dépend seulement de deux paramètres qui peuvent être exprimées en termes de constantes physiques basiques : l'indice de réactivité β [Higgins *et al.* 68] et la section efficace d'absorption σ_{1270} de la transition $O_2[^3\Sigma_g^-] \longrightarrow O_2[^1\Delta_g]$. L'indice de réactivité représente la concentration de piège chimique à laquelle le quenching d'$^1O_2$ par les molécules du solvant (k_d) est égale à la dégradation due au quenching total par le piège (k_r) : c'est en fait un bon estimateur de la réactivité du solvant où réagit $^1O_2$. L'intérêt de cette étude cinétique est que β et σ_{1270} peuvent être déterminés simultanément et indépendamment.

La variation du taux de consommation du piège chimique peut en fait se réécrire simplement à partir des équations 1.1, 1.2 et 1.4 :

$$\frac{d[T]}{dt} = -\frac{\Gamma}{1+\beta[T]^{-1}} \tag{1.5}$$

où $\beta = k_d/k_r$ est l'indice de réactivité et $\Gamma = \sigma_{1270} I[O_2]$ est le taux de production d'$^1O_2$ ($mol.L^{-1}.s^{-1}$) avec σ_{1270}, la section efficace d'absorption à 1270 nm (cm^2), I, le flux de photons et $[O_2]$, la concentration d'oxygène dissous dans le solvant ($mol.L^{-1}$) (Fig. 1.6).

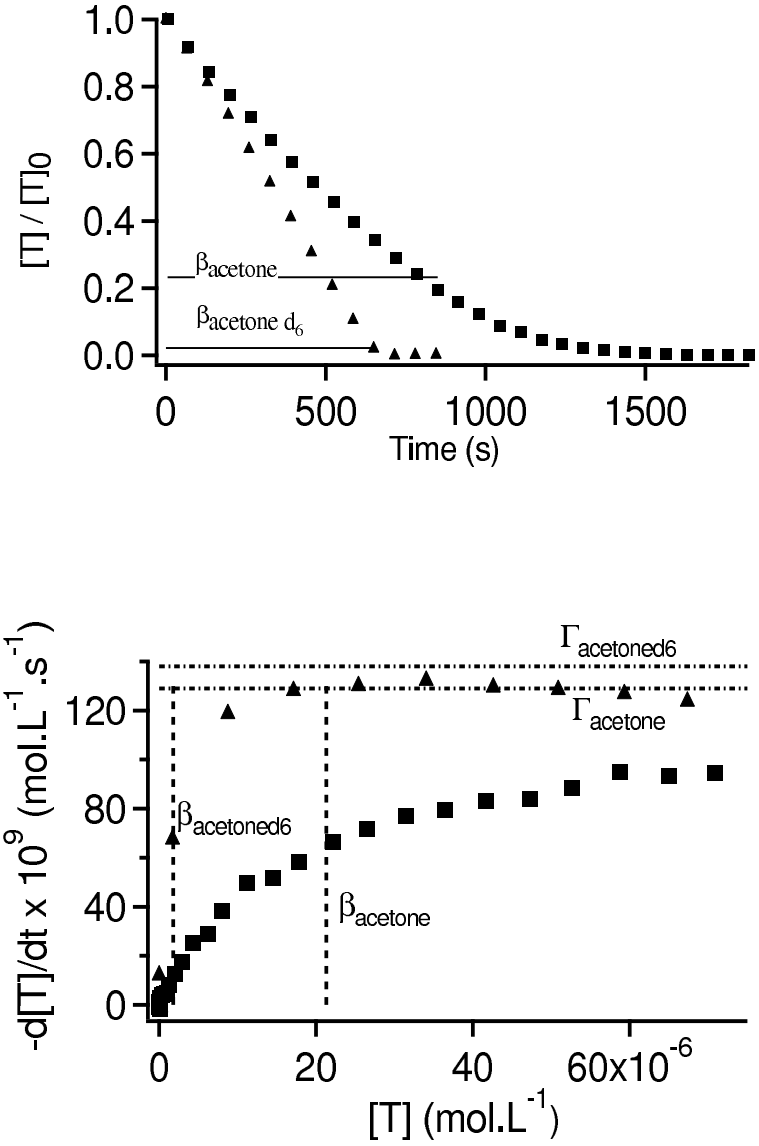

FIGURE 1.6 – Cinétique du DPIBF en solvant organique en présence d'oxygène singulet produit à 1270 nm. En haut, évolution de la concentration du DPIBF (renormalisée à sa concentration initiale $T_0 \sim 100\mu mol.L^{-1}$) dans l'acétone (carrés) et l'acétone d_6 (triangles). En bas, la même évolution dans la représentation de l'équation 1.5 où on peut évaluer indépendamment les paramètres β et σ_{1270}.

Cette méthode a tout d'abord été validée dans des solvants organiques et a permis d'obtenir des valeurs de β et σ_{1270} en très bon accord avec la littérature dans des

solvants organiques [Sivery *et al.* 13b].

Krasnovsky *et al.*, se sont récemment intéressés à l'excitation directe à 1270 nm de l'oxygène singulet dans l'eau (H_2O) et l'eau lourde (D_2O) [Jr. *et al.* 06, Jr. *et al.* 08]. Cette tâche est plus délicate à cause de deux raisons principales. En premier lieu, la concentration en dioxygène dissout est environ 10 fois plus faible dans l'eau que que dans les solvants organiques [Lide 09]. Il en résulte un taux de production dans l'eau proche de la limite de détection de la méthode avec de faibles puissances laser ($\sim 150\ mW$ à 1270 nm) [Jr. *et al.* 06]. Ce problème peut être en partie contourné grâce au laser de puissance développé au sein du laboratoire [Anquez *et al.* 10]. A cette première limitation, vient s'ajouter la non-solubilité du piège dans l'eau. En effet, DPIBF présente des parties hydrophobes qui provoquent sa cristallisation, dans l'eau à température ambiante, au bout d'un temps court [Jr. *et al.* 06].

Une collaboration avec l'équipe de chimistes du laboratoire de Chimie Moléculaire et Formulation de l'Université Lille 1 (C. Pierlot et J. M. Aubry) a permis d'obtenir des pièges chimiques solubles dans l'eau et ayant une grande réactivité avec $^1O_2$. Il s'agit du Rubrène TétraCarboxylique (tetrapotassium rubrene-2,3,8,9-tetracarboxylate) [Rigaudy et Cuong 62, Aubry *et al.* 81]. En suivant la cinétique de photo-dégrédation de ce piège, la section efficace d'absorption à 1270 nm a été évaluée dans D_2O $\sim 7.2 \times 10^{-24}\ cm^2$ et dans $H_2O \sim 7.6 \times 10^{-24}\ cm^2$. La valeur de section efficace dans H_2O est en très bon accord avec celle trouvée dans des mesures extrapolées d'encapsulation de DPIBF dans des milieux micellaires [Jr. *et al.* 08]. Fort de ces résultats, une estimation de la dose d'$^1O_2$ pour induire la mort cellulaire *in vitro* a pu être établie.

1.5.2 Dosimétrie d'un stress oxydant à 1270 nm

Dans les expériences d'irradiation à 1270 nm, il faut noter que le profil transverse du faisceau laser est gaussien (FWHM $\sim 300\mu m$), ce qui implique que les cellules subissent un stress oxydant qui dépend de leur position par rapport au centre du spot laser. Cette distribution est intéressante car elle permet de définir des doses seuils d'intensité I_{th} qui conduisent à la mort cellulaire (Fig. 1.7). Pour induire la mort cellulaire, le paramètre important est en fait la fluence $F_{th} = I_{th} \times \Delta t$ où Δt est le temps d'irradiation.

La concentration cummulée d'oxygène singulet créé s'écrit comme l'intégrale de son taux de production sur le temps d'irradiation. Cette définition est la même que celle utilisée par M. S. Patterson et ses collaborateurs [Dysart *et al.* 05]. Il s'agit de la concentration d'oxygène singulet totale créée ayant ou non réagi.

Dans le cas d'excitation direct le taux de production, Γ (s^{-1}) est à priori quasi-invariant dans le temps et la concentration d'oxygène singulet cummulée s'écrit :

$$[^1O_2]_{cum} = \int_0^{T_{irr}} \Gamma.dt = \Gamma \times T_{irr} = \sigma_{1270}.\frac{I}{h.\nu}.[^3O_2].T_{irr} \tag{1.6}$$

où T_{irr} est le temps d'irradiation (h), σ_{1270} la section efficace d'absorption (cm^2) conduisant à la production d'oxygène singulet, I l'intensité lumineuse ($W.cm^{-2}$) à 1270 nm, $[^3O_2]$ la concentration de dioxygène dans l'état fondamental ($mol.L^{-1}$). h

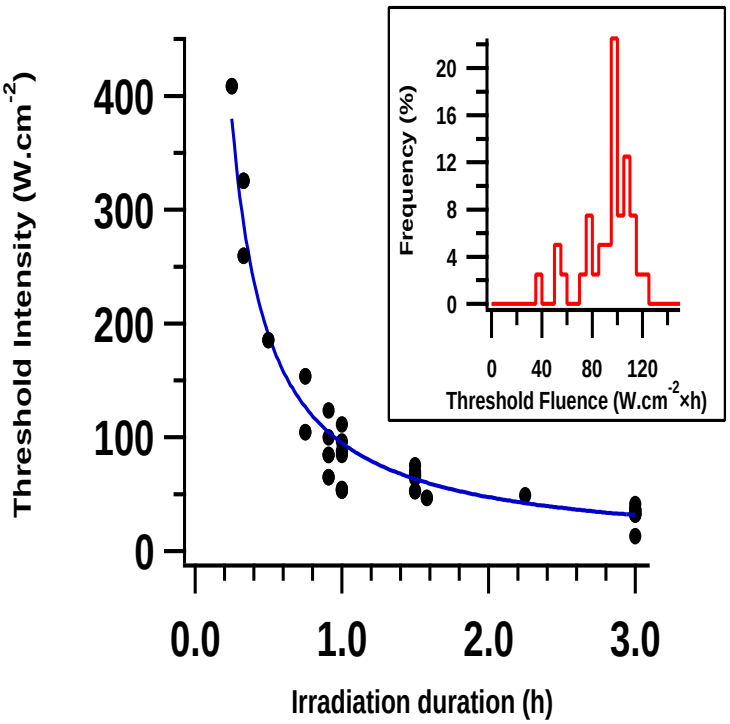

FIGURE 1.7 – Compilation d'expériences d'irradiation à 1270 nm pour la détermination des conditions seuils permettant d'induire la mort cellulaire. Dans ces expériences réalisées à 21 degrés pour minimiser les effets thermiques, l'intensité du laser (I) et le temps d'irradiation (δt) varient respectivement de 50 à 500 $W.cm^{-2}$ et 15 à 180 min. Le paramètre permettant de définir un seuil léthal n'est pas l'intensité seuil d'irradiation I_{th} mais la fluence $F_{th} = I_{th} \times \delta t = 95 W.cm^{-2}.h$ (représentée en bleu sur le graphe). En traçant un histogramme des valeurs F_{th} mesurées (encart), on trouve une valeur moyenne $F_{th} \sim 93 W.cm^{-2}.h$, en bon accord avec la valeur précédemment ajustée.

est la constante de Planck et ν la fréquence d'une radiation à 1270 nm donc $h.\nu$ représente l'énergie (J) d'un photon à cette longueur d'onde.

La section efficace d'absorption associée à la transition du dioxygène vers on état singulet est de l'ordre de $\sigma_{1270} \sim 10^{-23} cm^{-2}$ dans l'eau (voir section précédente).

La concentration en dioxygène dans les cellules est sensiblement égale à la concentration de dioxygène dissout dans le milieu de culture [Finikova *et al.* 08]. Cette dernière peut être estimée à partir de la concentration de dioxygène dissout dans l'eau à $25^{\circ}C$ qui vaut $[^3O_2] \approx 200\ \mu mol.L^{-1}$ [Lide 09]. Lee Koo *et al.* ont mesuré la concentration de dioxygène dissout dans des macrophages. Ils trouvent une valeur environ deux fois plus grande de $[^3O_2] \approx 433\ \mu mol.L^{-1}$ [Koo *et al.* 04].

Ainsi, à partir de la fluence seuil F_{th}, on peut donner un encadrement de la concentration cummulée d'oxygène singulet créée minimum nécessaire à la mort des cellules ($[^1O_2]_{seuil}$). On trouve entre $[^1O_2]_{seuil} \sim 4,6 \pm 0,7$ et $[^1O_2]_{seuil} \sim 9,2 \pm 1,4\ mmol.L^{-1}$ selon la valeur choisie pour la concentration de dioxygène. La dose minimum estimée se situe dans la gamme haute des valeurs disponibles dans la

littérature de la PDT ($[^1O_2]_{seuil} \sim 12 \pm 1\ mmol.L^{-1}$ [Georgakoudi *et al.* 97] ou encore $[^1O_2]_{seuil} \sim 8 \pm 2\ mmol.L^{-1}$ [Coutier *et al.* 01]). Il est probable que d'autres effets cytotoxiques, liés au photo-agent, soient à prendre en compte selon le type cellulaire et la nature du PS.

Conclusions et perspectives

Les études réalisées montrent pour la première fois qu'une excitation directe de l'oxygène singulet à 1270 nm sans PS est efficace pour induire la mort cellulaire, avec notamment la prise en compte des effets de température. Ces études peuvent aider à la compréhension des mécanismes en PDT qui est un système dynamique à plusieurs partenaires. On peut noter que l'excitation directe d'$^1O_2$ peut également fournir une référence pour les études en PDT afin de pouvoir discriminer les réactions de type I (radical) et de type II ($^1O_2$) dans les réponses au stress cellulaire.

Concernant la détection d'$^1O_2$ en cellule vivante, les expériences de cinétique chimique sont prometteuses car elles ouvrent la voie de mesures de réactivité avec des macromolécules impliquées dans le stress oxydant. Nous avons engagé une collaboration avec l'équipe "Nanobiointerfaces" de l'Institut de Recherche Interdisciplinaire de Lille (A. Barras et R. Boukherroub) pour rendre hydrophyle le DPIBF dans des nanoparticules lipidiques et l'internaliser dans des cellules afin de pouvoir mesurer la production d'$^1O_2$ ainsi que sa réactivité.

Une perspective très intéressante de ce projet concerne la réponse au stress oxydant d'une cellule unique. La production d'un stress spatialement localisé à l'échelle d'une cellule entière, ouvre la voie à l'étude d'effets de type bystander sur la propagation de signaux de stress. Ces effets peuvent être générés soit par la diffusion d'espèces réactives de longue durée de vie, comme par exemple H_2O_2, hors des cellules vers les cellules voisines [Redmond et Kochevar 06], soit par communication inter-cellules via les jonctions GAP [Dahle *et al.* 00]. En PDT, la sensibilité d'une cellule en réponse à un stress oxydant dépend de la vectorisation du PS dans différents compartiments cellulaires comme la mitochondrie, le cytoplasme, le noyau ou encore le reticulum endoplasmique (RE). Par exemple, des cellules présentant un déficit en respiration mitochondriale peuvent être moins sensibles en PDT : dans les travaux de Zhao *et al.*, la mitochondrie pourrait être une source d'ERO à faible dose de PDT [Zhao *et al.* 11]. Récemment, il a été aussi observé que le RE et les lysosomes sont aussi impliqués dans l'induction d'ERO lorsque les cellules sont photosensibilisées [Moserova et Kralova 12]. Dans ce contexte, la production directe d'$^1O_2$ est intéressante d'un point de vue de la réponse cellulaire. En effet, en PDT, la localisation du PS (membrane plasmique, lysosomes, noyau, mitochondrie...) génère une production d'$^1O_2$ elle aussi localisée dans les mêmes organites. En excitation directe à 1270 nm, en focalisant un laser dans l'organite d'intérêt, on a la possibilité de pouvoir adresser un stress résolu spatialement ($\sim \mu m$). Cette perspective est intéressante pour pouvoir identifier quels sont les compartiments cellulaires les plus sensibles à la génération d'$^1O_2$.

Une imagerie d'autres ERO permettrait aussi de savoir si en PDT, $^1O_2$ est directement impliqué ou s'il est amplifié dans des cycles pour produire de larges quan-

tités d'autres espèces cytotoxiques. Il existe aujourd'hui des senseurs fluorescents (HyPer) qui permettent non seulement de détecter mais aussi de doser le peroxyde d'hydrogène intracellulaire [Belousov *et al.* 06]. Il serait intéressant de coupler de telles sondes et observer leur dynamique avec l'induction d'un stress à 1270 nm.

Chapitre 2

Étude d'un réseau de régulation minimal : cas du stress thermique

2.1 Contexte et motivation

Il est intéressant de pouvoir proposer un modèle simple de réseau moléculaire de régulation de stress, qui est un système multi échelle partenaires, pour (i) prévoir des stratégies et des mécanismes de réponses (ii) évaluer les contributions des réactions majeures impliquées (iii) trouver les partenaires moléculaires clés comme senseurs du stress. Nous avons initié un nouveau projet autour du stress thermique car les mécanismes de régulation sont assez bien décrits dans la littérature et que l'activation par laser est un moyen de pouvoir contrôler finement les "séquences" temporelles du stress thermique. C'est dans ce contexte qu'a débutée la thèse d'A. Sivéry, avec une collaboration étroite avec Q. Thommen du groupe de "dynamique de régulation des réseaux génétiques " du PhLAM, afin de pouvoir confronter des expériences de suivi temporel de stress thermiques avec une modélisation simplifiée de ces cinétiques.

Lorsqu'une cellule est soumise à un stress thermique, les protéines peuvent se dénaturer et s'agglomérer en perdant leur activité biologique. Pour prévenir cette dénaturation, la cellule va alors produire des protéines chaperons pour renforcer la nature ternaire des protéines et restaurer leur conformation. Historiquement, les protéines associées à une réponse à stress thermique ont été appelées Heat Shock Proteins ou HSPs, même si elles peuvent être impliquées dans d'autres réponses cellulaires comme le stress oxydatif, la présence de métaux lourds ou l'infection virale [Linquist et Craig 88, Stewart et Young 04].

La réponse au choc thermique est caractérisée par l'activation de l'expression des HSPs, sous le contrôle de facteurs de transcription appelés « Heat Shock Factors » (HSFs). Chez les cellules eucaryotes, c'est la facteur de transcription HSF1 qui est le principal activateur transcriptionnel chez les mammifères [Mcmillan *et al.* 98]. L'activation d'HSF1 dans le mécanisme de réponse à un stress thermique est un processus complexe à plusieurs étapes et plusieurs partenaires [Cotto et Morimoto 99, Anckar et Sistonen 11] (Fig. 2.1). En cas d'élévation de la température la protéine HSF1 est libérée du complexe avec HSP70 et HSP90 et se trimérise : elle est alors transportée dans le noyau où elle est hyperphosphorylée et se lie à l'ADN

sur des cibles chromosomiques appelées "Heat Shock Element" (HSE) qui sont des zones promotrices des gènes Hsp. La transcription des principales protéines de choc thermique telle que HSP90 et HSP70 est ainsi activée, permettant de répondre activement au stress thermique. L'atténuation de la réponse au stress thermique implique les HSPs : elles vont réguler négativement l'activité d'HSF1 en le décrochant des HSE. Ces mécanismes vont permettre de réguler finement l'expression des chaperons moléculaires dans la réponse au stress thermique [Kregel 02, Akerfelt *et al.* 10].

Dans la réponse au stress thermique sur des cellules humaines, HSF1 ne se localise pas seulement sur les HSE mais il va aussi s'accumuler vers d'autres régions du génome riches en séquences répétées du satellite (sat) III, péricentromérique du chromosome 9, pour former des "granules" de stress ou Nuclear Stress Bodies (nSBs) [Cotto *et al.* 97, Jolly *et al.* 97, Jolly *et al.* 02]. Les nSBs sont des structures complexes et leur rôle pas complètement élucidé. Par exemple, les transcrits de sat III restent associés, plusieurs heures après leur synthèse à des facteurs d'épissage : les nSBs pourraient agir comme des centres répresseurs pour la transcription au sein du noyau ou avoir un rôle dans la structure et la fonction de la chromatine [Metz *et al.* 04, Chiodi *et al.* 04, Biamonti et Vourc'h 10]. Les nSBs ont des structures temporelles très riches associées à la réponse au stress thermique : ils peuvent être activés en seulement quelques secondes et présenter des relaxations de plusieurs heures suivant l'intensité et les répétitions de stress. Par ailleurs leur taille de 2 à 3 μm les rendent accessibles pour leur observation en microscopie [Sarge *et al.* 97, Jolly *et al.* 99].

Nos études sur le stress oxydant et l'activation à 1270 nm de l'oxygène singulet nous ont conduit à évaluer quantitativement les effets thermiques associés. L'activation d'un stress thermique par laser permet de contrôler i) temporellement des élévations de température induite sur les cellules ii) spatialement les zones où on induit un stress. C'est dans ce contexte, que nous nous sommes intéressés à la dynamique temporelle d'activation et de relaxation de nSBs sur une population de cellules HEK transfectées HSF1-GFP en microscopie de fluorescence. La transfection stable de ces cellules a été réalisée dans l'équipe du "Stress, Cancer et Dynamique de l'organisation du génome" de C. Souchier et C. Vourc'h de l'Institut A. Bonniot (Grenoble).

2.2 Modélisation de la réponse au stress thermique : cas d'un stress continu

La réponse au stress thermique est un processus complexe contrôlé par des mécanismes de régulation ayant des activations induites par le stress lui-même et des rétroactions avec des partenaires multiples [Anckar et Sistonen 11]. Dans ce contexte, il est important de proposer un modèle moléculaire pour le réseau génétique qui régule la réponse au choc thermique de manière à i) prévoir des stratégies et des mécanismes de stress thermique ii) évaluer les contributions des diverses réactions.

Nous avons choisi de modéliser dans un premier temps un premier réseau de régulation décrivant les cinétiques d'activation et de relaxation d'HSF1 pour des stress continus (41, 42, 43 degrés C - 4 heures) [Abravaya *et al.* 91]. Des modèles

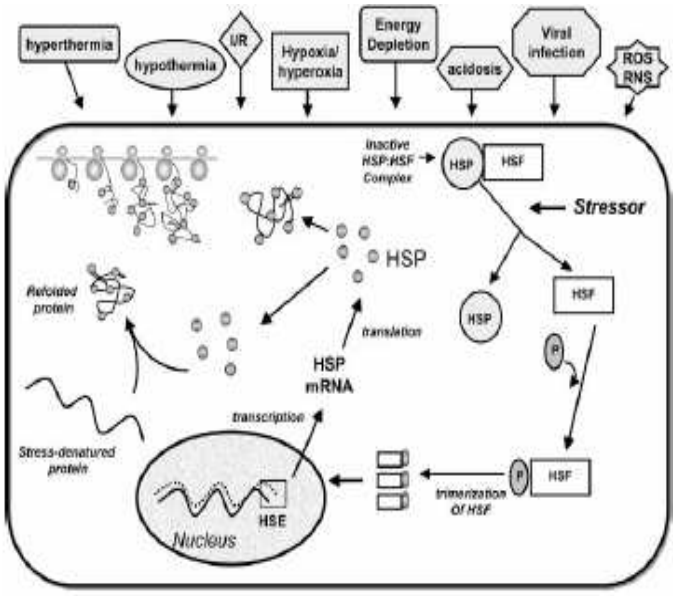

FIGURE 2.1 – Mécanismes de régulation du choc thermique [Kregel 02]. Sous l'effet d'une élévation de température, le nombre de protéines dénaturées augmentent nécessitant le recrutement de protéines chaperons (HSPs) pour leur éventuel renaturation et le complexe [HSF1 :HSP] (HSP70 et HSP90) va de dissocier. Les HSPs vont aller se fixer sur les protéines dénaturées et HSF1, initialement sous forme monomérique va se trimériser dans le cytosol puis se transloquer vers le noyau. Afin de pouvoir activer la transcription pour synthétiser de nouvelles HSPs, des modifications post-translationnelles d'HSF1 (phosphorylation, sumolylation et acétylation) vont permettre de se fixer sur des sites d'activation (HSE, Heat Shock Element) des régions promotrices des gènes hsp. Il y a alors transcription d'ARN messager qui va se transloquer du noyau vers le cytosol pour former de nouvelles HSPs. Lorsque les HSPs ont réalisé la renaturation des protéines, elles viennent à nouveau former un complexe [HSF1 :HSP] et stopper la transcription.

moléculaires existent dans la littérature pour décrire la réponse au choc thermique

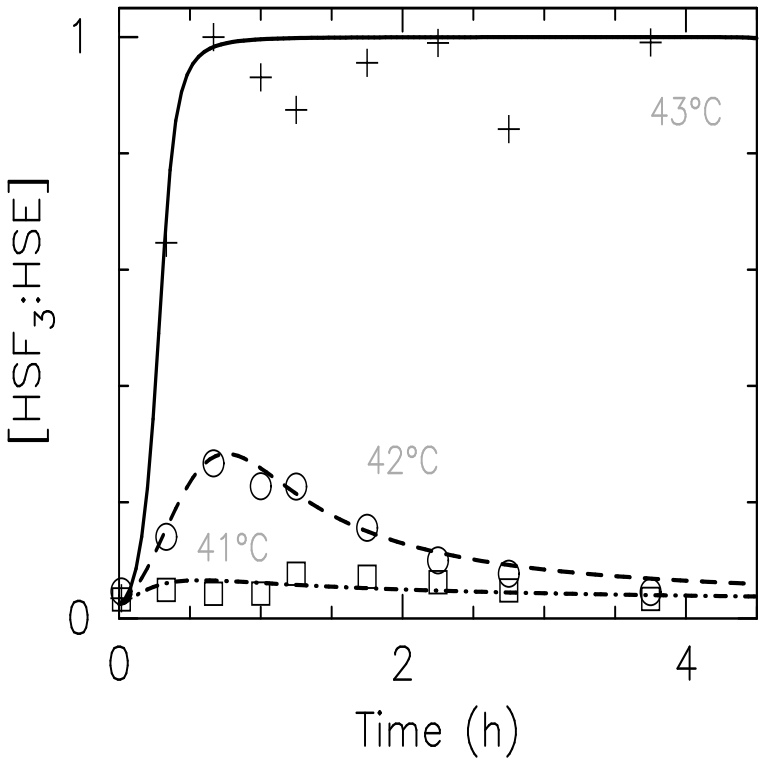

FIGURE 2.2 – Cinétique du complexe [HSF :HSE] décrivant la transcription durant un stress continu. On peut distinguer 3 régimes : lorsque la température du stress est inférieure à 42 degrés C (stress "normal") on observe une pseudo-adaptation thermique, entre 42 et 43 degrés C (stress "aigu") il y a une transcription active d'HSP alors que pour des températures supérieures à 43 degrés (stress "chronique") on a une accumulation des MFP et une transcription constante. Il y a un bon accord entre le modèle simplifié (traits) et les données (points) expérimentales de [Abravaya *et al.* 91].

chez les cellules humaines [Rieger *et al.* 05, Szymanska et Zylicz 09, Petre *et al.* 11] : ils décrivent les équilibres chimiques prenant en compte la dénaturation des protéines induites par la température, l'activité des HSPs et la rétroaction sur leur transcription au niveau du gène. Bien que ces modélisations soient très détaillées, elles ne permettent pas de rendre compte complètement de la cinétique d'activation et de relaxation d'HSF1 en fonction de l'amplitude et de la durée du stress (Fig. 2.2).

En vue de reproduire ces données expérimentales, et notamment l'activation constante d'HSF1 à 43 degrés, un paramètre clé dans la modélisation repose sur l'introduction d'une cinétique de type Michaelis-Menten qui tient compte de la saturation des ressources pour la dissociation du complexe [HSP :MFP] (Fig. 2.3). Ce type de mécanisme peut par exemple décrire la forme active de HSP90, impliquée dans le complexe [HSP :MFP]. En effet HSP90 est produite dans un cycle ATP-dépendant qui est un mécanisme où la saturation des ressources énergétiques peut-être important [Hessling et Buchner 09].

Afin d'avoir une intuition des mécanismes de réponse, nous avons aussi cherché

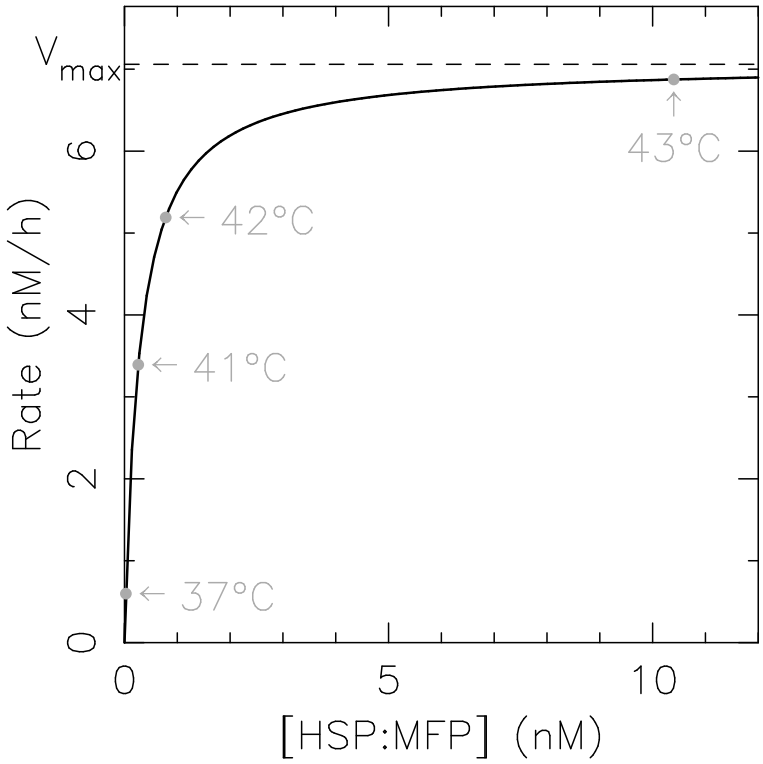

FIGURE 2.3 – Evolution en fonction de la température de la constante de dissociation du complexe [HSP :MFP] dans une réaction de type Michaelis-Menten. A 43 degrés, la vitesse de dissociation du complexe est maximum et peut-être liée à un cycle ATP-dépendant de la forme active (hyperphosphorylée) d'HSP90 [Hessling et Buchner 09].

une représentation plus simple, minimale, de la modélisation en se basant sur l'élimination adiabatique des variables rapides de la réponse au stress (trimérisation, modifications post-traductionnelles comme la phosphorylation sumoylation et acétylation, accrochage sur HSE, transcription d'ARN messager...) dans le cadre de stress continus. Avec ce réseau minimal, les résultats expérimentaux de [Abravaya *et al.* 91] peuvent en effet être reproduits avec 5 équations différentielles (au lieu de 27 dans les modèles actuels) (Fig. 2.4). La description de la réponse du stress thermique peut simplement s'expliquer en terme de dissociation du complexe [HSP :MFP] qui semble être le paramètre important pour expliquer l'adaptation thermique de la réponse. Grâce à ce modèle, nous avons trouvé un bon accord pour reproduire entre les données de [Abravaya *et al.* 91] (Fig. 2.2).

La simulation des cinétiques des différentes populations permet d'appréhender des mécanismes permettant de décrire la réponse à un stress thermique continu (Fig. 2.5). A 43 degrés, le complexe [HSF :HSP] se dissocie, les HSPs vont se lier sur les protéines dénaturées (MFPs) et HSP, une fois trimérisé va transcrire de nouvelles HSPs en formant un complexe [HSF :HSE]. 4 heures post-stress, le pool d'HSF suffit non seulement à chaperonner les MFPs (leur population retrouve leur niveau initial à 37 degrés) mais aussi à réprimer leur propre transcription. Par contre, la population des MFPs est telle que l'on est limité par la vitesse de transcription des HSPs par HSFs formant ainsi un plateau d'activation d'HSF. A 41 et 42 degrés, la

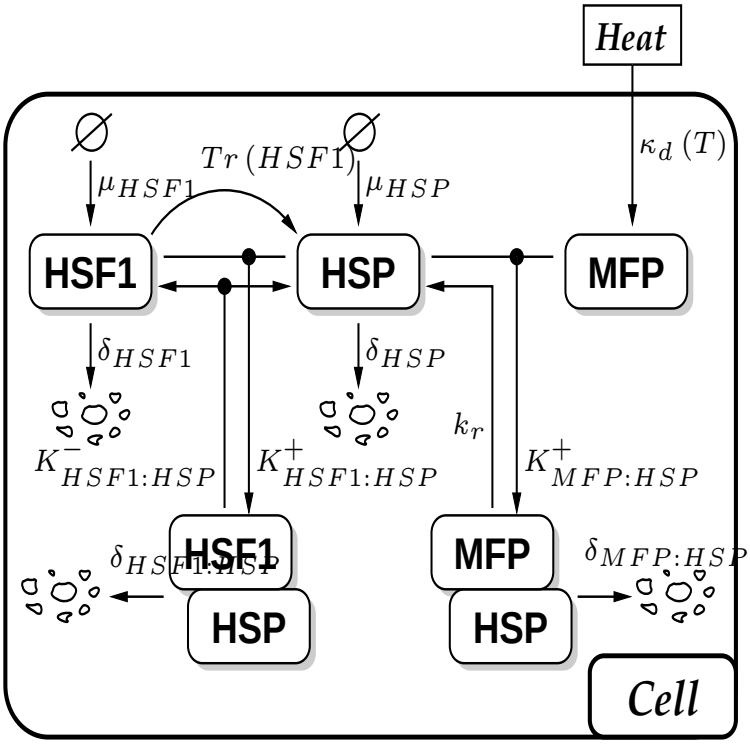

FIGURE 2.4 – Réseau moléculaire simplifié et minimal de régulation de la réponse à choc thermique continu. Dans les modèles actuels, la constante cinétique k_r est considérée constante dans la réaction $[HSP : MFP] \xrightarrow{k_r} MFP$ correspondant à la séquestration des HSPs. Afin de tenir compte d'un mécanisme limité (par exemple ATP dépendant), cette réaction est décrite par une équation de type Michaelis-Menten (saturation des ressources).

quantité d'HSF libre suffit quasi seule (très faible transcription de nouvelles HSPs à 42 degrés) à chaperonner les MFPs.

2.3 Cinétique temporelle des nSBs activés par chauffage laser

Avec le laser Raman décrit dans la section précédente, on peut induire des élévations de température jusqu'à des $\Delta T = 30$ degrés pour une puissance laser de 1 W (à 1250 nm) avec un objectif $40X$. Le profil thermique spatial, caractérisé avec de la rhodamine [Sakakibara et Adrian 99], est gaussien avec une largeur FWHM ~ 600 μm : on peut ainsi en repérant la position des cellules par rapport au centre du spot laser, avoir en une seule expérience, des cinétiques de choc thermique pour plusieurs élévations de température (Fig. 2.6).

Nous avons développé dans un premier temps des algorithmes permettant le suivi cinétique des granules de stress thermique (nSBs). On peut ainsi extraire des données quantitatives quant à la position (pour évaluer l'amplitude du stress thermique), l'amplitude et la taille des granules par cellule. Afin d'extraire les granules du fond de

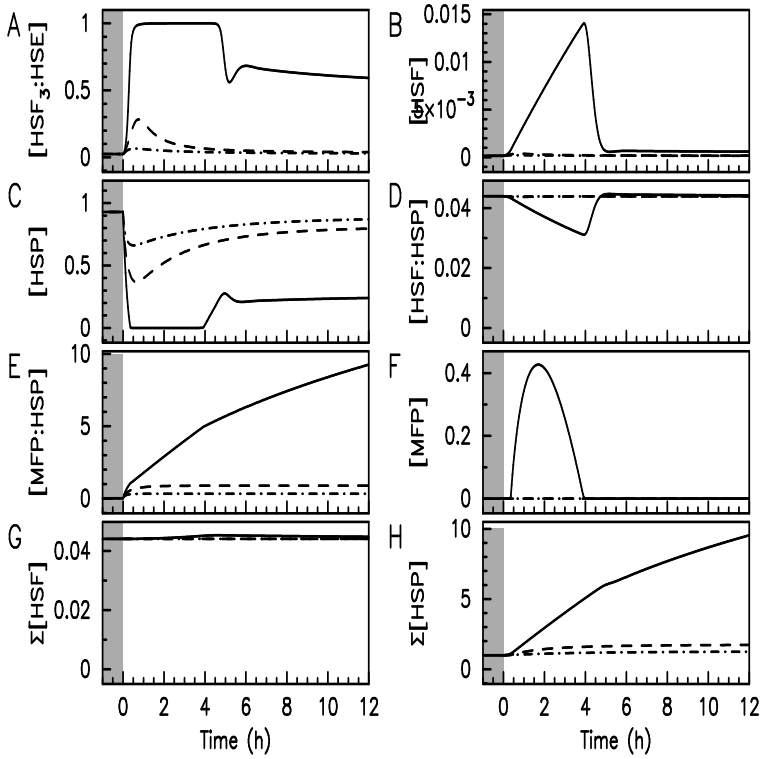

FIGURE 2.5 – Simulation des cinétiques des populations activées avec un stress continu à 41 (tirets points), 42 (tirets) et 43 (traits pleins) degrés avec le modèle simplifié. Avant chaque stress, on impose une température de 37 degrés à toutes les populations (aire grisée).

la cellule, les algorithmes utilisés reposent sur des techniques standard de traitement d'images. Dans un premier temps, un filtre médian permet de séparer les granules (variable rapide) des cellules (variable lente) : chaque pixel de l'image à filtrer est remplacé par la valeur médiane des pixels voisins. Le filtre médian est un filtre spatial non linéaire qui est très robuste à différents types de bruit, comme le bruit impulsionnel (bruit poivre et sel). La bonne performance du filtre médian pour ce type de bruit découle de la propriété de la médiane d'être, contrairement à la moyenne, quasiment insensible aux valeurs extrêmes. Enfin, ce filtre est bien adapté à la définition de contours contrairement aux filtres de flou, par exemple gaussien, qui réalisent une moyenne pondérée des valeurs dans le voisinage, avec un poids fort au centre du voisinage et faible à la périphérie. Le filtre médian conserve la netteté des contours : le bruit n'est pas étalé mais supprimé (Fig. 2.6) [Pitas et Venetsanopoulos 90]. Grâce au développement de traitement d'images, nous pouvons dès lors nous intéresser au suivi cinétique de formation et de relaxation de nSBs (Fig. 2.7). On peut noter que dans ce traitement d'images nous pouvons non seulement détecter les cellules et nSBs mais aussi obtenir des informations concernant leurs nombres, leurs tailles.

Nous utilisons le même dispositif expérimental que celui du stress oxydant en utilisant le laser Raman à 1250 nm. Le laser nous permet d'activer en moins d'une seconde des élévations de température jusqu'à 60 degrés. Le chauffage induit par

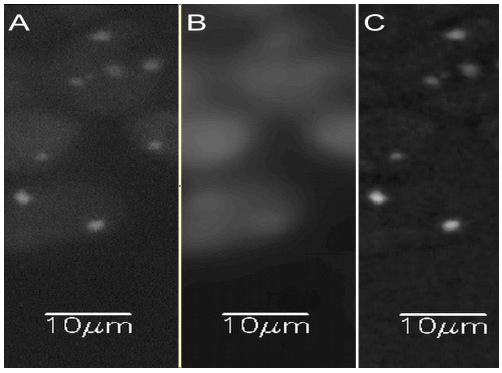

FIGURE 2.6 – Filtrage médian de nSBs. En (A) est représenté l'image brute en fluorescence de cellules HEK transfectée stablement HSF1–GFP et activant des nSBs (granules brillants) lorsqu'elles sont soumises à un stress thermique. La diploïdie des cellules HEK induit l'apparition de deux granules. En (B) est représentée la même image traitée par un filtre médian permettant d'obtenir les variations lentes d'intensité, i. e. les cellules. En (C), les granules apparaissent plus clairement en faisant la soustraction de l'image brute et filtrée : c'est à partir de cette image que l'on peut réaliser le suivi cinétique de nSBs lorsqu'ils sont activés.

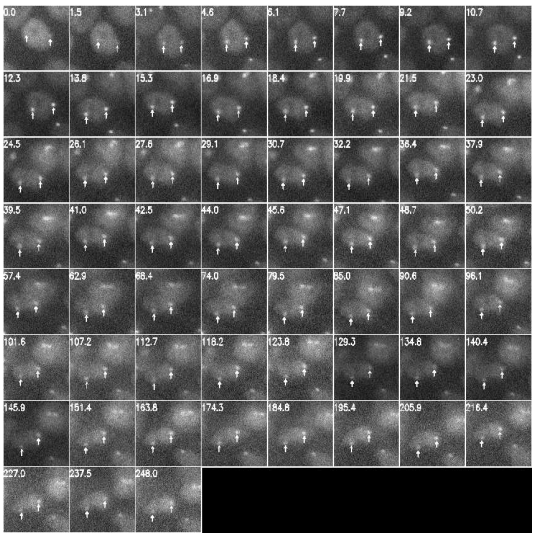

FIGURE 2.7 – Exemple de suivi cinétique de nSBs activés par un stress thermique (43 degrés continu - 4 heures) sur une cellule unique.

laser peut être modulé temporellement et permet de sonder des échelles de temps associés à la réponse au stress.

Pour des stress continus (Fig. 2.8), on retrouve des cinétiques (activation et relaxation) de nSBs comparables aux résultats de [Abravaya *et al.* 91] avec un plateau à 43 degrés (stress chronique), une relaxation à 42 degrés (stress aigu) et à 41 degrés

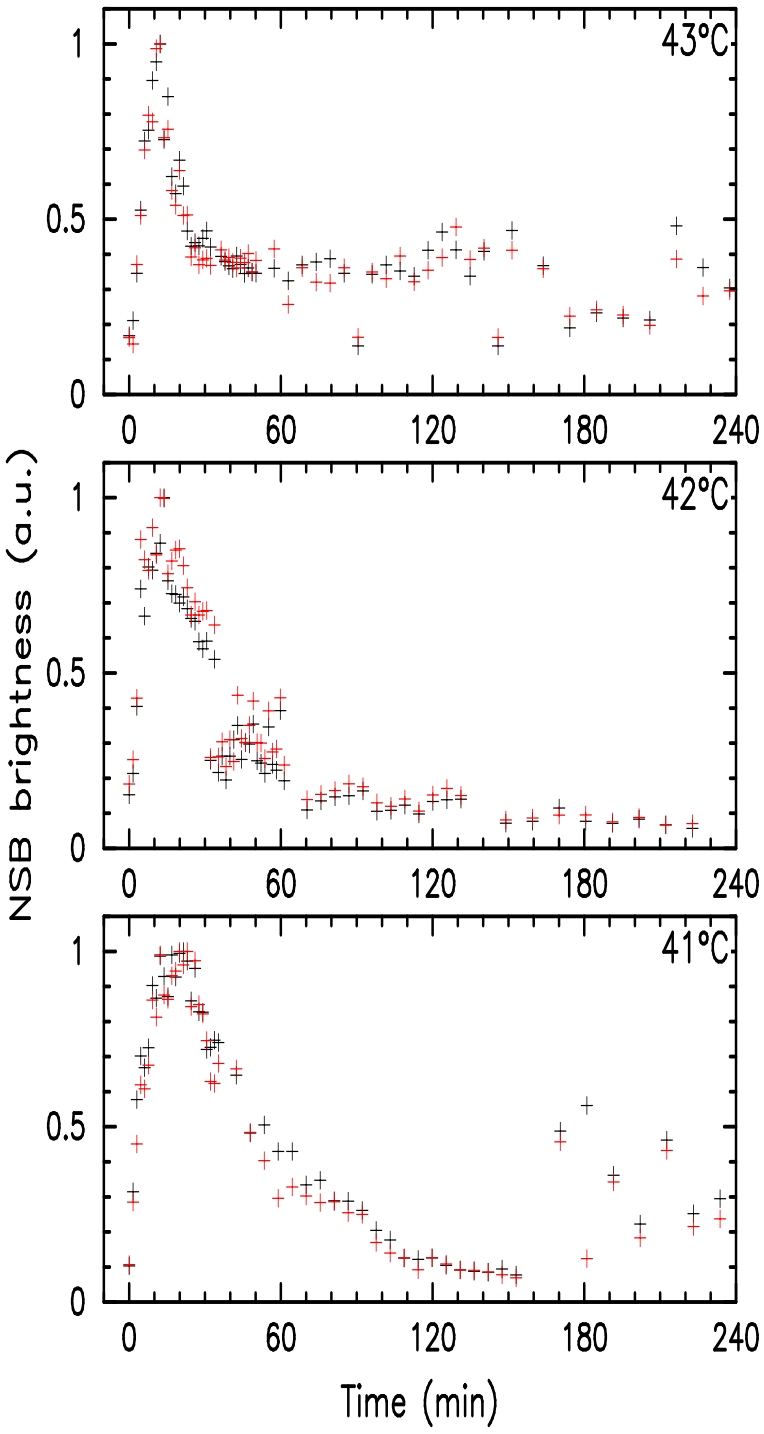

FIGURE 2.8 – Cinétique des nSBs pour des stress thermiques continus sur cellule unique. On retrouve les mêmes cinétiques pour chacun des granules (rouge et noir) d'une même cellule. Les cinétiques sont comparables aux résultats de [Abravaya *et al.* 91] avec un plateau à 43 degrés (stress chronique), une relaxation à 42 degrés (stress aigu) et à 41 degrés (stress normal). On observe une hyper activation des nSBs 5–10 post stress qui pourraient être associée à un remodelage chromatinien.

(stress normal). Il est intéressant de noter que la très bonne résolution temporelle expérimentale du suivi de fluorescence, permet l'observation d'une hyper activation des nSBs environ 5–10 minutes post-stress. L'une des pistes pour expliquer cette hyper activation serait liée à des échelles de temps associées au remodelage chromatinien. Un stress thermique induit un arrêt global de la transcription s'accompagnant d'une déacétylation et d'un changement de la structure chromatinienne liée à HSF1 alors que dans les nSBs, apparait une hyperacétylation [Fritah *et al.* 09, Akerfelt *et al.* 10]. Des études récentes de diffusion d'HSF1 dans des cellules HeLa soumises à un stress thermique ont montré un remodelage de la chromatine environ 15 minutes post stress [Landsberg *et al.* 12].

Conclusion du chapitre

La construction d'un modèle de régulation minimal met en évidence les ingrédients clés de la cinétique de la réponse au stress thermique corrélé avec les données expérimentales sur les nSBs. L'élément central de ce réseau est une compétition entre deux complexes impliquant les HSP : un avec HSF1 [HSF1 : HSP], et l'autre avec les MFP [MFP : HSP]. Le fait que l'affinité d'accrochage des deux complexes diffère de plusieurs ordres de grandeur implique la prévalence du complexe de renaturation [MFP : HSP] par rapport à celui de séquestration [HSF1 : HSP]. L'ingrédient clé qui a permis une description quantitative des données avec ce modèle minimal est l'introduction d'une cinétique de type Michaelis-Menten qui tient compte de la saturation des ressources pour la dissociation du complexe [HSP :MFP].

Le développement d'une expérience de suivi temporel de nSBs au niveau cellulaire couplée avec un réseau de régulation dans le cadre de stress thermiques continus, permet non seulement de reproduire les données obtenues expérimentalement, mais également de pouvoir faire des prédictions quant au comportement dynamique d'HSF1 vis-à-vis d'un stress thermique modulé temporellement. En se plaçant dans le cadre particulier de stress continus, nous avons aujourd'hui une bonne intuition des mécanismes impliqués et de leur dynamique temporelle. Les mécanismes réactionnels de réponse au stress thermique peuvent être associés à des échelles de temps très différentes, allant de la seconde pour des modifications post-traductionnelles (phosphorylation sumoylation et acétylation), à quelques heures pour l'expression d'HSP. Par exemple, on peut observer des pics d'expression d'HSP70 à 3 et 12h post stress thermique avec une translocation du cytoplasme vers le noyau entre 6 et 16h dans des expériences de suivi des cinétiques d'expression d'HSP70-GFP en microscopie [Wang *et al.* 08]. L'activation d'un stress thermique par laser permet de sonder et moduler différentes échelles de temps avec des temps de montée inférieure à la seconde. Dans ce contexte, il serait intéressant d'observer les dynamiques des nSBs, et d'HSP, avec des stress "courts" (quelques secondes à la minute) ou des stress répétés (thermotolérance) et pouvoir comparer ces résultats au modèle de régulation et ainsi le raffiner.

Le recrutement depuis un an d'A. Stankiewicz, post-doc en biochimie et biologie moléculaire, permet de compléter les études de la dynamique de nSBs par microscopie de fluorescence avec des méthodes biochimiques de type western blot ou immuno-

fluorescence. Cette collaboration permet non seulement d'obtenir des données quantitatives sur les partenaires impliqués dans le stress thermique ($(HSF1)$, $(HSF1)_{phospho}$, HSP90, HSP70) mais aussi de réaliser de nouvelles constructions cellulaires fluorescentes pour observer la dynamique en microscopie d'autres partenaires impliqués dans le stress.

Un autre axe de recherche aujourd'hui explorée est celui du couplage du modèle de régulation de la réponse à un stress thermique avec d'autres réseaux génétiques comme le cycle cellulaire (via l'interaction entre HSF1 et P53) avec comme réponse la viabilité cellulaire et une description plus raffinée de la thermotolérance. L'autre couplage est celui du stress thermique et oxydant avec des partenaires communs comme FOXO qui peut-être activé (phosphorylé) par des kinases JNK dans un stress oxydant [Essers *et al.* 04] et transcrire des déacétylases SIRT1 qui assure un meilleur accrochage d'HSF sur les HSE [Westerheide *et al.* 09].

Chapitre 3

Conclusion générale

Les travaux présentés dans ce mémoire synthétisent les activités de recherche d'une nouvelle thématique, initiée en 2006-2007 au laboratoire PhLAM, à l'interface entre physique, chimie et biologie sur la dynamique du stress en cellules vivantes. Le démarrage de cette activité, portant sur la possibilité d'induire de la mort cellulaire par excitation directe de l'oxygène singulet, draine aujourd'hui de multiples collaborations et de nouveaux axes de recherche dans une vision intégrative des questions biologiques avec notamment un couplage étroit entre expériences et modélisation. D'un point de vue expérimental, l'équipe est maintenant dotée d'une plateforme d'imagerie, d'une salle de culture cellulaire et d'interactions avec des biologistes (I. El-Yazidi Belkoura du laboratoire de Glycobiologie Structurale et Fonctionnelle de l'Université Lille 1) et chimistes (C. Pierlot, J. M. Aubry du laboratoire de Chimie Moléculaire et Formulation de l'Université Lille 1, A. Barras et R. Boukherroub de l'équipe "Nanobiointerfaces" de l'Institut de Recherche Interdisciplinaire de Lille). Une nouvelle collaboration avec V. Mezger du laboratoire d'épigénétique et destin cellulaire de l'Université Paris Diderot va aujourd'hui démarrer sur la dynamique de facteurs de transcription (HSF1 et HSF2) activés par un stress thermique. D'un point de vue des collègues physiciens du laboratoire PhLAM, la participation dès la genèse de ces activités de P. Suret et S. Randoux pour la partie optique, et aujourd'hui de Q. Thommen pour la partie modélisation, permet un développement et des projections pertinentes des activités dans une approche de biologie des systèmes. Les pistes explorées dans l'ensemble de ces activités ont été portées par des questions biologiques projetées dans une culture de physiciens à savoir des approches quantitatives des mécanismes au niveau temporel et spatial de la réponse au stress. Par ailleurs, les expertises développées dans l'équipe ont permis d'être impliqué aujourd'hui dans un important contrat industriel, entre une société de biotechnologie, le CNRS et l'Université Lille 1. Ce contrat implique 2 enseignants-chercheurs et 2 ingénieurs d'étude du PhLAM ainsi qu'un enseignant-chercheur de l'Institut d'Electronique, de Microélectronique et de Nanotechnologie de l'Université Lille 1. Le contrat qui a démarré en avril 2013 durera sur une période de 2 ans et conduira à une valorisation importante sous forme de brevet.

Concernant le côté spatial, un stress généré par laser permet de s'adresser soit à des populations de cellules et aller sonder des effets collectifs de type bystander, ou sur le rôle des communications extracellulaires, soit à l'organisation d'une cellule

unique. Sur ce dernier point, la possibilité de produire directement de l'oxygène singulet, sans localisation de photosensibilisant, pourrait permettre d'identifier quels sont les compartiments cellulaires les plus sensibles au stress oxydant ainsi que d'évaluer quantitativement les doses létales. Afin de compléter nos études à l'échelle d'une population de cellules, nous démarrons aujourd'hui une nouvelle activité liée au développement d'une imagerie à l'échelle de la molécule unique pour étudier l'organisation spatiale d'acteurs impliqués dans la réponse au stress à l'échelle intracellulaire.

L'induction d'un stress au niveau cellulaire par laser ouvre des perspectives de recherche intéressantes dans des expériences couplées à la microscopie optique. Dans le cadre d'un "chauffage" laser, on peut accéder à des cinétiques d'activation de stress très rapides (inférieure à la seconde) qui ne sont pas accessibles avec un bain marie (de l'ordre de 10 minutes) et ainsi aller sonder des échelles de temps de mécanismes réactionnels liés à la réponse cellulaire au stress. La modulation temporelle d'un stress permet, dans une approche de biologie des systèmes des voies de signalisation et de régulation, d'induire des formes de stress associées aux constantes de temps de l'organisation de la réponse au stress. En effet, les mécanismes de réponses à un stress sont des processus dynamiques multi échelles et multi partenaires impliquant une complexité de causes et d'effets dans des réseaux biologiques. La modélisation des réseaux moléculaires pour décrire ces mécanismes est une approche permettant non seulement d'appréhender la dynamique des partenaires clefs impliqués mais aussi d'avoir une description plus simple des dynamiques observées. L'intérêt d'une description a minima d'un réseau est de pouvoir étudier les régulations croisées du stress thermique avec d'autres réseaux comme le cycle cellulaire ou le stress oxydant.

Chapitre 4

Curriculum Vitae

Formation et Qualification

(2005–) Maître de Conférences (Laboratoire PhLAM/IUT A Mesures Physiques/Université de Lille 1)

Dynamique du stress en cellule vivante

Dynamique d'atomes froids dans un réseau optique de piège annulaire

(2004–2005) ATER (Laboratoire PhLAM/IUT A Mesures Physiques/Université de Lille 1)

Dynamique d'atomes froids dans un réseau optique de piège annulaire

(2002–2004) Post-doctorat (Dipartimento di Fisica Enrico Fermi/Pise, Italie)

Propriétés collisionnelles d'un mélange ultrafroid de Rb-Cs

Dynamique d'un condensat de Bose Einstein dans un réseau optique

Ionisation et superfluidité d'un condensat de Bose Einstein

(1997–2001) Thèse de doctorat (Laboratoire Kastler Brossel, Département de Physique de l'ENS, Paris)

Pompage Optique de l'He en conditions non-standard

(1996–1997) DEA "Laser et Matière" (Université Paris-Sud, Orsay)

(1992–1996) Maîtrise de Physique Fondamentale (Université Paul Sabatier, Toulouse)

Collaborations

– I. El Yazidi-Belkoura (Laboratoire de Glycobiologie structurale et fonctionnelle, Lille 1) pour les stress oxydant et thermique en cellule vivante

- V. Mezger (Laboratoire d'épigénétique et destin cellulaire, Université Paris Diderot, Paris) et Q. Thommen (PhLAM) sur le stress thermique en cellule vivante
- C. Pierlot et J. M. Aubry (Laboratoire de Chimie Moléculaire et Formulation, Lille 1) sur la photochimie sur les réactivités et cinétiques de l'oxygène singulet
- A. Barras et R. Boukherroub (Institut de Recherche Interdisciplinaire, Lille 1) sur le stress oxydant

Responsabilités administratives

- Responsable de la Licence Professionnelle « Métrologie en mesures environnementales et biologiques » à l'IUTA de l'Université de Lille 1
- Membre de la commission des spécialistes (section 30)
- Coordinateur de l'axe Physique Biologique et Médicale de la Fédération de Physique et Interfaces de l'Université de Lille 1

Enseignement

Au sein du département Mesures Physiques, j'ai pris la responsabilité des enseignements d'électrocinétique (cours, TD, TP) au S1 et depuis quatre ans j'ai mis en place de nouveaux enseignements en métrologie. Je suis responsable d'une nouvelle Licence Professionnelle « Métrologie en Mesures Environnementales et Biologiques » qui a ouvert à la rentrée 2010.

Encadrement

Encadrement de thèse

- Thèse d'A. Sivéry (2010-2014) : *Induction d'un stress oxydant et thermique par laser*
- Thèse de F. Anquez (2007-2010) : *Mort cellulaire induite in vitro par activation directe à 1270 nm de l'oxygène singulet*

Encadrement de Master 2 Recherche

- A. Sivéry (2009-2010) : *Création et détection d'oxygène singulet en solutions*
- C. Nouaim (2008-2009) : *Mesure par fluorescence d'un échauffement thermique par laser*
- F. Anquez (2006-2007) : *Interaction entre lumière et cellules cancéreuses : vers une nouvelle photothérapie de cancer*
- J. F. Clément (2004-2005) : *Dynamique d'atomes froids dans un réseau optique de pièges annulaires*
- N. Malossi (2002-2003) : *Propriétés collisionnelles d'un mélange ultra froid Rb-Cs*

– F. Marion (1999-2000) : *Spectroscopie jusqu'à 1.5 Tesla de l'hélium en phase gazeuse*

Encadrement de Master 2 Professionnel

– M. Askoura (2011-2012) : *Caractérisation de la mort cellulaire induite in vitro par activation optique directe à 1270 nm de l'oxygène singulet*
– M. Dewitte (2006-2007) : *Réalisation d'un microscope confocal*

Encadrement de Master 1

– M. Ducatillon (2013) : *Etude de la cinétique du stress oxydant et du stress thermique en cellules vivantes*
– Alexandre Baillieul (2011) : *Stress thermique en cellule vivante*

Publications

1. A. Barras, L. Boussekey, E. Courtade, and R. Boukherroub, *Hypericin-loaded lipid nanocapsules for photodynamic cancer therapy in vitro*, Nanoscale, in press (2013).
2. A. Sivéry, F. Anquez, C. Pierlot, J. M. Aubry, and E. Courtade, *Singlet oxygen ($^1O_2$) generation upon 1270 nm laser irradiation of ground state oxygen ($^3O_2$) dissolved in organic solvents : Simultaneous and independent determination of $^1O_2$ production rate and reactivity with chemical traps*, Chem. Phys. Lett. **555**, 252 (2013).
3. F. Anquez, I. El Yazidi-Belkoura, S. Randoux, P. Suret, and E. Courtade, *Cell death induced by direct laser activation of singlet oxygen at 1270 nm*, Laser Physics **23**, 025601 (2013).
4. F. Anquez, I. El Yazidi-Belkoura, S. Randoux, P. Suret, and E.Courtade, *Cancerous Cell Death from Sensitizer Free Photoactivation of Singlet Oxygen*, Photochem. Photobiol. **88**, 167 (2012).

   Article ayant fait la couverture de la revue Photochem. Photobiol. (janvier 2012) et remarqué dans un article "highlight" de M.R. Detty, Direct 1270 *nm* Irradiation as an Alternative to Photosensitized Generation of Singlet Oxygen to Induce Cell Death, Photochem. Photobiol **88**, 2 (2012). Article remarqué dans un communiqué de presse du CNRS, mars 2012.
5. F. Anquez, E. Courtade, A. Sivery, P. Suret, and S. Randoux, *A high-power tunable Raman fiber ring laser for the investigation of singlet oxygen production from direct laser excitation around 1270 nm*, Opt. Exp. **18**, 22928 (2010).
6. E. Courtade, O. Houde, J. F. Clément, P. Verkerk and D. Hennequin, *Dark optical lattice of ring traps for cold atoms*, Phys. Rev. A **74**, 031403 (2006).
7. D. Ciampini, E. Courtade, D. Cossart, C. Sias, G. Carelli, F. Mango, O. Morsch, and E. Arimondo, *Manipulation of ultracold atomic mixtures using microwave techniques*, Opt. Comm. **257**, 340 (2006).

8. E. Courtade, O. Houde, P. Verkerk and D. Hennequin,*Dynamics of atoms in a lattice of ring traps* , European Quantum Electronics Conference (IEEE), **227** (2005).
9. M. Anderlini, D. Ciampini, D. Cossart, E. Courtade, M. Cristiani, C. Sias, O. Morsch and E. Arimondo,*Model for collisions in ultracold atom mixtures*, Phys. Rev. A **72**, 033408 (2005).
10. M. Anderlini, E. Courtade, M. Cristiani, D. Cossart, D. Ciampini, C. Sias, O. Morsch and E. Arimondo, *Sympathetic cooling and collisional properties of a Rb-Cs mixture*, Phys. Rev. A **71**, 061401 (2005).
11. D. Ciampini, M. Anderlini, E. Courtade, D. Cossart, M. Cristiani, C. Sias, O. Morsch and E. Arimondo, *An ultracold Rb-Cs mixture in a magnetic trap*, European Quantum Electronics Conference (IEEE) **236** (2005).
12. B. Bhattacherjee, E. Courtade, and E. Arimondo, *Rotational bosonic current in a quasi-condensate confined in an optical toroidal trap*, J. Phys. B **37**, 4397 (2004).
13. M. Jona-Lasinio, O. Morsch, M. Cristiani, N. Malossi, J.H. Müller, E. Courtade, M. Anderlini, and E. Arimondo, *Nonlinear effects in periodic potentials : Asymetric Landau-Zener tunneling of a Bose-Einstein condensate*, Laser Phys. Lett. **3**, 147 (2004).
14. M. Cristiani, O. Morsch , N. Malossi, M. Jona-Jasino, M. Anderlini, E. Courtade, and E. Arimondo, *Instabilities of a Bose-Einstein condensate in a periodic potential : an experimental investigation*, Optics Express **12**, 4 (2004).
15. E. Courtade, M. Anderlini, D. Ciampini, J.H. Müller, O. Morsch, E. Arimondo, M. Aymar and E.J. Robinson, *Two-photon ionization of cold rubidium atoms with a near resonant intermediate state*, J. Phys. B **37**, 967 (2004).
16. M. Anderlini, E. Courtade, D. Ciampini, J.H. Müller, O. Morsch and E. Arimondo, *Two-photon ionization of cold rubidium atoms*, J. Optic. Soc. Am. B **21**, 480 (2004).
17. G. Tastevin, E. Courtade, S. Bordais and S. Grot, *A broadband ytterbium-doped tunable fiber laser for 3He optical pumping at 1083 nm*, Appl. Phys. B **78**, 145 (2004).
18. M. Jona-Jasino, O. Morsch, M. Cristiani, N. Malossi, J.H. Müller, E. Courtade, M. Anderlini and E. Arimondo, *Asymmetric Landau-Zener tunneling in a periodic potential*, Phys. Rev. Lett. **91**, 230406 (2003).
19. M. Anderlini, D. Ciampini, E. Courtade, F. Fuso, O. Morsch, J.H. Müller and E. Arimondo, *Dynamics of atoms in a lattice of ring traps*, Proceedings of the International Conference on Laser Spectroscopy (ICOLS 03)(2003).
20. E. Courtade, F. Marion, P.-J. Nacher, G. Tastevin, T. Dohnalik and K. Kiersnowski, *Magnetic Field Effecs on the 1083 nm Atomic Line of Helium ; Optical Pumping of Helium and Optical Polarisation Measurement in High Magnetic Field*, Eur. Phys. J. D **21**, 25 (2002).
21. G. Tastevin, E. Courtade, S. Bordais and S. Grot, *Fiber lasers tailored to helium optical pumping : atomic response to spectral characteristics*, Europhysics Conference Abstracts **26** C, 61 (2002).

22. P.-J. Nacher, E. Courtade, M. Abboud, A. Sinatra, G. Tastevin and T. Dohnalik, *Optical pumping of helium-3 at high pressure and magnetic*, Acta Phys. Pol. B **33**, 2225 (2002).
23. M. Leduc, P.-J. Nacher, G. Tastevin, and E. Courtade, *Kinetics of helium-3 Laser Optical pumping*, Hyperfine Interaction **127**, 443 (2000).
24. E. Courtade, F. Marion, P.-J. Nacher, G. Tastevin, T. Dohnalik and K. Kiersnowski, *Spectroscopy of the Helium 23S-23P Transition above 0.01 Tesla, Application to Optical Pumping Studies*, Hyperfine Interaction **127**, 451 (2000).
25. M. Leduc et E. Courtade, *Nouveaux lasers à fibre pour polariser les spins nucléaires d'un gaz d'hélium : applications médicales à l'Imagerie par Résonance Magnétique*, EDP Sciences **7**, 1 (2002).

Communications

Communications orales

1. F. Anquez, S. Randoux, P. Suret, I. El Yazidi-Belkoura and E. Courtade, *Oxidative stress in biological cells by direct optical excitation of singlet oxygen : towards new strategies for photodynamic cancer therapy*, International Meeting on Atomic and Molecular Physics and Chemistry 2013, Lille (France).
2. F. Anquez, I. El Yazidi, P. Suret, S. Randoux and E. Courtade, *Cell Death Induced by Direct Excitation of Singlet Oxygen at 1270 nm*, 20th International Laser Physics Workshop 2011, Sarajevo (Bosnie-Herzegovine).
3. F. Anquez, S. Randoux, P. Suret, I. El Yazidi-Belkoura and E. Courtade, Stress oxydant dans des cellules induit par excitation optique directe de l'oxygène singulet : vers de nouvelles stratégies pour la photothérapie photodynamique du cancer, JFLPI 2011, Lille (France).
4. F. Anquez, I. El Yazidi, P. Suret, S. Randoux and E. Courtade, *Cell Death Induced by Direct Excitation of Singlet Oxygen at 1270 nm*, 35th ASP meeting 2010, Providence (Etats-Unis).
5. F. Anquez, I. El Yazidi, P. Suret, S. Randoux and E. Courtade, *Oxidative Stress in Biological Cells by Direct Excitation of Singlet Oxygen*, Metamorphose 2010, Bruxelles (Belgique).
6. E. Courtade, M. Anderlini, D. Ciampini, J.H. Müller, O. Morsch, F. Fuso and E. Arimondo, *Two-photon ionization of cold rubidium*, Mid Term Review Meeting of the Cold Quantum Gases European Network 2003, Camogli (Italie).
7. E. Courtade, D. Ciampini, M. Anderlini, J.H. Müller, F. Fuso, O. Morsch, J.W. Thomsen and E. Arimondo, *Photoionisation of ultracold and Bose-Einstein condensed Rb atoms, Benasque 2002 workshop on Physics of Ultracold Dilute Atomic Gases*, Benasque (Espagne).

Communications par affiche

1. D. De Kuyssche, R. Charpentier, M. Penhoat, E. Courtade et P. Guarini, *Incertitude associée au dosage des micropolluants minéraux dans des eaux naturelles*

et résiduaires : disparités observées entre méthodes d'analyse lors d'essais interlaboratoires, Congrès International de Métrologie 2013, Paris (France).

2. A. Sivéry, Q. Thommen and E. Courtade, *Modeling of the eukaryotic heat shock response kinetics*, Molecular Chaperones and Stress Responses, Cold Spring Harbor Laboratory 2012 (Etats-Unis).
3. F. Devisscher, R. Charpentier, A. Treizebre, E. Courtade et Ph. Guarini, *Analyses en physico-chimie de base sur eaux naturelles : quantification des écarts entre méthodes grâce aux essais interlaboratoires*, Journées Information Eaux 2012, Poitiers (France).
4. A. Sivery, F. Anquez, I. El-Yazidi-Belkoura, Q. Thommen and E. Courtade, *Measurement and Modeling of Rapid Nuclear Stress Bodies Kinetics*, International conference on "Stress Proteins in Growth, Development and Disease" 2011, Barga (Italie).
5. A. Sivery, F. Anquez and E. Courtade, *Creation and Detection of Singlet Oxygen in Homogenous and Heterogenous Solutions*, 35th ASP meeting 2010, Providence (Etats-Unis).
6. F. Anquez, I. El Yazidi, P. Suret, S. Randoux and E. Courtade, *Optical Excitation and Detection of Singlet Oxygen : : Towards New Optical Tools to study the Oxidative Stress and Applications in Cancer Therapy*, 8th Winter Research Conference 2009, Oxidative DNA Damage, Les Houches (France).
7. E. Courtade, J. F. Clément, O. Houde, P. Verkerk and D. Hennequin, *Dynamique d'atomes froids dans un réseau de piège annulaire*, COLOQ 9 2005, Dijon (France).
8. J. F. Clément, E. Courtade, O. Houde, P. Verkerk and D. Hennequin,*Dynamique d'atomes froids dans un réseau de piège annulaire*, Congrès SFP 2005, Lille (France).
9. E. Courtade, O. Houde, P. Verkerk and D. Hennequin, *Dynamics of cold atoms in a lattice of ring traps*, ICOLS 2005 (International Conference on Laser Spectroscopy), Aviemore (Ecosse).
10. E. Courtade, O. Houde, P. Verkerk and D. Hennequin, *Dynamics of cold atoms in a lattice of ring traps*, Quantum Optics VI 2005, Krynica (Pologne).
11. E. Courtade, O. Houde, P. Verkerk and D. Hennequin, *Dynamics of cold atoms in a lattice of ring traps*, CLEO 2005 (Conference on Laser and Electro-Optics), Munich (Allemagne).
12. E. Courtade, M. Anderlini, D. Cossart, M. Cristiani, O. Morsch and E. Arimondo, *Collisional properties of an ultracold 87Rb-133Cs mixture*, International conference on Bose-Einstein Condensation 2004, Durham (Angleterre).
13. E. Courtade, M. Anderlini, D. Cossart, M. Cristiani, N. Malossi, O. Morsch and E. Arimondo, *Collisional properties of an ultracold 87Rb-133Cs mixture, 34th meeting of the Division of Atomic 2003*, Molecular and Optical Physics, Boulder (Etats-Unis).
14. E. Courtade, M. Cristiani, D. Ciampini, J.H. Müller, O. Morsch, and E. Arimondo, *Asymmetric Landau-Zener tunneling in a periodic potential*, Work-

shop on Nonlinear Dynamics in Classical and Quantum Mechanics 2003, Sammommé (Italie).

15. E. Courtade, M. Cristiani, D. Ciampini, J.H. Müller, O. Morsch, and E. Arimondo, *Creation of solitons and vortices by Bragg reflection of Bose-Einstein condensates in an optical lattice*, Workshop on Nonlinear Dynamics in Classical and Quantum Mechanics 2002, Sammommé (Italie).
16. E. Courtade, M. Anderlini, D. Ciampini, J.H. Müller, O. Morsch, F. Fuso and E. Arimondo, *Photoionisation of a BEC*, Lunteren 2002 7th International Workshop on Atom Optics and Interferometry, Lunteren (Hollande).
17. E. Courtade, P.-J. Nacher, C. Dedonder, C. Jouvet and T. Dohnalik, *Enhancement of the 3He2 (a3 ?u+) molecular state population by selective excitation of the 23P atomic state*, ECAMP VII 2001 (European Conference on Atomic and Molecular Physics), Berlin (Allemagne).
18. E. Courtade and P.-J. Nacher, *Spectral characterisation of 1083 nm lasers for optical pumping of helium*, ECAMP VII 2001 (European Conference on Atomic and Molecular Physics), Berlin (Allemagne).
19. E. Courtade, P.-J. Nacher and G. Tastevin, *Etude de la cinétique du pompage optique de l'hélium 3 gazeux, caractérisation d'un laser à fibre 2 Watts à 1.083 μm*, PAMO 2000 (Physique Atomique, Moléculaire et Optique), Lyon (France).
20. M. Leduc, P.-J. Nacher, G. Tastevin, and E. Courtade, *Kinetics of helium-3 Laser Optical pumping*, APAC 1999 (First Euroconference on Atomic Physics at Accelerators), Mainz (Allemagne).
21. E. Courtade, P.-J. Nacher, G. Tastevin, T. Dohnalik and K. Kiersnowski, *Study of hyperpolarised helium3 gas above 0.01 Tesla : spectroscopy of the 23S-23P states and efficiency of optical pumping*, ICOLS 1999 (International Conference On Laser Spectroscopy), Innsbruck (Autriche).
22. E. Courtade, P.-J. Nacher, G. Tastevin, T. Dohnalik and K. Kiersnowski, *Hyperpolarised helium-3 gas above 0.01 Tesla : Optical pumping techniques and applications to MRI*, ECAMP VI 1998 (European Conference on Atomic and Molecular Physics), Siena (Italie).

Chapitre 5

Publications

Publications atomes froids

480 J. Opt. Soc. Am. B/Vol. 21, No. 3/March 2004 Anderlini *et al.*

Two-photon ionization of cold rubidium atoms

Marco Anderlini, Emmanuel Courtade, Donatella Ciampini, Jörg H. Müller, Oliver Morsch, and Ennio Arimondo*

Istituto Nazionale per la Fisica della Materia, Dipartimento di Fisica E. Fermi, Università di Pisa, Via Buonarroti 2, I-56127 Pisa, Italy

Received July 11, 2003; revised manuscript received November 3, 2003; accepted November 12, 2003

Two-photon ionization cross sections from the rubidium ground state have been measured with both a cw 421-nm laser and a combination of cw 421- and 1002-nm lasers. The measurements were performed within a high-vacuum magneto-optical trap while the trapping lasers were switched off, exploiting the long trap lifetime and also the trap laser confinement. The two-photon cross sections were determined for the blue laser near resonance with the $6P_{1/2}$ and $6P_{3/2}$ states and compared with the estimates of a theoretical model. In near resonance with the $6P$ states, large two-photon photoionization cross sections were measured. © 2004 Optical Society of America

OCIS codes: 020.7010, 140.3320.

1. INTRODUCTION

The absolute determination of transition rates for multiphoton ionization represents a considerable experimental challenge. Those absolute measurements are, however, important in testing atomic structure calculations. Laser-cooled atomic samples have offered new tools for these ionization investigations, for instance, trap-loss ionization spectroscopy, i.e., the determination of the losses induced by a photoionization laser on a trapped sample of cold atoms. The photoionization rate can be precisely measured from the additional trap decay for atoms confined in a magneto-optical trap (MOT) or a magnetic trap. This technique was introduced by Dinneen *et al.*[1] for rubidium atoms in a MOT and later applied to the ionization of other alkali and alkali-earth atoms. Ciampini *et al.*[2] investigated the application of trap-loss spectroscopy to ultracold atoms, either thermal or condensed, confined within a magnetic trap.[3]

We applied trap-loss spectroscopy to determine the two-photon ionization cross section of laser-cooled ^{87}Rb atoms in the $5S_{1/2}$ ground state. The $6P$ states at 2.94 eV (421-nm excitation wavelength) above the $5S_{1/2}$ ground state were used as near-resonance intermediate states for the two-photon absorption. The ionization continuum was reached from the $6P$ states by absorption of either a second 421- or a 1002-nm photon of 1.24-eV energy, leading to ionization with respective excess energies ΔE = 1.70 eV and ΔE = 9.45 meV. cw radiation generated from laser diode sources was used for photoionization, and we achieved a nonnegligible photoionization fraction (as much as a few percent) by tight focusing of narrow-band laser radiation on the cold atomic cloud.

In a MOT the trapping lasers excite the cooled atoms to the first excited state, which are occupied with a fairly large probability. In the large majority of previous MOT photoionization experiments the ionization cross sections were then determined from this excited state. Our aim is to measure the two-photon ionization cross section from the ground state of ^{87}Rb atoms. To eliminate the contribution of photoionization from the excited state we alternated between the trapping lasers, which cool and spatially confine the atoms, and the photoionizing lasers, which produce the additional MOT loss. After the trapping lasers are switched off, the excited-state atoms return quickly to the ground state, and the photoionization laser will ionize ground-state atoms only. A small expansion of the atomic cloud occurs while the trapping lasers are off. Moreover, for a photoionization laser that is nearly resonant with an atomic transition, a real intermediate-state population may be produced that returns to the ground state with spontaneous emission of photons. That emission (from the $6P$ state in our investigation) increases the atomic temperature and hence modifies the atomic sample. To counteract these processes we switch the trapping lasers back on. In addition, strong focusing of the radiation that is nearly resonant with the intermediate state may lead to considerable dipole force acting locally on the cloud. The alternate operation of the MOT and photoionization lasers, with different time windows, allows us to keep these additional heating processes under control.

The ionized atoms that are unaffected by the MOT lasers constitute a trap loss. The nonionized atoms, by contrast, are recaptured and recooled by the trap lasers. Choosing the duty cycle of trap and loss phases allows us to tune the trap loss and therefore to operate the trap-loss spectroscopy with the highest accuracy. Furthermore, the long lifetime of the ultrahigh-vacuum (UHV) MOT enables us to detect correspondingly small loss rates with high sensitivity. Recently Lowell *et al.*[5] applied a similar approach of alternate application of photoionization and trapping lasers to measure the one-photon photoionization cross section of the $5S_{1/2}$ state of rubidium.

In Section 2 we describe the experimental setup. In Section 3 we introduce the basic elements of the photoionization process for the MOT atoms. In Section 4 we discuss our experimental findings and the results of photoionization as a function of the laser detuning, and in Section 5 we offer our conclusions.

0740-3224/2004/030480-06$15.00

2. EXPERIMENT

The experiment was performed in a MOT apparatus used for Bose–Einstein condensation as described in Ref. 6. Because previous studies showed[2] that, despite the advantages of magnetic traps such as better-defined geometry and more-accurate determination of the number of atoms, ionization losses in magnetic traps are prone to being masked by other processes, so we used magneto-optically trapped atoms here. We prepared the cold atom sample by loading 10^8 atoms from a high-vapor-pressure laser-cooled source into the UHV MOT. The atoms, which occupied a sphere of a little less than 2-mm diameter, were stored in the $F = 2$ hyperfine state at a temperature of 100 μK inside the UHV MOT. During photoionization, both the loading and the MOT confining lasers were blocked and the atomic cloud decayed at a rate γ that was due to collisions with the background gas and to intratrap collisions. We measured the number of atoms in the MOT and its dimensions by imaging the cold atomic cloud on a CCD.

To generate 421-nm radiation, a grating-stabilized diode laser operating at 842 nm was injected into a tapered amplifier that delivered power in excess of 500 mW. The 842-nm light was then frequency doubled by a lithium niobate crystal placed inside an external resonator (Model TA-SHG-100, Toptica). The 20-mW output power was tuned continuously over both the $5S_{1/2} \rightarrow 6P_{1/2}$ and the $5S_{1/2} \rightarrow 6P_{3/2}$ transitions. The 1002-nm laser source, based on a grating-stabilized laser diode (Model TEC 100, Sacher), provided ~60-mW output power. Both lasers operated in a free-running mode, and their frequencies were continuously monitored on a Fabry–Perot cavity. For the blue and infrared lasers we measured drifts of a few megahertz and a fraction of 1 MHz, respectively, over the 100-s acquisition time, determined by the MOT's decay lifetime. The wavelengths were measured on a wavemeter with 8-MHz resolution. Temporal control over the lasers was provided by acousto-optic modulators (AOMs). Synchronized pulse generators triggered the rf drivers for the MOT and ionization laser AOMs. The typical pulse length τ_{ph} for the ionization laser application was 2 μs.[7] The MOT lasers were switched off at least 0.5 μs before the start of an ionization pulse to leave ample time for the atoms to decay back to the ground state even in the presence of radiation trapping in view of the spontaneous-emission lifetime $\tau_{5P_{3/2} \rightarrow 5S_{1/2}} = 27$ ns of the $5P_{3/2}$ state. The residual MOT light transmitted by the AOM (extinction ratio, $\sim 1 \times 10^{-3}$) caused a small residual fraction of the $5P$ atoms ($\sim 1 \times 10^{-4}$) to be ionized by the 421-nm light. A numerical simulation of the ionization process allowed us to verify that the contribution to ionization from this residual $5P$ population was negligible compared with that of the $5S$ atoms that we are investigating. The ionized fraction per excitation pulse, with the MOT laser off, ranged from a fraction of a percent to a few percent, depending on the ionization wavelength. Repeating the ionization–trapping sequence several times, as many as 2×10^6 pulses in 100 s, caused the trap-loss rate to be large enough to allow for precise measurements.

Typically 3 mW of power of 421-nm radiation was focused within the trap to 30 μm $\times$ 90 μm, $w_{0x} \times w_{0y}$ laser beam waists; the elliptical character was due to the beam profile of the frequency-doubled blue light. We focused 25 mW of the infrared laser radiation down to 30 μm on the atomic cloud and aligned it parallel to the blue beam. The beam waists were measured in a setup outside the MOT, and we verified the spatial superposition of the lasers inside the vacuum chamber by using each photoionization laser separately to optically trap a Rb condensate created within the UHV chamber. The high intensity of the 1002-nm laser, ~1 kW/cm^2, produced dipole forces that deformed the atomic cloud, which we detected by using a Bose–Einstein condensate sample. The temperature increase of the cold Rb cloud owing to the 421-nm photon scattering from the $6P$ level was estimated to be ~6 μK for each ionization process and hence was easily compensated for by reapplication of the MOT lasers.

3. IONIZATION ANALYSIS

The ionization rate was derived from the change in the decay of the number N of trapped atoms after the application of the photoionization laser. The two-photon photoionization rate γ_{ph} produced by a weak laser with frequency ν_{ph} and intensity I_{ph} is given by

$$\gamma_{\mathrm{ph}} = \sigma_{5S}^{(2)} \beta^{(2)} \left(\frac{I_{\mathrm{ph}}}{h \nu_{\mathrm{ph}}} \right)^2, \tag{1}$$

where $\sigma_{5S}^{(2)}$ is the two-photon cross section and $\beta^{(2)}$ is a geometrical coefficient with the spatial distribution of the laser beam and the atomic sample taken into account.[2] For the one-color, two-photon ionization by a Gaussian laser beam with laser beam waists w_{0x} and w_{0y} centered on a Gaussian atomic distribution of sizes L_x and L_y, and assuming that the density distribution of the target atoms is not depleted by the laser, the geometrical correction is[9]

$$\beta^{(2)} = \frac{1}{\{[1 + 2(L_x/w_{0x})^2][1 + 2(L_y/w_{0y})^2]\}^{1/2}}. \tag{2}$$

A similar expression applies to the geometrical coefficient for two-color, two-photon ionization. The geometrical correction approaches unity for laser beam sizes larger than the atomic sample size. Equation (1), with a square dependence on laser intensity I_{ph}, is valid only at weak laser intensities I_{ph}, where the shifts and widths of the intermediate states, which are near resonance for the two-photon process, are not important.[10]

In the MOT's constant-density regime[11] and in the absence of loading, MOT number $N(t)$ decreases exponentially with rate γ. Applying the ionization laser additionally for a time τ_{ph} causes the probability for an atom to remain in the trap to be reduced; the decay in number of atoms is then described by

$$\frac{\mathrm{d}N}{\mathrm{d}t} = -\gamma N - \gamma_{\mathrm{ph}} N. \tag{3}$$

Therefore at the end of ionization time τ_{ph} the MOT number becomes

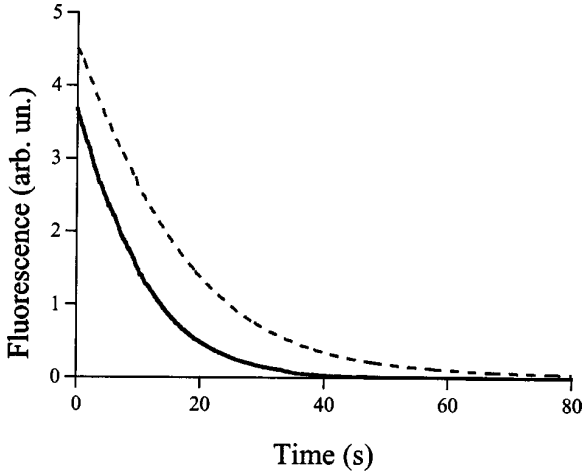

Fig. 1. Time decay for the fluorescence of the MOT Rb atoms in the absence (dashed curve) and in the presence (continuous curve) of the 421-nm laser. The ionizing laser, applied in pulses with $\tau_{ph} = 2\ \mu s$ and $r_{ph} = 20\ kHz$, had intensity $I_{ph} = 48.7\ W/cm^2$ and detuning $\delta = -16.8 \pm 12\ MHz$ from the $5S_{1/2}, F = 2 \rightarrow 6P_{1/2}, F' = 2$ transition.

$$N = N_0 \exp(-\gamma\tau_{ph})\exp(-\gamma_{ph}\tau_{ph}). \quad (4)$$

While one could produce a larger photoionization loss simply by increasing photoionization time τ_{ph}, the need to counteract heating and expansion of the cloud puts an upper limit on τ_{ph}. The minimum duration of a trapping and cooling phase is given instead by typical time constants for sub-Doppler laser cooling, i.e., tens of microseconds. Applying a sequence of pulses with duration τ_{ph} at a rate r_{ph} causes the number of atoms inside the trap to evolve as

$$N(t) = N_0 \exp(-\gamma t)\exp(-\gamma_{ph}\tau_{ph}r_{ph}t). \quad (5)$$

This decrease in the number of atoms is an exponential decay, with an effective ionization decay rate $\gamma_{ph}^{eff} = \gamma_{ph}\tau_{ph}r_{ph}$. We verified that this relation is valid by changing repetition rate r_{ph}, and thus the time between successive pulses, and obtained consistent results for γ_{ph}. Equations (4) and (5) are valid for weak ionization losses, not for modifying the MOT's dimensions L_x and L_y that appear in Eq. (2) for the $\beta^{(2)}$ parameter. In the presence of large depletion in the MOT number, as for a large number of ionization pulses, $N(t)$ can be derived through numerical integration of Eqs. (1) and (3).

Number of atoms N is proportional to the fluorescent intensity excited by the 780-nm trapping laser. Time evolutions for the fluorescent light emitted by the synchronously switched MOT, in the absence and in the presence of the ionizing lasers, are shown in Fig. 1. Decay traces consist of 1000 data points, each averaged over 100 ms. The dashed curve represents the fluorescence decay without the ionizing laser, produced by the background and by intratrap collisions. That evolution is well fitted by an exponential decay with $\gamma^{-1} = 16\ s$.[12] The continuous curve shows the fluorescence decay in the presence of the 421-nm ionizing laser, with a lower initial value because the high-vacuum MOT was loaded with the blue ionization laser switched on. The fluorescence decay in the presence of photoionization was fitted by an exponential decay with $(\gamma + \gamma_{ph}^{eff})^{-1} = 6\ s$. From the difference between the two decay rates we derived γ_{ph}^{eff}, and from that the two-photon ionization cross section $\sigma_{5S}^{(2)}$, by making use of Eq. (1).

4. RESULTS

We initially used the CCD images to verify that the MOT operated in a density-limited regime; the MOT volume varied linearly with the number of atoms in the MOT, N, as predicted in Ref. 11. Therefore we determined the changes in MOT radii L_x and L_y with the number atoms in the cold cloud depleted by photoionization. This information was required for the analysis of the photoionization losses.

We also tested whether photoionization was produced by two-photon absorption from the Rb ground state, for instance, for the one-color blue laser experiment with the expected quadratic dependence of the blue laser's intensity. Figure 2 shows our experimental results for photoionization rate γ_{ph} versus intensity I_{ph} of the blue laser at two laser detunings δ from the $5S_{1/2}F = 2 \rightarrow 6P_{3/2}F' = 3$ state. The quadratic fit to the photoionization rate confirmed the presence of one-color, two-photon ionization. The change in quadratic dependence as the laser detuning was varied agreed with the expected value. We also fitted the data of Fig. 2 by assuming simultaneous contributions from one-color, two-photon ionization from the ground state with a quadratic dependence on the blue laser's intensity and from one-photon ionization from a residual MOT-induced population in the excited $5P_{3/2}$ state with a linear dependence on the blue laser's intensity. The results of the fitting allowed us to estimate that the linear ionization rate from the excited states is 100 times smaller than the quadratic two-photon rate, at least for the range of laser detunings and intensities that we explored.

Figure 3(a) shows measured one-color, two-photon cross section $\sigma_{5S}^{(2)}$ as a function of detuning δ from the $6P_{1/2}$

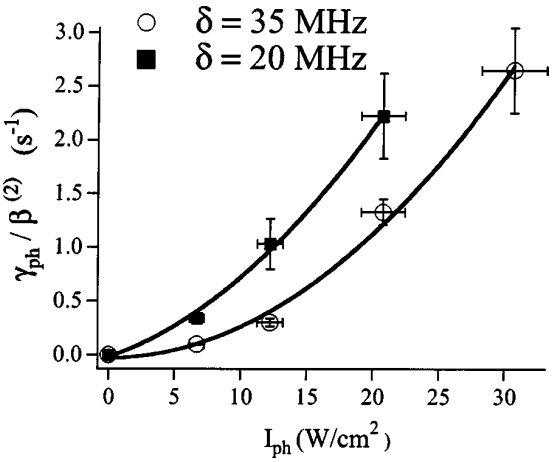

Fig. 2. Ratio $\gamma_{ph}/\beta^{(2)}$ for one-color, two-photon ionization of the Rb ground state by a 421-nm laser versus laser intensity I_{ph} for laser detunings δ from the $5S_{1/2}, F = 2 \rightarrow 6P_{3/2}, F' = 3$ transition at $\tau_{ph} = 2\ \mu s$ and $r_{ph} = 20\ kHz$. Solid curves, results of a fit with a quadratic dependence on the blue laser's intensity.

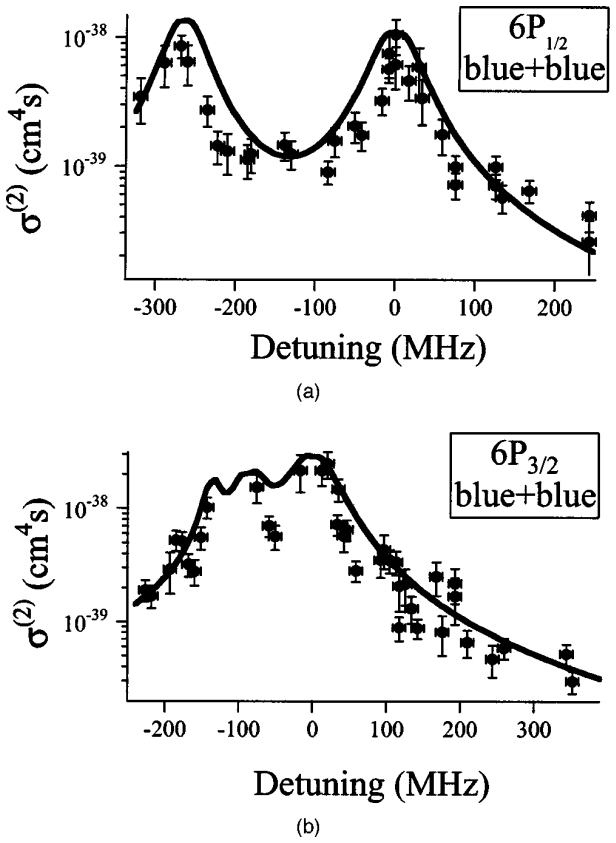

Fig. 3. One-color, two-photon cross sections $\sigma_{5S}^{(2)}$ for Rb $5S$ ionization by a 421-nm laser in near resonance with (a) the $6P_{1/2}$ intermediate state and (b) the $6P_{3/2}$ intermediate state, as functions of laser detuning. Solid curve, results of a numerical simulation without free parameters with the $6p \rightarrow$ continuum dipole moments described in the text.

state. The two peaks, at $\delta_2 = 0$ and $\delta_1 = \delta_2 - 265$ MHz, correspond to the $5S_{1/2}$, $F = 2 \rightarrow 6P_{1/2}$, $F' = 2$ and the $5S_{1/2}$, $F = 2 \rightarrow 6P_{1/2}$, $F' = 1$ transitions, respectively. Figure 3(b) shows the measured two-photon cross section as a function of detuning δ from the $6P_{3/2}$ state. The three peaks at $\delta_3 = 0$, $\delta_2 = \delta_3 - 51.5$, and $\delta_1 = \delta_2 - 51.5$ MHz correspond to the transitions from the $5S_{1/2}F = 2$ to the $F' = 3, 2, 1$ hyperfine levels of the $6P_{3/2}$ state. Data from several runs for the MOT ionization losses with different alignments of the MOT and ionization lasers are shown in the same figure. We analyzed photoionization runs with small ionization losses, and hence a small modification of the MOT radii, using Eq. (5). By contrast, photoionization runs with large number losses were analyzed through the numerical solution of Eq. (3), with the measured dependence of MOT radii, and hence of $\beta^{(2)}$, on number N taken into account. We noticed that a good fit of the $N(t)$ MOT decay was given by the exponential decay of Eq. (5), which introduced a $\beta^{(2)}$ value that was the average of the initial and final values, even when $\beta^{(2)}$ varied by more than 1 order of magnitude, for instance from 0.05 to 1 at the ionization peak with 2×10^6 ionization pulses over the 100-s acquisition time. The scatter in the $\sigma_{5S}^{(2)}$ data and in their uncertainties was highly sensitive to the optical overlap between MOT and photoionization lasers. In the presence of a slight misalignment the photoionized atoms experienced a photoionization laser intensity I_{ph} that was different from the peak value inserted into Eq. (1), so $\beta^{(2)}$ was not determined exactly from Eq. (2). The cross-section uncertainty shown in Fig. 3 is due to the uncertainty in $\beta^{(2)}$ and to the standard deviation for the fit of the temporal dependence of N in the presence of the ionization laser. The uncertainty in the I_{ph} laser intensity resulted in a negligible contribution to the cross-section error bar. For good optical alignment a good fit of the dependence of N on time allowed cross-section determinations with small error bars, depending only on the uncertainty in $\beta^{(2)}$. Moreover, we noticed that the smallest uncertainty in the determination of $\sigma_{5S}^{(2)}$ was achieved for repetition rate r_{ph} such that ionization rate $\gamma_{\mathrm{ph}}^{\mathrm{eff}}$ was nearly equal to collisional decay rate γ.

The maximum value of the cross section was $\sim 10^{-38}$ cm^4 s. By comparison, a theoretical analysis of one-color, two-photon ionization of cesium in the vicinity of the second excited P intermediate-state resonance, which explored a range of large detuning only, produced a maximum value for the cross section near 10^{-43} cm^4 s at 2-GHz detuning from the intermediate state.[13] Our investigation, however, demonstrates that large photoionization cross sections are reached with narrowband lasers operating near resonance with an intermediate level. The theoretical results at large detuning cannot be used to extrapolate to the small detunings of our investigations, and an *ad hoc* theory is required.

In two-color (421 + 1002), two-photon photoionization, the high intensity of the infrared laser, $\sim I_{\mathrm{ph}} = 1$ kW/cm^2, and the larger ionization rate associated with the smaller excess energy ($\Delta E = 9.45$ meV) lead to higher losses from the MOT. Figure 4 shows the measured two-color, two-photon cross section $\sigma_{5S}^{(2)}$ as a function of detuning δ from the $5S_{1/2}$, $F = 2 \rightarrow 6P_{1/2}$, $F' = 3$ transition. As for the one-color ionization, data from several runs with different alignments of the MOT

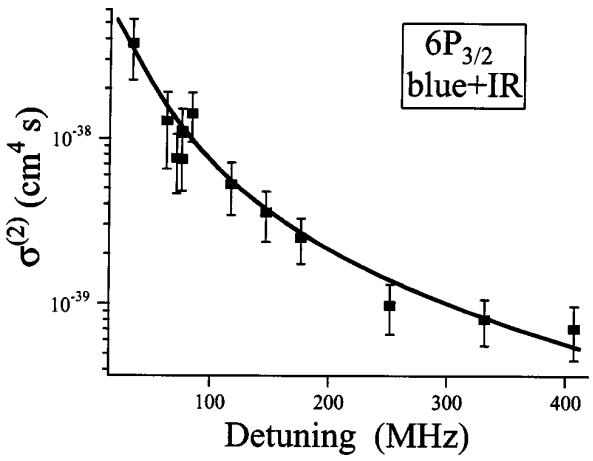

Fig. 4. Two-color, two-photon cross sections $\sigma_{5S}^{(2)}$ for Rb $5S$ ionization by 421 + 1002-nm lasers near resonance with the $6P_{3/2}$ intermediate state as a function of the blue laser detuning from the $5S_{1/2}$, $F = 2 \rightarrow 6P_{3/2}$, $F' = 3$ transition. Solid curve, results of a numerical simulation without free parameters with the $6p \rightarrow$ continuum dipole moments described in the text.

and ionization lasers are shown in the same figure. Also, here the cross-section error bars and the scatter in the data reflect mainly the uncertainty in the determination of the geometrical factor $\beta^{(2)}$. To derive the ionization cross section from the analysis of the two-color data we included the few-percent contribution to the ionization rate by one-color, two-photon ionization at 421 nm. For the intermediate laser at $\delta = 33.6\,\mathrm{MHz}$ from $5S_{1/2}F = 2 \rightarrow 6P_{3/2}F' = 3$, a maximum cross section of 4×10^{-38} cm^4 s was measured.

We simulated the ionization data by numerical integration of the equations that describe the interactions of the lasers with the discrete and continuum atomic states. Atomic states filled by cascade decay and optical pumping were also included in the model. The calculation, without free parameters, used estimates for the dipole matrix elements to the continuum as input parameters. For one-color, two-photon ionization, dipole moments of 2.7 atomic units for the $6p \rightarrow \epsilon s$ transition and of -5.9 atomic units for the $6p \rightarrow \epsilon d$ transition were used,[14] whereas the $5S_{1/2} \rightarrow 6P$ dipole moments were derived from the $6P$ lifetimes.[8] The ionized fraction derived from the numerical integration allowed us to derive a value for the two-photon ionization cross section and its dependence on detuning. The continuous curves in Figs. 3 and 4 show the results of the calculations, which are in good agreement with the experimental data. The description of ionization by a single two-photon cross section, in both the experimental analysis and the model, automatically takes into account the two-step and one-step processes that contribute nonlinearly to ionization for near-resonance excitation.[10]

5. CONCLUSIONS

In conclusion, we have used an original technique for the absolute determination of the ionization cross sections from ground state atoms confined in an ultrahigh-vacuum magneto-optical trap. The method, an extension of trap-loss measurements, requires only relative measurements of time constants and does not require absolute calibration of the number of atoms. The high sensitivity achieved by the alternate application of trapping and ionizing lasers within a high-vacuum MOT allowed us to measure the ionization rate produced by weak cw lasers on a cold atomic sample.

We investigated the alkali photoionization for near-resonant excitation of the intermediate state, leading to two-photon cross sections that were much larger than those typically measured with pulsed lasers at larger detunings. In those conditions with near-resonance complications, the simple I_{ph} dependence that we used to fit our data may be questioned. In effect, the simultaneous excitation of several intermediate states may produce shifts and broadenings of the intermediate states, thereby modifying the quadratic dependence.[10] It should be noted that our experimental investigation was performed with laser intensities larger than those typically applied in laser cooling experiments but still much weaker than those applied in the pulsed regimes of most multiphoton ionization experiments. Furthermore, our laser sources have a narrow bandwidth, and therefore the simultaneous excitation of several intermediate states was negligible, as demonstrated by the resolution of the hyperfine splitting within the ionization spectra. In summary, the high resolution achieved by cold atomic sources and narrowband lasers permitted the exploration of an ionization regime in which the lowest-order multiphoton perturbation theory is still valid.

The limitation of our present approach is connected to the residual population in the $5P$ states after the MOT lasers are switched off. In the present investigation, with an extinction ratio of 1×10^{-3} we were able to measure large photoionization cross sections near resonance with an intermediate state. To measure weak photoionization cross sections, for instance in our case at detunings from resonance larger than 300 MHz for which the cross section is reduced by 2 order of magnitude, careful control of the residual MOT light is required. In fact, Ref. 5 reported that weaker photoionization cross sections from the Rb ground state were measured in a Rb MOT by insertion of a long delay time between switching the MOT laser off and the photoionization laser on to reduce the residual MOT light. We could produce a strong additional decrease of the atomic excitation owing to residual MOT light by shifting the MOT laser frequency far from the resonance line during the photoionization phase. With this additional control the present technique may be used for investigation of other regimes of ionization with narrowband lasers, with highly accurate results.

ACKNOWLEDGMENTS

The authors are grateful to M. Aymar for providing us with atomic structure data and to E. Robinson for useful comments on rubidium photoionization. This research was supported by the Sezione A of the Istituto Nazionale per la Fisica della Materia—Italy through a PAIS project, by the MIUR-Italy through a COFIN Project, and by the European Commission through the Cold Quantum-Gases Network contract HPRN-CT-2000-00125.

*E-mail address: arimondo@mail.df.unipi.it.

REFERENCES AND NOTES

1. T. P. Dinneen, C. D. Wallace, K. N. Tan, and P. L. Gould, "Use of trapped atoms to measure absolute photoionization cross section," Opt. Lett. **17**, 1706–1708 (1992).
2. D. Ciampini, M. Anderlini, J. H. Müller, F. Fuso, O. Morsch, J. W. Thomsen, and E. Arimondo, "Photoionization of ultracold and Bose–Einstein-condensed Rb atoms," Phys. Rev. A **66**, 043409 (2002).
3. Another important application of work with trap-loss includes molecular spectroscopy, as reviewed in Ref. 4.
4. F. Masnou-Seeuws and P. Pillet, "Formation of ultracold molecules via photoassociation in a gas of laser cooled atoms," Adv. At., Mol., Opt. Phys. **47**, 53–127 (2001).
5. J. R. Lowell, T. Northup, B. M. Patterson, T. Takekoshi, and R. J. Knize, "Measurement of the photoionization cross section of the $5S_{1/2}$ state of rubidium," Phys. Rev. A **66**, 062704 (2002).
6. J. H. Müller, D. Ciampini, O. Morsch, G. Smirne, M. Fazzi,

INSTITUTE OF PHYSICS PUBLISHING JOURNAL OF PHYSICS B: ATOMIC, MOLECULAR AND OPTICAL PHYSICS

J. Phys. B: At. Mol. Opt. Phys. **37** (2004) 967–979 PII: S0953-4075(04)73090-4

Two-photon ionization of cold rubidium atoms with a near resonant intermediate state

E Courtade[1], M Anderlini[1], D Ciampini[1,4], J H Müller[1,5], O Morsch[1], E Arimondo[1], M Aymar[2] and E J Robinson[3]

[1] INFM, Dipartimento di Fisica E Fermi, Università di Pisa, Via Buonarroti 2, I-56127 Pisa, Italy
[2] Laboratoire Aimé Cotton, Centre National de la Recherche Scientifique, Bâtiment 505, 91405 Orsay Cedex, France
[3] Physics Department, New York University, 4 Washington Place, New York, NY 10003, USA

E-mail: arimondo@df.unipi.it

Received 28 November 2003
Published 17 February 2004
Online at stacks.iop.org/JPhysB/37/967 (DOI: 10.1088/0953-4075/37/5/002)

Abstract

By means of a simple theoretical model and experimental results, we analyse the two-photon ionization of cold rubidium atoms. We consider a two-step process in which ground state atoms are ionized by two blue (421 nm) photons, chosen to be quasi-resonant with the 5S → 6P transition. We show that for a good description of the process we have to take into account not only the three states coupled by the laser radiation, but also all the atomic states involved in the spontaneous emission cascade from the 6P to the 5S state, since optical pumping from $5S_{1/2}$ ($F = 2$) to the $5S_{1/2}$ ($F = 1$) states modifies the ionization efficiency when ionizing near resonance. The experimental and theoretical determination of ionization cross sections for excitations near resonance with the $6P_{1/2}$ and the $6P_{3/2}$ intermediate levels is presented.

1. Introduction

The recent development of laser cooling and trapping techniques allowing the controlled production of dense and cold clouds has opened the path to spectroscopic investigations not easily accessible with conventional techniques. Cold atoms in magneto-optical traps (MOT) have been used as excellent tools for the absolute measurements of ionization cross sections. In laser cooled atomic samples, the investigation of the trap population dynamics represents a sensitive monitor of the ionization processes, allowing the extraction of accurate values for the cross sections and their wavelength dependences. In this paper, we discuss an investigation of the ionization process through the losses from a cold cloud inside a MOT. This technique was

[4] Present address: Atomic Physics Division, National Institute of Standards and Technology, Gaithersburg, MD, USA.
[5] Present address: Niels Bohr Institute, Copenhagen, Denmark.

0953-4075/04/050967+13$30.00

introduced by Dinneen *et al* [1] for rubidium atoms, and later applied to other investigations in rubidium [1–5] as well as in other alkali and alkaline-earth atoms. In [6] trap loss spectroscopy was applied to ultracold Rb atoms, both thermal and condensed, confined within a magnetic trap.

In a MOT the trapping lasers excite the atoms to the first excited state, occupied with a fairly large probability. In order to measure the two-photon ionization cross section from the ground state of ^{87}Rb atoms, eliminating the photoionization contribution from the excited state, the trapping lasers that cool and spatially confine the atoms and the photoionizing lasers, which produce the additional MOT loss, are applied alternatively [5, 7]. After switching off the trapping lasers, the excited state atoms return quickly to the ground state, and the photoionization laser may ionize the ground state atoms only. A small expansion of the atomic cloud occurs while the trap is off. Moreover for a photoionization laser nearly resonant with an atomic transition, a real excited state population may be produced that returns to the ground state with the emission of spontaneous photons. That emission (from the 6P state in our investigation) increases the atomic temperature and hence affects the atomic sample. For balancing these processes the trapping lasers are turned back on within a few μs. The ionized atoms unaffected by the MOT lasers lead to a trap loss. The non-ionized atoms, in contrast, are recaptured and cooled by the trap lasers. This alternate operation of trap and loss phases allows one to tune the trap loss in order to operate the trap loss spectroscopy in the highest accuracy regime. Furthermore, by applying a very long sequence of alternate trap/photoionization lasers and accumulating the photoionization MOT losses, we make maximum use of the long lifetime associated with the confining high vacuum trap. Thus, a very high sensitivity in the cross section determination is reached.

In the present experimental determination of two-photon ionization cross section of cooled rubidium atoms in the $5S_{1/2}$ ground state by trap loss spectroscopy, the 6P state at 2.94 eV (421 nm wavelength excitation) above the $5S_{1/2}$ ground state is used as the near resonant intermediate state for two-photon absorption. The ionization is reached from the 6P state by absorbing a 421 nm photon, leading to ionization with an excess energy of 1.70 eV.

The ionization data are analysed by numerical integration of the equations describing the interactions of the lasers with the discrete and continuum atomic states. The ionized fraction derived from the numerical integration allows us to derive an estimate for the two-photon ionization cross section and the detuning dependence. Our analysis is based on estimates of the bound–free dipole moment that represent an essential part of this work. As the photoionization experiment is performed with a narrow band laser interacting with an excited state for a time longer than the excited state lifetime, spontaneous decay into lower lying states determines the photoionization process. Thus atomic states filled by the spontaneous decay cascade are included in the model. One-photon ionization from all these states is also considered. The spontaneous cascade transfers population into a dark hyperfine level of the 5S atomic ground state. As a consequence of this optical pumping (OP) phenomenon a fraction of the atoms is lost to the photoionization. OP decreases the photoionization efficiency with a larger reduction at longer times of interaction with the photoionization laser.

As pointed out by Lambropoulos [8], in a correct model of the photoionization process the first and second steps of the ionization should be considered to be a single process, mainly because of the nonlinear coupling between the one-step and the two-step channels. Therefore we analyse the ionization data through the two-photon ionization cross section, even though this coupling is less important for the present investigation based on low intensity lasers. The theoretical description of the ionization process may be based on the Schrödinger equation, as for instance applied to caesium atoms in [9], or instead through Bloch equations for the discrete atomic states where the ionization process appears as a damping rate for the populations and

coherences, as for instance in [10]. By following the second approach the coherent excitation of the 5S–6P transition is described using the density matrix formalism, and instead of the 6P ionization the interaction with the laser field is taken into account through an extra relaxation rate term.

Section 2 recalls the model for photoionization-induced trap loss. Section 3 describes the experiment. Section 4 discusses the theoretical determination of the ionization cross sections from the excited states involved in the present investigation. Section 5 describes the two-photon ionization model and discusses the OP process in the photoionization efficiency. Section 6 concludes the present investigation.

2. Trap loss spectroscopy

The dynamics of the number N of trapped atoms in a MOT, with the trap loading shut off and in the constant density regime [11], predicts an exponential decay, with a time constant $1/\gamma$, determined by collisions with the background gas and intra-trap collisions. In the presence of ionization by a continuous wave (cw) laser, additional losses, described by a photoionization rate, shorten the lifetime of the trap. For a cold rubidium cloud composed of atoms in the ground state, the two-photon ionization rate $\Gamma_{5S}^{(2)}$ produced by a single laser with frequency ν_{ph} and intensity I_{ph} can be written as [6]

$$\Gamma_{5S}^{(2)} = \sigma_{5S}^{(2)} \beta^{(2)} \left[\frac{I_{ph}}{h\nu_{ph}} \right]^2 \tag{1}$$

with $\sigma_{5S}^{(2)}$ being the two-photon ionization cross section which may take into account both coherent and incoherent ionization processes, with single-step and two-step contributions. The geometrical correction coefficient $\beta^{(2)}$ takes into account the spatial distribution of the laser beam and the atomic sample. For typical ionization experiments with pulsed lasers, equation (1) with a square dependence on the laser intensity I_{ph} is valid only when the shifts and widths of the intermediate states near resonance for the two-photon process are not important [8]. In the regime of weak laser intensities but long interaction times in which we operate, the saturation of the optical transitions also modifies the ionization process. Therefore, the proper use of the ionization cross section should be tested.

In the presence of an ionization process, the decay of the MOT number N becomes [1]

$$\frac{dN}{dt} = -\gamma N - \Gamma_{5S}^{(2)} N. \tag{2}$$

If the photoionization laser is applied in a sequence of pulses at a repetition rate r_{ph}, each of them for a time τ_{ph}, at the time t after $r_{ph}t$ pulses the number of atoms remaining in the trap is

$$N(t) = N_0 \, e^{-\gamma t} \, e^{-\Gamma_{5S}^{(2)} \tau_{ph} r_{ph} t} \tag{3}$$

with N_0 being the initial value. On time scales much longer than r_{ph}^{-1}, the decrease in the atom number is an exponential decay with rate $\gamma + \Gamma_{5S}^{(2),eff}$, where the photoionization process is described through the effective ionization decay rate

$$\Gamma_{5S}^{(2),eff} = \Gamma_{5S}^{(2)} \tau_{ph} r_{ph}. \tag{4}$$

The ionization cross section $\sigma_{5S}^{(2)}$ is derived from the measured $\Gamma_{5S}^{(2),eff}$ making use of equation (1).

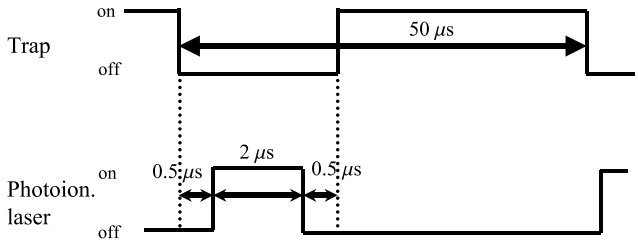

Figure 1. Timing diagram for the trapping lasers (trap) and the photoionizing laser. After switching off the trapping lasers in a 0.5 μs dark time the 5P excited state atoms return to the ground state. Then a 2 μs duration pulse of the 421 nm laser ionizes the atoms in the ground state. The trapping lasers are turned back on for a 47 μs period to cool down the non-ionized atoms, after which the whole sequence is repeated.

3. Experiment

Photoionization investigations are performed in the high vacuum MOT optimized for collecting Rb atoms. The MOT trap is filled with an atomic cloud less than 2 mm in diameter with 10^8 atoms in the $F = 2$ hyperfine state at about 100 μK temperature [7, 12]. The 20 mW power of the 421 nm photoionizing radiation, generated by frequency doubling a tapered amplifier, is tuned continuously over both the $5S_{1/2} \rightarrow 6P_{1/2}$ and $5S_{1/2} \rightarrow 6P_{3/2}$ transitions. This radiation is focused on a 30×90 μm^2 waist within the trap [7]. The ionizing laser is applied as a 2 μs pulse with a Gaussian rise time $\tau_{\text{rise}} \sim 0.14$ μs controlled by an acousto-optic modulator. During the application of the 421 nm ionizing radiation the MOT loading process is blocked (see figure 1). In order to compensate for any heating of the atomic cloud due to the 6P spontaneous emission in the case where the photoionization laser is nearly resonant, the trapping lasers are turned back on to cool down the non-ionized atoms for a 47 μs period.

In the absence of the photoionization laser the atomic cloud inside the high vacuum MOT decayed with a $1/\gamma$ lifetime, owing to the collision with the background gas and MOT intra-trap collisions. The fluorescence decay in the presence of photoionization was fitted by an exponential decay with $\left(\gamma + \Gamma_{\text{ph}}^{(2),\text{eff}}\right)^{-1}$ lifetime. From the difference between the two decay rates we derived $\Gamma_{\text{ph}}^{(2),\text{eff}}$ and the two-photon cross section.

Initially we tested the validity of equation (1) stating that the photoionization rate $\Gamma_{5S}^{(2)}$ is proportional to the square of the laser intensity I_{ph}, at least for the blue laser detuned out of resonance. Results are shown in figure 2 for different laser detunings δ from the $5S_{1/2}, F = 2 \rightarrow 6P_{3/2}, F' = 3$ transition. The quadratic fit to the photoionization rate confirmed the role of the one-colour two-photon ionization process. The change in quadratic dependences varying the laser detuning agreed with the expected one. From the numerical analysis reported in section 5 it results that the predicted quadratic dependence is not exactly verified for very small laser detunings.

Figure 3 reports the measured two-photon photoionization rates $\Gamma_{5S}^{(2)}$, divided by the geometric factor $\beta^{(2)}$, as a function of the laser detuning δ for the $5S_{1/2}, F = 2 \rightarrow 6P_{1/2}, F'$ transitions. The peaks in the spectrum of the ionization cross section correspond to resonances with the hyperfine levels of the $6P_{1/2}$ state. The two peaks at $\delta = 0$ and $\delta = -265$ MHz correspond to the $5S_{1/2}, F = 2 \rightarrow 6P_{1/2}, F' = 2$ and $5S_{1/2}, F = 2 \rightarrow 6P_{1/2}, F' = 1$ transitions. Figure 4 reports the measured two-photon ionization rates as a function of the laser detuning δ for the $5S_{1/2}, F = 2 \rightarrow 6P_{3/2}, F'$ transitions. The three peaks at $\delta = 0, \delta = -87$ and $\delta = -138.5$ MHz correspond to the transitions from the $5S_{1/2}, F = 2$ to the $F' = 3, 2, 1$ hyperfine levels of the $6P_{3/2}$ state. Making use of equation (1) for the

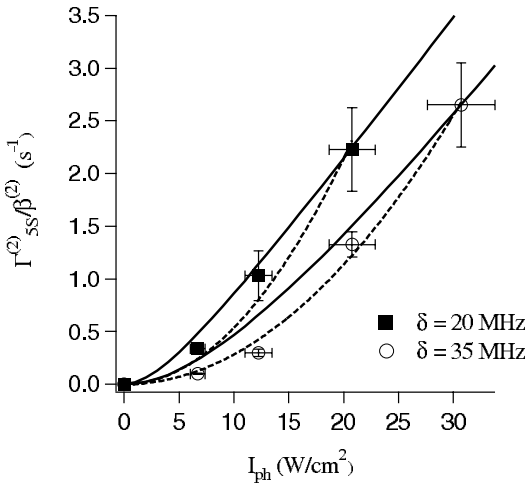

Figure 2. MOT photoionization rate $\Gamma^{(2)}_{5S}$, divided by the geometric factor $\beta^{(2)}$, plotted versus the photoionization intensity I_{ph} for different detunings from the intermediate $6P_{3/2}$ state: $\delta =$ 20 MHz (squares) and $\delta = 35$ MHz (circles). Simulations for both detunings are reported including the OP effect (solid lines). Note the discrepancy between the straight quadratic fits (dashed lines) and the numerical simulations.

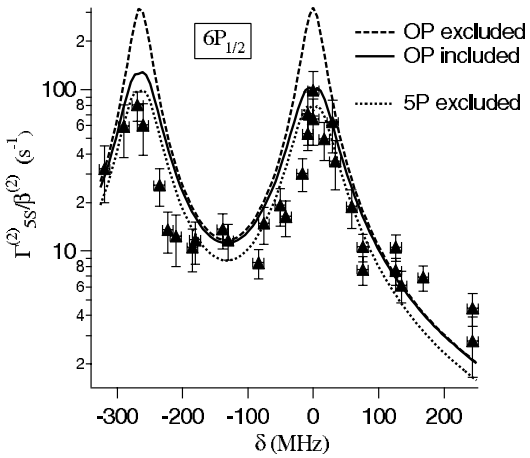

Figure 3. Comparison between measured and calculated (solid and dashed lines) two-photon ionization rates $\Gamma^{(2)}_{5S}/\beta^{(2)}$ varying the laser detuning δ of the near resonant intermediate $6P_{1/2}$ state. The photoionization intensity I_{ph} is 47 W cm ^{2}. The difference between solid (OP included) and dashed (OP excluded) lines is due to the OP into the dark $5S_{1/2}$, $F = 1$ state. The dotted line (5P excluded) is the calculated two-photon ionization rate when ionization from the 5P state is not allowed. The decay from the 6P state to 5P and the 5P ionization by the 421 nm laser gives rise to a 25% contribution in the ionization process.

maximum value of the rate we derived a cross section of $2.0(4) \times 10^{-38}$ cm^4 s, with the uncertainty mainly due to the determination of the $\beta^{(2)}$ geometric factor, as discussed in [7]. The values of the measured rates depend on several processes, such as the spontaneous decay into lower lying states and the OP into the dark $5S_{1/2}$, $F = 1$ state. Because of the occurrence of population saturation on the discrete transition at small detuning, the $\sigma^{(2)}_{5S}$ cross sections have not been used to take into account the complex phenomena underlying the photoionization dynamics. The lines in figures 3 and 4 are the numerical results of the two-photon photoionization model described in the following section, with the contribution

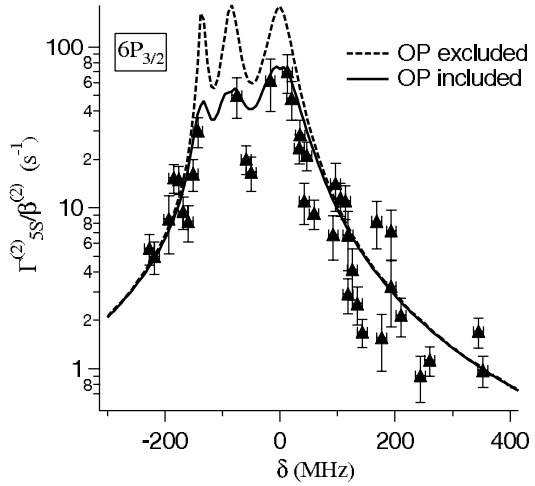

Figure 4. Comparison between measured and calculated (solid and dashed lines) two-photon ionization rates varying the detuning of the near resonant $6P_{3/2}$ state. The intensity of the ionizing laser was 24 W cm $^{-2}$. The three peaks at $\delta = 0, \delta = -87$ and $\delta = -138.5$ MHz correspond to transitions from the $5S_{1/2}, F = 2$ to the $F' = 3, 2, 1$ hyperfine levels of the $6P_{3/2}$ state. The difference between solid (OP included) and dashed (OP excluded) lines is due to OP into the dark $5S_{1/2}, F = 1$ state. The contribution of the 5P state to the ionization process is also included.

of the OP into the $5S_{1/2}, F = 1$ included or excluded. Furthermore the contribution from the photoionization of the 5P intermediate state is also evident, the state producing a large contribution owing to its occupation and its large one-photon photoionization cross section as presented in section 4.

4. One-photon ionization rate

As stated in the introduction, the photoionization process from all the excited states will be analysed through a phenomenological flux-dependent damping term inserted into the atomic density matrix equations for the discrete atomic states. Following the Weisskopf–Wigner approximation [13, 14] the one-photon photoionization rate of state j may be written as

$$\Gamma_j^{(1)} = \sigma_j^{(1)} * \left[\frac{I_{\rm ph}}{h\nu_{\rm ph}}\right] \tag{5}$$

where $\sigma_j^{(1)}$ is the one-photon ionization cross section. For the one-photon ionization from a bound state with effective quantum number n^* and angular momentum number l to a state in the continuum with angular momentum number l' and energy ΔE above the ionization threshold, the cross section can be evaluated using the formula of [15]

$$\sigma_j^{(1)} = \frac{4\pi\alpha a_0^2}{3}(E_{\rm ion} + \Delta E) \sum_{l'=l\pm1} C_{l'} \left| R_{n^*,l}^{\Delta E,l'} \right|^2 \tag{6}$$

with α being the fine-structure constant, a_0 the Bohr radius and $E_{\rm ion}$ the threshold ionization energy. The $C_{l'}$ are algebraic factors obtained from the integration over spin and angular coordinates. The evaluation of the bound–free radial transition integral $R_{n^*,l}^{\Delta E,l'}$ is very delicate as it depends on the asymptotic parts of the wavefunction for both the bound and the continuum states

$$R_{n^*,l}^{\Delta E,l'} = \int_0^\infty P_{n^*,l}(r) r G_{\Delta E,l'}(r)\, {\rm d}r \tag{7}$$

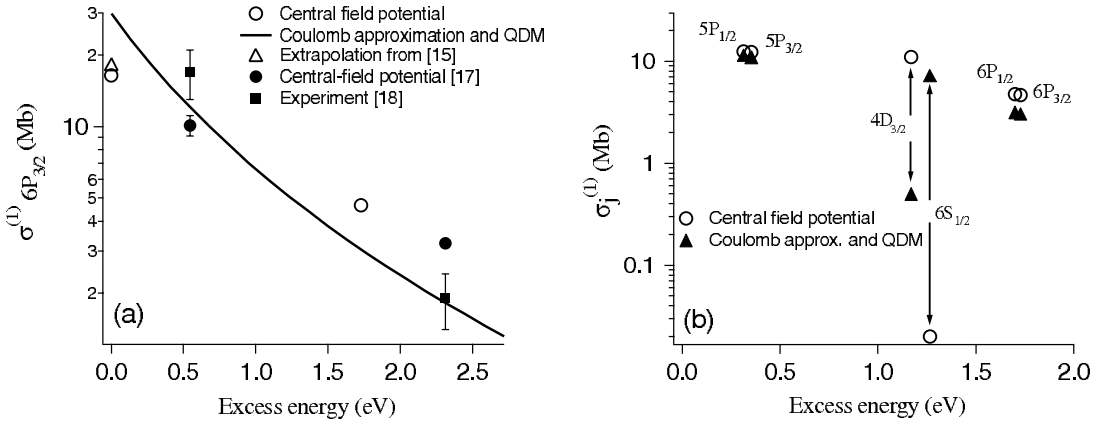

Figure 5. In (a) one-photon ionizing cross section $\sigma^{(1)}_{6P_{3/2}}$ (in Mbarn) versus the ΔE excess energies (in eV). Experimental values (closed squares) are from the previous investigation of [18]. Some theoretical values (closed circles) are from previously published work [17], while the solid line and the open symbols are from the present investigation. In (b) $\sigma^{(1)}_j$ for the 421 nm photoionization of the intermediate states involved in the rubidium ionizing process are plotted versus the excess energy ΔE. The open circles indicate values derived from the central-field model, while the closed triangles are those from the Coulomb approximation. The $\sigma^{(1)}_j$ values between 0.2 and 1.27 eV excess energy correspond to 421 nm ionization from the $5P_{1/2}$, $5P_{3/2}$, $4D_{3/2}$, $6S_{1/2}$, $6P_{1/2}$, $6P_{3/2}$ states.

where $P_{n^*,l}(r)$ and $G_{\Delta E,l'}(r)$ are the radial wavefunctions of the bound and free states, respectively. Based on the calculation of the oscillator strengths of non-hydrogenic atoms within the Coulomb approximation and using the quantum defect method (QDM), the approach of Dy and Regemorter [16] represents a simple semi-analytical method giving reasonably accurate results for the bound–free radial transition integral. Values for $\sigma^{(1)}_{6P_{3/2}}$ estimated within the Coulomb approximation for different excess energies ΔE are shown in figure 5(a) as a solid line. Even if the determination of the radial transition integrals within the Coulomb approximation is more accurate for transitions involving high quantum numbers as Rydberg states, it provides rapid, but reasonably accurate, estimates for $\sigma^{(1)}_j$ from the intermediate states involved in the ionization process. Figure 5(a) also shows more sophisticated calculations based on a central-field potential in the framework of a single-electron model. Some theoretical values were previously reported in [17] in order to interpret the experimental results of the photoionization at 632.9 and 316.4 nm by Ambartzumian *et al* [18]. New theoretical values from this approach are reported for the cross sections of figure 5(a) at zero excess energy, corresponding to the ionization by a 1002 nm photon [7], and at 1.70 eV excess energy corresponding to 421 nm ionization.

As explained in the previous work devoted to the central-field calculation of photoionization cross sections in rubidium [17], calculations can be carried out using different kinds of parametric potentials. In this work, we use the potential introduced by Klapisch [19] with a simple analytical form depending on three parameters which are determined by minimizing the root-mean-square deviations between experimental spin–orbit averaged energies and those calculated at zero order of perturbation theory. Values of 25 energy levels were reproduced with a rms deviation of 7.3×10^{-5} au. We checked that similar results are obtained by adding an effective polarization potential or by using a more complicated potential [20] depending on a four-parameter model describing the distribution of charges in the atomic core shells, with parameters now being adjusted by comparing experimental energies to first-order calculated ones. The photoionization cross sections of the $6S_{1/2}$ and, to a lesser extent of

the $4D_{3/2,5/2}$, were found to be most sensitive to the model. The photoionization cross sections of these levels presented marked non-hydrogenic character. Thus, it should be noted that the central-field potential approach predicts a very deep Cooper minimum in the ionization cross section starting from the $6S_{1/2}$ state, while this minimum is not predicted by the Coulomb–QDM approach (see data in figure 5(b)). Within a different theoretical analysis, the radial part $R_{n^*,l}^{\Delta E,l'}$ was evaluated making use of the results of [15]. This approach was used to produce a value for the cross section at zero excess energy.

An additional comparison between one-photon cross sections calculated in different approaches is shown in figure 5(b), examining the ionization from different rubidium excited states for a given 421 nm ionization photon (with an energy of 2.94 eV). New theoretical results based on the central-field potential are plotted there. The Coulomb approximation combined with QDM has also been used to derive estimates for the excited state photoionization cross sections. The differences between both approaches visible in figure 5(b) for $6S_{1/2}$ and for $4D_{3/2}$ states are due to the non-hydrogenic behaviour. The values predicted by the central-field potential have been used in all the numerical simulations presented here for the photoionization analysis.

5. Model and results

We investigated the two-photon ionization with the laser radiation close to resonance with an excited state. The blue radiation is quasi-resonant with the $5S \rightarrow 6P$ atomic transition. The detuning ranges from a few to some hundreds of MHz, much smaller than all the fine and the hyperfine structures of the 6P and the 5S states. To describe the photoionizing process, each of the hyperfine states involved in the transition has to be considered separately. The blue laser radiation is weak (on-resonance Rabi-frequency below 100 MHz) and out of resonance by several GHz from all transitions involving the $5S_{1/2}$, $F = 1$ state, so that the coherent coupling with the laser field involved only the $5S_{1/2}$, $F = 2 \rightarrow 6P_{1/2}$, F' transitions. The cases of quasi-resonance with the $6P_{1/2}$ or with the $6P_{3/2}$ are also treated independently because of the very large fine-structure splitting between the two excited states (2.32 THz).

As the 2 μs duration of the ionizing pulse is longer than the $6P_{3/2}$ (0.112 μs) and $6P_{1/2}$ (0.125 μs) lifetimes [21, 22], the 6P population has a non-negligible probability of spontaneous decay into lower lying states. Therefore, our model included the occupation of the 6S, 4D, $5P_{1/2,3/2}$ and $5S_{1/2}$, $F = 1$ states involved in the spontaneous decays from the 6P states. Moreover the atoms accumulated into the $5S_{1/2}$, $F = 1$ state are lost for the laser excitation, hence OP into that level plays an important role on the ionization process. A schematic diagram of the atomic levels included in the model for the case of quasi-resonance of the blue laser with the $6P_{1/2}$ state is shown in figure 6. The one-photon ionization process from all the intermediate states is also taken into account.

5.1. Coherent excitation

For the investigation of the population dynamics of the discrete states under the influence of the ionizing laser, the density matrix formalism is used. The time evolution of the density matrix ρ can be written as

$$i\hbar \frac{\partial}{\partial t}\rho = [H_0 + V, \rho] - i\hbar\Gamma\rho \tag{8}$$

where H_0 is the Hamiltonian of the unperturbed system, V the operator describing the interaction with the electromagnetic field and Γ the operator describing the relaxation

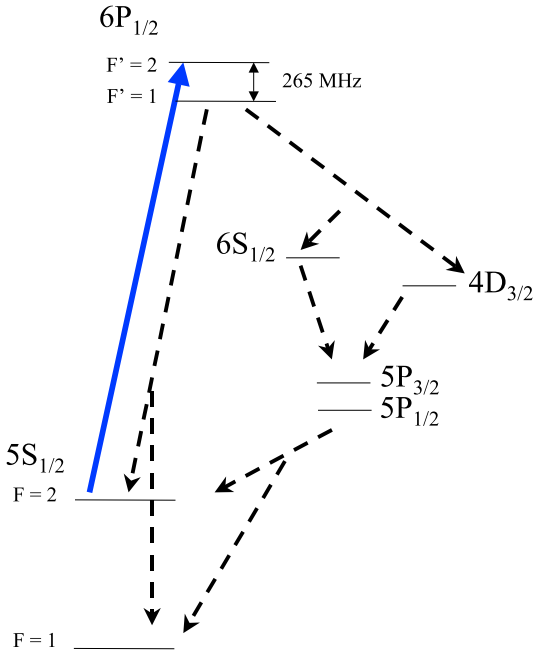

Figure 6. Schematic diagram of the atomic levels included in the model for the case of quasi-resonance of the blue laser with the $6P_{1/2}$ state. The solid arrow represents the excitation from the $5S_{1/2}$, $F = 2$ to the $6P_{1/2}$ states and the dashed arrows the spontaneous emission from the excited states.

processes. Within the dipole approximation the operator V defines the coupling between the atomic dipole moment d and the electric field E given by

$$E(t) = E_0\, e^{i\omega t} + \text{c.c.} \tag{9}$$

with E_0, ω being, respectively, the amplitude and the frequency of the laser field. For instance, in the case of blue radiation close to the $6P_{1/2}$ and within the rotating wave approximation, V has the following form:

$$V = \hbar \begin{bmatrix} 0 & \Omega_1/2 & \Omega_2/2 \\ \Omega_1/2 & -\delta_1 & 0 \\ \Omega_2/2 & 0 & -\delta_2 \end{bmatrix} \tag{10}$$

where Ω_i is the Rabi frequency of the transition $5S_{1/2}, F = 2 \rightarrow 6P_{1/2}, F' = i$, with $i = (1, 2)$, Ω_i being supposed real for simplicity, and δ_i is the corresponding detuning

$$\Omega_i = -\langle 6P_{1/2}, F' = i\,|d|\,5S_{1/2}, F = 2\rangle E_0/\hbar \tag{11}$$

$$\delta_i = \omega - (E_{6P_i} - E_{5S})/\hbar. \tag{12}$$

The relaxation processes in the density matrix equations involve the spontaneous cascade of population from the 6P back to the 5S through the intermediate states shown in figure 6.

5.2. Spontaneous decay and ionization efficiency

The spontaneous cascade from the 6P state back to the $5S_{1/2}$, $F = 1$ and $F = 2$ modifies the ionization rate owing to the occupation of several intermediate states through the cascade decay shown in figure 6. The intermediate states contribute to the ionization process through one-photon absorption processes. On the other hand, the ionization efficiency is reduced by

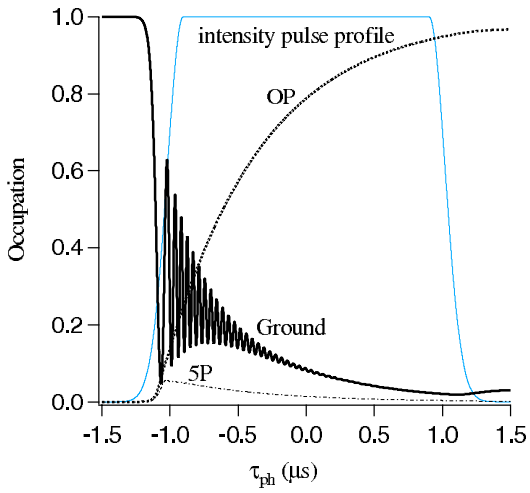

Figure 7. Occupation of the $5S_{1/2}$, $F = 2$ ground state (ground), of the intermediate 5P state and of the $5S_{1/2}$, $F = 1$ state (OP) under excitation by resonant 421 laser light ($\delta = 0$) for a laser intensity $I_{ph} = 47$ W cm ^{2}. The typical time sequence for blue excitation of the $6P_{1/2}$ state represented by the thin line is simulated. The ionization probability is around 2×10^{4}. At the end of the ionizing pulse, most of the atoms are pumped in the $5S_{1/2}$, $F = 1$ state.

OP into the $5S_{1/2}$, $F = 1$ dark state because it hides population from the ionization process. Because contributions to the cross section from the cascade occupied states increase or decrease the measured ionization rate, a precise analysis of the different processes is required.

For an examination of the contribution from the intermediate states, the temporal dependence of the atomic occupations is plotted in figure 7 for a typical ionizing pulse at resonance ($\delta = 0$) using the $6P_{1/2}$ intermediate state. The ground state population oscillates at the Rabi frequency $\Omega = 2\pi \times 23$ MHz. During the pulse time the 5P state is filled up to 6% by the intermediate states in the spontaneous cascade. From figure 5(b) $\sigma^{(1)}_{5P} \sim 3 \times \sigma^{(1)}_{6P}$, the atoms in the 5P state are ionized very efficiently and the 5P occupation contributes largely to the 421 nm ionization process. This additional ionization channel contributes with an increase up to 25% for the ionization rates shown in figure 3.

Including OP into the model decreases the photoionization efficiency at longer interaction times because of the atomic loss in the lower hyperfine ground state. The role of the $5S_{1/2}$, $F = 1$ OP on the ionization efficiency is clearly shown in the dependence of the effective $\sigma^{(2)}_{5S}$ cross section on the pulse duration of the ionization laser at different intensities of the photoionization laser. Figure 8 reports the calculated cross sections $\sigma^{(2)}_{5S}$ versus the duration of an ionizing pulse resonant with the $5S_{1/2}$, $F = 2 \rightarrow 6P_{3/2}$, $F' = 3$ transition. At $I_{ph} =$ 50 W cm^{-2} for a pulse duration shorter than the 0.112 μs $6P_{3/2}$ state spontaneous lifetime, OP is negligible (see figure 8(b)). For longer ionizing pulses where OP becomes important, the ionizing efficiency decreases. OP reduces by a factor 3 the two-photon photoionization rate in our typical ionization conditions (see figure 4). Note that because in the experiment the Gaussian rise time of the ionizing pulse is longer than the 6P spontaneous lifetime, OP is important also within the rising time. The small decrease in the calculated two-photon photoionization rates at the peak of the resonant values (see figures 3 and 4) is also due to OP into the $5S_{1/2}$, $F = 1$ state.

At very large values of the photoionization intensity I_{ph} the simultaneous presence of saturation on the $5S_{1/2}$, $F = 2 \rightarrow 6P_{3/2}$, $F' = 3$ transition and OP greatly modifies the $\sigma^{(2)}_{5S}$ cross section. In figure 8 effective $\sigma^{(2)}_{5S}$ values from the numerical simulation are plotted versus

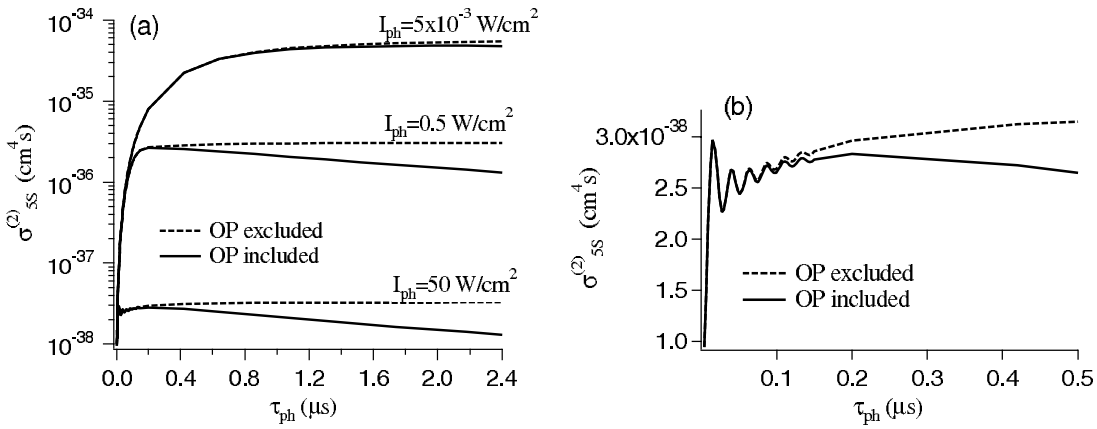

Figure 8. Numerical simulation results for the two-photon cross sections varying the photoionizing pulse duration for $\delta = 0$, i.e. at resonance with the $5S_{1/2}$, $F = 2 \rightarrow 6P_{3/2}$, $F' = 3$ intermediate state. In (a) $\sigma^{(2)}_{5S}$ calculated for different laser intensities including (solid line) or not including the OP contribution (dotted line). In (b) zoom of the curve at $I_{ph} = 50$ W cm ^{2} for pulse durations around the $6P_{3/2}$ 0.112 μs spontaneous lifetime where OP becomes non-negligible.

the duration τ_{ph} of the photoionizing pulse for different laser intensities. It is obvious that by increasing the photoionization intensity, a saturation of the population in the intermediate 6P state is reached. Saturation in the intermediate state takes place mainly because the 6P photoionization rate is not large enough to avoid a bottleneck in that level. In figure 8, above the saturation value $I_{sat} \sim 10$ mW cm^{-2},[6] a linear decrease of $\sigma^{(2)}_{5S}$ is observed for increasing ionizing intensities.

The presence of saturation and optical pumping also modifies the dependence of the two-photon ionization rate on the laser detuning. For the measured MOT losses varying the ionizing intensity reported in figure 2 for two different laser detunings, it appears that a straight quadratic fit of the measured values (dashed line) reproduces the measured intensity dependence. Instead the photoionization model predicts an intensity dependence quadratic only for very low laser intensities and with saturated losses at larger intensities. Moreover for low laser intensities the curvature of the quadratic behaviour predicted by the simulation is not proportional to the inverse of the squared laser detuning. This difference is due to the presence of the optical pumping with a different dependence on the laser detuning as shown in figure 4. However, owing to the limited number of data points we cannot exclude the presence of additional damping of the atomic coherences caused by the finite bandwidth of the blue laser radiation, or other features of the atomic response not included in our model.

6. Conclusion

Trap loss spectroscopy in a MOT is a very sensitive tool for ionization studies and in particular for absolute cross section measurements. This technique requires only relative measurements of time constants and avoids a delicate absolute calibration of the atom number. The alternate application of the trapping and photoionizing lasers, in order to compensate for the expansion and heating of the cold atomic cloud in the absence of the MOT lasers, allowed us to measure

[6] Note that $5S_{1/2}$, $F = 2 \rightarrow 6P_{1/2,3/2}$, F' transitions are open. The saturation intensity may be defined applying the analysis reported in [23] and taking into account that the excited state population decays back to the ground state through a cascade process. The saturation intensity is also modified by the population and coherence damping rates induced by the ionization process.

the two-photon ionization cross sections from the ground state of ^{87}Rb atoms for conditions of near resonance with the intermediate 6P states. However, for near resonant conditions and long ionization times, the spontaneous emission decay to other atomic states, and also to a dark ground state, greatly modifies the ionization efficiency. In order to extract a precise value of the ionization cross sections the population dynamics under the influence of the ionizing laser was simulated by a numerical integration of the equations describing the interaction with the ionizing laser including both discrete and continuum atomic states. Atomic intermediate states filled by cascade decay and OP are included in our model, and their ionization rates have been taken into account through additional decay rates. When ionizing near resonance, the competition between the OP through cascade decay and the ionization into the continuum becomes important in the ionization process efficiency. The contribution of the OP effect may amount to a factor 3 in the cross sections near resonance and cannot be neglected in the analysis of the ionization process. Furthermore for laser excitation in resonance with the discrete atomic transition, the saturation of the intermediate atomic states greatly modifies the ionization efficiency. For that regime the two-photon cross section shows a strong dependence on the laser intensity. Therefore the data analysis has been based on the photoionization rate. Even if our model reproduces most of the observed phenomena, an additional refinement is the inclusion of the optical pumping among the different Zeeman sublevels.

The ionization cross sections from rubidium excited states have been also derived from a theoretical description based on a central-field potential approach. Moreover, good qualitative agreement is found between a Coulomb approximation and a more sophisticated calculation based on a central-field potential in the evaluation of the $\sigma_j^{(1)}$ bound–free radial transition integral. However, some discrepancies between the results of both approaches occur for levels characterized by non-hydrogenic behaviour of their photoionization cross sections.

Acknowledgments

This research was supported by the Sezione A of INFM-Italy through a PAIS Project, by the MIUR-Italy through a COFIN Project and by the European Commission through the Cold Quantum-Gases Network, contract HPRN-CT-2000-00125.

References

[1] Dinneen T P, Wallace C D, Tan K N and Gould P L 1992 *Opt. Lett.* **17** 1706
[2] Gabbanini C, Gozzini S and Lucchesini A 1997 *Opt. Commun.* **141** 25
[3] Gabbanini C, Ceccherini F, Gozzini S and Lucchesini A 1998 *J. Phys. B: At. Mol. Opt. Phys.* **31** 4143
[4] Duncan B C, Sanchez-Villican V, Gould P L and Sadeghpour H R 2001 *Phys. Rev.* A **63** 043411
[5] Lowell J R, Northup T, Patterson B M, Takekoshi T and Knize R J 2002 *Phys. Rev.* A **66** 062704
[6] Ciampini D, Anderlini M, Müller J H, Fuso F, Morsch O, Thomsen J W and Arimondo E 2002 *Phys. Rev.* A **66** 043409
[7] Anderlini M, Courtade E, Ciampini D, Müller J H, Morsch O and Arimondo E 2004 *J. Opt. Soc. Am.* B at press
[8] Lambropoulos P 1974 *Phys. Rev.* A **9** 1992
[9] Adler A, Rachman A and Robinson E J 1995 *J. Phys. B: At. Mol. Opt. Phys.* **28** 5057
[10] Ackerhalt J R and Shore B W 1997 *Phys. Rev.* A **16** 277
[11] Townsend C G, Edwards N H, Cooper C J, Zetie K P, Foot C J, Steane A M, Szriftgiser P, Perrin H and Dalibard J 1995 *Phys. Rev.* A **52** 1423
[12] Müller J H, Ciampini D, Morsch O, Smirne G, Fazzi M, Verkerk P, Fuso F and Arimondo E 2000 *J. Phys. B: At. Mol. Opt. Phys.* **33** 4095
[13] Weisskopf V F and Wigner E P 1930 *Z. Phys.* **63** 54
[14] Bebb H B and Gold A 1966 *Phys. Rev.* **143** 1

RAPID COMMUNICATIONS

PHYSICAL REVIEW A **71**, 061401(R) (2005)

Sympathetic cooling and collisional properties of a Rb-Cs mixture

M. Anderlini, E. Courtade, M. Cristiani, D. Cossart, D. Ciampini, C. Sias, O. Morsch, and E. Arimondo
INFM, Dipartimento di Fisica E. Fermi, Università di Pisa, Largo B. Pontecorvo 3, I-56127 Pisa, Italy
(Received 28 February 2005; published 1 June 2005)

We report on measurements of the collisional properties of a mixture of ^{133}Cs and ^{87}Rb atoms in a magnetic trap at μK temperatures. By selectively evaporating the Rb atoms using a radio-frequency field, we achieved sympathetic cooling of Cs down to a few μK. The interspecies collisional cross section was determined through rethermalization measurements, leading to good agreement with a theoretical prediction of $595a_0$ for the triplet s-wave scattering length for Rb in the $|F=2,m_F=2\rangle$ and Cs in the $|F=4,m_F=4\rangle$ magnetic states. We briefly speculate on the prospects for reaching the Bose-Einstein condensation of Cs inside a magnetic trap through sympathetic cooling.

DOI: 10.1103/PhysRevA.71.061401 PACS number(s): 32.80.Pj, 34.20.Cf

Laser cooling of neutral atoms, combined with evaporative cooling in conservative (magnetic and optical) traps, has led to a number of important breakthroughs in atomic physics, most notably the observation of Bose-Einstein condensation (BEC) in a dilute gas of alkali-metal atoms in 1995 [1]. In recent years, research on ultracold atoms has expanded into the realms of atomic mixtures. Adding a second atomic species has, among other things, opened up the possibility to sympathetically cool one atomic species through collisional energy exchange with the other species [2]. On the one hand, this has proved an invaluable tool for reaching the quantum degeneracy regime with fermionic atoms for which Pauli blocking reduces the evaporative cooling efficiency at low temperatures. On the other hand, ultracold atomic mixtures are also interesting in their own right. In particular, the possibility of creating cold heteronuclear molecules could be an important ingredient in neutral atom quantum computing due to the expected large permanent dipole moment of such molecules. Furthermore, ultracold mixtures can lead to interesting quantum phases when loaded into an optical lattice [3]. A number of mixtures has been studied in magneto-optical traps (MOTs) [4,5], and recent experiments by Kerman *et al.* [6] have yielded information about the rovibrational structure of the ^{85}Rb^{133}Cs molecule. Furthermore, a few combinations of ultracold atoms have also been experimentally investigated in conservative traps, among them Li-Cs [7], K-Rb [8,9], and Na-Li [10].

In this paper we study the collisional properties of a mixture of ultracold ^{87}Rb and ^{133}Cs atoms in a magnetic trap. Both Rb and Cs have been used in laser cooling of atoms for more than 15 years now and are important as time and frequency standards. However, not much is known about their interatomic potentials and collisional properties. While for the lighter alkali metals the interatomic potentials can be calculated relatively easily, it has been difficult to do the same for the Rb-Cs potential. Jamieson *et al.* [11] calculated the collisional parameters using several similar-looking choices for the interatomic potentials, and found that even for small changes in the potential the s-wave scattering length varies by up to two orders of magnitude. Furthermore, the adverse collisional properties (large inelastic cross sections) of Cs in the magnetically trappable states make experimental studies of Rb-Cs mixtures challenging.

The experimental apparatus used for this work is similar to our Rb-BEC setup described in detail elsewhere [12]. We use a double-chamber vacuum system with a two-dimensional (2D) collection MOT in the upper chamber and a six-beam MOT in the lower chamber. In order to trap and cool both Rb and Cs atoms, the trapping and repumping light for the two species is superimposed and the same optics (mirrors, lenses, and wave plates) is used to create the beams for both MOTs. Once the atoms have been transferred into the lower MOT, after a brief compressed MOT and molasses phase, the trapping beams are switched off and the atoms are optically pumped into the $|F=2,m_F=2\rangle$ and $|F=4,m_F=4\rangle$ magnetically trappable states of Rb and Cs, respectively. Immediately after that, the time-averaged orbiting potential (TOP) magnetic trap is switched on. Since the two atomic species have different equilibrium positions in the magnetic trap (due to gravitational sag), the positions of the MOTs have to be adjusted accordingly in order to avoid subsequent oscillations in the TOP trap. This is achieved by tuning the radiation pressure in the MOT using the (wavelength-selective) quarter-wave plates inserted into the optical path of the trapping beams.

In order to demonstrate sympathetic cooling, after loading the atoms into the magnetic trap, we first performed circle-of-death evaporative cooling (which exploits the rotating zero-of-field locus on which spin-flips can occur) by continuously reducing the strength of the rotating bias field [13]. Because this cooling technique is not species selective, cooling one or the other species separately (i.e., loading only that species into the MOT) made little difference.

We then proceeded to apply a radio-frequency field resonant with a $\Delta m_F=\pm 1$ Zeeman transition in the Rb atoms. By ramping down the frequency of the RF field, forced evaporative cooling is induced as the radius of the surface on which atoms are transferred into untrapped states shrinks. Radio-frequency evaporation is species selective as it depends on the Zeeman sublevel spacing. Therefore, only the Rb atoms were evaporatively cooled in this way. Nevertheless, the measured temperature of the Cs atoms exactly followed the Rb temperature down to a few μK, clearly indicating that sympathetic cooling was taking place [see Fig. 1(a)]. In fact, repeating the experiment with Cs atoms only, a much smaller cooling rate, consistent with residual circle-of-

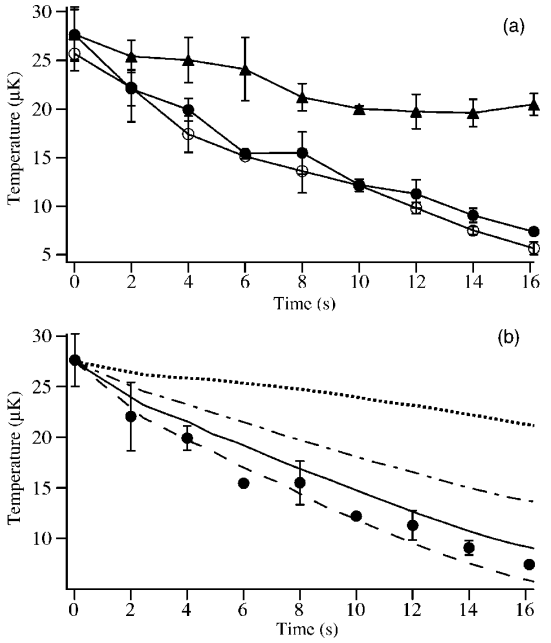

FIG. 1. (a) Sympathetic cooling of Cs atoms (filled circles) through RF evaporation of Rb (open circles). Removing the Rb atoms before the RF sweep, Cs atoms are only cooled slightly by residual circle-of-death evaporation at a fixed bias field (triangles). (b) A comparison of experiment and Monte Carlo simulations results for Cs: no interspecies collisions (dotted line), data set C (dash-dotted line), data set A (solid line), data set B (dashed line). Rb temperatures were only slightly sensitive of the cross section.

death evaporation, was observed. Initially, the atom numbers in the trap were $N_{\mathrm{Rb}} \approx 2 \times 10^6$ and $N_{\mathrm{Cs}} \approx 10^5$. Towards the end of the ramp, the number of Rb atoms had dropped by a factor of 10. As expected, sympathetic cooling was efficient as long as the number of Rb atoms was larger than the number of Cs atoms; once there were fewer Rb than Cs atoms, sympathetic cooling stopped.

In order to understand the dynamics of sympathetic cooling and to extract information on the interspecies scattering properties, we solved the kinetic equations for the atomic dynamics inside the magnetic trap in the presence of interatomic collisions, treating the collisions through a Monte Carlo approach [14] (in the following to be called "Monte Carlo simulations"). Those simulations were extended to samples of two species with different masses, atom numbers, and trap frequencies. Since the known values of the C_6 coefficient for the Rb-Cs molecular potential [15] give a threshold energy for p-wave scattering of about 50 μK [16], we took into account both the s-wave and the the p-wave contributions to the interspecies elastic cross section. Using the effective range approximation [17,18], the s-wave term was written in terms of a scattering length a and an effective range r_e, while the p-wave term was expressed in terms of a p-wave volume A_1 [19]

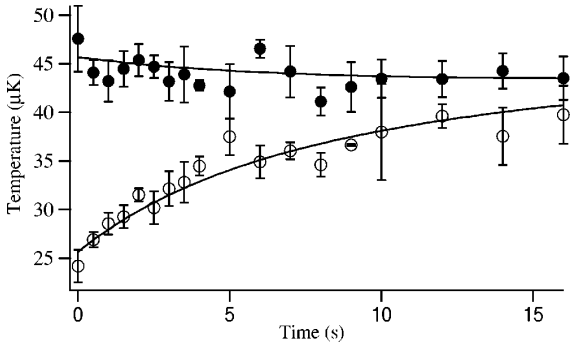

FIG. 2. Rethermalization in a Rb-Cs mixture. The initial difference between the Rb temperature (open circles) and the Cs temperature (filled circles) was created by a fast RF evaporation of the Rb atoms. The solid lines are best fits obtained by a numerical integration of the differential equations describing the rethermalization process (see text).

$$\sigma_{tot} = \frac{4\pi a^2}{\left(1 - \frac{1}{2} a r_e k^2\right)^2 + a^2 k^2} + \frac{12\pi A_1^2 k^4}{1 + A_1^2 k^6}, \qquad (1)$$

where k is the modulus of the wave vector of the relative atomic motion. The angular dependence of the $l=1$ partial wave does not affect the efficiency of the p-wave contribution in the interspecies thermalization process (in contrast to single-species cross-dimensional relaxation, where it reduces the p-wave contribution by a factor 3/5 [20]). In order to analyze the experimental results, we considered the theoretical sets of scattering parameters $\{a, r_e, A_1\}$ for the triplet interaction reported in [11], corresponding to data set A $=\{595.2a_0, 190.2a_0, -168.5 \times 10^4\, a_0^3\}$, data set B $=\{177.2a_0, 126.4a_0, -4681 \times 10^4\, a_0^3\}$, data set C $=\{-317.6a_0, 424.2a_0, -112.3 \times 10^4\, a_0^3\}$, and data set D $=\{-45.37a_0, 3075a_0, -84.22 \times 10^4\, a_0^3\}$ (where a_0 is the Bohr radius). Numerical simulations using those parameters showed that only the two sets A and B were consistent with the observed efficiency of the sympathetic cooling [Fig. 1(b)]. However, systematic effects mainly related to the uncertainties in the efficiency of the evaporation processes prevented an accurate extraction of the scattering parameters from this data.

In order to obtain a more accurate measurement of the scattering cross section, we performed rethermalization measurements. First, Rb and Cs were cooled down to temperatures between 5 and 60 μK by circle-of-death evaporative cooling. Thereafter, a radio-frequency ramp was applied in such a way that the Rb atoms were cooled, but with a fast enough sweep so that there was no energy exchange between Cs and Rb during the evaporation time. At the end of the RF ramp there was thus a temperature difference between the Rb and Cs atoms [21]. The mixture was then held in the magnetic trap for up to 20 s and the temperatures of both species were measured as a function of time. These measurements were repeated for various mean temperatures of the mixture.

Figure 2 shows the result of such a rethermalization mea-

surement. In order to suppress systematic effects as much as possible, for each experimental run we measured both the Rb and Cs temperatures *without* the other species by eliminating one or the other through a resonant flash before the rethermalization process started. Typically, we observed single-species heating rates of up to 350 nK s^{-1}.

Rethermalization techniques have been extensively used to measure collisional scattering lengths and p-wave cross sections [8,18,22–25]. For mixtures of two clouds prepared at different temperatures, the relaxation of the temperatures due to elastic collisions with a certain constant cross section proceeds exponentially with a rate that can be calculated analytically through the model of [7]. From the rates obtained by exponential fits of observed thermalizations one can generally extract the value of the cross section. We extended that model to cross sections that explicitly depend on the energy of the colliding particles [as in Eq. (1)]. In this case the relaxation rate of the temperatures in the mixture depends linearly on the effective cross section σ_e [18,26,27], which, in the case of Eq. (1), is

$$\sigma_e = \int_0^\infty dx x^5 e^{-x^2} \left(\frac{4\pi a^2}{\left(1 - \frac{1}{2} C a r_e x^2\right)^2 + C a^2 x^2} + \frac{12\pi C^2 A_1^2 x^4}{1 + C^3 A_1^2 x^6} \right), \tag{2}$$

where $C = 2\mu k_B (m_1 T_2 + m_2 T_1)/(\hbar^2 M)$, μ is the reduced mass, and $M = m_1 + m_2$.

We checked that exponential fits to this model and to Monte Carlo simulations gave the same thermalization rates to within a few percent [28]. However, due to the decay of the number of atoms during the thermalization and to the observed intrinsic heating independent of the interspecies interactions, we could not determine the effective cross section through a simple exponential fit to the data. Those cross sections were determined by running a numerical simulation using the model discussed above for different σ_e and initial temperatures of the two species, taking into account the experimental single-species heating rates and atom number decay. We then compared the results of these simulations with the experimental data, and from the combination of parameters giving the least χ^2 we finally determined σ_e. The results of this analysis are plotted in Fig. 3 as a function of the initial weighted average temperature of the mixed sample.

Having measured the effective scattering cross sections, we calculated the effective cross sections corresponding to the scattering parameters predicted by Jamieson *et al.* [11] for the temperature range relevant to our experiment. The agreement with our data is best for the scattering parameters of data set A (see Fig. 3).

We note here that due to imperfect optical pumping (and, possibly, other depolarizing processes during the evaporation cycle), both the Rb and Cs clouds had admixtures of atoms in other Zeeman sublevels. In the case of Rb, around 90% of the atoms were in the desired state $|F=2,m_F=2\rangle$, with around 10% in the $|F=2,m_F=1\rangle$ sublevel, while for Cs we measured (by performing a Stern-Gerlach-type experiment to separate the Zeeman levels in time of flight) relative populations of 70–80 % in the $|F=4,m_F=4\rangle$ sublevel and 20–30 % in $|F=4,m_F=3\rangle$. This posed two problems in interpreting our data. Firstly, the scattering cross sections for atoms in the various Zeeman sublevels are not necessarily the same. Since we could not eliminate the populations in the other sublevels, we can only quote them here to indicate the possible error involved in our determination of the Rb$|F=2,m_F=2\rangle$ –Cs$|F=4,m_F=4\rangle$ cross section. Secondly, the presence of other Zeeman sublevels distorted the density profiles from which we calculated the Rb and Cs temperatures. This problem was solved by fitting a double-Gaussian curve with a fixed separation and extracting the temperature from the widths of these two Gaussians.

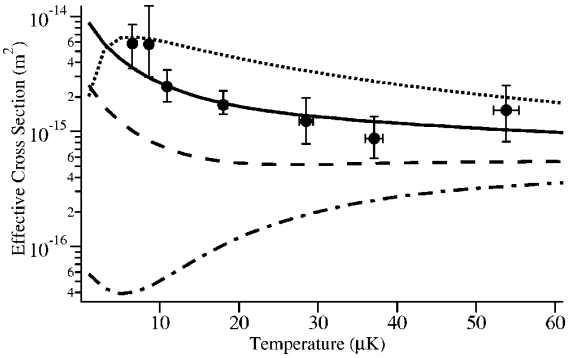

FIG. 3. Effective elastic scattering cross sections for Rb-Cs collisions as a function of temperature. The theoretical predictions by Jamieson *et al.* [11] plotted in this graph are: data set B (dotted line), data set A (solid line), data set C (dashed line), and data set D (dash-dotted line). The error bars on the experimental points are derived from the χ^2 fit (see text).

Concerning the *inelastic* collisional properties of the Rb-Cs mixture, we found that in the temperature range 5–40 μK and for typical densities of $(0.5–2)\times10^{10}$ cm^{-3}, no additional losses in either Rb or Cs in the presence of the other species occurred. We can, therefore, put the upper limit of $\sim10^{-12}$ cm^3 s^{-1} on the inelastic coefficient for Rb-Cs collisions in magnetic fields in the range 4–40 G. In the same range we also performed a slow sweep of the bias field, but observed no pronounced losses. This rules out the possibility of broad interspecies Feshbach resonances (as observed recently for a Na-Li mixture [10]).

Finally, the fact that Cs can be sympathetically cooled by Rb and that the scattering length for interspecies collisions is large leads us to speculate whether it might be possible to reach Bose-Einstein condensation of Cs inside a magnetic trap using a sympathetic cooling approach. Although Cs was recently condensed inside an optical trap [29], it would still be interesting to achieve condensation in a magnetic trap, thus avoiding the complicated setup of [29]. Since in our current experiment the number of Rb atoms we could initially trap was too small to extend the sympathetic cooling below a few μK, we conducted Monte Carlo simulations with larger numbers of atoms. Our simulations took into account the inelastic losses especially of Cs, which in the $|F=4,m_F=4\rangle$ Zeeman sublevel has a zero-energy resonance [30] associated with a large inelastic collision rate responsible for the failure of all attempts so far to reach Bose-

Einstein condensation in a magnetic trap. Running simulations with up to 2×10^7 Rb atoms in the $|F=2,m_F=2\rangle$ sublevel, 10^5 Cs atoms in $|F=4,m_F=4\rangle$ and an initial temperature of 10 μK for both species clearly showed that even with a large (but still realistic) number of Rb atoms and very low final trap frequencies (chosen so as to reduce the Cs density and hence inelastic losses), it is not possible to reach quantum degeneracy in such a scheme. However, using the $|F=1,m_F=-1\rangle$ and $|F=3,m_F=-3\rangle$ sublevels for Rb and Cs, respectively, we found that with the same numbers of atoms as in the first simulation, the same initial temperature and similarly large scattering lengths (i.e., $>300a_0$), the threshold for condensation of Cs was reached with roughly 5×10^4 Cs atoms left in the mixture. While we have no precise knowledge of the scattering length involved in the collisions between atoms in those sublevels it still seems likely that the effective scattering length will be sufficiently large to make the condensation of Cs possible. Nevertheless, further work needs to be done to experimentally verify the scattering properties of those sublevels.

In conclusion, we have demonstrated sympathetic cooling of Cs atoms down to very low temperatures in a Rb-Cs mixture, even in the presence of large inelastic losses in Cs. We have characterized the ultracold collisions between the two species by measuring rethermalization rates. Monte Carlo simulations yielded a precise reproduction of the overall collision processes. Our results are consistent with a large interspecies triplet *s*-wave scattering length. If the scattering length between atoms in the $|1,-1\rangle$ state of Rb and $|3,-3\rangle$ state of Cs is similarly large, it appears feasible to reach Bose-Einstein condensation of Cs in a magnetic trap through sympathetic cooling with Rb.

We thank T. Bergeman, D. Guéry-Odelin, M. Holland, and M. Jamieson for useful discussions, and J.H. Müller and N. Malossi for help in the early stages of the experiment. This research was supported by the INFM (PRA Photonmatter), by Progetto MIUR-COFIN 2004 and by the EU Network Cold Quantum Gases, Contract No. HPRN-CT-2000-00125.

[1] K. B. Davis *et al.*, Phys. Rev. Lett. **75**, 3969 (1995); C. C. Bradley *et al.*, *ibid.* **75**, 1687 (1995); M. H. Anderson *et al.*, Science **269**, 198 (1995).
[2] For a general review of ultracold atomic collisions, see J. Weiner *et al.*, Rev. Mod. Phys. **71**, 1 (1999); J. Weiner, *Cold and Ultracold Collisions in Quantum Microscopic and Mesoscopic Systems* (Cambridge University Press, Cambridge, 2003).
[3] M. Lewenstein *et al.*, Phys. Rev. Lett. **92**, 050401 (2004).
[4] G. D. Telles *et al.*, Phys. Rev. A **63**, 033406 (2001).
[5] M. W. Mancini *et al.*, Phys. Rev. Lett. **92**, 133203 (2004).
[6] A. J. Kerman *et al.*, Phys. Rev. Lett. **92**, 153001 (2004); **92**, 033004 (2004).
[7] A. Mosk *et al.*, Appl. Phys. B **73**, 791 (2001).
[8] G. Ferrari *et al.*, Phys. Rev. Lett. **89**, 053202 (2002).
[9] J. Goldwin *et al.*, Phys. Rev. A **70**, 021601(R) (2004).
[10] C. A. Stan *et al.*, Phys. Rev. Lett. **93**, 143001 (2004).
[11] M. J. Jamieson *et al.*, J. Phys. B **36**, 1085 (2003).
[12] J. H. Müller *et al.*, J. Phys. B **33**, 4095 (2000).
[13] W. Petrich *et al.*, Phys. Rev. Lett. **74**, 3352 (1995).
[14] H. Wu and C. J. Foot, J. Phys. B **29**, L321 (1996); H. Wu *et al.*, Phys. Rev. A **56**, 560 (1997).
[15] M. Marinescu and H. R. Sadeghpour, Phys. Rev. A **59**, 390 (1999).
[16] B. De Marco and D. S. Jin, Phys. Rev. A **58**, R4267 (1998).
[17] C. J. Joachain, *Quantum Collision Theory* (North Holland, Amsterdam, 1983).
[18] P. O. Schmidt *et al.*, Phys. Rev. Lett. **91**, 193201 (2003).
[19] G. Gutiérrez *et al.*, Phys. Rev. B **29**, 5211 (1984).
[20] B. De Marco *et al.*, Phys. Rev. Lett. **82**, 4208 (1999).
[21] At the end of this fast evaporation the rubidium cloud is not in thermal equilibrium, having a temperature in the *x* and *y* directions different from the temperature in the *z* direction. Monte Carlo simulations showed that the relaxation of the average temperature $T=(2T_x+T_z)/3$ for a cloud out of equilibrium is in fact identical to the temperature relaxation of a cloud at equilibrium. In the following, the rubidium temperature is understood to be the average temperature.
[22] M. Arndt *et al.*, Phys. Rev. Lett. **79**, 625 (1997).
[23] R. Legere and K. Gibble, Phys. Rev. Lett. **81**, 5780 (1998).
[24] G. Delannoy *et al.*, Phys. Rev. A **63**, 051602(R) (2001).
[25] I. Bloch *et al.*, Phys. Rev. A **64**, 021402(R) (2001).
[26] G. M. Kavoulakis *et al.*, Phys. Rev. A **61**, 053603 (2000).
[27] P. J. J. Tol *et al.*, Phys. Rev. A **70**, 013404 (2004).
[28] The validity of this model is restricted to mixtures in the *collisionless* regime, i.e., where the harmonic trap frequencies are much bigger than the thermalization rates, as was the case for our experimental conditions. In other regimes a more complex model, taking into account space-velocity correlations, is needed [D. Guéry-Odelin (private communication)].
[29] T. Weber *et al.*, Science **299**, 5604 (2003).
[30] J. Söding *et al.*, Phys. Rev. Lett. **80**, 1869 (1998).

PHYSICAL REVIEW A **72,** 033408 (2005)

Model for collisions in ultracold-atom mixtures

M. Anderlini,* D. Ciampini, D. Cossart, E. Courtade,† M. Cristiani, C. Sias, O. Morsch, and E. Arimondo
INFM, Dipartimento di Fisica E. Fermi, Università di Pisa, Largo B. Pontecorvo 3, I-56127 Pisa, Italy
(Received 10 May 2005; published 14 September 2005)

We present a model for the collisional properties of a mixture of ^{133}Cs and ^{87}Rb atoms in a magnetic trap at μK temperatures. The experimental sequence we model corresponds to a selective evaporation of the Rb atoms using a radio-frequency field, leading to sympathetic cooling of the Cs atoms or, if selective evaporation is carried out fast, to a difference in temperature between the two atomic species. In the latter case, the two atomic clouds reached an equilibrium temperature starting from an Rb temperature lower than that of Cs. By supposing that each atomic cloud was in thermal equilibrium we modeled this rethermalization process through differential equations for the two atomic temperatures. An alternative approach was based on the Monte Carlo simulations of the individual collisional processes. The sympathetic cooling and the rethermalization were analyzed in terms of the inter-species collisional cross-section.

DOI: 10.1103/PhysRevA.72.033408 PACS number(s): 32.80.Pj, 34.20.Cf

I. INTRODUCTION

Laser cooling of neutral atoms, combined with evaporative cooling in conservative traps, has led to the production of ultracold atoms, culminating in the realization of Bose-Einstein condensates and degenerate Fermi gases. The collisional properties at ultralow temperatures have opened new research areas of physics and chemistry (see Refs. [1,2]). In recent years, research on ultracold atoms has expanded into the realm of atomic mixtures. Adding a second atomic species has opened up the possibility to sympathetically cool one atomic species through collisional energy exchange with the other species. Moreover the simultaneous trapping of two different atomic species in a conservative trap allows the study of several phenomena not observed in single-species samples. Since the different components can have largely different intrinsic properties, such as different masses, spins, elastic, and inelastic scattering properties and quantum statistics, the collisional and thermodynamical properties of the mixture may be completely different from those of the individual components. Thus new phenomena can be studied, such as mixing and de-mixing phenomena in Bose-Einstein condensates [3,4], superfluid dynamics in Bose-Einstein condensates [5] or the production of ultracold heteronuclear molecules [6–8], as well as the realization of new quantum phases when loaded into an optical lattice [9]. Recent experiments by Kerman *et al.* [7] have yielded information about the rovibrational structure of the ^{85}Rb^{133}Cs molecule, and photoassociation to the ground vibronic state of that molecule was achieved in Ref. [8]. Furthermore, a few combinations of ultracold atoms have also been experimentally investigated in conservative traps, among them Rb in two different internal states [10], Li-Cs [11], K-Rb [12–14], and Na-Li [15,16].

In a recent experimental study [17], we looked at the collisional properties of a mixture of ultracold ^{87}Rb and ^{133}Cs atoms in a magnetic trap. We investigated the sympathetic cooling of Cs by collisions with Rb and the rethermalization of the atomic mixture following the creation of a temperature difference between Rb and Cs. Even if both atoms have been used in laser cooling for many years, very little is known about their interatomic potentials and collisional properties. We have compared the results of our HRb-Cs collisional investigations to the *s*-wave scattering length estimated by Jamieson *et al.* [18]. Sympathetic cooling and rethermalization techniques have been used previously to measure collisional scattering lengths and *p*-wave cross sections, for instance in Refs. [12,19].

In order to use and control the interspecies interactions the proper tools for modeling the collisional processes occurring in an ultracold mixture are required. The present work describes the theoretical tools we developed in order to analyze Rb-Cs collisions. We consider the properties of an ultracold mixture mainly from a thermodynamic point of view. The processes of sympathetic cooling and rethermalization of samples initially prepared out of thermal equilibrium are investigated. We examine how these processes depend on the interactions between the two species and, as a consequence, how it is possible to study the atomic properties by performing sympathetic cooling and rethermalization experiments. The Rb-Cs collisional data are analyzed by making use of the effective cross section, an average of the cross section over the kinetic energies of the colliding partners [19–21]. We have interpreted the time evolution of the temperature of the atomic mixture through an analytical model based on the approach developed by Mosk *et al.* [11]. The original contribution of the present work is the derivation of an analytical model describing the relaxation processes of the Rb-Cs atomic mixture, including the complex dependence of the interspecies elastic cross section on the energy of the colliding particles. Such an analytical model allowed a simple analysis of the experimental data for the temperature relaxation of the two species, without relying on heavy numerical simulations for each experimental run. That target was reached by including the effective collisional cross section into equations for the evolution of the atomic temperatures in the rethermalization process. We also noticed that experi-

*Present address: National Institute of Standards and Technology, Gaithersburg, MD 20899, USA.
†Present address: Université de Lille I, Villeneuve d'Ascq, France.

mental complexities such as the different equilibrium positions of the two atomic clouds and the inelastic losses of each species could be easily incorporated into the temperature equations. In order to test the validity of our analytical approach we have also compared, for a few cases, the analytical model to the results of Monte Carlo simulations based on the extension of previous analyses applied to describe the collisional properties of a single species [22,23] to the case of a mixture.

The theoretical analysis of the present work was applied to analyze the experimental results described in Ref. [17]. The experimental results reported here belong to the large set of data collected during that investigation and not completely reported within that work.

This paper is organized as follows: After briefly reminding the reader of the basic notions involved in (single-species) atomic collisions, in Sec. III we present a model for the temporal evolution of an atomic mixture. Thereafter, we introduce into that model the corrections associated with the gravitational sag and for the lifetimes of the atomic clouds in the magnetic trap. Section V presents the results of our Monte Carlo simulations for the collisional evolution of the atomic mixture, and then compares that simulation to the temperature model of the preceding sections. Finally, in Sec. VI we compare the results of our models and simulations with experimental data for ultracold Rb-Cs collisions.

II. ATOMS IN HARMONIC POTENTIALS

A. Collision rate

Before studying the atomic mixture, it is useful to recall the collisional properties of a single-species cloud at temperature T confined by a harmonic potential, as in standard textbooks [24,25]. The spatial and the velocity variables follow a Gaussian phase-space distribution $f(\mathbf{r},\mathbf{v})$ given by

$$f(\mathbf{r},\mathbf{v}) = N\left(\frac{m\bar{\omega}}{2\pi k_B T}\right)^3 \prod_{j=x,y,z} e^{-(m\omega_j^2 r_j^2/2k_B T)-(mv_j^2/2k_B T)}, \quad (1)$$

where N is the total number of atoms, m is their mass, and $\bar{\omega}$ is the geometric average of the harmonic potential frequencies given by $\bar{\omega}=\sqrt[3]{\omega_x\omega_y\omega_z}$. If the atoms have a velocity-dependent collisional cross-section $\sigma(\mathbf{v}_1,\mathbf{v}_2)$, the average collision rate γ_c is given by the collision cross section averaged over the distribution (1)

$$\gamma_c = \frac{\int d^3r d^3v_1 d^3v_2 \sigma(\mathbf{v_1},\mathbf{v_2})|\mathbf{v_1}-\mathbf{v_2}| f(\mathbf{r},\mathbf{v_1}) f(\mathbf{r},\mathbf{v_2})}{\int d^3r d^3v f(\mathbf{r},\mathbf{v_1})}. \quad (2)$$

The inverse of the collision rate γ_c determines the time scale on which the atomic cloud relaxes to the form of Eq. (1) when brought out of equilibrium by processes such as evaporative cooling. If we suppose the cross section σ to depend only on the modulus of the relative velocity $\mathbf{v_R}=\mathbf{v_1}-\mathbf{v_2}$ between the colliding particles and use the phase-space distribution function $f(\mathbf{r},\mathbf{v})$ given by Eq. (1), the collision rate becomes

$$\gamma_c = N\frac{m\bar{\omega}^3}{2\pi^2 k_B T}\left[2\int_0^\infty dy\, y^3 e^{-y^2}\sigma\left(\sqrt{\frac{4k_B T}{m}}y\right)\right]. \quad (3)$$

Then, following Refs. [19–21], we introduce an effective collisional cross section $\sigma_{c,\mathrm{eff}}$ defined by

$$\sigma_{c,\mathrm{eff}} = 2\int_0^\infty dy\, y^3 e^{-y^2}\sigma\left(\sqrt{\frac{4k_B T}{m}}y\right), \quad (4)$$

which represents the energy-dependent cross section weighted by the product of the relative interparticle velocities and the Boltzmann distribution of the thermal sample. Then we express Eq. (3) in the following form:

$$\gamma_c = N\frac{m\bar{\omega}^3}{2\pi^2 k_B T}\sigma_{c,\mathrm{eff}}. \quad (5)$$

While in general the integral appearing in Eq. (4) must be evaluated numerically, there are cases in which one can calculate the collision rate analytically. For an energy-independent cross section of the form

$$\sigma = 8\pi a^2 = \sigma_0, \quad (6)$$

where a is the scattering length, the collision rate becomes

$$\gamma_c = N\frac{m\bar{\omega}^3}{2\pi^2 k_B T}\sigma_0. \quad (7)$$

For a cross section of the form

$$\sigma(v_R) = \frac{8\pi a^2}{1+\frac{\mu}{\hbar}v_R^2 a^2} = \frac{\sigma_0}{1+k_R^2 a^2}, \quad (8)$$

where k_R is the modulus of the wave vector $\mathbf{k}_R=\mu\mathbf{v}_R/\hbar$ of the interparticle relative momentum and $\mu=m/2$ the reduced mass, the collision rate becomes

$$\gamma_c = N\frac{m\bar{\omega}^3}{2\pi^2 k_B T}\sigma_0\zeta(1-\zeta e^{\zeta}\Gamma(0,\zeta)), \quad (9)$$

with $\zeta=\hbar^2/(mk_B T a^2)^{-1}$, and

$$\Gamma(a,x) = \int_x^\infty y^{a-1}e^{-y}dy. \quad (10)$$

In Ref. [17], Rb-Cs ultracold collisions were analyzed using a combination of s-wave and p-wave terms. There, the s-wave term was written (within the effective range approximation [19,26]) in terms of a scattering length and an effective range r_e, while the p-wave term was expressed in terms of a p-wave volume A_1 [27]. For a single species the cross section becomes

$$\sigma(k_R) = \frac{(1+\varepsilon)4\pi a^2}{\left(1-\frac{1}{2}k_R^2 a r_e\right)^2 + k_R^2 a^2} + \frac{(1-\varepsilon)12\pi A_1^2 k_R^4}{1+A_1^2 k_R^6}, \quad (11)$$

where $\varepsilon=1$ for bosons and $\varepsilon=-1$ for fermions [28]. The effective cross section is then

$$\sigma_{c,\mathrm{eff}} = 2\int_0^\infty dx\, x^3 e^{-x^2}\left(\frac{(1+\varepsilon)4\pi a^2}{\left(1-\frac{1}{2}r_e C x^2\right)^2 + a^2 C x^2} + \frac{(1-\varepsilon)12\pi C^2 A_1^2 x^4}{1+C^3 A_1^2 x^6}\right), \tag{12}$$

where $C=\mu k_B T/\hbar^2$.

B. Atomic mixtures

When two atomic species are simultaneously confined, the average interspecies collision rate can be calculated starting from the total interspecies collision rate $\Gamma_{12,\mathrm{tot}}$, expressing the total number of collisions between atoms of different species per unit of time. Indicating with $\{N_i, m_i, \langle\omega_i\rangle, T_i, f_i(\mathbf{r},\mathbf{v})\}$ $(i=\{1,2\})$ the total number of particles, the mass, the average trap frequency, the temperature, and the phase-space density distribution of species i, and indicating with σ_{12} the interspecies elastic cross section, $\Gamma_{12,\mathrm{tot}}$ is defined by

$$\Gamma_{12,\mathrm{tot}} = \int d^3r d^3v_1 d^3v_2 \sigma_{12}(\mathbf{v_1},\mathbf{v_2})|\mathbf{v_1}-\mathbf{v_2}| f_1(\mathbf{r},\mathbf{v_1}) f_2(\mathbf{r},\mathbf{v_2}). \tag{13}$$

By substituting Eq. (1) into Eq. (13) and by assuming that the frequencies of the harmonic potentials confining the two species are related by $m_2\omega_{2,j}^2=\beta^2 m_1\omega_{1,j}^2$ $(j=\{x,y,z\})$, one finds

$$\Gamma_{12,\mathrm{tot}} = \frac{N_1 N_2 m_1^{3/2}\bar{\omega}_1{}^3}{\pi^2 k_B (T_1+\beta^2 T_2)^{3/2}}\sqrt{\frac{T_1}{m_1}+\frac{T_2}{m_2}}\,\sigma_{12,\mathrm{eff}}. \tag{14}$$

The quantity $\sigma_{12,\mathrm{eff}}$ appearing in Eq. (14) represents the effective interspecies cross section, analogous to the effective intraspecies cross section defined by Eq. (4),

$$\sigma_{12,\mathrm{eff}} = 2\int_0^\infty dy\, y^3 e^{-y^2}\sigma_{12}\left(\sqrt{\frac{2k_B(m_1T_2+m_2T_1)}{m_1 m_2}}\,y\right). \tag{15}$$

The collision rate $\Gamma_{12,\mathrm{tot}}$ can be expressed in terms of the two-species average density $\bar{n}_{12}$,

$$\bar{n}_{12} = \int d^3r n_1(\mathbf{r}) n_2(\mathbf{r}) = \frac{N_1 N_2 m_1^{3/2}\bar{\omega}_1^3}{[(2\pi k_B)(T_1+\beta^2 T_2)]^{3/2}} \tag{16}$$

and of the average relative interspecies velocity $\bar{v}_{R,12}$, given by

$$\bar{v}_{R,12} = \frac{\int d^3v_1 d^3v_2 f_1(0,\mathbf{v}_1) f_2(0,\mathbf{v_2})|\mathbf{v_1}-\mathbf{v_2}|}{\int d^3v_1 d^3v_2 f_1(0,\mathbf{v_1}) f_2(0,\mathbf{v_2})} = \sqrt{\frac{8k_B}{\pi}\left(\frac{T_1}{m_1}+\frac{T_2}{m_2}\right)}. \tag{17}$$

The interspecies collision rate then assumes the compact form

$$\Gamma_{12,\mathrm{tot}} = \bar{n}_{12}\bar{v}_{\mathrm{R},12}\sigma_{12,\mathrm{eff}}. \tag{18}$$

The average collision rate $\gamma_{c,12}$ experienced by each atom of species 1 with atoms of species 2 is given by the total collision rate $\Gamma_{12,\mathrm{tot}}$ divided by the number of particles of species 1,

$$\gamma_{c,12} = \frac{\Gamma_{12,\mathrm{tot}}}{N_1} = \frac{N_2 m_1^{3/2}\bar{\omega}_1^3}{\pi^2 k_B (T_1+\beta^2 T_2)^{3/2}}\sqrt{\frac{T_1}{m_1}+\frac{T_2}{m_2}}\,\sigma_{12,\mathrm{eff}}. \tag{19}$$

Let us now consider the case in which the difference between the two temperatures T_1 and T_2 is small compared to the thermodynamic average temperature T_F of the mixture,

$$T_F = \frac{N_1T_1+N_2T_2}{N_1+N_2}. \tag{20}$$

Then, the quantities defined above can be approximated by the simplified expressions,

$$\tilde{\sigma}_{12,\mathrm{eff}} = 2\int_0^\infty dy\, y^3 e^{-y^2}\sigma\left(\sqrt{\frac{2k_BT_F}{\mu}}\,y\right), \tag{21}$$

$$\tilde{\Gamma}_{12,\mathrm{tot}} = \frac{N_1 N_2 m_1 m_2 M^{1/2}\bar{\omega}_1^3\bar{\omega}_2^3}{\pi^2(m_1\bar{\omega}_1^2+m_2\bar{\omega}_2^2)^{3/2}k_BT_F}\tilde{\sigma}_{12,\mathrm{eff}}, \tag{22}$$

$$\tilde{\gamma}_{c,12} = N_2\frac{m_1 m_2 M^{1/2}\bar{\omega}_1^3\bar{\omega}_2^3}{\pi^2(m_1\bar{\omega}_1^2+m_2\bar{\omega}_2^2)^{3/2}k_BT_F}\tilde{\sigma}_{12,\mathrm{eff}}, \tag{23}$$

where the total mass $M=m_1+m_2$ and the reduced mass $\mu=m_1m_2/M$ have been used.

III. THERMALIZATION OF ATOMIC MIXTURES

The experimental determination of the collision rate in a mixture allows us to determine the effective elastic cross section between the two species. If an atomic mixture is driven out of thermodynamic equilibrium, for instance by creating a difference between the temperatures of the two species, the mixture relaxes towards the equilibrium condition as a consequence of the interspecies collisions. From the observation of the time evolution of the two temperatures we may extract the value of the elastic cross section [12,19]. The simplest model of the thermalization process ([10,11]) assumes that the two clouds are described by phase-space distribution functions of the form of Eq. (1) at temperatures T_1 and T_2.

For atoms confined in a harmonic potential the temperature is related to the average energy through

$$\langle E_i\rangle = 3k_BT_i. \tag{24}$$

In order to calculate the rate at which the two temperatures approach their final common value T_F, we determine the rate at which energy is exchanged between the two species due to elastic collisions. The rate of change of the temperature is then derived by using Eq. (24). This procedure is correct for the collisionless regime, defined by the condition that the collision rate is smaller than the frequency of the

confining potential. Estimating the collision rate for a Rb-Cs mixture under typical experimental conditions [17], even for the largest value of the elastic cross section allowed by the unitary limit we find that our mixtures are always in the collisionless regime, so that the study of thermalization by means of Eq. (24) is correct.

The total energy exchanged between the two samples per unit time is obtained by summing, for each pair of colliding particles in the mixture, the kinetic energy ΔE_i^k transferred by a particle of species i to a particle of the other species weighted by the rate at which each pair of particles collides. The time derivative of the total energy of species i is then given by

$$\frac{dE_{\mathrm{tot},i}}{dt} = -\int d^3r d^3v_1 d^3v_2 f_1(\mathbf{r},\mathbf{v_1}) f_2(\mathbf{r},\mathbf{v_2}) \times \sigma_{12}(\mathbf{v_1},\mathbf{v_2})|\mathbf{v_1}-\mathbf{v_2}|\Delta E_i^k. \quad (25)$$

For each species, the use of Eq. (24) leads to

$$\frac{dT_i}{dt} = \frac{1}{3k_B}\frac{d\langle E_i\rangle}{dt} = \frac{1}{3k_B N_i}\frac{dE_{\mathrm{tot},i}}{dt}. \quad (26)$$

Performing the integration over the spatial and velocity variables according to Eq. (25), and using Eq. (26) one finds

$$\frac{dT_i}{dt} = \frac{\xi}{3} N_j \frac{m_1^{3/2}\bar{\omega}_1^3\sigma_{\mathrm{th}}}{\pi^2 k_B (T_1+\beta^{-2}T_2)^{3/2}}\sqrt{\frac{T_1}{m_1}+\frac{T_2}{m_2}}(T_j - T_i). \quad (27)$$

Here ξ defined as

$$\xi = \frac{4\mu}{M} \quad (28)$$

takes into account the fact that the energy exchanged through elastic collisions between particles with different masses is smaller than the energy exchanged between particles with the same mass. The effective cross section σ_{th} for the thermalization process is given by

$$\sigma_{\mathrm{th}} = \int_0^\infty dy\, y^5 e^{-y^2}\sigma_{12}\left(\sqrt{\frac{2k_B(m_1T_2+m_2T_1)}{m_1m_2}}y\right). \quad (29)$$

The conservation of energy in the total system, expressed by the relation $N_1T_1+N_2T_2=E_{\mathrm{tot}}/3k_B=(N_1+N_2)T_F$ together with Eq. (27) allows us to write the equations describing the evolution of the two temperatures in the following form:

$$\frac{d(T_1(t)-T_{\mathrm{F}})}{dt} = -\frac{1}{\tau_{\mathrm{th}}(T_1(t),T_2(t))}(T_1(t)-T_{\mathrm{F}}),$$

$$\frac{d(T_2(t)-T_{\mathrm{F}})}{dt} = -\frac{1}{\tau_{\mathrm{th}}(T_1(t),T_2(t))}(T_2(t)-T_{\mathrm{F}}) \quad (30)$$

with

$$\tau_{\mathrm{th}}(T_1,T_2) = \left(\frac{\xi m_1^{3/2}\bar{\omega}_1^3\sigma_{\mathrm{th}}(N_1+N_2)}{3\pi^2 k_B(T_1+\beta^{-2}T_2)^{3/2}}\sqrt{\frac{T_1}{m_1}+\frac{T_2}{m_2}}\right)^{-1}. \quad (31)$$

The time evolution of the two temperatures is similar to an exponential relaxation towards the stationary value T_F, but with a time-varying time constant given by τ_{th}.

For small deviations of the initial temperatures from the final temperature T_F, i.e., for $(T_1-T_F)\simeq(T_2-T_F)\ll T_F$, the variation of the time constant during the thermalization can be neglected and the evolution of the temperatures follows an exponential law with a fixed time constant

$$\tilde{\tau}_{\mathrm{th}} = \left(\frac{\xi}{3}\frac{m_1m_2M^{1/2}\bar{\omega}_1^3\bar{\omega}_2^3\tilde{\sigma}_{\mathrm{th}}}{\pi^2 k_B(m_1\bar{\omega}_1^2+m_2\bar{\omega}_2^2)^{3/2}T_F}\right)^{-1}, \quad (32)$$

where $\tilde{\sigma}_{\mathrm{th}}$ is given by Eq. (29) with $T_1=T_2=T_F$. By comparing Eqs. (19) and (31) one sees that the collision rate $\gamma_{c,12}$ and the thermalization rate are related by

$$\gamma_{c,12} = \frac{3}{\xi}\frac{N_2}{N_1+N_2}\frac{\sigma_{12,\mathrm{eff}}}{\sigma_{\mathrm{th}}}\frac{1}{\tau_{\mathrm{th}}}. \quad (33)$$

For a binary mixture with equal numbers of atoms having the same mass, and for temperatures low enough that the elastic cross section can be considered constant, the thermalization rate is 2/3 of the interspecies collision rate, so that on average each atom experiences 1.5 interspecies collisions within a time τ_{th}, as first determined by Monroe *et al.* by means of Monte Carlo simulations [29]. For binary mixtures with different numbers of atoms, on the other hand, the ratio between the collision rate and the thermalization rate depends on the composition of the mixture.

IV. RETHERMALIZATION IN EXPERIMENTS

The above model for the temperature relaxation of an atomic mixture allows the extraction of the value of the elastic cross section or, more precisely, the value of the effective cross section, from the observed evolution of the temperatures of the two atomic species. The model, however, does not take into account two main characteristics of real samples confined in magnetic traps. The first one concerns the spatial displacement of one cloud with respect to the other due to the gravitational sag.

The balance between the magnetic potential and gravity g displaces the center of the density distribution of species i from the magnetic trap center by the gravitational sag $z_{0,i}=-g/\omega_{z,i}^2$, where $\omega_{z,i}$ is the magnetic trap frequency along the vertical axis [35]. For a mixture of atoms of different species, or even for atoms of the same species but in states with different magnetic moments, the spatial displacement of the density distributions modifies the overlap of the two spatial densities and also the total collision and thermalization rates. By considering the collisions between two clouds distributed around different centers separated by a differential sag $\Delta z_0=z_{0,1}-z_{0,2}$, one finds a correction factor $F(\Delta z_0)$ to be included into all the collisional rates that depends on the overlap of the two atomic distributions and is given by

$$F(\Delta z_0) = e^{-[m_1(\omega_{z,1}\Delta z_0)^2/2k_B(T_1+\beta^2 T_2)]}. \quad (34)$$

A relative displacement of the two clouds that is larger than the sum of the their spatial widths leads to a significant decrease of the density overlap, and thus of the collision and thermalization rates.

The second complication to be taken into account is the fact that in real-life experiments the atoms inside the magnetic trap have a finite lifetime due to collisions with the background gas and also due to inelastic collisions between ultracold atoms. If the lifetime of the atomic sample is comparable to the thermalization time, then Eqs. (30) should be modified to include a decay in the atomic number of species i in the trap with lifetime τ_i. For the case of small temperature changes, $T_1(t)-T_F, T_2(t)-T_F \ll T_F$, i.e., close to the equilibrium value, the analytical solution for the time dependence of the atomic temperature difference $\Delta T(t)=T_1(t)-T_2(t)$ becomes

$$\Delta T(t) = \Delta T(0) e^{-t_r/\tilde{\tau}_{th}}, \quad (35)$$

where the renormalized time t_r is given by

$$t_r = \frac{\tau_1 N_1(0)(1-e^{-t/\tau_1}) + \tau_2 N_2(0)(1-e^{-t/\tau_2})}{N_1(0)+N_2(0)}, \quad (36)$$

and $\tilde{\tau}_{th}$ is given by Eq. (32) evaluated for the initial atomic number of the two species. Therefore, in units of renormalized time the difference of the two temperatures is still described by an exponential decay.

V. SIMULATIONS

A. Monte Carlo approach

The above thermalization model is based on the fundamental assumption that each cloud is described by a distribution with a well-defined value of the temperature. In many cases this assumption cannot be taken for granted. For instance, during evaporative cooling the distribution of the sample cannot be described by a thermal distribution, as analyzed in Refs. [30–32]. A more flexible approach without preliminary assumptions as to the phase-space distribution is provided by the numerical Monte Carlo (MC) technique, developed by Bird for molecular gas dynamics [33], which allows us to study rethermalization, evaporation and sympathetic cooling of one or more species [22,23].

In the case of a single species, the atomic sample is described in terms of macroatoms, i.e., the numerical simulation takes into account a number of simulated macroatoms N_s such that $N=fN_s$, where N is the total number of atoms and f is chosen to be an integer power of 2. If the number of atoms of the sample decreases during the simulated process as a consequence of the finite lifetime of the sample or of the removal of atoms due to evaporation, as soon as the number of macroatoms N_s becomes smaller than one-half of the initial number its value is doubled through a duplication technique [22].

The atoms are treated as classical particles with positions and velocities evolving in time under the influence of the confining potential and of elastic collisions. The flow of time is discretized, and at each time step dt the dynamical variables evolve according to the deterministic evolution in the harmonic potential, which is exactly integrable, and to collisions, which are included as stochastic instantaneous binary processes. The effect of the collisions is taken into account as an instantaneous change in the velocities of the two particles in which the total energy and the total momentum of the pair are conserved. In order to respect the locality of the collisions, the spatial volume occupied by the sample is divided into a large number of cells whose linear dimensions are much smaller than both the length scale over which the gas density changes significantly and the collisional mean free path, and collisions are considered only between particles occupying the same spatial cell.

In this work, we have extended the method just described to the case of a binary mixture. The simulation scheme was essentially analogous to the single-species case. For each species a sample of macroatoms was distributed over the spatial cells according to the Boltzmann distribution corresponding to the temperature of the sample. The spatial region of the simulation was chosen according to the size of the largest atomic cloud. The time step dt was chosen on the basis of the smallest of the collision times for intraspecies and interspecies collisions. The requirement to take into account independently the collisions between particles of the same species and those between particles of different species was the only feature to be handled with care. In particular, when the number of atoms of one species was significantly larger than that of the other species, largely different representative factors f_1 and f_2 had to be used in order to simulate a comparable number of macroatoms, thus avoiding both large statistical fluctuations and the requirement of excessive memory capacity or computation times.

B. Simulation results

In order to check the validity of the analytical model discussed in the preceding section we have performed a numerical simulation of the thermalization process using the Monte Carlo technique. The MC simulation and the numerical integration of Eqs. (30) for ΔT were in good agreement. Figure 1 shows the evolution of the temperatures ΔT of a mixture composed of 4×10^4 Rb atoms and 3.5×10^5 Cs atoms. Figure 1(a) refers to an isotropic, energy independent cross section given by Eq. (6) with a relative scattering length $a=500a_0$. In this case the Rb-Cs clouds reach the equilibrium temperature in a few seconds. Figure 1(b) refers to an energy dependent cross section given by Eq. (8) with the same scattering length a. The energy dependence significantly reduces the effective cross section with respect to the zero-energy limit, and the rethermalization is significantly slower than in the preceding case. The MC simulation included the presence of inelastic losses, corresponding to lifetimes of 50 and 17 s for Rb and Cs, respectively. In Fig. 2(a) the temperature difference ΔT of case (a) is plotted versus the renormalized time defined by Eq. (36). In Fig. 2(b), by contrast, the difference ΔT of case (c) is plotted versus real time. For the first case an exponential fit to the temperature curve is in good agreement with the results of the simulation. On the other

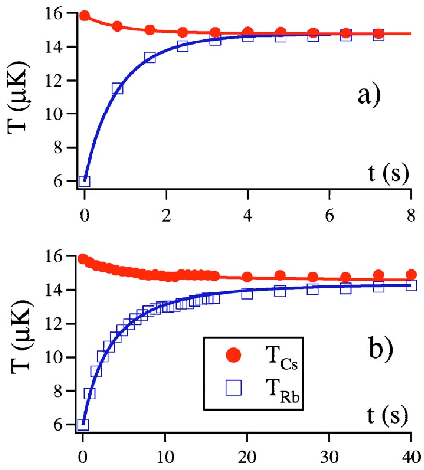

FIG. 1. (Color online) Thermal relaxation in a Rb-Cs mixture, for an elastic cross section with relative scattering length $a = 500\, a_0$, in (a) without and in (b) with energy dependence. The symbols are the results of MC simulations, whereas the lines are the results of the numerical integration of Eqs. (30).

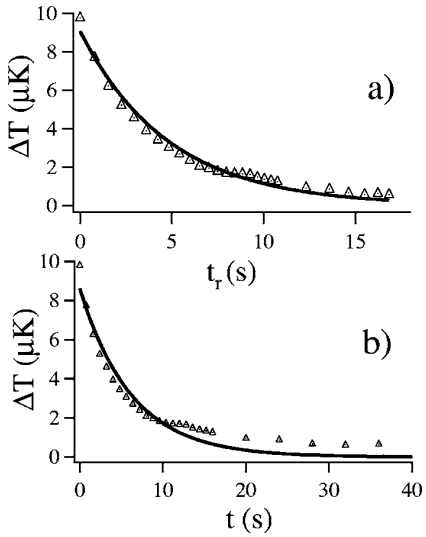

FIG. 2. In (a) and (b) the symbols show the evolution of ΔT corresponding to the data of Fig. 1(b), and the lines are exponential fits to the simulated data. In (a) ΔT is displayed versus the renormalized time t_r defined in Eq. (36), whereas in (b) it is displayed versus real time.

hand, in the second case the exponential decay does not reproduce the slowing down of the relaxation.

We have also simulated the rethermalization for an atomic mixture in which initially one of the two atomic species was not in thermal equilibrium. This situation arises naturally in our experiments in which we prepared the two clouds at different temperatures by performing a fast rf sweep on the Rb atoms and is due to the fact that rf evaporation is not truly three dimensional [30,32]. In fact, if the rf cut is swept down on a time scale that is short compared to the atomic collision time, the cloud can end up with different thermal distributions described by three different temperatures $T_{x,1}, T_{y,1}, T_{z,1}$. In our experiment on Rb-Cs mixtures, the rf cut on Rb acted mainly in the horizontal (x,y) plane and led to different temperatures in the horizontal and vertical directions. Figure 3 shows the time dependence of the temperatures for the two atomic clouds of the mixture, supposing different initial temperatures, $T_{x,1}=T_{y,1}=4.2\ \mu$K, $T_{z,1}=9.6\ \mu$K for the Rb atoms. The MC simulation confirmed that a thermal equilibrium along the different axes was reached and that the Rb-Cs rethermalization time with an anisotropic Rb temperature was essentially the same as in the isotropic case. This implies that using the average temperature of the species with an anisotropic thermal distribution does not alter the outcome of a rethermalization measurement (at least not for the small anisotropies present in our experiments).

VI. COMPARISON WITH EXPERIMENT

A. Experimental configuration and protocol

In order to demonstrate the validity of our theoretical approach, we compare the results of our model calculations with the experimental data obtained in a Rb-Cs mixture. The experimental setup and protocol is reported in detail in our previous work [17,35], and here we limit ourselves to describing briefly their essential features. We started with a sample of ultracold atoms in a time-averaged orbiting potential (TOP) magnetic trap, with Rb and Cs in the magnetically trapped stretched states, $|F=2,m_F=2\rangle$ and $|F=4,m_F=4\rangle$, respectively. By means of a fast initial stage of circle-of-death evaporation, we produced samples of about 2.5×10^6 Rb atoms and 5×10^5 Cs atoms, at temperatures around 25 μ. After circle-of-death evaporation, further cooling was effected by applying a radio-frequency field resonant with a $\Delta m_F=\pm1$ Zeeman transition, whose frequency was slowly swept. Because rf evaporation depends on the Zeeman-sublevel spacing and is species selective, only Rb atoms were evaporatively cooled. Nevertheless, owing to sympathetic cooling the Cs temperature followed the Rb temperature decrease. The properties of the two atomic clouds at variable times during the evaporation were measured.

In a different approach after circle-of-death evaporative cooling, rf evaporative cooling was applied to Rb, with a frequency sweep that was fast enough so that no energy exchange between Cs and Rb took place, and hence at the end of the rf ramp a temperature difference between the Rb and Cs atoms remained. Immediately afterwards, the temperature of both species was measured as a function of time. These rethermalization measurements were performed at various temperatures of the mixture. Before rethermalization, the atom numbers in the trap were $N_{Rb}\approx2\times10^6$ and $N_{Cs}\approx10^5$, with Rb temperatures in the 5–10 μK range and Cs temperatures in the 10–30 μK range.

B. Experimental data

Figure 4 shows experimental and theoretical results for the Rb-Cs mixture for the case of rf evaporation of Rb and sympathetic cooling of Cs. The Cs temperature closely fol-

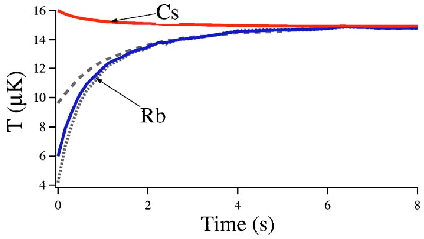

FIG. 3. (Color online) Evolution of the temperatures in a Rb-Cs atomic mixture with a temperature anisotropy in one species. The Rb atoms had different initial temperatures for the x,y directions (dotted line) and for the z direction (dashed line). The solid line for the colder species is the average temperature $\bar{T}=(2T_x+T_z)/3$.

lowed the Rb temperature during the evaporation, from the initial value of 27 μK to about 7 μK. In the absence of Rb, the Cs atoms were only very slightly cooled due to residual circle-of-death evaporation. In order to extract from these measurements the magnitude of the interspecies elastic cross section we performed numerical MC simulations of the evaporation and sympathetic cooling process. Simulations neglecting the interspecies collisions reproduced the observed behavior of a single species, and also the Cs circle-of-death cooling. For the Rb-Cs interspecies elastic scattering parameters, we relied on the theoretical predictions by Jamieson *et al.* [18], and for the effective cross section of the Rb-Cs collisions we used Eq. (12). In particular we considered the theoretical sets of scattering parameters (a_0,r_e,A_1) for the triplet interaction indicated in the following: data set $A=\{595.2a_0,190.2a_0,-168.5\times10^4a_0^3\}$, data set $B=\{177.2a_0,126.4a_0,-4681\times10^4a_0^3\}$, data set $C=\{-317.6a_0,424.2a_0-112.3\times10^4a_0^3\}$, and data set $D=\{-45.37a_0,3075a_0,-84.22\times10^4a_0^3\}$. Figure 4(a) shows that only the two sets A and B, corresponding to a large elastic cross section, are consistent with our measurements, while the data set C corresponding to a smaller cross section leads to the simulated temperature of Cs being larger than the experimental value. Figure 4(b) shows the Rb temperatures for the x and z directions. The temperatures T_x and T_z were different at the beginning of the evaporation stage since the previous circle-of-death evaporation was fast compared to the atomic thermalization rate. The MC simulation reproduced the differential cooling of Rb in the horizontal and vertical directions. We noticed that the elastic collisions with Cs atoms increased the thermalization rate, and T_z approached T_x more quickly. For the scattering parameters of data set B, this effect is slightly more pronounced, since the effective elastic cross section given by Eq. (12) was larger than in the case of data set A. Therefore the average temperature of the rubidium sample was lower in the mixture than in the single-species system. The simulation also reproduced the measured decrease in the Rb atomic number during the sympathetic cooling process.

Figure 5 shows the results of rethermalization measurements. After the fast rf-evaporation phase of Rb, the temperatures were $T_1(t=0)=25$ μK and $T_2(t=0)=46$ μK for Rb and Cs, respectively. At later times the temperatures of the two clouds approached one another and eventually became

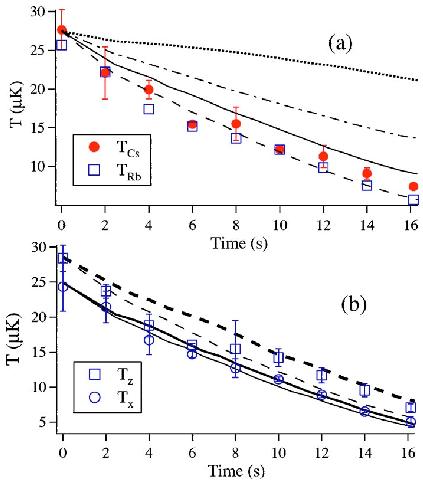

FIG. 4. (Color online) Sympathetic cooling of Cs atoms through rf evaporation of Rb atoms. In (a) data for Rb (open squares) and for Cs (filled circles) and results of Monte Carlo simulations for Cs, no interspecies collisions (dotted line), data set C (dashed-dotted line), data set A (solid line), data set B (dashed line). Rb error bars are similar to those for Cs. In (b) data and simulations for T_x and T_z of the Rb atoms. The solid and dashed lines are the results of the numerical simulations for the temperatures T_x and T_z, respectively. The thick lines correspond to data set A, the thin lines to data set B.

equal within times on the order of 10 seconds. The measurements performed with a single species showed that both atomic clouds were affected by a temperature increase, with intrinsic heating rates between 100 $nK\,s^{-1}$ and 350 $nK\,s^{-1}$ presumably due to technical noise in the magnetic field sources. For the thermalization data of Fig. 5, the Rb temperature shows a significant increase. The Cs temperature, on the other hand, showed only a small decrease because of the inelastic collisions in the central region of the cloud [34], and also because the Cs number was about 4 times larger than the number of Rb atoms. The analysis of the rethermalization measurements was based on the integration of Eqs. (30) for several values of the effective scattering cross section. The overlap of the density distribution of the two species was

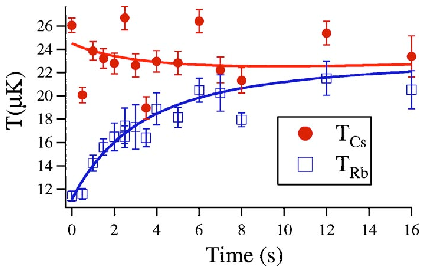

FIG. 5. (Color online) Rethermalization in a Rb-Cs mixture, after the creation of an initial temperature difference between Rb (squares) and Cs (circles) by a fast rf evaporation of the Rb atoms. Each point is the average of four independent measurements, and the error bar is their standard deviation. The solid lines are best fits obtained by a numerical integration of the equations describing the rethermalization process.

calculated according to Eq. (34). The analysis included the intrinsic heating and the presence of Rb and Cs atoms in other Zeeman sublevels due to imperfect optical pumping (10 percent for Rb and 20–30 percent in Cs) and depolarizing processes occurring during the evaporation cycle [36]. We calculated the χ^2 between the simulation results and the experimental data. For each thermalization measurement we extracted the value of the effective cross section by considering the range of cross sections minimizing the value of the χ^2. For the case of Fig. 5, for instance, we obtained a cross section corresponding to an effective scattering length $a_{\mathrm{eff}} = 180^{+30}_{-20} a_0$. From an analysis of the rethermalization measurements for different temperatures of the atomic mixture we concluded that the data set *A* provided the best fit of the Rb-Cs collisional data [17].

VII. CONCLUSIONS

The integration of Eqs. (30) reproduced the evolution for the temperatures of the two species within the atomic mixture. Our method constitutes a very efficient way to analyze the experimental data with the inclusion of all the atomic processes actually observed in the experiments. The substantial decay of the number of atoms during the thermalization process, the presence of a significant intrinsic heating, the relative displacement of the samples due to gravity and the correction to the overlap of the density distributions of the two species were included into our model. Neither the two atomic temperatures nor their difference followed a relaxation which could be modeled in a simple way, and a straightforward exponential fit to the relaxation of those quantities cannot be used to extract the correct value of the elastic cross section. The minimization of the difference between the numerical simulation and the experimental data was, therefore, our procedure of choice to determine the actual value of the effective interspecies cross section. Sympathetic cooling and rethermalization of the atomic mixture, combined with our theoretical model, may be applied to explore Rb-Cs ultracold collisions in the lower hyperfine states, too.

ACKNOWLEDGMENTS

The authors thank T. Bergeman, D. Guéry-Odelin, M. Holland, and M. Jamieson for useful discussions and J.H. Müller and N. Malossi for help in the early stages of the experiment. This research was supported by the INFM (PRA Photonmatter), by Progetto MIUR-COFIN 2004, and by the EU Network Cold Quantum Gases, Contract No. HPRN-CT-2000-00125.

[1] J. Weiner, V. S. Bagnato, S. Zilio, and P. S. Julienne, Rev. Mod. Phys. **71**, 1 (1999).
[2] J. Weiner, *Cold and Ultracold Collisions in Quantum Microscopic and Mesoscopic Systems* (Cambridge University Press, Cambridge, 2003).
[3] J. Stenger, S. Inouye, D. M. Stamper-Kurn, H.-J. Miesner, A. P. Chikkatur, and W. Ketterle, Nature **396**, 345 (1998).
[4] H. Pu and N. P. Bigelow, Phys. Rev. Lett. **80**, 1130 (1998).
[5] E. Timmermans and R. Coté, Phys. Rev. Lett. **80**, 3419 (1998).
[6] H. Wang and W. C. Stwalley, J. Chem. Phys. **108**, 5767 (1998).
[7] A. J. Kerman, J. M. Sage, S. Sainis, T. Bergeman, and D. DeMille, Phys. Rev. Lett. **92**, 033004 (2004); **92**, 153001 (2004).
[8] J. M. Sage, S. Sainis, T. Bergeman, and D. DeMille, Phys. Rev. Lett. **94**, 203001 (2005).
[9] M. Lewenstein, L. Santos, M. A. Baranov, and H. Fehrmann, Phys. Rev. Lett. **92**, 050401 (2004).
[10] G. Delannoy, S. G. Murdoch, V. Boyer, V. Josse, P. Bouyer, and A. Aspect, Phys. Rev. A **63**, 051602 (2001).
[11] A. Mosk, S. Kraft, M. Mudrich, K. Singer, W. Wohlleben, R. Grimm, and M. Weidemüller, Appl. Phys. B: Lasers Opt. **73**, 791 (2001).
[12] G. Ferrari, M. Inguscio, W. Jastrzebski, G. Modugno, G. Roati, and A. Simoni, Phys. Rev. Lett. **89**, 053202 (2002).
[13] G. Roati, F. Riboli, G. Modugno, and M. Inguscio, Phys. Rev. Lett. **89**, 150403 (2002).
[14] J. Goldwin, S. Inouye, M. L. Olsen, B. Newman, B. D. DePaola, and D. S. Jin, Phys. Rev. A **70**, 021601(R) (2004).
[15] Z. Hadzibabic, C. A. Stan, K. Dieckmann, S. Gupta, M. W. Zwierlein, A. Görlitz, and W. Ketterle, Phys. Rev. Lett. **88**, 160401 (2002).
[16] C. A. Stan, M. W. Zwierlein, C. H. Schunck, S. M. F. Raupach, and W. Ketterle, Phys. Rev. Lett. **93**, 143001 (2004).
[17] M. Anderlini, E. Courtade, M. Cristiani, D. Cossart, D. Ciampini, C. Sias, O. Morsch, and E. Arimondo, Phys. Rev. A **71**, 061401(R) (2005).
[18] M. J. Jamieson, H. Sarbazi-Azad, H. Ouerdane, G.-H. Jeung, Y. S. Lee, and W. C. Lee, J. Phys. B **36**, 1085 (2003).
[19] P. O. Schmidt, S. Hensler, J. Werner, A. Griesmaier, A. Görlitz, T. Pfau, and A. Simoni, Phys. Rev. Lett. **91**, 193201 (2003).
[20] G. M. Kavoulakis, C. J. Pethick, and H. Smith, Phys. Rev. A **61**, 053603 (2000).
[21] P. J. J. Tol, W. Hogervorst, and W. Vassen, Phys. Rev. A **70**, 013404 (2004).
[22] D. Guéry-Odelin, J. Söding, P. Desbiolles, and J. Dalibard, Opt. Express **2**, 323 (1998).
[23] E. Cerboneschi, C. Menchini, and E. Arimondo, Phys. Rev. A **62**, 013606 (2000), and references therein.
[24] S. Chapman and T. G. Cowling, *The Mathematical Theory of Non-uniform Gases* (Cambridge University, Cambridge, 1970).
[25] K. Huang, *Statistical Mechanics* (Wiley, New York, 1987).
[26] C. J. Joachain, *Quantum Collision Theory* (North-Holland, Amsterdam 1983).
[27] G. Gutiérrez, M. de Llano, and W. C. Stwalley, Phys. Rev. B **29**, 5211 (1984).
[28] The interference between the *s*-wave and *p*-wave is not included in the formula.

[29] C. R. Monroe, E. A. Cornell, C. A. Sackett, C. J. Myatt, and C. E. Wieman, Phys. Rev. Lett. **70**, 414 (1993).
[30] K. B. Davis, M. O. Mewes, and W. Ketterle, Appl. Phys. B: Lasers Opt. **60**, 155 (1995).
[31] O. J. Luiten, M. W. Reynolds, and J. T. M. Walraven, Phys. Rev. A **53**, 381 (1996).
[32] W. Ketterle, D. S. Durfee, and D. M. Stamper-Kurn, in *Bose-Einstein Condensation in Atomic Gases*, edited by M. Inguscio, S. Stringari, and C. Wieman (IOS, Amsterdam, 1999).
[33] G. A. Bird, *Molecular Gas Dynamics and the Direct Simulation of Gas Flows* (Clarendon, Oxford, 1994).
[34] J. Söding, D. Guéry-Odelin, P. Desbiolles, G. Ferrari, and J. Dalibard, Phys. Rev. Lett. **80**, 1869 (1998).
[35] J. H. Müller, D. Ciampini, O. Morsch, G. Smirne, M. Fazzi, P. Verkerk, and E. Arimondo, J. Phys. B **33**, 4095 (2000).
[36] We assumed the same interspecies elastic cross section for the atoms in all the magnetic sublevels involved in the thermalization.

Available online at www.sciencedirect.com
SCIENCE DIRECT®
Optics Communications 257 (2006) 340–348
OPTICS COMMUNICATIONS
www.elsevier.com/locate/optcom

Manipulation of ultracold atomic mixtures using microwave techniques

D. Ciampini *, E. Courtade, C. Sias, D. Cossart, G. Carelli, F. Mango, O. Morsch, E. Arimondo

INFM, Dipartimento di Fisica E.Fermi, Università di Pisa, Largo Pontecorvo 3, I-56127 Pisa, Italy

Received 24 March 2005; received in revised form 19 July 2005; accepted 19 July 2005

Abstract

We used microwave radiation to evaporatively cool a mixture of of ^{133}Cs and ^{87}Rb atoms in a magnetic trap. A mixture composed of an equal number (around 10^4) of Rb and Cs atoms in their doubly polarized states at ultracold temperatures was prepared. We also used microwaves to selectively evaporate atoms in different Zeeman states.

PACS: 32.80.Pj; 32.10.Fn; 84.40.Ba

Keywords: Alkali mixture; Microwave evaporation; Microwave selection

1. Introduction

Laser cooling techniques, combined with evaporative cooling in magnetic traps, allow the Bose-Einstein condensation (BEC) of a dilute atomic gas [1]. Typically, the atoms are trapped in conservative magnetic potentials and ultracold temperatures are reached through evaporative cooling using, for instance, radiofrequency (rf), microwave (mw) or circle-of-death techniques. The evaporation methods have different applicability and efficiency, which is more evident when dealing with combinations of ultra-cold atoms. A few combinations of ultra-cold atoms have been studied in conservative traps, among them Li–Cs [2], K–Rb [3–5], and Na–Li [6,7].

In experiments on ultracold atoms and atomic mixtures the use of mw radiation in evaporative cooling has been explored by a number of groups and has become a commonly used technique in the field. For example, controlled state selective evaporation of a single species was applied in [8]. Selective evaporative cooling of a single species in a two-species magnetic trap was used in [4,9,10],

* Corresponding author. Tel.: +39 050 2214292; fax: +39 050 2214333.
E-mail address: ciampini@df.unipi.it (D. Ciampini).

0030-4018/$ - see front matter © 2005 Elsevier B.V. All rights reserved.
doi:10.1016/j.optcom.2005.07.051

for the sympathetic cooling of ^{6}Li by ^{7}Li in [11] and for the sympathetic cooling of ^{6}Li by ^{23}Na in [6]. We have applied mw evaporation to a mixture of ultra-cold ^{87}Rb and ^{133}Cs atoms in a magnetic trap in order to explore sympathetic cooling and the collisional rethermalization between the two species, as reported in [12]. With the aim of producing a very cold Cs sample, we explored the temperature limits associated with circle-of-death, rf and mw evaporation. This detailed exploration is the topic of the present work.

Our best approach for evaporating the Rb–Cs mixture was the sequential application of different evaporative cooling processes: an initial stage of circle-of-death evaporation active on both species, followed by direct mw evaporative cooling of Cs, and finally rf cooling of Rb that led to sympathetic cooling of Cs through collisional energy exchange with Rb atoms. Applying the usual sequence of circle-of-death followed by radio-frequency evaporation for achieving BEC in a TOP trap, we verified that, to a good approximation, circle-of-death evaporation is equally efficient on Cs and Rb atoms. We discovered that owing to the large Cs–Rb interspecies scattering length $a_{\mathrm{Rb-Cs}} \simeq 590a_0$ [12] sympathetic cooling of Cs atoms by collisions with Rb is a very effective process. However, the Rb atom population is substantially depleted before very low Cs temperatures are achieved. Therefore, in order to reach very low Cs temperatures, we introduced an intermediate stage of mw evaporation. This sequence of different evaporation techniques was optimised in order to allow us to measure the Cs–Rb relative scattering length at a temperature of 6 μK, as we reported in [12]. In the case where rf evaporation of Rb was applied without the intermediate step of microwave evaporation, the lowest temperature achieved for performing the scattering length measurement was at least two times larger.

While characterizing the Rb–Cs ultracold mixture we faced the presence of ultracold atoms in Zeeman sublevels different from the desired doubly polarized state. For several degenerate gas investigations, an incomplete atomic magnetization represents a great difficulty. Therefore, we employed a mw irradiation technique to selectively evaporate Rb or Cs atoms in specific Zeeman sublevels [13]. While rf evaporation drives transitions between all the Zeeman sublevels of a hyperfine state, the applied mw evaporation acts only on a given Zeeman sublevel. We report magnetization measurements for the Rb and Cs atoms before and after selective mw evaporation. This magnetization purification process could be useful for exploring the dependence of the scattering length on the Zeeman state.

This manuscript is organized as follows: Section 2 describes the experimental setup used for the preparation of the cold Rb–Cs mixture, the generation of mw radiation and its delivery to the atomic sample and mw spectroscopy within the magnetic trap. The evaporative cooling of the atomic mixture by mw radiation is described in Section 3, while the state-selective removal of atoms is in Section 4. Section 5 presents some conclusions.

2. Experimental setup and techniques

2.1. Optical components

We used a double-chamber vacuum system with a 2D collection MOT and a six-beam MOT [15,12]. Once the two species MOT was filled, after brief compressed MOT and molasses phases the trapping beams were switched off and the atoms were optically pumped into the $|F=2,\ m_F=2\rangle$ and $|F=4,\ m_F=4\rangle$ doubly polarized states of Rb and Cs, respectively. Immediately after that, the TOP magnetic trap was switched on. The bias field B_0 of the TOP rotating at 10 kHz in the horizontal plane was created by two pairs of coils, fed by a common function generator through a 90° phase shifter. A schematic of the coils for the TOP trap is presented in Fig. 1.

The temperature of the atomic mixture was then lowered first by circle-of-death evaporation and afterwards by radiative evaporation (rf and/or mw radiation). The atom number and temperature were measured by flashing on a beam resonant with one of the atomic species and recording the resulting shadow cast on a CCD camera by the atom cloud. For a given atom, different Zeeman sublevels can be magnetically trapped and, after switching off the magnetic trap,

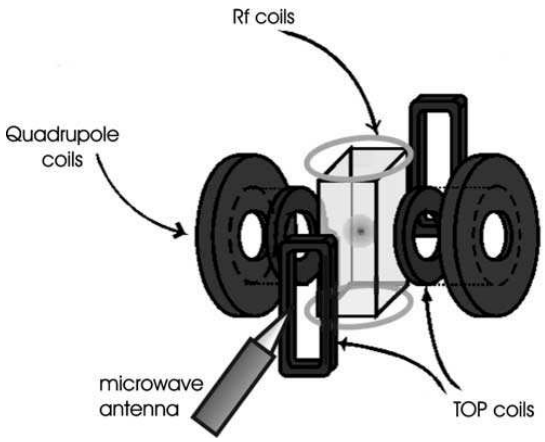

Fig. 1. Schematic of the coils for the magnetic trap. The quadrupole axis is along the horizontal direction while the bias field, produced by the TOP coils, rotates in the horizontal plane. The rf coils and the mw antenna are visible.

all of them were imaged by the same resonant laser flash. In order to observe their relative populations for Rb, we used a very shallow magnetic potential in order to maximize the spatial separation along the vertical direction between the equilibrium positions of the sublevels [15], the so-called gravity sag. For Cs atoms, it was not possible to spatially distinguish the atoms in the $|F=4, m_F=4\rangle$ Zeeman sublevel from those in the $|F=4, m_F=3\rangle$ state using the differential gravity sag, the ratio of the magnetic moments of the two trapped states being only $\frac{4}{3}$, compared to the value of 2 for Rb. Thus in order to monitor the Cs atoms in different sublevels as separate clouds, we performed a Stern–Gerlach type experiment (3 ms in which the atoms are in the quadrupole field only) separating the Zeeman levels in time-of-flight.

2.2. Microwave source

The mw radiation was produced by a frequency locked oscillator system composed of a Sweep Oscillator (HP 8350B), a Frequency Counter (HP 5343A) and a Source Synchronizer (HP 5344A). The frequency sweep and the mw switch were computer-controlled and synchronized to the experimental cycle. The mw radiation was amplified up to 5 W by a second power amplifier (Kuhne, model KU702 for the C-band, 4–8 GHz, and model KU922 for the X-band, 8–12 GHz). The mw radiation was delivered to the atoms by a dielectric rod antenna. In our experiment we used two different antennas, one made of teflon, optimized to deliver radiation at 9.2 GHz and one made of plexiglass, used in the region around 6.8 GHz. The antennas consist of a circular-section dielectric rod directly inserted into the circular end of a metal waveguide for the X (Cs) and C (Rb) bands. The rod is conically shaped at both ends, with the cone lengths equal to 6 and 8 cm for the Cs and Rb antennas, respectively. Such linearly tapered-rod antennas have been extensively studied, and the presence of a dielectric close to the conductor structure profoundly modifies the performance of the antenna [16].

In a preliminary experiment, we verified the behavior of the mw antennas by monitoring the reflection coefficient with a network analyzer over a band of frequencies around the desired frequency. For both antennas, the reflected power fraction never exceeded −10 dB, with a modulation structure related to the presence of objects adjacent to the antenna. The effect of the dielectric rod is to concentrate the mw field in a lobe in the direction of the cone termination [17], and the directivity gain is determined primarily by the antenna length. We experimentally found that for the same on-axis distance from the conductor waveguide, the field intensity was amplified by a factor 2.4 when the dielectric rod was inserted (see Fig. 2). We also noticed a large reflection of the mw radiation due to metallic objects located in front of the antenna.

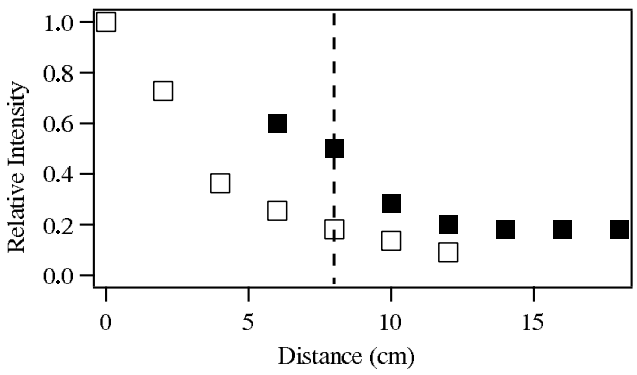

Fig. 2. Relative intensity of the e.m. field measured at various distances from the end of the X-band metal waveguide, in the presence (solid squares) and in the absence (open squares) of the dielectric rod extension. The dashed line marks the distance where the cold atoms are located during the experiment.

2.3. Microwave spectroscopy

We performed mw precision spectroscopy of the trapped Rb and Cs atoms by inducing transitions between their hyperfine levels $|F = I + 1/2, m_F = I + 1/2\rangle$ and $|F = I - 1/2, m_F = I - 1/2\rangle$. As pointed out previously [18–20], for a cloud of magnetically trapped atoms the inhomogeneity due to the energy level shifts broadens the transition frequency and limits the attainable precision. Furthermore, in a TOP trap the presence of the time-varying field of the trap introduces a time-varying detuning that greatly complicates the interaction between trapped atoms and mw radiation [21]. Our mw spectroscopical investigation within the TOP trap for an interaction time long compared to the rotating field period demonstrated a strong dependence of the mw transition linewidth on the temporal variation of the modulus of the rotating bias field. The analysis of the condensate micromotion in the TOP [22] shows that the atoms follow an orbit corresponding to a constant total modulus of the magnetic field if the amplitude B_0 of the bias field is constant during the horizontal rotation. On the other hand, the total magnetic field experienced by the atoms during their motion contains components varying at the rotating field and its harmonics in the presence of an elliptical rotating bias field. Such an elliptical bias field appears, for instance, if the two linearly oscillating magnetic fields whose superposition produces the rotating bias field are not very precisely matched in amplitude and phase. This behavior is confirmed by the data of Fig. 3 for the number of Rb atoms remaining in the magnetic trap after 10 s application of 5 W mw radiation whose frequency was scanned over the resonant value. For a 30% ellipticity of the bias field we observed a well-defined double peak structure for the mw transition (open squares). When the ellipticity of the bias field was compensated by adjusting the relative value of the magnetic field amplitudes in the two pairs of TOP coils and the phase, the two peaks coincided (solid circles). This method is very sensitive: operating at our maximum amplitude of the bias field, a phase mismatch of 5° between the two oscillating fields and an ellipticity of 10% broadens the mw transition by

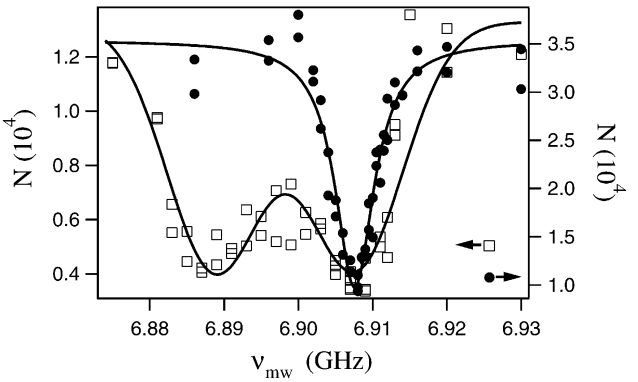

Fig. 3. Number of Rb atoms after application of mw radiation for 10 s in the TOP trap as a function of the mw frequency for two different choices of the relative amplitude of the oscillating fields of the TOP trap, leading to a 30% ellipticity (open squares, left axis) and to a circular rotating bias field, compensated in ellipticity and phase as described in the text (full circles, right axis). The full lines are double Gaussian and Lorentzian fits, respectively, to the data sets.

~4 MHz. We found this fine adjustment procedure of the bias field based on the linewidth of the mw transition to be more sensitive than the procedure based on the optimization of the circle-of-death evaporation efficiency. Moreover, we performed mw spectroscopy within the TOP trap for an interaction time short compared to the period of rotation of the TOP field, and finally performing spectroscopy in time of flight in the presence of a rotating bias field or a weak homogeneous magnetic field. In this sequence of experiments we eliminated the residual inhomoegenous broadening and measured a decreasing linewidth. The final limiting linewidth at full mw power, 5 W (the power injected into the waveguide), was around 100 kHz, in good agreement with the theoretical value obtained by estimating the amplitude of the mw magnetic field (~70 mG) at the position of the atoms from the power inserted into the waveguide and the enhancement factor due to the teflon cone (as seen in Fig. 2).

3. Evaporation procedure

3.1. Circle of death

In a TOP trap the temperature of the atomic mixture can be lowered through circle-of-death

evaporative cooling, defined by the rotating zero of field created by the (static) quadrupole and the (rotating) bias field. By continuously reducing the strength of the rotating bias field the circle-of-death shrinks and atoms from the high energy tail of the distribution are progressively removed from the sample. In the double polarized Zeeman states Cs and Rb atoms have the same magnetic moment. Therefore, at the same temperature they have the same spatial extension in a magnetic trap, and circle-of-death evaporation is simultaneously applied to both species. At low temperatures and high atomic density, circle-of-death evaporation becomes inefficient because it requires a continuous increase of the trapping frequencies leading to an increased atomic density, resulting in large three-body losses. At the end of our circle-of-death evaporation phase, Rb and Cs atoms were in thermal equilibrium at ~15 μK.

3.2. Radiative evaporation: radiofrequency

Radiative evaporation uses an e.m. radiation field to transfer atoms from a trapped to an untrapped state in an energy-selective way. The advantages of radiative evaporation (rf and mw) are that the magnetic potential does not have to be modified to sustain the evaporation since the escape rate is precisely controlled by the amplitude and the frequency of the applied radiation.

Rf induced evaporation between $|F,\ m_F = F\rangle$ and $|F,\ m_F = F-1\rangle$ states exploits spin-flips of atoms on a resonant energy shell defined by

$$g_F \mu_B B(\vec{x}) = h\omega_{rf}, \tag{1}$$

where $B(\vec{x})$ is the modulus of the instantaneous local magnetic field defining the cut energy of the shell, μ_B is the Bohr magneton, $g_F = 2/(2I+1)$ is the Landé factor, with $I = 3/2$ for ^{87}Rb and $I = 7/2$ for ^{133}Cs, and ω_{rf} is the rf field frequency. Notice that Eq. (1), and the following one for the mw evaporation, is derived in the limit of weak Zeeman splitting. For $F > 1$ the rf transition defined by Eq. (1) transfers atoms into a different Zeeman state that is still magnetically trapped. However, because of power broadening the rf radiation induces a chain of transitions between different Zeeman levels starting from trapped states to untrapped ones leading to a loss of atoms from the magnetic trap. By ramping down the frequency ω_{rf}, the radius of the surface volume where the resonance condition is fulfilled shrinks, leading to an effective forced evaporation [1].

Eq. (1) specifies that rf evaporation depends on the Zeeman-sublevel spacing. When rf radiation is applied to a mixture of atoms, the cut energy of the atoms to be evaporated is different. In a Rb–Cs mixture, owing to the difference in the Landé factor, the Cs cut energy is half that for Rb atoms. Thus, when the most energetic Cs atoms are removed by the rf radiation, cold Rb atoms at the bottom of the potential are also removed. On the contrary, cooling the Rb atoms with rf has no direct effect on the Cs temperature, because the rf field is not resonant with the trapped Cs atoms.

3.3. Radiative mw evaporation

For a mixture of atomic species mw evaporative cooling represents an efficient alternative to rf evaporative cooling. Mw evaporation uses transitions between Zeeman sublevels belonging to *different* hyperfine levels of the ground states. For a transition between the hyperfine states $|F,\ m_F = F\rangle$ and $|F-1,\ m_F = F-1\rangle$ of an alkali atom, the resonance condition is

$$h\omega_{hf} + g_F(2m_F - 1)\mu_B B(\vec{x}) = h\omega_{mw}, \tag{2}$$

where $\omega_{hf}/2\pi$ is the hyperfine splitting (~9.2 GHz for Cs, ~6.8 GHz for Rb), and $\omega_{mw}/2\pi$ the mw frequency. The previous equation indicates that the mw resonance conditions for Cs and Rb are always very different and the two evaporation processes are independent.

Fig. 4 shows the temperature and atom number of the Cs cloud at the end of mw evaporation in the absence of Rb atoms in the magnetic trap. During the evaporative cooling the mean temperature of the Cs cloud decreased in direct proportion to the number of atoms. The cloud was irradiated by a mw frequency ramp with a fixed starting frequency and varying final frequency. The evaporation took place after a magnetic compression phase and a circle-of-death cooling stage. The data points at the far right describe the initial condition before the application of the mw radiation. The

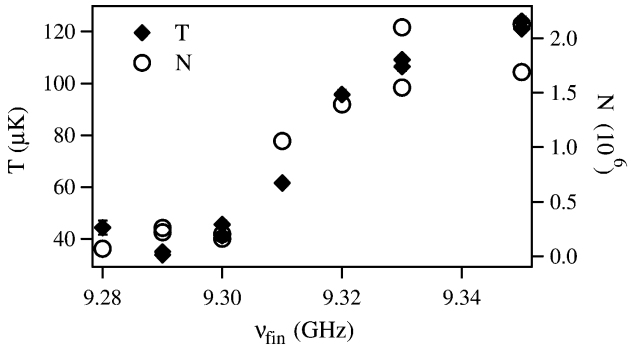

Fig. 4. Temperature (full diamonds) and number of atoms (open circles) of the Cs cloud as a function of the final value of the mw frequency. Initial frequency 9.40 GHz, trap bottom 9.271 GHz, duration of the evaporation ramp 5 s and mw power 3 W. These data were from single experimental runs and the uncertainties due to the fit of the single images were smaller than the size of the data points.

dependence of the final temperature of the Cs cloud on the mw intensity is shown in Fig. 5. In our experiments, we generally observed a lower efficiency for the mw evaporation compared to rf evaporation. Owing to imperfect optical pumping (and, possibly, other depolarizing processes during the evaporation cycle), both the Rb and Cs cold clouds had admixtures of atoms in other Zeeman sublevels, as discussed in the following Section. While the radio-frequency radiation, inducing a chain of transitions between the equally spaced Zeeman sublevels, evaporates atoms from all of them, the mw transitions of Eq. (2) are well separated in frequency, at 30–40 G trap field and in the absence of saturation broadening. Thus, the mw field is resonant with one Zeeman state only, leaving the residual population of the other sublevels uncooled by the mw radiation. This residual population is eventually cooled through sympathetic cooling collisions with the atoms in the other Zeeman state, but the overall efficiency of the mw evaporation is reduced. From the data of Fig. 4 for Cs, assuming an atomic occupation of the single Zeeman sublevel $|F=4,\ m_F=4\rangle$, we derived that under mw evaporation the increase of the phase space density followed a N^{-2} law with N the atom number, a law similar to that required for the runaway regime reached by the rf evaporation [1]. However, the occupation of the $|F=4,\ m_F=3\rangle$ sublevel for the data in Fig. 4 is around 30–40%, as extracted from the Stern–Gerlach type experiments performed with ultracold Cs atoms (see Section 4), and that occupation greatly decreases the effective efficiency of the phase-space compression by the mw evaporation.

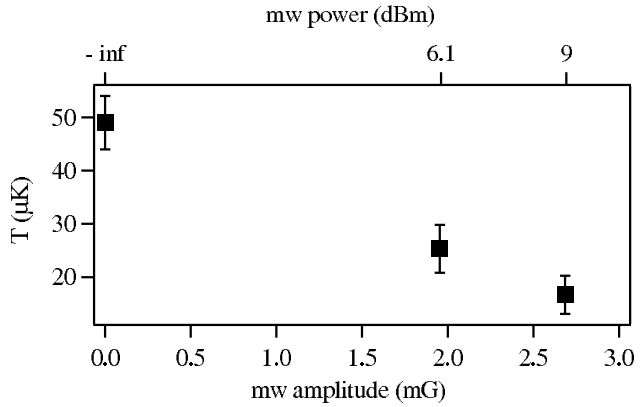

Fig. 5. Cs temperature as a function of the mw power (in the upper horizontal scale), and of the mw field amplitude at the atom position (in the lower scale), for a given evaporation ramp (from 9.3 to 9.22 GHz) with 5 s duration. The data uncertainty is due to statistical averaging over several experimental runs.

3.4. Sympathetic cooling

After the preparative stages of circle-of-death and mw evaporation we verified that when performing rf evaporation on the Rb atoms, the measured temperature of the Cs atoms exactly followed the Rb temperature down to a few μK, indicating that sympathetic cooling was taking place, as long as the remaining number of Rb atoms, compared to the Cs atom number, was sufficient to sustain the thermalization. By applying mw techniques, we were able to prepare a mixture of 4×10^4 Rb atoms in the $|F=2,\ m_F=2\rangle$ state and 10^4 Cs atoms in the $|F=4,\ m_F=4\rangle$ state at about 6 μK (mean trapping frequency 70 Hz). This temperature is of the same order of magnitude as that reported by the ENS group [24] for Cs in the same atomic state in their early search for condensation of Cs. From our data we extrapolated that for Cs a temperature around 3 μK could be achieved if all of the Rb was evaporated. A detailed model of the sympathetic cooling phase was developed in [12] in order to derive the Rb–Cs interspecies scattering length.

4. State selective evaporation

Another application of the state selectivity provided by the mw evaporation technique is state purification. Since at the end of the circle-of-death evaporation phase we measured a percentage of around 80% of Rb atoms in the desired doubly polarized state $|F=2, m_F=2\rangle$, with around 20% in the $|F=2, m_F=1\rangle$ sublevel, we used the mw radiation to eliminate the populations in the sublevels other than the desired doubly polarized state. This is not achievable using rf radiation since, owing to saturation broadening, the resonance condition of Eq. (1) is equally fulfilled for atoms in all trapped Zeeman states. The results of the state selective evaporation in a Rb atomic sample is shown in Fig. 6. The two peaks in the upper record correspond to the absorption profile of 0.8 μK Rb atoms in the different Zeeman states, spatially separated along the vertical direction because of the differential sag. In Fig. 6(b), atoms in the $|F=2, m_F=1\rangle$ state have been reduced from 10% to an undetectable level, with no loss of atoms from the $|F=2, m_F=2\rangle$ state, when 100 mW mw radiation at 6.858 GHz resonant with the the hyperfine transition at the bottom of the magnetic trap was applied for 10 s. Even if the mw radiation was not resonant with the whole sample because of inhomogeneous broadening, rethermalizing collisions allowed the evaporation to act on the whole hyperfine level occupation. In Fig. 6(c), mw radiation at 6.904 GHz was applied to the $|F=2, m_F=2\rangle$ hyperfine level with a residual 6% final occupation in that state.

For Cs atoms, performing a Stern–Gerlach type experiment separating the Zeeman levels in time-of-flight at the end of the circle-of-death evaporation phase we detected relative populations of Cs atoms in the $|F=4, m_F=4\rangle$ Zeeman sublevel and in $|F=4, m_F=3\rangle$ of 60% and 40%, respectively. The percentage of atoms in the unwanted Zeeman sublevel was higher for Cs atoms than for Rb atoms. In Fig. 6(d), the density profile of a Cs cloud is shown after the application of 5 s of mw radiation at 9.250 GHz resonant with the $|F=4, m_F=3\rangle \rightarrow |F=3, m_F=2\rangle$ transition at the bottom of the trap, followed by a Stern–Gerlach phase, with a remaining fraction of $m_F=3$ atoms of

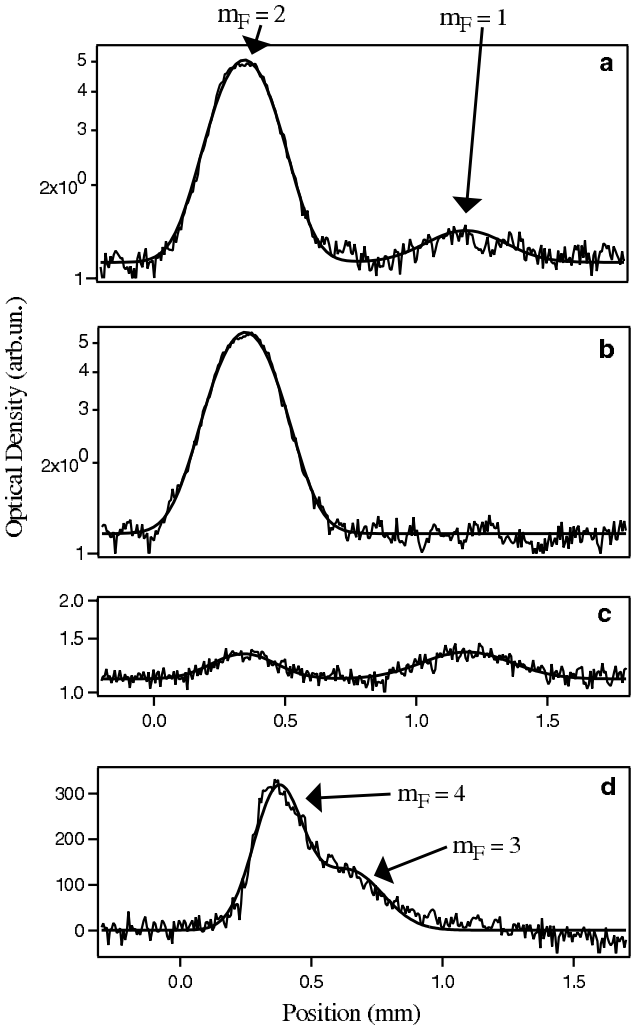

Fig. 6. Rb integrated absorption profile in free fall (a) before and (b), (c) after selective mw evaporation, as in the text. The two peaks correspond to the $|F=2, m_F=2\rangle$ and $|F=2, m_F=1\rangle$ states experiencing a different gravitational sag for a mean trap frequency of 25.7 Hz, with the atomic position measured downwards from the quadrupole symmetry center. In (b), (c) and (d) mw evaporative cooling produced a purification of Rb magnetization, as in the text. In (d), integrated absorption profile of Cs atoms, detected though a Stern–Gerlach type experiment, after selective removal of atoms in the $|F=4, m_F=3\rangle$ state, with the procedure explained in the text. Note that for better visibility we chose in (a), (b) and (c) a logarithmic vertical scale, while in (d) the vertical scale is linear.

30%. The number of Cs atoms before the application of the mw was around 10^4 and their temperature ~4 μK at 51 Hz mean trapping frequency. By applying a 10 s mw evaporation phase, similar to that applied to the Rb atoms, we were able to reduce the fraction of atoms in the $|F=4, m_F=3\rangle$

state to about 20%. The different Zeeman occupations for Rb and Cs that we found to start with in the magnetic trap and the different efficiency of the selective mw removal of atoms in the Rb and Cs case are compatible with the rate of density-dependent inelastic collisions of Cs atoms leading to a change of the m_F quantum number, as reported by [23]. From our data taken at a Cs density of 8×10^{10} cm^{-3} we infer an inelastic rate coefficient around 1×10^{-13} cm^{3}s^{-1}. This value is in agreement with the losses reported in the experiment of [23] performed at a different magnetic field and a higher temperature.

5. Conclusions

In a two-species experiment, mw techniques are a very useful method to perform radiative evaporation, in particular when combined with other cooling techniques. Mw evaporation is very flexible with respect to the choice of the magnetic trap confining the atoms, because even for a large change of the local magnetic field determining the mw resonance, the shift of the mw resonance frequency remains within the emission bandwidth of the mw source. We showed that both Rb and Cs atoms can be efficiently evaporated using mw radiation. For a Rb–Cs mixture the insertion of a Cs mw evaporation stage allowed us to reach temperatures in the 15 μK range for both species. A similar temperature could be reached through sympathetic cooling only wasting approximatively 50% of the Rb atoms. The combination of circle-of-death, mw and rf evaporative cooling allowed us to perform collisional studies of the Rb–Cs mixture and to derive the value of the interspecies scattering length, around $590a_0$ [12]. As the main difference between rf and mw evaporation, owing to the presence of multiphoton transitions the rf field depletes all Zeeman sublevels of a target hyperfine state. By contrast, the mw evaporation is Zeeman sublevel selective. In fact we have made use of this selectivity associated with the mw radiation to remove either Rb or Cs atoms from specific Zeeman sublevels, manipulating and purifying the magnetization of our Rb–Cs mixture. Making use of the differential gravitational sag or of the Stern–Gerlach separation we verified the efficiency of the mw selective evaporation. On the basis of precise simulations for the mw or rf evaporation, a quantitative comparison between the efficiencies reached in rf and mw evaporation could be performed. Furthermore additional information on the elastic, and inelastic, collisional properties of the ultracold mixture could be derived. However, owing to the complexity of atomic Zeeman/hyperfine level structure such a simulation represents a very difficult task. Finally, we used mw spectroscopy to precisely calibrate the ellipticity of the rotating bias field of a TOP trap. All these applications of the mw evaporation are useful for the preparation of an atomic mixture in precisely controlled conditions.

Acknowledgments

We thank J. Reichel for preliminary discussions on the microwave equipment, A. Piombini for the network analyzer measurements, M. Giordano for the loan of microwave equipment, and A. Alberti and G. Tumino for help in the early stages of the experiment. This research was supported by the INFM (PRA Photonmatter), and by the EU Network Cold Quantum Gases.

References

[1] For a review of early experiments on Bose–Einstein condensation, see W. Ketterle, D.S. Durfee, D.M. Stamper-Kurn, Bose–Einstein condensation in atomic gases, in: M. Inguscio, S. Stringari, C.E. Wieman (Eds.), Proceedings of the International School of Physics 'Enrico Fermi', Course CXL, IOS Press, Amsterdam, 1999, p. 67.
[2] A. Mosk, S. Kraft, M. Mudrich, K. Singer, W. Wohlleben, R. Grimm, M. Weidemüller, Appl. Phys. B 73 (2001) 791.
[3] G. Modugno, G. Ferrari, G. Roati, R.J. Brecha, A. Simoni, M. Inguscio, Science 294 (2001) 1320.
[4] G. Ferrari, M. Inguscio, W. Jastrzbeski, G. Modugno, G. Roati, A. Simoni, Phys. Rev. Lett. 89 (2002) 053202.
[5] J. Goldwin, S. Inouye, M.L. Olsen, B. Newman, B.D. DePaola, D.S. Jin, Phys. Rev. A 70 (2004) 021601(R).
[6] Z. Hadzibabic, C.A. Stan, K. Dieckmann, S. Gupta, M.W. Zwierlein, A. Görlitz, W. Ketterle, Phys. Rev. Lett. 88 (2002) 160401.
[7] C.A. Stan, M.W. Zwierlein, C.H. Schunck, S.M.F. Raupach, W. Ketterle, Phys. Rev. Lett. 93 (2004) 143001.

VOLUME 91, NUMBER 23 PHYSICAL REVIEW LETTERS week ending 5 DECEMBER 2003

Asymmetric Landau-Zener Tunneling in a Periodic Potential

M. Jona-Lasinio, O. Morsch, M. Cristiani, N. Malossi, J. H. Müller, E. Courtade, M. Anderlini, and E. Arimondo
INFM, Dipartimento di Fisica E. Fermi, Università di Pisa, Via Buonarroti 2, I-56127 Pisa, Italy
(Received 9 June 2003; published 4 December 2003)

Using a simple model for nonlinear Landau-Zener tunneling between two energy bands of a Bose-Einstein condensate in a periodic potential, we find that the tunneling rates for the two directions of tunneling are not the same. Tunneling from the ground state to the excited state is enhanced by the nonlinearity, whereas in the opposite direction it is suppressed. These findings are confirmed by numerical simulations of the condensate dynamics. Measuring the tunneling rates for a condensate of rubidium atoms in an optical lattice, we have found experimental evidence for this asymmetry.

DOI: 10.1103/PhysRevLett.91.230406 PACS numbers: 03.65.Xp, 03.75.Lm

The phenomenon of Landau-Zener (LZ) tunneling [1] is a basic quantum mechanical process. It is based on the solution of the Schrödinger equation for a two-level dynamics when a parameter of the Hamiltonian system is time dependent. If at time $t = -\infty$ the system is prepared in one adiabatic state of the Hamiltonian, the time dependence of the Hamiltonian implies that at time $t = +\infty$ there is a finite probability that the system will occupy the other adiabatic state. As far as this tunneling behavior is concerned, complete symmetry exists between the adiabatic states. Variations of the LZ model have been studied [2–4], and an observation of LZ dynamics in classical optical systems has been reported [5]. More recently, LZ tunneling within a periodic potential was studied for a nonlinear two-level system in which the level energies depend on the occupation of the levels [6,7]. It was discovered that a nonlinearity with a positive sign enhances the tunneling probability between the ground band and the first excited band. Moreover, Niu and coworkers discovered a nonzero LZ tunneling probability even in the fully adiabatic limit when the nonlinearity was larger than a critical value [7]. Critical values for deformations of the energy level structures were obtained in Refs. [6,8,9]. In a Bose-Einstein condensate (BEC) inside a periodic potential such as an optical lattice, the mean-field interaction between the atoms can be comparable to other energy scales of the system, and hence the level-dependent energy shift can lead to an observable modification of the tunneling behavior.

In the present work we explore, theoretically and experimentally, the Landau-Zener tunneling between Bloch bands of a Bose-Einstein condensate in an accelerated optical lattice. The optical lattice depth controls the tunneling barrier, while the optical lattice acceleration controls the time dependence of the Hamiltonian. We show that the mean-field nonlinearity produces an asymmetry for the tunneling probability. More precisely, the tunneling probability from the lower energy adiabatic state to the upper one is enhanced, while the inverse tunneling probability is suppressed. Numerical integration of the one-dimensional Gross-Pitaevskii equation and a simple two-state model demonstrate this asymmetry. Moreover, our experimental data obtained with a rubidium Bose-Einstein condensate confirms this prediction.

The asymmetry in the tunneling transition probabilities can be explained qualitatively as follows: The nonlinear term of the Schrödinger equation acts as a perturbation whose strength is proportional to the energy level occupation. If the initial state of the condensate in the lattice corresponds to a filled lower level of the state model, then the lower level is shifted upward in energy while the upper level is left unaffected. This reduces the energy gap between the lower and upper levels and enhances the tunneling. On the contrary, if all atoms fill the upper level, then the energy of the upper level is increased while the lower level remains unaffected. This enhances the energy gap and reduces the tunneling.

The motion of a Bose-Einstein condensate in an accelerated 1D optical lattice (see Fig. 1) is described by the Gross-Pitaevskii equation

$$i\hbar\frac{\partial\psi}{\partial t} = \frac{1}{2M}\left(-i\hbar\frac{\partial}{\partial x} - Ma_L t\right)^2\psi + \frac{V_0}{2}\cos(2k_L x)\psi + \frac{4\pi\hbar^2 a_s}{M}|\psi|^2\psi, \quad (1)$$

where M is the atomic mass, $k_L = \pi/d$ is the optical lattice wave number with d the optical lattice step, and V_0 is the strength of the periodic potential depth. The s-wave scattering length a_s determines the nonlinearity of the system. Equation (1) is written in the comoving frame of the lattice, so the inertial force Ma_L appears as a momentum modification. The wave function ψ is normalized to the total number of atoms in the condensate, and we define n_0 as the average uniform atomic density. Defining the dimensionless quantities $E_{\mathrm{rec}} = \hbar^2 k_L^2/2M$, $\tilde{x} = 2k_L x$, $\tilde{t} = 8E_{\mathrm{rec}}t/\hbar$, and rewriting $\tilde{\psi} = \psi/\sqrt{n_0}$, $\tilde{v} = V_0/16E_{\mathrm{rec}}$, $\tilde{\alpha} = Ma_L/16E_{\mathrm{rec}}k_L$, $C = \pi a_s n_0/k_L^2$, Eq. (1) is cast in the following form [7]:

$$i\frac{\partial\psi}{\partial t} = \frac{1}{2}\left(-i\frac{\partial}{\partial x} - \alpha t\right)^2\psi + v\cos(x)\psi + C|\psi|^2\psi, \quad (2)$$

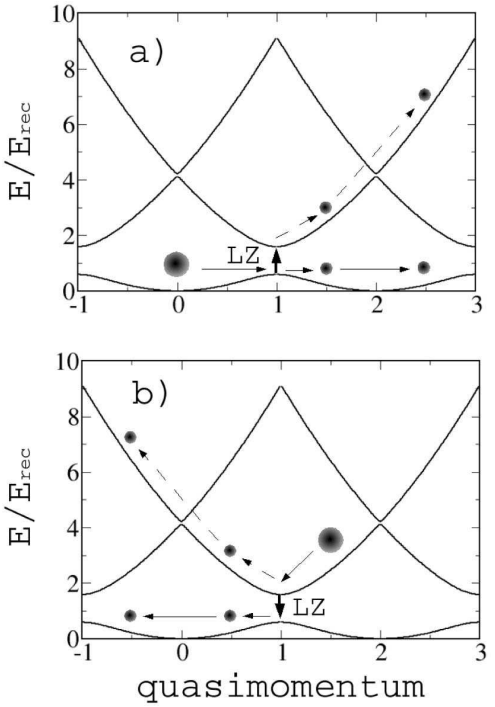

FIG. 1. Band structure of a BEC in an optical lattice ($V_0 = 2E_{\rm rec}$) and LZ tunneling [ground to excited state (a) and excited to ground state (b)]. When the BEC is accelerated across the edge of the Brillouin zone (BZ) at quasimomentum 1, LZ tunneling can occur. Further acceleration will result in the condensate part in the upper level undergoing LZ tunneling to higher bands with a large probability (due to the smaller gaps between higher bands), leaving them essentially unaffected by the lattice. After the first crossing of the edge of the BZ, increasing the lattice depth and decreasing the acceleration leads to a much reduced tunneling rate from the ground-state band at successive BZ-edge crossings (see text).

where we have replaced $\tilde{x}$ with x, etc. In the neighborhood of the Brillouin zone edge we can approximate the wave function by a superposition of two plane waves (the two-level model of Ref. [7]), assuming that only the ground state and the first excited state are populated. We then substitute $\psi(x,t) = a(t)e^{iqx} + b(t)e^{i(q-1)x}$, with $|a(t)|^2 + |b(t)|^2 = 1$, in Eq. (2). Comparing the coefficients of e^{iqx} and $e^{i(q-1)x}$, linearizing the kinetic terms, and dropping the irrelevant constant energy $1/8 + C[1 + (|a|^2 + |b|^2)/2]$, Eq. (2) assumes the form

$$i\frac{\partial}{\partial t}\begin{pmatrix} a \\ b \end{pmatrix} = \left[\frac{\alpha t}{2}\sigma_3 + \frac{v}{2}\sigma_1\right]\begin{pmatrix} a \\ b \end{pmatrix} + \frac{C}{2}(|b|^2 - |a|^2)\sigma_3\begin{pmatrix} a \\ b \end{pmatrix}, \tag{3}$$

where σ_i, $i = 1, 2, 3$, are the Pauli matrices [10]. The adiabatic energies of Eq. (3) have a butterfly structure at the band edge of the Brillouin zone for $C \geq v$ [7–9], but in the present work we always work in a regime where $C \ll v$; hence that structure plays no role.

In the linear regime ($C = 0$), evaluating the transition probability in the adiabatic approximation, we find the linear LZ formula for the tunneling probability r

$$r = e^{-\pi v^2/2\alpha}. \tag{4}$$

In the nonlinear regime, as the nonlinear parameter C grows, the lower to upper tunneling probability grows as well. The upper to lower tunneling probability, on the other hand, decreases with increasing nonlinearity [11]. We derived the tunneling rate from the numerical integration of Eq. (3). In Fig. 2(a) we plot the lower to upper tunneling rates [initial $(a, b) = (1, 0)$] and the upper to lower tunneling rates [initial $(a, b) = (0, 1)$] of the Bose-Einstein condensate as a function of the nonlinear parameter C for different accelerations of the optical lattice. We see that for $C = 0$ the rate is the same for both tunneling directions, whereas for $C \neq 0$ the two rates are different, and the smaller the acceleration the larger the difference. This result is intuitive since for very small accelerations the main contribution originates from the nonlinear effect [the linear tunneling of Eq. (4) being small], while for large accelerations the main contribution comes from the linear effect. We confirmed the presence of a tunneling asymmetry by integrating directly Eq. (1) (taking into account the full experimental protocol

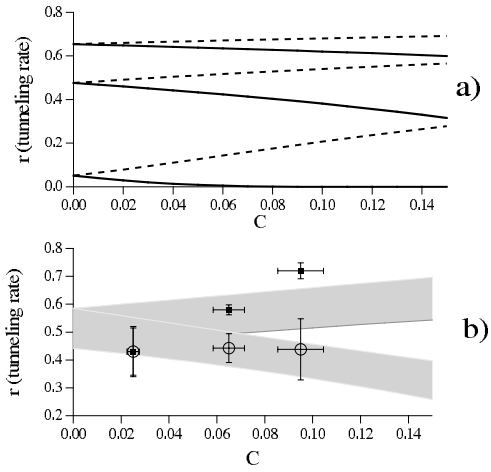

FIG. 2. LZ tunneling rate r within the two-level model as a function of the nonlinear parameter C for different accelerations. Results are for $v = 0.134$ corresponding to $V_0 = 2.2E_{\rm rec}$, in (a) for $\alpha = 0.01, 0.04, 0.07$, corresponding to $a_L = 0.8, 3.2, 5.6\ {\rm m\,s^{-2}}$ from bottom to top, and in (b) for $\alpha = 0.036$ corresponding to $a_L = 2.9\ {\rm m\,s^{-2}}$. In (a), the dashed (solid) lines correspond to tunneling from the excited (ground-state) band. In (b) experimental results denoted by open (filled) symbols correspond to tunneling from the excited (ground state) band. The experimental points at $C = 0.025$ have been rescaled from Fig. 4 using the Landau-Zener formula to match the acceleration to the one used to obtain the other experimental points. The shaded area represents the confidence region for the prediction of the two-level model, taking into account the uncertainty in our measurement of the lattice depth.

VOLUME 91, NUMBER 23 PHYSICAL REVIEW LETTERS week ending 5 DECEMBER 2003

described below), finding qualitative agreement with the prediction of the two-state model. For small C values, we have fitted the C dependence of the tunneling rate of Fig. 2(a) through the following expression [6,7]:

$$r(C) = e^{-(\pi v^2/2\alpha)(1\pm\beta C/v)} \quad (5)$$

with $\beta = 0.75, 0.17, 0.14$ for the different acceleration values.

Experimentally, we investigated the asymmetric tunneling using a setup described in detail in [12,13]. Briefly, we create condensates of $N \approx 10^4$ rubidium atoms in a time-orbiting potential trap. Once condensation has been achieved, the mean trapping frequency $\overline{\nu}_{\text{trap}}$ of the magnetic trap is adiabatically reduced to values between 15 and 50 Hz. Thereafter, two laser beams with waists of 1.8 mm and intersecting at an angle $\theta = 38°$ at the position of the condensate are switched on with a linear ramp of duration $\tau_{\text{ramp}} = 10$ ms, thus ensuring adiabaticity of the loading process. The beams are detuned to the red side of the rubidium atomic resonance by ≈ 30 GHz and have a variable frequency difference $\Delta\nu$ between them, controllable through two acousto-optic modulators which are also used to vary the intensity of the beams. In this way, a periodic potential with lattice constant $d = 1.18$ μm and lattice recoil energy $E_{\text{rec}}/h = 455$ Hz is created, which through the frequency difference $\Delta\nu$ can be made to move at a constant velocity $v = d\Delta\nu$ or accelerated with $a_L = d\frac{d\Delta\nu}{dt}$.

Landau-Zener tunneling between the two lowest energy bands of a condensate inside an optical lattice is investigated in the following way (see Fig. 1). Initially, the condensate is loaded adiabatically into one of the two bands. Subsequently, the lattice is accelerated in such a way that the condensate crosses the edge of the Brillouin zone once, resulting in a finite probability for tunneling into the other band (higher-lying bands can be safely neglected as their energy separation at the edge of the Brillouin zone is much larger than the band gap). After the tunneling event, the two bands have populations reflecting the Landau-Zener tunneling rate (assuming that, initially, the condensate populated one band exclusively). In order to experimentally determine the number of atoms in the two bands, we then *increase* the lattice depth (from $\approx 2E_{\text{rec}}$ to $\approx 4E_{\text{rec}}$) and *decrease* the acceleration (from $\approx 3\,\text{m s}^{-2}$ to $\approx 2\,\text{m s}^{-2}$). In this way, successive crossings of the band edge will result in a much reduced Landau-Zener tunneling probability (of order a few percent). The fraction of the condensate that after the first tunneling event populated the ground-state band will, therefore, remain in that band, whereas the population of the first excited band will undergo tunneling to the second excited band with a large probability (around 90%) as the relevant gap is smaller by a factor of ≈ 5 for our parameters. Once the atoms have tunneled into the second excited band, they essentially behave as free particles since higher-lying band gaps are smaller still, so they will no longer be accelerated by the lattice. In summary, using this experimental sequence we selectively accelerate that part of the condensate further that populates the ground-state band. In practice, in order to get a good separation between the two condensate parts after a time of flight, we accelerate the lattice to a final velocity of $4 - 6v_{\text{rec}}$ [14] and absorptively image the condensate after 22 ms (see Fig. 3).

In order to investigate tunneling from the ground-state band to the first excited band [Fig. 1(a)], we adiabatically ramped up the lattice depth with the lattice at rest and then started the acceleration sequence. The tunneling from the first excited to the ground-state band is investigated [Fig. 1(b)] by initially preparing the condensate in the first excited band by moving the lattice with a velocity of $1.5v_{\text{rec}}$ when switching it on. In this way, in order to conserve energy and momentum, the condensate must populate the first excited band at a quasimomentum halfway between zero and the edge of the first Brillouin zone [15]. Thereafter, the same acceleration sequence as described above is used. For both tunneling directions, the tunneling rate is measured as

$$r = \frac{N_{\text{tunnel}}}{N_{\text{tot}}}, \quad (6)$$

where N_{tot} is the total number of atoms measured from the absorption picture. For the tunneling from the first excited band to the ground band, N_{tunnel} is the number of atoms accelerated by the lattice, i.e., those detected in the final velocity class $4\,v_{\text{rec}}$, whereas for the inverse tunneling direction, N_{tunnel} is the number of atoms detected in the $v = 0$ velocity class.

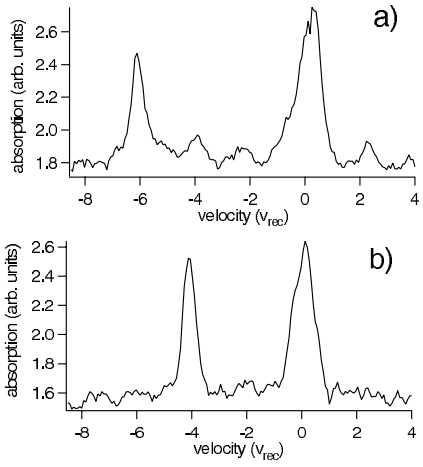

FIG. 3. Profiles of absorption images taken after 22 ms of time of flight of condensates released after the acceleration procedure described in the text. The condensates were prepared in the ground-state band in (a) and in the first excited band in (b) in an optical lattice with depth $V_0 = 2.6E_{\text{rec}}$ and $a_L = 2.9\,\text{m s}^{-2}$.

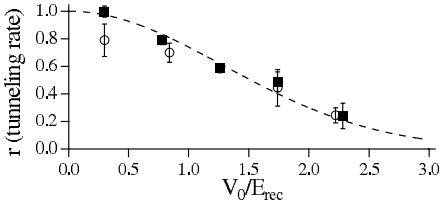

FIG. 4. Landau-Zener tunneling between the two lowest energy bands of a condensate in an optical lattice as a function of the lattice depth (carrying a $\pm 10\%$ systematic error) for $\alpha = 0.025$ corresponding to $a_L = 2.0\ \mathrm{m\,s^{-2}}$. Tunneling rates from the ground-state band to the first excited band (filled symbols) and vice versa (open symbols) are virtually identical and agree with the linear prediction (dashed line) as the nonlinear parameter $C \approx 0.025$ is small for the trap used in these measurements ($\bar{\nu}_{\mathrm{trap}} = 15$ Hz).

In Fig. 4 we report the two tunneling rates as a function of lattice depth for a condensate in a weak magnetic trap and hence a small value of the interaction parameter C [16]. In this case, both tunneling rates are essentially the same and agree well with the linear Landau-Zener prediction. By contrast, when C is increased, the two tunneling rates begin to differ, as can be seen in Fig. 2(b). Qualitatively we find agreement with the theoretical predictions of the nonlinear Landau-Zener model, whereas quantitatively there are significant deviations. We believe these to be partly due to experimental imperfections. In particular, the sloshing (dipolar oscillations) of the condensate inside the magnetic trap can lead to the condensate not being prepared purely in one band due to nonadiabatic mixing of the bands if the initial quasimomentum is too close to a band gap. Furthermore, a numerical simulation of the experiment shows that for large values of C, for which the magnetic trap frequency was large, the measured tunneling rates are significantly modified by the presence of the trap. We have, however, verified that when C in the simulation is varied without varying the trap frequency, the asymmetric tunneling effect persists. In order to test our theory more quantitatively in BEC systems, the condensate could be held in an optical dipole trap with a small longitudinal trap frequency.

In summary, we have numerically simulated Landau-Zener tunneling between two energy bands in a periodic potential and found that, in the presence of a nonlinear interaction term, an asymmetry in the tunneling rates arises. Experimentally, we have measured these tunneling rates for different values of the interaction parameter and found qualitative agreement with the simulations. Future experiments could probe the complicated and time-dependent tunneling behavior due to the changing tunneling rate for multiple crossings of the zone edge. Furthermore, when the two lowest bands are initially equally populated, the tunneling behavior should again be linear. We also note here that the phenomenon of asymmetric tunneling should be a rather general feature of quantum systems exhibiting a nonlinearity. For instance, calculating the energy shift due to a nonlinearity for two adjacent levels of a harmonic oscillator, one finds that both levels are shifted upwards in energy, the shift being proportional to the population of the respective level. The energy difference between the levels, therefore, decreases if only the lower state is populated and increases if all the population is in the upper level. Finally, we note that state-dependent mean-field shifts have also been observed in measurements of the clock shift in ultracold and Bose-condensed atomic samples [18].

This work was supported by the MURST (COFIN2000 Initiative), by the INFM (PRA "Photonmatter"), and by the EU through Contract No. HPRN-CT-2000-00125.

[1] L. D. Landau, Phys. Z. Sowjetunion **2**, 46 (1932); G. Zener, Proc. R. Soc. London, Ser. A **137**, 696 (1932).
[2] K. Mullen, E. Ben-Jacob, Y. Gefen, and Z. Schuss, Phys. Rev. Lett. **62**, 2543 (1989).
[3] Y. Gefen, E. Ben-Jacob, and A. O. Caldeira, Phys. Rev. B **36**, 2770 (1987).
[4] S. Fishman, K. Mullen, and E. Ben-Jacob, Phys. Rev. A **42**, 5181 (1990).
[5] D. Bouwmeester, N. H. Dekker, F. E. v. Dorsselaer, C. A. Schrama, P. M. Visser, and J. P. Woerdman, Phys. Rev. A **51**, 646 (1995).
[6] O. Zobay and B. M. Garraway, Phys. Rev. A **61**, 033603 (2000).
[7] B. Wu and Q. Niu, Phys. Rev. A **61**, 023402 (2000); J. Liu *et al.*, *ibid.* **66**, 023404 (2002).
[8] D. Diakonov, L. M. Jensen, C. J. Pethick, and H. Smith, Phys. Rev. A **66**, 013604 (2002); M. Machholm, C. J. Pethick, and H. Smith, Phys. Rev. A **67**, 053613 (2003).
[9] E. J. Mueller, Phys. Rev. A **66**, 063603 (2002).
[10] An equivalent equation is obtained using wave functions $\exp(ikx)\cos(kx)$ and $\exp(ikx)\sin(kx)$ describing the eigenstates at the band edge.
[11] For occupation with equal amplitude of the lower and upper states $|a|^2 = |b|^2$, the nonlinear corrections leading to the asymmetric tunneling play no role.
[12] O. Morsch *et al.*, Phys. Rev. Lett. **87**, 140402 (2001).
[13] M. Cristiani *et al.*, Phys. Rev. A **65**, 063612 (2002).
[14] In order to keep the total interaction time with the lattice constant, the final velocity of the lattice when the condensate is prepared in the upper state is $\approx 4\nu_{\mathrm{rec}}$ since initially the lattice is moving at $-1.5\nu_{\mathrm{rec}}$.
[15] E. Peik *et al.*, Appl. Phys. B **65**, 685 (1997).
[16] For the nonuniform condensate density in the optical lattice, described by Pedri *et al.* [17] with a separation of the variables parallel and orthogonal to the optical latttice, the parameter C of the 1D Eq. (1) was determined from the maximum condensate density.
[17] P. Pedri *et al.*, Phys. Rev. Lett. **87**, 220401 (2001).
[18] D. M. Harber, H. J. Lewandowski, J. M. McGuirk, and E. A. Cornell, Phys. Rev. A **66**, 053616 (2002), and references therein.

Laser Phys. Lett. **1**, No. 3, 147–153 (2004) / **DOI** 10.1002/lapl.200310039 Laser Physics Letters 147

Abstract: From a two-level model for nonlinear Landau-Zener tunnelling between two energy bands of a Bose-Einstein condensate in a periodic potential we obtain unequal tunnelling rates for the two directions of tunnelling. With increasing nonlinearity, tunnelling from the ground state to the excited state is enhanced, whereas in the opposite direction it is suppressed. These findings are confirmed by numerical simulations of the condensate dynamics. Measuring the tunnelling rates for a condensate of rubidium atoms in an optical lattice, we have found experimental evidence for this asymmetry. We discuss the limitations of our approach and possible future experiments.

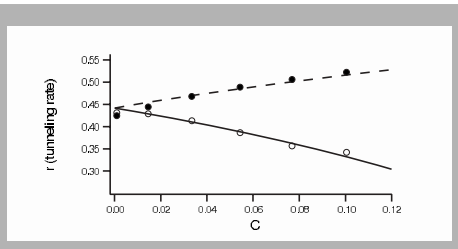

Landau-Zener tunnelling rate r as a function of the nonlinear parameter C

Nonlinear effects in periodic potentials: asymmetric Landau-Zener tunnelling of a Bose-Einstein condensate

M. Jona-Lasinio, O. Morsch, M. Cristiani, N. Malossi, J.H. Müller, E. Courtade, M. Anderlini, and E. Arimondo*

INFM, Dipartimento di Fisica E. Fermi, Università di Pisa, Via Buonarroti 2, I-56127 Pisa, Italy

Received: 27 October 2003, Accepted: 1 December 2003
Published online: 7 February 2004

Key words: Landau-Zener tunnelling; nonlinearity; Bose-Einstein condensation

PACS: 03.65.Xp, 03.75.Lm

1. Introduction

Cold atoms and, more recently, Bose-Einstein condensates (BECs) in optical lattices have attracted increasing interest since their first realization. In particular, the formal similarity between the wavefunction of a BEC inside the periodic potential of an optical lattice and electrons in a crystal lattice have triggered theoretical and experimental efforts alike. Many phenomena from condensed matter physics, such as Bloch oscillations and Landau-Zener tunnelling have since been shown to be observable also in optical lattices.

The phenomenon of Landau-Zener (LZ) tunnelling [1] is a basic quantum mechanical process. It is based on the solution of the Schrödinger equation for a two-level dynamics when a parameter of the Hamiltonian system is time dependent. If at time $t = -\infty$ the system is prepared in one adiabatic state of the Hamiltonian, the time dependence of the Hamiltonian implies that at time $t = +\infty$ there is a finite probability that the system will occupy the other adiabatic state. As far as this tunnelling behavior is concerned, complete symmetry exists between the adiabatic states. Variations of the LZ model have been studied [2–4], and an observation of LZ dynamics in classical optical systems has been reported [5]. More recently, LZ tunnelling within a periodic potential was studied for a nonlinear two-level system in which the level energies depend on the occupation of the levels [6, 7]. It was discovered that a nonlinearity with a positive sign enhances the tunnelling probability between the ground band and the first excited band. Moreover, Niu and coworkers discovered a nonzero LZ tunnelling probability even in the fully adiabatic limit when the nonlinearity was larger than a critical value [7]. Critical values for deformations of the energy level structures were obtained in refs. [6, 8, 9]. In a Bose-Einstein condensate inside a periodic potential such as an optical lattice, the mean-field interaction between the atoms can be comparable to other energy scales of the system and hence the level-dependent energy shift can lead to an observable modification of the tunnelling behavior.

In a recent work we have explored, theoretically and experimentally, the asymmetric Landau-Zener tunnelling between Bloch bands of a Bose-Einstein condensate in an accelerated optical lattice [10]. In the present work we

* Corresponding author: e-mail: morsch@df.unipi.it

provide additional theoretical and experimental evidence. In our experimental system, the optical lattice depth controls the tunnelling barrier, while the optical lattice acceleration controls the time dependence of the Hamiltonian. We show that the mean-field nonlinearity produces an asymmetry for the tunnelling probability between the adiabatic states of the Hamiltonian. More precisely the tunnelling probability from the lower energy adiabatic state to the upper one is enhanced, while the tunnelling probability from the higher energy level to a lower level is suppressed. Numerical integration of the one-dimensional Gross-Pitaevskii equation and a simple two-state model demonstrate this asymmetry. Moreover, our experimental data obtained with a rubidium Bose-Einstein condensate confirms this prediction.

The asymmetry in the tunnelling transition probabilities can be explained qualitatively as follows: the nonlinear term of the Schrödinger equation acts as a perturbation whose strength is proportional to the energy level occupation. If the initial state of the condensate in the lattice corresponds to a filled lower level of the state model, then the lower level is shifted upward in energy while the upper level is left unaffected. This reduces the energy gap between the lower and upper level and enhances the tunnelling. On the contrary, if all atoms fill the upper level then the energy of the upper level is increased while the lower level remains unaffected. This enhances the energy gap and reduces the tunnelling. The overall balance leads to an asymmetry between the two tunnelling processes.

This paper is organized as follows. After describing our theoretical approach in section 2, we explain the experimental technique in section 3. Section 4 presents a discussion of our results and the experimental and conceptual difficulties encountered in obtaining them. Finally, our conclusions are given in section 5.

2. Theory

The motion of a Bose-Einstein condensate in an accelerated 1D optical lattice (see Fig. 1) is described by the Gross-Pitaevskii equation

$$ih\frac{\partial\psi}{\partial t} = \frac{1}{2M}\left(-ih\frac{\partial}{\partial x} - Ma_L t\right)^2\psi + \tag{1}$$

$$+\frac{V_0}{2}\cos(2k_l x)\psi + \frac{4\pi h^2 a_s}{M}|\psi|^2\psi,$$

where M is the atomic mass, $k_L = \pi/d$ is the optical lattice wavenumber with d the optical lattice step, and V_0 is the strength of the periodic potential depth. The s-wave scattering length a_s determines the nonlinearity of the system. Equation (1) is written in the comoving frame of the lattice, so the inertial force Ma_L appears as a momentum modification. The wavefunction ψ is normalized to the total number of atoms in the condensate and we define n_0 as the average uniform atomic density. Defining the dimensionless quantities

$$E_{rec} = h^2k_L^2/2M, \quad \tilde{x} = 2k_L x, \tilde{t} = 8E_{rec}t/h,$$

and rewriting

$$\tilde{\psi} = \psi/\sqrt{n_0}, \quad \tilde{v} = V_0/16E_{rec},$$

$$\tilde{\alpha} = Ma_L/16E_{rec}k_L, \quad C = \pi a_s n_0/k_L^2,$$

Eq. (1) is cast in the following form [7]:

$$i\frac{\partial\psi}{\partial t} = \frac{1}{2}\left(-i\frac{\partial}{\partial x} - \alpha t\right)^2\psi + v\cos(x)\psi + C|\psi|^2\psi, \tag{2}$$

where we have replaced $\tilde{x}$ with x, etc. In the neighborhood of the Brillouin zone edge we can approximate the wave function by a superposition of two plane waves (the two level model of ref. [7]), assuming that only the ground state and the first excited state are populated. We then substitute in Eq. (2)

$$\psi(x,t) = a(t)e^{iqx} + b(t)e^{i(q-1)x}, \tag{3}$$

with $|a(t)|^2 + |b(t)|^2 = 1$. Comparing the coefficients of e^{iqx} and $e^{i(q-1)x}$, linearizing the kinetic terms and dropping the irrelevant constant energy

$$1/8 + C[1 + (|a|^2 + |b|^2)/2],$$

Eq. (2) assumes the form

$$i\frac{\partial}{\partial t}\begin{pmatrix}a\\b\end{pmatrix} = \left[\frac{\alpha t}{2}\sigma_3 + \frac{v}{2}\sigma_1\right]\begin{pmatrix}a\\b\end{pmatrix} + \tag{4}$$

$$+\frac{C}{2}(|b|^2 - |a|^2)\sigma_3\begin{pmatrix}a\\b\end{pmatrix},$$

where σ_i $(i = 1, 2, 3)$ are the Pauli matrices. The adiabatic energies of Eq. (4) have a butterfly structure at the band edge of the Brillouin zone for $C \geq v$ [7–9], but in the present work we only consider a regime where $C \ll v$, hence that structure plays no role.

In the linear regime $(C = 0)$, evaluating the transition probability in the adiabatic approximation, we find the linear LZ formula for the tunnelling probability r

$$r = \exp\left\{-\frac{\pi v^2}{2\alpha}\right\} \tag{5}$$

expressing the occupation changes in terms of the rate α at which the diagonal energies of the linear Hamiltonian change their value, and of the off-diagonal interaction energy v. In the nonlinear regime, as the nonlinear parameter C grows, the lower to upper tunnelling probability grows as well until an adiabaticity breakdown occurs at $C = v$ [7]. The upper to lower tunnelling probability, on the other hand, decreases with increasing nonlinearity [11]. We derived the tunnelling rate from the numerical integration of Eq. (4). In Fig. 2 we plot the lower to upper tunnelling rate (initial $(a, b) = (1, 0)$) and the upper to lower

Laser Phys. Lett. **1**, No. 3, (2004) / www.lphys.org Laser Physics Letters 149

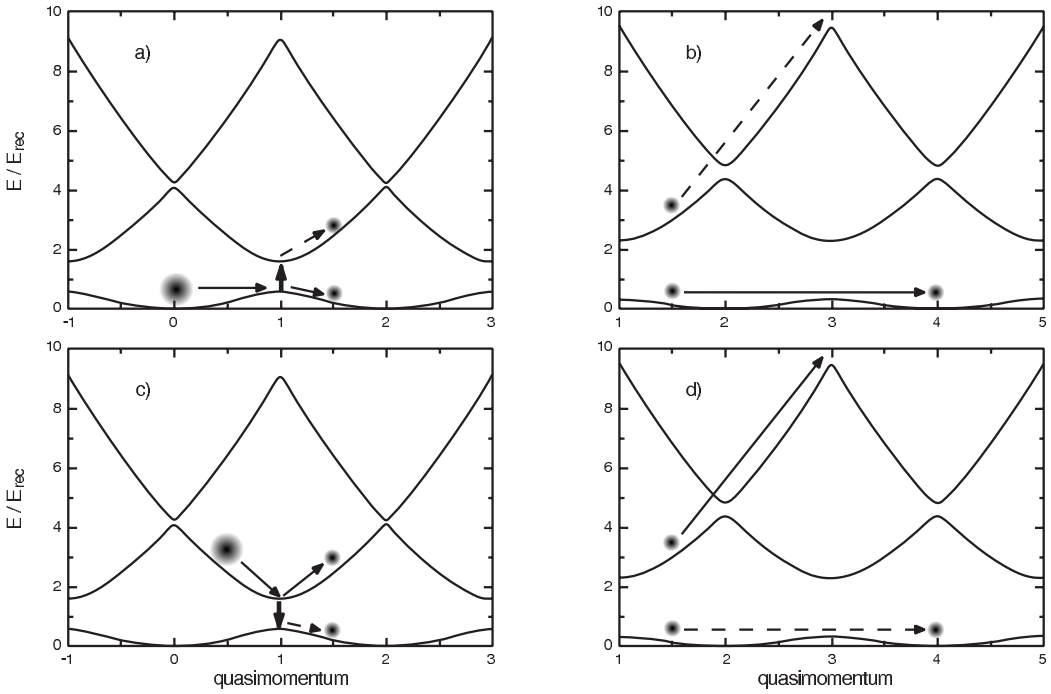

Figure 1 Band structure of a BEC in an optical lattice ($V_0 = 2\,E_{rec}$) and LZ-tunnelling (ground to excited state (a) and excited to ground state (c)). When the BEC is accelerated across the edge of the Brillouin zone (BZ) at quasimomentum 1, LZ tunnelling can occur. Further acceleration will result in the condensate part in the upper level undergoing LZ tunnelling to higher bands with a large probability (due to the smaller gaps between higher bands), leaving them essentially unaffected by the lattice. After the first crossing of the edge of the BZ, illustrated in (a) and (c), increasing the lattice depth and decreasing the acceleration leads to a much reduced tunnelling rate from the ground state band at successive BZ-edge crossings, as shown in (b) for the ground to excited state tunnelling and in (d) for excited to ground state

tunnelling rate (initial $(a, b) = (0, 1)$) of the Bose-Einstein condensate as a function of the nonlinear parameter C. We see that for $C = 0$ the rate is the same for both tunnelling directions whereas for $C \neq 0$ the two rates are different. We confirmed the presence of a tunnelling asymmetry by integrating directly Eq. (1) (taking into account the full experimental protocol described below), finding qualitative agreement with the prediction of the two-state model.

The nonlinear regime is interpreted straightforwardly by writing Eq. (4) as

$$i\frac{\partial}{\partial t}\begin{pmatrix} a \\ b \end{pmatrix} = \left[\frac{\alpha}{2}\sigma_3 + \frac{v}{2}\sigma_1\right]\begin{pmatrix} a \\ b \end{pmatrix} + \qquad (6)$$

$$-\frac{C}{2}\begin{pmatrix} |a|^2 & -b^*a \\ -a^*b & |b|^2 \end{pmatrix}\begin{pmatrix} a \\ b \end{pmatrix}.$$

The nonlinear off-diagonal terms modify the interaction term v in a way equivalent to a Rabi frequency in the two-level model. Using the adiabatic approximation technique of [12], we evaluated the off-diagonal scalar product between the two states a^*b and found

$$a^*b = -\frac{v}{2\sqrt{\alpha^2 t^2 + v^2}} \exp\left\{i\frac{\alpha}{\alpha^2 t^2 + v^2}\right\} \qquad (7)$$

for a transition from the lower state to the upper one. For the opposite tunnelling direction the expression simply changes sign. In Eq. (6) we can identify an off-diagonal term $v + C\,a^*b$ which acts as an effective potential. Thus for small C values we can modify the linear LZ formula Eq. (5) to include nonlinear corrections, substituting the potential v with the effective potential $v_{eff} \equiv |v + C\,a^*b|$ (modulus is needed since a^*b is complex). The explicit expression for v_{eff} is then

$$v_{eff} = v\sqrt{1 \pm \frac{C}{\sqrt{\alpha^2 t^2 + v^2}} + \frac{C^2}{4(\alpha^2 t^2 + v^2)}}, \qquad (8)$$

and within the spirit of this adiabatic approximation we can put $\alpha = 0$ obtaining

$$v_{eff} = v\sqrt{1 \pm \frac{C}{v} + \frac{C^2}{4v^2}}, \qquad (9)$$

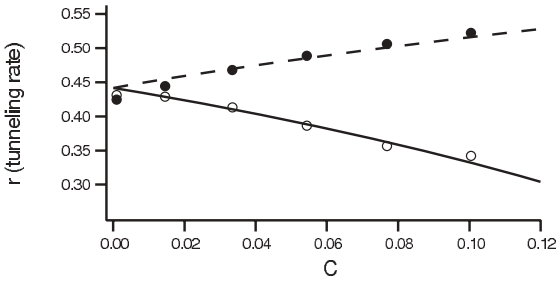

Figure 2 LZ tunnelling rate r as a function of the nonlinear parameter C. The dashed and continuous lines represent the result of the two-level model Eq. (4) for a transition from the lower level to the upper one and vice versa, respectively. The open and filled symbols are the results of the numerical integration of Eq. (1) taking into account the presence of the harmonic trap and simulating the full experimental procedure. Transition rates are evaluated by mean of the Fourier transform method. Results are for $v = 0.134$ corresponding to $V_0 = 2.2\,E_{rec}$ and $\alpha = 0.036$ corresponding to $a_L = 2.9\ \mathrm{ms}^{-2}$. Here C was varied by varying the trap frequency

where the upper and lower signs corresponds to initial conditions of excited/ground states. For small C values, we have fitted the C dependence of the tunnelling rate of Fig. 2 through the following expression [6,7]:

$$r(C) = \exp\left\{-\frac{\pi v^2}{2\alpha}(1 \pm \beta\frac{C}{v})\right\} \tag{10}$$

with $\beta = 0.17$, neglecting the small correction of second order in C/v.

The interpretation of the nonlinear diagonal elements in Eq. (6) is not as straightforward as for the off-diagonal ones and the nonlinearity seems to act in the opposite way. In reality this is not the case. We are interested in the behavior of the energy levels at the band edge where the correct hamiltonian eigenfuntions are sine and cosine eigenstates, *i.e.*, $\sin(x/2)$ and $\cos(x/2)$ wavefunctions. Therefore the nonlinear behavior cannot be derived from Eq. (6) where the basis functions were plane waves, and instead we must write an equivalent version in the sine-cosine base. It is worth noting that because of nonlinearity the hamiltonian matrix cannot simply be transformed into the new basis with a rotation matrix: the new hamiltonian matrix must be recalculated from scratch. We start from a wavefunction in the following form:

$$\psi(x,t) = e^{iqx}\left[a'(t)(1-e^{-ix}) + b'(t)(1+e^{-ix})\right] \tag{11}$$

with $|a'(t)|^2 + |b'(t)|^2 \equiv 1$. By substituting this expression into Eq. (2), within the same approximations, the potential and nonlinear terms now become

$$i\frac{\partial}{\partial t}\begin{pmatrix} a' \\ b' \end{pmatrix} = \frac{1}{2}v\sigma_3\begin{pmatrix} a' \\ b' \end{pmatrix} + \tag{12}$$

$$+\frac{C}{2}\begin{pmatrix} (|a'|^2 - |b'|^2) & -2\,a'^* b' \\ -2\,b'^* a' & -(|a'|^2 - |b'|^2) \end{pmatrix}.$$

The last term of this equation simplifies in

$$\frac{1}{2}\begin{pmatrix} -v+C & 0 \\ 0 & v-C \end{pmatrix} \quad \frac{1}{2}\begin{pmatrix} -v-C & 0 \\ 0 & v+C \end{pmatrix}, \tag{13}$$

when considering a filled lower level $(a', b') \equiv (1, 0)$ (Eq. (13), left) or a filled upper level $(a', b') \equiv (0, 1)$ (Eq. (13), right). In this representation the diagonal elements directly express the energy eigenvalues at the band edge. Evaluating the energy gap ΔE we have: $\Delta E = v - C$ when starting with a filled lower level and $\Delta E = v + C$ when starting with a filled upper level. In the first situation the gap will be smaller than in the linear case and tunnelling will be enhanced while in the second one it will be larger and tunnelling will be suppressed. This situation is illustrated in Fig. 3 for parameter values similar to those realized in our experiment.

3. Experiment

Experimentally, we investigated the phenomenon of asymmetric tunnelling between the energy bands of Bose-Einstein condensates in an optical lattice using a setup described in detail in [13,14]. Briefly, we create condensates of $N \approx 10^4$ rubidium atoms in a time-orbiting potential (TOP) trap. Once condensation has been achieved, the mean trapping frequency $\overline{\nu}_{trap}$ of the magnetic trap is adiabatically reduced to values between 15 Hz and 50 Hz. Thereafter, two laser beams with waists of 1.8 mm and intersecting at an angle $\theta = 38\,\mathrm{deg}$ at the position of the condensate are switched on with a linear ramp of duration $\tau_{ramp} = 10\,\mathrm{ms}$, thus ensuring adiabaticity of the loading process. The beams are detuned to the red side of the rubidium atomic resonance by $\approx 30\,\mathrm{GHz}$ and have a variable frequency difference $\Delta\nu$ between them, controllable through two acousto-optic modulators which are also used to vary the intensity of the beams. In this way, a periodic potential with lattice constant $d = 1.18\,\mu\mathrm{m}$ and lattice recoil energy $E_{rec}/h = 455\,\mathrm{Hz}$ is created, which through the frequency difference $\Delta\nu$ can be made to move at a constant velocity $v = d\Delta\nu$ or accelerated with $a_L = d\frac{d\Delta\nu}{dt}$. For the current experiment, lattice depths between $0.25\,E_{rec}$ and $2.5\,E_{rec}$ were used.

Landau-Zener tunnelling between the two lowest energy bands of a condensate inside an optical lattice is investigated in the following way (see Fig. 1). Initially, the condensate is loaded adiabatically into one of the two bands. Subsequently, the lattice is accelerated in such a way that the condensate crosses the edge of the Brillouin zone once, resulting in a finite probability for tunnelling into the other band (higher-lying bands can be safely neglected as their energy separation at the edge of the Brillouin zone is much larger than the band gap). After the tunnelling event, the two bands have populations reflecting the Landau-Zener tunnelling rate (assuming that, initially, the condensate populated one band exclusively). In

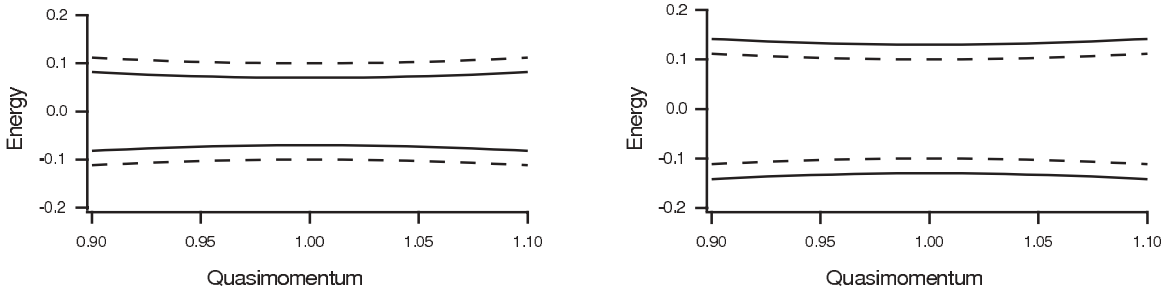

Figure 3 Bloch bands in the neighborhood of the band edge. Dashed and continuous lines represent the linear and nonlinear bands, respectively. The upper picture shows the situation for a transition from the lower band to the upper one. The opposite transition is shown in the lower picture. Parameters are $v = 0.2$ and $C = 0.08$. The energy gap is reduced by nonlinearity in the upper picture whereas in the lower one it is enlarged, enhancing or reducing the tunnelling rate, as the case may be

order to experimentally determine the number of atoms in the two bands, we then *increase* the lattice depth (from $\approx 2\,E_{rec}$ to $\approx 4\,E_{rec}$) and *decrease* the acceleration (from $\approx 3\,\mathrm{ms}^{-2}$ to $\approx 2\,\mathrm{ms}^{-2}$). In this way, successive crossings of the band edge will result in a much reduced Landau-Zener tunnelling probability between the ground state band and the first excited band (of order a few percent), as pictoriall1y illustrated in Fig. 1(b) and (d). The fraction of the condensate that after the first tunnelling event populated the ground state band will, therefore, remain in that band, whereas the population of the first excited band will undergo tunnelling to the second excited band with a large probability (around 90 percent) as the gap between these two bands is smaller than the gap between the two lowest bands by a factor ≈ 5 for our parameters. Once the atoms have tunnelled into the second excited band, they essentially behave as free particles since higher-lying band-gaps are smaller still, meaning that the fraction of the condensate that populated the first excited band after the first tunnelling event will no longer be accelerated by the lattice. In summary, using this experimental sequence we selectively accelerate that part of the condensate further that populates the ground state band. In practice, in order to get a good separation between the two condensate parts after a time-of-flight, we accelerate the lattice to a final velocity of $4 - 6\,v_{rec}$ [15] and absorptively image the condensate after 22 ms (see Fig. 4).

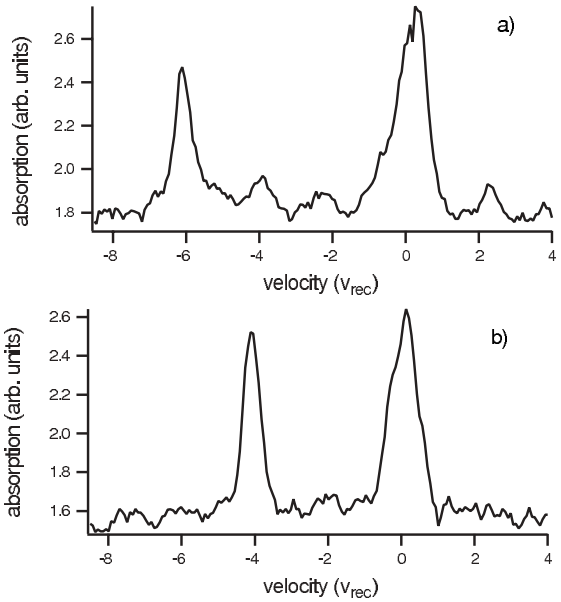

Figure 4 Profiles of absorption images taken after 22 ms of time-of-flight of condensates released after the acceleration procedure described in the text. The condensates were prepared in the ground state band in (a) and in the first excited band in (b) within an optical lattice with depth $V_0 = 2.6\,E_{rec}$ and $a_L = 2.9$ ms^{-2}. In this experiment, $C \approx 0.1$

4. Results and discussion

In order to investigate tunnelling from the ground state band to the first excited band (Fig. 1 (a)), we adiabatically ramped up the lattice depth with the lattice at rest and then started the acceleration sequence. The tunnelling from the first excited to the ground-state band is investigated in a similar way (Fig. 1 (c)), except that in this case we initially prepare the condensate in the first excited band by moving the lattice with a velocity of $1.5\,v_{rec}$ (through the frequency difference $\Delta\nu$ between the acousto-optic modulators) when switching it on. In this way, in order to conserve energy and momentum the condensate must populate the first excited band at a quasi-momentum half-way between zero and the edge of the first Brillouin zone [16]. Thereafter, the same acceleration sequence as described

above is used in order first to induce Landau-Zener tunnelling and then to separate the fraction of the condensate that underwent tunnelling to the lowest band from the one that remained in the first excited band. For both tunnelling directions, the tunnelling rate is measured as

$$r = \frac{N_{tunnel}}{N_{tot}}, \tag{14}$$

where N_{tot} is the total number of atoms measured from the absorption picture. For the tunnelling from the first excited band to the ground band, N_{tunnel} is the number of atoms accelerated by the lattice, i.e. those detected in the final velocity class $4\,v_{rec}$, whereas for the inverse tunnelling direction, N_{tunnel} is the number of atoms detected in the $v = 0$ velocity class.

When C is small, both tunnelling rates are essentially the same and agree well with the linear Landau-Zener prediction. By contrast, when C is increased, the two tunnelling rates begin to differ, as can be seen in Fig. 4, where the tunnelling rate from the ground to excited state, calculated using Eq. (14), is 0.72 ± 0.10, whereas from the excited to the ground state we measured $r = 0.37 \pm 0.05$. The errors on the tunnelling rates are statistical errors obtained by averaging over roughly 20 experimental runs in each case, giving a relative error of $\approx 15\%$. Qualitatively we find agreement with the theoretical predictions of the nonlinear Landau-Zener model, whereas quantitatively there are significant deviations. We believe these to be partly due to experimental imperfections. In particular, the sloshing (dipolar oscillations) of the condensate inside the magnetic trap can lead to the condensate not being prepared purely in one band due to non-adiabatic mixing of the bands if the initial quasimomentum is too close to a band-gap. Furthermore, a numerical simulation of the experiment shows that for large values of C, for which the magnetic trap frequency was large, the measured tunnelling rates are significantly modified by the presence of the trap. We have, however, verified that when C in the simulation is varied without varying the trap frequency, the asymmetric tunnelling effect persists.

One of the basic problems one has to face in studying periodic potentials experimentally is that the periodicity is only approximated: the experiment is not infinitely wide. Moreover, in our case the presence of the harmonic trap leads to additional difficulties. If the condensate is dragged too far from the rest position of the harmonic potential, the dragged part starts to feel the elastic force due to the potential and hence does not feel a *constant* force anymore. For this reason it is not possible to study large C values by varying only the harmonic trap frequency (for our experimental parameters, $C \approx 0.11$ was found to be the largest acceptable value both from numerical simulations and from experiment, corresponding to a harmonic trap frequency of about 50 Hz). In future experiments, one might study large C values by increasing the atomic density in the condensate by using an additional optical trap in order to increase the radial trapping frequency or, alternatively, by using Feshbach resonances to vary the atomic

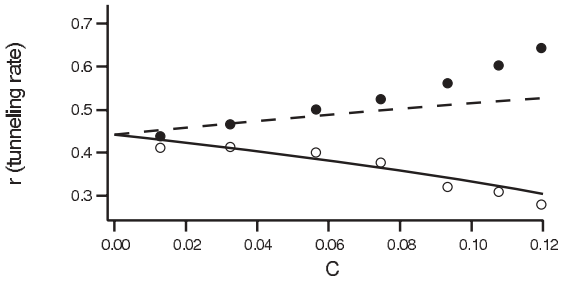

Figure 5 LZ tunnelling rate r as a function of the nonlinear parameter C. Lines and data as in Fig. 2. In contrast to that figure, here C was varied by varying the atomic scattering length a_s; the harmonic trap frequency was fixed at 20 Hz

scattering length a_s. The results of a numerical simulation using this last method are reported in Fig. 5.

Because of the elastic force of the magnetic harmonic trap, it is important not to drag the condensate too far from the rest position. Whereas in the experiment it was necessary to accelerate the condensate sufficiently in order to separate the fraction that underwent tunnelling from that which remained in the original band, in the numerical simulation we could limit ourselves to crossing the edge of the BZ once. Thereafter, rather than simulating the entire time-of-flight procedure, we performed a Fourier transform of the density profiles. From the intensities of the Fourier components we could then calculate the tunnelling probabilities. Also, this method showed us that the presence of the harmonic potential makes it difficult to have a pure ground state or a pure excited state. Even when loading the condensate into the ground band (with the lattice at rest during the loading process), a small fraction of atoms is typically loaded into the excited band because of the presence of the harmonic trap. This means that when we measure the fraction of atoms in the excited band after the tunnelling process, we are measuring the sum of the atoms that were in the ground band and underwent tunnelling into the excited band *plus* the atoms that already were in the excited band and did not undergo tunnelling into the ground band. This situation is explained in Fig. 6.

Numerical simulations confirm that this effect is not negligible and is even more important when measuring the tunnelling process from the excited band to the ground one. In order to extract the "true" tunnelling rate from the numerical data, we reason as follows. Let $|a(-\infty)|^2$ and $|b(-\infty)|^2$ be the population of the two levels *before* the tunnelling occurs and $|a(+\infty)|^2$ and $|b(+\infty)|^2$ the population *after* the tunnelling has occurred; for a transition from the lower level to the upper one we have

$$|a(+\infty)|^2 = |a(-\infty)|^2\, P_1 + |b(-\infty)|^2 (1 - P_2)$$

where P_1 is the nonlinear tunnelling probability we want to measure and $(1 - P_2)$ is the probability for the atoms in

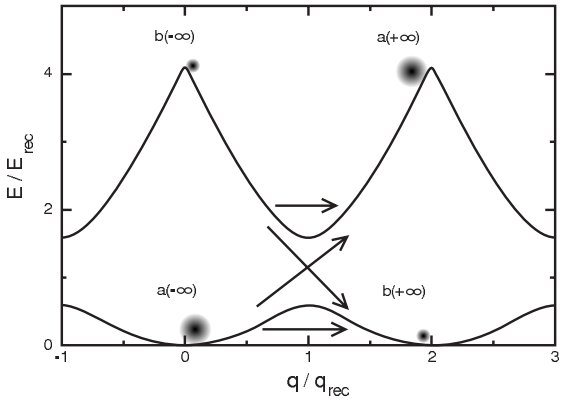

Figure 6 An example of tunnelling from the lower band to the upper one. On the left hand side of the picture we see a large population in the a state *plus* a small population in the b state due to the finite size of the condensate. At the edge of the BZ, arrows indicate the possible paths for the two populations. The final state is represented on the right hand side of the picture

the excited band to remain in the excited band. The non-linear tunnelling probability is then

$$P_1 = \frac{|a(+\infty)|^2}{|a(-\infty)|^2} - \frac{|b(-\infty)|^2}{|a(-\infty)|^2}(1 - P_2).$$

Here P_2 plays the role of a free parameter since it is not possible *a priori* to evaluate it and since we are in a non-linear regime it is not even possible to take the linear probability 5 as an approximation. In Fig. 5 and 2 we used $P_2 = 1$ for tunnelling from the lower state to the upper one and $P_2 = 0$ for the opposite direction.

5. Conclusions

In summary, we have numerically simulated Landau-Zener tunnelling between two energy bands in a periodic potential and found that, in the presence of a nonlinear interaction term, an asymmetry in the tunnelling rates arises. Experimentally, we have measured these tunnelling rates for different values of the interaction parameter and found qualitative agreement with the simulations. Future experiments could probe the complicated and time-dependent tunnelling behavior due to the changing tunnelling rate for multiple crossings of the zone edge. Furthermore, when the two lowest bands are initially equally populated, the tunnelling behavior should again be linear. We also note here that the phenomenon of asymmetric tunnelling should be a rather general feature of quantum systems exhibiting a nonlinearity. For instance, calculating the energy shift due to a nonlinearity for two adjacent levels of a harmonic oscillator, one finds that both levels are shifted upwards in energy, the shift being proportional to the population of the respective level. The energy difference between the levels, therefore, decreases if only the lower state is populated and increases if all the population is in the upper level. Finally, we note that state-dependent mean-field shifts have also been investigated in measurements of the clock-shift in ultra-cold and Bose-condensed atomic samples [19, 20].

Acknowledgements This work was supported by the MURST (COFIN2000 Initiative), the INFM (PRA 'Photonmatter'), and by the EU through Contract No. HPRN-CT-2000-00125.

References

[1] L.D. Landau, Phys. Z. Sowjetunion **2**, 46 (1932); G. Zener, Proc. R. Soc. London A **137**, 696 (1932).
[2] K. Mullen, E. Ben-Jacob, Y. Gefen, and Z. Schuss, Phys. Rev. Lett. **62**, 2543 (1989).
[3] Y. Gefen, E. Ben-Jacob, and A.O. Caldeira, Phys. Rev. B **36**, 2770 (1987).
[4] S. Fishman, K. Mullen, and E. Ben-Jacob, Phys. Rev. A **42**, 5181 (1990).
[5] D. Bouwmeester, N.H. Dekker, F.E.V. Dorsselaer, C.A. Schrama, P.M. Visser, and J.P. Woerdman, Phys. Rev. A **51**, 646 (1995).
[6] O. Zobay and B.M. Garraway, Phys. Rev. A **61**, 033603 (2000).
[7] B. Wu and Q. Niu, Phys. Rev. A **61**, 023402 (2000); J. Liu, et al., Phys. Rev. A **66**, 023404 (2002).
[8] D. Diakonov, L.M. Jensen, C.J. Pethick, and H. Smith, Phys. Rev. A **66**, 013604 (2002); M. Machholm, C.J. Pethick, and H. Smith, Phys. Rev. A **67**, 053613 (2003).
[9] E.J. Mueller, Phys. Rev. A **66**, 063603 (2002).
[10] M. Jona-Lasinio, O. Morsch, M. Cristiani, N. Malossi, J.H. Müller, E. Courtade, M. Anderlini, and E. Arimondo, cond-mat/0306210.
[11] For occupation with equal amplitude of the lower and upper states $|a|^2 = |b|^2$, the nonlinear corrections leading to the asymmetric tunneling play no role.
[12] M.D. Crisp, Phys. Rev. A **8**, 2128 (1973).
[13] O. Morsch, et al., Phys. Rev. Lett. **87**, 140402 (2001).
[14] M. Cristiani, et al., Phys. Rev. A **65**, 063612 (2002).
[15] In order to keep the total interaction time with the lattice constant, the final velocity of the lattice when the condensate is prepared in the upper state is $\approx 4\, v_{rec}$ since initially the lattice is moving at $-1.5\, v_{rec}$.
[16] E. Peik, et al., Appl. Phys. B **65**, 685 (1997).
[17] For the non-uniform condensate density in the optical lattice, described by Pedri, et al. [18] with a separation of the variables parallel and orthogonal to the optical latttice, the parameter C of the 1D Eq. (1) was determined from the maximum condensate density.
[18] P. Pedri, et al., Phys. Rev. Lett. **87**, 220401 (2001).
[19] D.M. Harber, H.J. Lewandowski, J.M. McGuirk, and E.A. Cornell, Phys. Rev. A **66**, 053616 (2002); references therein.
[20] S. Gupta, Z. Hadzibabic, M.W. Zwierlein, C.A. Stan, K. Dieckmann, C.H. Schunck, E.G.M. van Kempen, B.J. Verhaar, and W. Ketterle, Science **300**, 1723 (2003).

INSTITUTE OF PHYSICS PUBLISHING JOURNAL OF PHYSICS B: ATOMIC, MOLECULAR AND OPTICAL PHYSICS

J. Phys. B: At. Mol. Opt. Phys. **37** (2004) 4397–4404 PII: S0953-4075(04)83250-4

Rotational bosonic current in a quasi-condensate confined in an optical toroidal trap

Aranya B Bhattacherjee[1,2], **E Courtade**[1] **and E Arimondo**[1]

[1] INFM, Dipartimento di Fisica E Fermi, Università di Pisa, Via Buonarroti 2, I-56127 Pisa, Italy
[2] Department of Physics, A.R.S.D. College, University of Delhi (South Campus), Dhaula Kuan, New Delhi 110021, India

E-mail: arimondo@df.unipi.it

Received 30 June 2004, in final form 22 September 2004
Published 8 November 2004
Online at stacks.iop.org/JPhysB/37/4397
doi:10.1088/0953-4075/37/22/001

Abstract

We investigate the possibility of inducing a bosonic current which is rotational ($\vec{\nabla} \times \vec{v} \neq \vec{0}$) in a pseudo 1D quasi-condensate confined in an optical toroidal trap. The stability of such a current is also analysed using a hydrodynamics approach. We find that such a current is uniform when the circular symmetry is preserved and energetically stable when the modes of elementary excitations are restricted to one dimension. This scheme allows us to distinguish between a quasi and a true condensate by measuring the rotational spectra of the sample.

1. Introduction

Bose–Einstein condensates (BECs) provide an important quantum system where one can observe many important phenomena such as the superfluid-Mott insulator transition [1] and vortices [2–5]. Recent advances in experimental techniques [6, 7] have stimulated interest in one-dimensional (1D) Bose gases. The 1D case leads to some interesting physics which does not occur in higher dimensions. The experimental feasibility of realizing a tightly confined (1D) trapped gas has been investigated theoretically using Bessel light beams [8]. It is well known that a true BEC cannot occur at any finite temperature in an interacting homogeneous Bose gas in 1D [9], due to long wavelength fluctuations; nor can it occur in the limit of zero temperature [10], due to quantum fluctuations. However, the presence of a trapping potential changes the density of states at low energies, and in the weakly interacting limit a BEC may be formed [11]. Recently Petrov *et al* discussed three different regimes of quantum degeneracy which can occur in a condensate confined in a 1D trap [12]: BEC, quasi-condensate and Tonks–Girardeau gas. In the weakly interacting limit a BEC exists, but as the interaction becomes stronger the mean field energy becomes important. When this energy becomes of the order of the energy level spacing of the trap, fluctuations again become significant. In this regime, the system forms a quasi-condensate, with local phase coherence, rather than the global coherence

0953-4075/04/224397+08$30.00

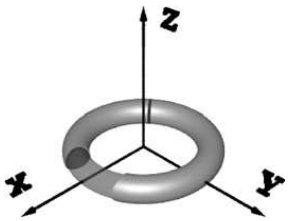

Figure 1. Schematic representation of the optical torus described by equation (1). This optical torus can be generated by the interference of a standard Gaussian beam with a counter-propagating hollow beam generated by a pair of axicon [18, 19].

associated with a true condensate. The quasi-condensate density has the same smooth profile as a true condensate but the phase fluctuates in space and time. Phase fluctuations of the condensate are caused mainly by low energy collective excitations [12]. Quasi-condensates in 3D have been observed experimentally in equilibrium [13, 14] and non-equilibrium [15]. The fact that the velocity of a true condensate $\vec{v_s}(\vec{r},t) = \hbar/m\,\vec{\nabla}\phi(\vec{r},t)$ (with $\phi(\vec{r},t)$ being the phase of the condensate) leads to the important constraint namely irrotationality $\vec{\nabla} \times \vec{v_s}(\vec{r},t) = 0$. On the other hand, the normal component which is substantially higher in a quasi-condensate as compared to a true condensate is not constrained by the condition of irrotationality. Hence we take advantage of this property of the quasi-condensate and propose in this work the use of a 2D optical rotator to produce a rotational bosonic current ($\vec{\nabla} \times \vec{v} \neq 0$ where $\vec{v} = \vec{v_s} + \vec{v_n}$ and $\vec{v_n}$ is the velocity of the normal component) in a quasi-condensate and study the conditions under which this current is stable. We show that using this scheme, it is possible to distinguish between quasi-condensate and true condensate. It is to be noted that such a current is not a vortex. Such a rotator has been proposed for cold atoms based on the principle of transfer of angular momentum of the photons to the atoms [16] using a TEM_{01} circularly polarized Laguerre–Gaussian beam. It has been experimentally demonstrated that a blue-detuned hollow Bessel laser beam formed by an axicon can be successfully used to trap laser cooled metastable xenon atoms [17]. Experimentally, caesium atoms have been trapped in an all blue-detuned stack of optical rings by the interference of a standard Gaussian beam with a counter-propagating hollow beam generated by a pair of axicon [18, 19]. We propose the use of such an experimental scheme with a TEM_{01} beam in order to realize the 2D optical rotator.

2. Description of the optical torus

We will examine the motion of a condensate within an optical toroidal ring trap as experimentally realized in [19] and previously theoretically analysed by Wright *et al* [16]. The potential created by the optical laser may be written as

$$V(r) = \tfrac{1}{2}m\omega_r^2(r - r_0)^2 + \tfrac{1}{2}m\omega_z^2 z^2 \tag{1}$$

where $x^2 + y^2 = r^2$ and r_0 is the location of the potential minimum and also the mean radius of the torus. $\omega_z(\omega_r)$ is the oscillation frequency along the $z(r)$ direction. Because we suppose the plane of the ring is perpendicular to the direction of gravity (z direction in our system), the atomic energies are not affected by gravity. The optical torus described by the potential of equation (1) is represented in figure 1.

The atomic motion within the toroidal trap includes also a rotational energy along the centre of the torus, described by the following rotational Hamiltonian:

$$H_r = -\frac{\hbar^2}{2I}\frac{\delta^2}{\delta\theta^2} \tag{2}$$

where the moment of inertia for an atom with mass m is given by $I = mr_0^2$. If p is the rotational quantum number, then the rotational Hamiltonian defines an energy spectrum whose energy spacing is linked to the rotation frequency Ω for $\Delta p = 1$ as

$$\Omega = \frac{(2p+1)\hbar}{2mr_0^2}. \tag{3}$$

Note that the rotational frequency Ω depends only on the radius of the ring r_0. In the radial direction, the ring radius is approximately the radius of the laser beam. Extending the experimental parameters of [18] to Rb atoms, with a beam radius of about 50 μm, potential height of 10 E_R and $\omega_R \sim 2\pi \times 3.7$ kHz, where E_R and ω_R are respectively the recoil energy and frequency, one can find $\omega_r \sim 2\pi \times 0.06$ kHz, $\omega_z \sim 2\pi \times 15$ kHz and $\Omega \sim 2\pi \times 0.023$ Hz (for the $p = 0 \to p = 1$ transition).

Moreover we will suppose, as in [16] that using for the laser field a high order circularly polarized Laguerre–Gaussian mode, an orbital angular momentum is transferred by the laser field to the atoms. Therefore, the rotational motion of the condensate atoms at the frequency Ω can be excited by the laser field. Let us now systematically investigate the collective modes of a true condensate and that of a quasi-condensate (in the presence of a rotational velocity field) in an optical torus.

3. Collective modes of a true condensate in an optical torus

For a true condensate the velocity is the gradient of a scalar, the velocity field is thus irrotational, unless the phase of the order parameter has a singularity (vortex). A simple description of the collective oscillations is provided by the irrotational hydrodynamics equations of superfluids

$$\frac{\partial n_s}{\partial t} + \vec{\nabla} \cdot [n \vec{v_s}] = 0 \tag{4}$$

$$m\frac{\partial \vec{v_s}}{\partial t} + \vec{\nabla}\left[\frac{m v_s^2}{2} + V(\vec{r}, t) + g_{3d} n_s\right] = 0 \tag{5}$$

where $n_s(\vec{r}, t)$ is the superfluid spatial density, $v_s(\vec{r}, t)$ is the superfluid velocity field in the laboratory frame and m is the mass of the atom. The parameter g_{3d} characterizes the strength of the inter-atomic interactions and is related to the s-wave scattering length a_s for a 3D gas by $g_{3d} = 4\pi\hbar^2 a_s/m$. These equations are valid in the Thomas–Fermi limit, where the so-called quantum pressure term is neglected. The density can be written as $n_s = n_0 + \delta n_s$, and $\vec{v_s} = \vec{v_0} + \delta\vec{v_s}$ where $n_0(\vec{v_0})$ is the equilibrium density (velocity) and $\delta n_s(\delta\vec{v_s})$ is a small perturbation of the density (velocity) from its equilibrium value. The equilibrium density n_0 is given by $n_0 = (\mu - V(r))/g_{3d}$. The collective oscillations can be derived by looking for general time-dependent solutions of the form (see [20, 21])

$$\delta n_s(\vec{r}, t) = \alpha_0 + \alpha_1(x^2 + y^2) + \alpha_2 z^2 + \alpha_3 xy + \alpha_4 xz + \alpha_5 yz \tag{6}$$

$$\delta\vec{v_s}(\vec{r}, t) = \vec{\nabla}(\beta_0 + \beta_1(x^2 + y^2) + \beta_2 z^2 + \beta_3 xy + \beta_4 xz + \beta_5 yz) \tag{7}$$

where α_i and β_i are time-dependent parameters to be determined. In the linear limit, one can look for solutions varying in time like $e^{-i\omega t}$. Linearizing equations (4) and (5) and inserting δn_s and $\delta\vec{v_s}$ and solving for the modes ω for $\omega_x = \omega_y = \omega_r$, one finds

$$\omega_\pm^2 = \tfrac{1}{2}\left(4\omega_r^2 + 3\omega_z^2\right) \pm \tfrac{1}{2}\sqrt{16\omega_r^4 + 9\omega_z^4 - 16\omega_r^2\omega_z^2} \tag{8}$$

$$\omega^2(l = 0, m = \pm 1) = \omega_r^2 + \omega_z^2 \tag{9}$$

$$\omega^2(l = 2, m = \pm 2) = 2\omega_r^2. \tag{10}$$

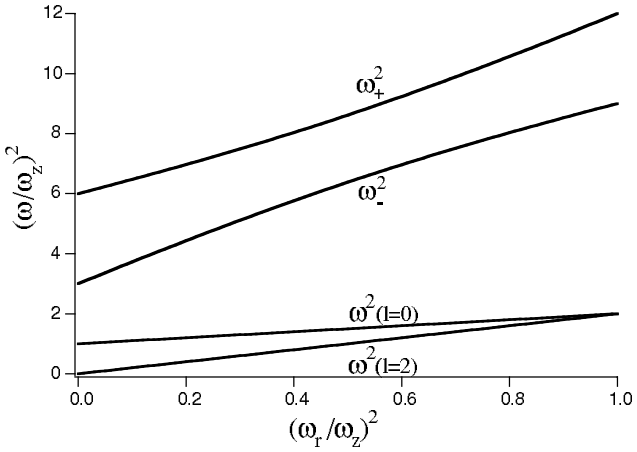

Figure 2. Mode frequencies of equations (8), (9) and (10) as functions of the radial trap frequency ω_r.

We recover the dispersion laws in an anisotropic potential which are well known to be independent of the interatomic strength [22]. Figure 2 displays these modes as a function of the radial frequency which are seen to be stable. The frequencies are normalized with respect to the ω_z axial frequency. In the following we will allow for the condition of 'rigid ring' (tight confinement) condensate, i.e. the particles are constrained to move only along the path $x^2 + y^2 = r_0^2$. Moreover, at sufficiently low temperatures with the radial motion of particles (the centre of mass modes along the x and y directions) essentially frozen because the radial frequency ω_r is much more than the mean-field interaction energy, a tight confinement regime is reached. The experimental configuration of [18, 19] is so flexible that it can satisfy these conditions very easily, as in section 2. In that regime, some degrees of freedom are eliminated and the radial motion of particles (the centre of mass modes along the x and y directions) is essentially frozen.

4. Collective modes of a quasi-condensate in an optical torus

4.1. Rotational velocity field of a quasi-condensate

The special properties of superfluids are a consequence of their motions being constrained by the fact that the velocity $(\vec{v_s}(\vec{r},t))$ of the condensate is proportional to the gradient of the phase $(\phi(\vec{r},t))$ of the wavefunction, that is, $\vec{v_s}(\vec{r},t) = \hbar/m\,\vec{\nabla}\phi(\vec{r},t)$. We see directly from this definition that $\vec{v_s}(\vec{r},t)$ satisfies two important constraints, namely the condition of irrotationality $\vec{\nabla} \times \vec{v_s}(\vec{r},t) = 0$ and the Onsager–Feynman quantization condition $\oint \vec{v_s}(\vec{r},t) \cdot \mathrm{d}\vec{l} = nh/m$ $(n = 0, \pm 1, \pm 2 \ldots)$. Obviously, in a simply connected geometry with condensate wavefunction finite everywhere, the condition of irrotationality implies the Onsager–Feynman quantization condition with $n = 0$, but for more general cases involving vortices or in a torus (multiply connected geometry), n can be nonzero.

In stable or metastable equilibrium the total bosonic current will have contributions from both the normal and the superfluid components (Landau's two fluid hypothesis). Now if by some mechanism, the condensate in the torus with mean radius r_0 is made to rotate with an angular velocity Ω, then the linear velocity of the normal component will be simply Ωr_0 while the linear velocity of the superfluid component will be constrained by the quantization condition and in general cannot be equal to Ωr_0. In fact, a simple statistical mechanical

argument shows that the lowest free energy is obtained when n takes the value closest to Ω/Ω_c where $\Omega_c = \hbar/mr_0^2$. For $\Omega/\Omega_c \ll 1, n$ is equal to zero and consequently the superfluid component no longer contributes to the circulating current. At larger values of Ω ($>\Omega_c/2$), the superfluid will contribute to the total angular momentum an amount $\sim n\Omega_c$. From an inspection of equation (3) for the $p = 0 \rightarrow p = 1$ transition together with the definition of Ω_c, we find that $\Omega/\Omega_c = 0.5$ irrespective of the radius of the 2D optical rotator. Consequently, in a true condensate, where the normal component is extremely low, the total bosonic current is almost zero for $\Omega/\Omega_c \ll 1$. Based on the above discussion, we argue that in a quasi-condensate, where the normal component is substantially higher than a true condensate, for $\Omega/\Omega_c \ll 1$, the normal component will contribute significantly to the bosonic current, which one could detect. Thus using this proposal, it could be possible to distinguish between a quasi-condensate and a true one.

We propose that the theoretical scheme introduced in [16] may be used to transfer orbital angular momentum of the photon to a cloud of ultra-cold atoms in a quasi-condensate state. A velocity field created in such a manner is rotational. This velocity field can be visualized by introducing a vector potential $\vec{A}$ in the quasi-condensate total velocity $\vec{v} = \vec{v_s} + \vec{v_n}$

$$\vec{v}(\vec{r}) = \frac{\hbar}{m}[\vec{\nabla}\phi(\vec{r}) + \vec{A}] \tag{11}$$

where the vector potential $\vec{A}$ is associated with the rotational component of the velocity

$$\vec{A} = \frac{m}{\hbar}\vec{\Omega} \times \vec{r} \tag{12}$$

with $\vec{\Omega} = \Omega\hat{k}$. Ω is the rotational angular velocity of the sample. The corresponding rotational velocity field which is actually the velocity of the normal component

$$\vec{v}_{\text{rot}} = \vec{v}_n = \Omega(-y\hat{i} + x\hat{j}) \tag{13}$$

with $\vec{\nabla} \times \vec{v}_n = 2\vec{\Omega}$. The angular velocity of the sample is easily adjusted by the mean ring radius r_0 (see equation (3)).

4.2. Stability conditions for stable persistent current

Let us now analyse the condition for the existence of a steady velocity field $\vec{v}_n$ of the form of equation (13) in a quasi-condensate for a ring in the presence of a weak perturbation (a slightly distorted potential). The perturbed potential is written as

$$V(r) = \tfrac{1}{2}m\omega_r^2(r - r_0)^2 + \tfrac{1}{2}m\omega_z^2 z^2 + \tfrac{1}{2}m(\delta\omega_x)^2x^2 + \tfrac{1}{2}m(\delta\omega_y)^2y^2 \tag{14}$$

where $\delta\omega_x$ and $\delta\omega_y$ are small external perturbations in the frequencies along the x and y directions. In the presence of the perturbation, the irrotational component of the velocity field is now also included which is written as $\vec{v}_{\text{irrot}} = \vec{v}_s = \alpha\vec{\nabla}(xy)$. Therefore, the total velocity field is

$$\vec{v}(\vec{r}) = (\alpha - \Omega)y\hat{i} + (\alpha + \Omega)x\hat{j}. \tag{15}$$

The macroscopic description of modes with circulation is provided by the equations of two component rotational hydrodynamics [21, 23]

$$m\frac{\partial\vec{v}}{\partial t} + \vec{\nabla}\left[\frac{mv^2}{2} + V(\vec{r}, t) + g_{3d}n_s + 2g_{3d}n_n\right] = m\vec{v} \times (\vec{\nabla} \times \vec{v}). \tag{16}$$

In the following, we will ignore fluctuations in the density of the normal component n_n: this is the static Popov approximation which corresponds to treating the dynamics of the condensate moving in the static mean field of the condensate thermal cloud [23]. We will also

neglect damping due to interaction between superfluid and normal component. The modes obtained by neglecting damping corresponds to the undamped finite temperature Stringari normal modes [23]. The continuity equation leads to the following expression for α:

$$\alpha = \frac{\Omega((\delta\omega_y)^2 - (\delta\omega_x))^2}{2\Omega^2 - ((\delta\omega_y)^2 + (\delta\omega_x)^2)}. \tag{17}$$

Thus we see from equation (15) that the irrotational component of the velocity field which comes into the picture as a result of the perturbation destroys the bosonic current with uniform angular velocity Ω. From equation (17) we infer that for such a uniform current to exist, we must have $(\delta\omega_x)^2 = (\delta\omega_y)^2$. The conservation of circular symmetry guarantees a uniform current in the quasi-condensate. In the presence of a weak, static, asymmetric perturbation, angular momentum is not conserved. In a rotating quasi-condensate, scattering of particles against such an asymmetric perturbation will ultimately bring the fluid to rest. Having found circular symmetry as a necessary criterion for a uniform current to exist, we now proceed to calculate the collective modes in the non-equilibrium state. Collective modes in the presence of a rotational velocity field for a trap with circular symmetry can be derived as in section 3 by looking for time-dependent solutions for δn and $\delta \overrightarrow{v}$. We now allow for rigid ring condensate and assume that we still have motion in xz (yz) planes and also centre of mass motion along the z direction. The density and velocity fluctuations are now proportional to z^2, xz, yz. These modes from the usual hydrodynamic approach are found to be

$$\omega^2 = 3\omega_z^2 \tag{18}$$

and roots of the equation

$$\omega^3 + \Omega\omega^2 - \left(\Omega^2 + \omega_z^2\right)\omega - \Omega\left(\Omega^2 + \omega_z^2\right) = 0. \tag{19}$$

Equation (19) reveals that due to the rotational velocity component, the system does not satisfy Kohn's theorem, i.e. $\omega^2 \neq \omega_z^2$. As $\Omega \to 0$, we regain Kohn's theorem. The modes calculated from equations (18) and (19) are plotted in figure 3. Negative frequencies of excitations are taken as the signature of energetic instability which is a result of the absence of thermodynamic equilibrium [24]. The mode corresponding to the centre of mass motion along the z direction from equation (18) (dashed line in figure 3) is always positive and constant. This nondependence on Ω is a consequence of the absence of excitations in the xy plane due to the rigid ring. We find that for a non-zero value of Ω, one of the modes in the xz (yz) planes of equation (19) (lower curve in figure 3) is always negative. This signals energetic instability because the magnitude of the smallest root is always equal to the angular velocity Ω. This is equivalent to the Landau criterion of super-fluid stability [25, 26] with respect to proliferation of elementary excitations, i.e. the bosonic current becomes unstable when the frequency of the lowest energy excitation becomes equal to or more than the angular velocity. This implies that the presence of fluctuations in the xz and yz planes will not support the rotational velocity of the normal component and Kohn's theorem will be restored. A similar result is found for a Bose gas in a toroidal container using the Bogoliugov approximation [27]. The instability in [27] originates from the possibility for a single vortex to escape gradually from a bulk condensate. Thus to have an energetically stable current we need to freeze the motion in xz and yz planes. This means that we restrict the modes of the elementary excitations to only the z direction whose frequency is given by equation (18). It is to be noted that the dipole mode $\left(\omega^2 = \omega_z^2\right)$, which is also the motion of the centre of mass is only decoupled from the internal degree of freedom. The rotation of the normal component is still capable of destroying this dipole more because the normal component is acting like an impurity and its motion around the torus is constantly changing the centre of mass of the condensate. This is unlike in the case of a vortex where the entire condensate is uniformly rotating and hence keeping the centre of mass intact.

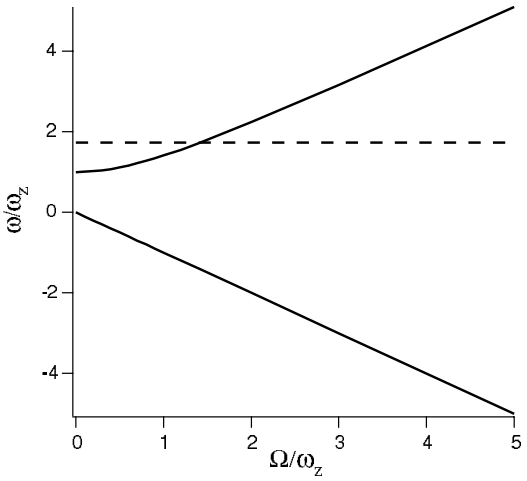

Figure 3. Calculated mode frequencies as functions of the angular frequency Ω. The dashed line corresponds to the centre of mass frequency along the z direction from equation (18). The other two solid line curves correspond to the scissoring modes in the $xz\,(yz)$ planes of equation (19). The negative frequencies of the lower curve are the signature of instability (see text).

Let us now look into the possible experimental realization of such a pseudo quasi-condensate in our proposed scheme. The mean field interaction frequency $g_{3d}N/\hbar 2\pi r_0^3$ for $N = 10^4$ and $a_s = 5$ nm (in the case of Rb) is found to be $\sim 2\pi \times 0.6$ Hz, much less than the radial trap frequency ($\sim 2\pi \times 60$ Hz, see section 2) which implies that we are indeed in the pseudo 1D regime. Following [12], one can introduce a dimensionless quantity $\alpha = 4\pi a_s/l$, where $l = \sqrt{\hbar/m\omega_z}$ is the amplitude of axial zero point oscillations. The regime of a weakly interacting gas corresponds to $\alpha \ll 1$. In this regime, the condensate is in the Thomas–Fermi regime if the number of particles $N > \alpha^{-1}$. The decrease of temperature to below the degeneracy temperature $k_B T_d = N\hbar\omega_z$ leads to the appearance of a quasi-condensate which at $T < T_{cr}$ turns to a true condensate. The critical temperature T_{cr} is determined by $k_B T_{cr} = \hbar\omega_z (32N/9\alpha^2)^{1/3}$. For $N \sim 10^4$ and using the values of the trap parameters given earlier (see section 2), we find $T_d = 1.1$ mK and $T_{cr} = 8.7$ μK. Working between these two temperature limits and having $\omega_r > g_{3d}N/\hbar 2\pi r_0^3$, one can thus be in the pseudo 1D quasi-condensate regime. This scheme allows us to distinguish between a quasi-condensate and a true condensate by simply measuring the rotational spectrum of the sample. The rotational spectrum of the sample can be measured by using two consecutive Bragg pulses probing the momentum distribution in a trapped Bose gas at low temperature [28, 29]. A stimulated Raman transition involves absorption of a photon from one beam followed by stimulated emission into the other; if the system is in a quasi-condensate and tight confinement regime then this process will transfer orbital angular momentum off to the atom, but no linear momentum in the axial or radial directions.

5. Conclusion

In conclusion, we have proposed the use of a new type of optical toroidal trap to induce a uniform rotational bosonic current (which is not a vortex) in a quasi-condensate. The principle of producing such a rotational current is based on the transfer of angular momentum of the photon to the atoms of the normal component. The angular velocity induced by the proposed 2D optical rotator is exactly half the critical angular velocity required by the superfluid component to contribute to the total bosonic current. Hence, the given optical rotator is unable

to transfer any angular momentum to the atoms in the superfluid component. We are thus able to distinguish between a quasi-condensate and a true condensate by measuring the rotational spectrum of the sample by two-photon Bragg spectroscopy. Our analysis indicates that such a rotational current is uniform when the circular symmetry of the ring trap is conserved and energetically stable when the elementary excitations are completely frozen in the transverse direction (xy plane).

Acknowledgments

Fruitful discussions with I Carusotto and A Recati, and a careful check of the manuscript by C Menotti are acknowledged. This research was supported by the Abdus Salam International Centre for Theoretical Physics, Trieste, Italy under the ICTP-TRIL fellowship scheme, by the Sezione A of INFM-Italy through a PAIS Project, by the MIUR-Italy through a COFIN Project and by the European Commission through the Cold Quantum-Gases Network, contract HPRN-CT-2000-00125.

References

[1] Greiner M, Mandel O, Esslinger T, Hansch T W and Bloch I 2002 *Nature* **415** 39
[2] Matthews M R, Anderson B P, Halijan P C, Hall D S, Wieman C E and Cornell E A 1999 *Phys. Rev. Lett.* **83** 2498
[3] Madison K W, Chevy F, Wohlleben W and Dalibard J 2000 *Phys. Rev. Lett.* **84** 806
[4] Madison K W, Chevy F, Wohlleben W and Dalibard J 2000 *J. Mod. Opt.* **47** 2715
[5] Chevy F, Madison K W and Dalibard J 2000 *Phys. Rev. Lett.* **85** 2223
[6] Gorlitz A *et al* 2001 *Phys. Rev. Lett.* **87** 130402
[7] Schreck F, Khaykovich L, Corwin K L, Ferrari G, Bourdel T, Cubizolles J and Salomon C 2001 *Phys. Rev. Lett.* **87** 080403
[8] Arlt J, Dholakia K, Soneson J and Wright E M 2001 *Phys. Rev. A* **63** 063602
[9] Hohenberg P C 1967 *Phys. Rev.* **158** 383
[10] Pitaevskii L and Stringari S 1991 *J. Low Temp. Phys.* **85** 377
[11] Ketterle W and Van Druten N 1996 *Phys. Rev. A* **54** 656
[12] Petrov D S, Shlyapnikov G V and Walraven J 2000 *Phys. Rev. Lett.* **85** 3745
[13] Dettmer S, Hellweg D, Ryytty P, Arlt J J, Ertmer W, Sengstock K, Petrov D S and Shlyapnikov G V 2001 *Phys. Rev. Lett.* **87** 160406
[14] Hellweg D *et al* 2001 *Appl. Phys.* B **73** 781
[15] Shvarchuck I, Buggle Ch, Petrov D S, Dieckmann K, Zielonkowski M, Kemmann M, Tiecke T G, Von Klitzing W, Shlyapnikov G V and Walraven J T M 2002 *Phys. Rev. Lett.* **89** 270404
[16] Wright E M, Jessen P S and Lapeyere G J 1996 *Opt. Commun.* **129** 423
[17] Kulin S, Aubin S, Christe S, Peker B, Rolston S L and Orozco L A 2001 *J. Opt. B: Quantum Semiclass. Opt.* **3** 353
[18] Depret B, Verkerk P and Hennequin D 2002 *J. Physique* IV **12** 137
Depret B, Verkerk P and Hennequin D 2002 *Opt. Commun.* **211** 31
[19] Verkerk P and Hennequin D 2003 *Preprint* physics/0306155
[20] Menotti C and Stringari S 2002 *Phys. Rev. A* **66** 043610
[21] Cozzini M and Stringari S 2003 *Phys. Rev. A* **67** 041602
[22] Dalfovo F, Giorgini S, Pitaevskii L P and Stringari S 1999 *Rev. Mod. Phys.* **71** 463
[23] Griffin M 2000 *Mod. Phys. Lett.* B **14** 65
[24] Recati A, Zambelli F and Stringari S 2001 *Phys. Rev. Lett.* **86** 377
[25] Javanainen J, Paik S M and Yoo S M 1997 *Phys. Rev.* A **58** 580
[26] Javanainen J and Zheng Yi 2001 *Phys. Rev. A* **63** 063610
[27] Rokhsar D S 1997 *Preprint* cond-math/9709212
[28] Stenger J, Inouye S, Chikkatur A P, Stamper-Kurn D M, Pritchard D E and Ketterle W 1999 *Phys. Rev. Lett.* **82** 4569
[29] Brunello A, Dalfovo F, Pitaevskii L and Stringari S 2000 *Phys. Rev. Lett.* **85** 4422

RAPID COMMUNICATIONS

PHYSICAL REVIEW A **74**, 031403(R) (2006)

Dark optical lattice of ring traps for cold atoms

Emmanuel Courtade, Olivier Houde, Jean-François Clément, Philippe Verkerk, and Daniel Hennequin*
Laboratoire de Physique des Lasers, Atomes et Molécules, UMR CNRS, Centre d'Études et de Recherche Lasers et Applications, Université des Sciences et Technologies de Lille, F-59655 Villeneuve d'Ascq cedex, France
(Received 22 May 2006; published 20 September 2006)

We propose an optical lattice for cold atoms made of a one-dimensional stack of dark ring traps. It is obtained through the interference pattern of a standard Gaussian beam with a counterpropagating hollow beam obtained using a setup with two conical lenses. The traps of the resulting lattice are characterized by a high confinement and a filling rate much larger than unity, even if loaded with cold atoms from a magneto-optical trap. We have implemented this system experimentally, and demonstrated its feasibility. Applications in statistical physics, quantum computing, and Bose-Einstein condensate dynamics are conceivable.

DOI: 10.1103/PhysRevA.74.031403 PACS number(s): 32.80.Pj, 39.25.+k

Optical lattices provide a versatile tool to study the dynamical properties of cold and ultracold atoms. They are presently the topic of intense research activity, in particular because they represent an outstanding toy model for various domains. In statistical physics, cold atoms in optical lattices, through their tunability, made possible the observation of the transition between Gaussian and power-law tail distributions, in particular the Tsallis distributions [1]. Condensed matter systems and strongly correlated cold atoms in optical lattices offer deep similarities, as in the superfluid–Mott-insulator quantum phase transition [2], in the Tonks-Girardeau regime [3] or for the emergence of a macroscopic current in periodic potentials [4]. In quantum computing, optical lattices appear to be an efficient implementation of a Feynman universal quantum simulator [5], and are among the most promising candidates for the realization of a quantum computer [6].

One of the main advantages of the optical lattices is their high flexibility. By varying the shape of the lattice, a wide range of configurations is reached. Currently, many studies deal with one-dimensional (1D) lattices, in particular because quantum effects are stronger in low-dimensional systems [7]. A particularly interesting situation concerns 1D lattices with periodic boundary conditions, because many new effects appear [8]. Recently, an experimental implementation has been proposed, where the lattice sites are distributed along rings [9]. In a more complex configuration, the sites themselves could have the shape of a ring, allowing, e.g., the study of solitons in 1D Bose-Einstein condensates (BECs) with periodic boundary conditions [10] or atomic-phase interferences between such BECs [11]. Experimental realization of such 1D rings is still an open question, as either a lattice or a single trap. Large magnetic single-ring traps have been produced, in connection with the study of the atomic Sagnac effect [12,13], but their transverse confinement is weak, and they cannot be considered as 1D rings. A more promising proposition is an optical trap built with twisted light obtained from two counterpropagating Laguerre-Gaussian beams with an azimuthal phase dependence [14]. Those authors suggest that an optical lattice of such ring traps could be created by combining several twisted molasses. Such an arrangement has the drawback of trapping the atoms where the light intensity is maximum. This may result in serious perturbations of the atoms due to the trapping beams [15]. In particular, some applications in quantum computation require trapping of the atoms in dark lattices, to make the system robust against decoherence [16]. Contrary to bright lattices, where even a 1D configuration leads to 3D trapping, 1D dark lattices do not trap atoms in 3D: only 3D dark lattices trap atoms in 3D [15]. So far, the only proposal for such a lattice consists in a Gaussian beam making a round trip in a confocal cavity [17]. A difference of waist between the two directions of propagation leads to a lattice of ring traps with $\lambda/2$ periodicity, where λ is the optical wavelength. Such a device has the advantage of generating high light intensity inside the cavity and so deeper traps than with free-propagating beams. But this is obtained at the cost of flexibility: for example, changing the ring radius requires changing the cavity mirrors. These difficulties probably explain why, to our knowledge, this proposal has not yet been realized experimentally.

We propose here a different geometry for a dark lattice of ring traps, obtained from a hollow beam and a counterpropagating Gaussian beam, without any cavity. The radius and the thickness of the rings can be adjusted independently, and due to the stiff edges of the hollow beam, the trap steepness is much larger than in [17]. Finally, the filling rate of each site is much larger than unity, even when loaded with a magneto-optical trap (MOT), unlike 3D dark lattices, which require the use of a BEC. The filling rate should even reach values in excess of 1000 atoms per site if an adequate sequence is used to turn on the lattice.

The paper is organized as follows: We first discuss the principle of the lattice of ring traps, then describe the experimental realization, and finally show preliminary results concerning cold atoms loaded in the lattice.

Each individual trap is a 3D dark ring, and the lattice is a 1D stack of such rings. Thus, the global shape of the potential is a bright full cylinder with a pile of ring wells inside. To obtain this potential, a standard Gaussian beam interferes with a counterpropagating hollow beam with no azimuthal phase dependence [18], unlike the Laguerre-Gaussian beams used, e.g., as waveguides [19]. Both beams have the same blue-detuned frequency, so that the trapping sites correspond to the zero-intensity places. Both beams propagate along the

*Electronic address: daniel.hennequin@univ-lille1.fr

RAPID COMMUNICATIONS

COURTADE *et al.* PHYSICAL REVIEW A **74**, 031403(R) (2006)

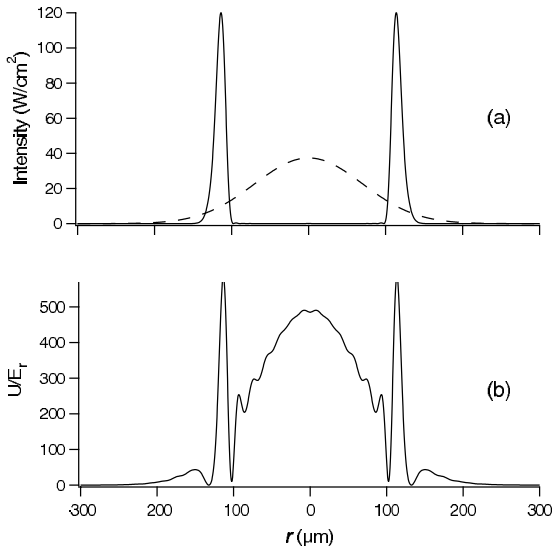

FIG. 1. (a) Theoretical transverse profile of the Gaussian (dashed) and hollow (full) beams used in the experiment. (b) The resulting transverse potential at the bottom of the well. Parameters are those used in the experiments.

z vertical axis, and the hollow beam is a cylindrical beam, with an intensity distribution along the radial direction r as illustrated in Fig. 1(a) (solid line). When the two beams are out of phase, two pairs of zeros of intensity appear symmetrically on each side of the center, at $r=100$ and 130 μm on Fig. 1(b), where the two beam intensities are equal. Because of the cylindrical symmetry, these zeros correspond to two concentric rings along the azimuthal direction. In contrast, when the two beams have the same phase, the intensity profile reaches its maximum. This interference pattern results in a potential U which is, in the limit of weak saturation and large detuning, proportional to the light intensity I:

$$U=\frac{\hbar}{8}\frac{\Gamma^2}{\Delta}\frac{I}{I_S}, \tag{1}$$

where Δ is the detuning, I_S the saturation intensity, and Γ the width of the atomic transition. Because the outer ring is shallow, only the inner ring, at $r=100$ μm, is a trap.

A hollow beam as described above is easily produced by a conical lens [18]. Conical lenses are extensively used to produce Bessel-Gauss [20] or annular beams [21,22]. To generate an annular hollow beam, we use a converging lens L to shape the incident Gaussian beam, and then a conical lens. Each incident ray is deviated toward the optical axis z by the conical lens, and thus the incident Gaussian beam is transformed into a ring [18]. A second conical lens is used to collimate the radius r of the ring, so that after this second lens, r becomes constant with z. The resulting hollow beam has a radius r which depends only on the distance between the two conical lenses, while its thickness Δr depends on the focal length of L. Thus r and Δr are adjustable independently.

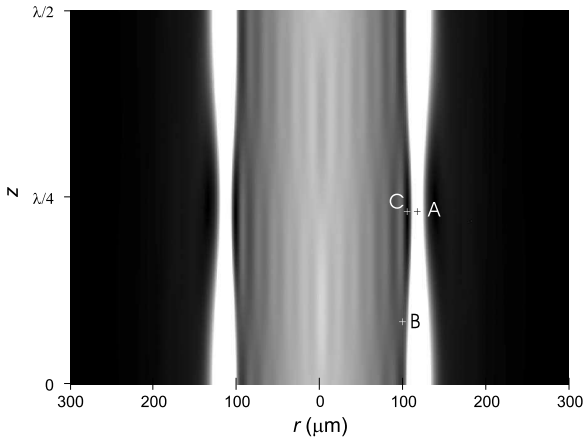

FIG. 2. 2D representation of the potential as a function of the radius r and the longitudinal coordinate z. The complete potential has a revolution symmetry around the axis $r=0$. Parameters are those of Fig. 1. Note that the scales along z and r are different. Dark corresponds to a zero potential. Significance of points A, B, and C is given in the text.

The potential is obtained by focusing the Gaussian beam and the counterpropagating hollow beam at the same point, so that the wave surfaces are planes perpendicular to the propagation axis. The resulting potential has a periodicity of $\lambda/2$, with a shape depending locally on the phase ϕ between the two beams. It is illustrated through the theoretical plots of Figs. 1(b) and 2 where, for the sake of simplicity, we used the parameters of the experimental demonstration described below: the hollow and Gaussian intensities are, respectively, $I_H=14$ mW and $I_G=11.5$ mW [Fig. 1(a)], with $\Delta/2\pi=70$ GHz. Figure 1(b) shows the potential transverse profile at the bottom of the wells. The geometry of the ring appears clearly, with a confinement of the order of $r/10$ for $U<200E_r$, and a height for the external barrier of $580E_r$, where E_r is the recoil energy. Secondary minima, originating in the residual diffraction produced by the mask used to remove inner rings of the hollow beam [18], appear inside the main ring, but because of their weak depth, they should not be annoying in most applications.

A better understanding of the potential distribution can be obtained from Fig. 2, where U is plotted in gray scale versus r and z. The potential is periodic along z, with a period $\lambda/2$. Atoms with low enough energy are confined in a torus with a half-ellipse cross section with axes of the order of 0.1 and 10 μm, corresponding on the figure to the dark zone at the point C. The height of the external barrier varies with z. The minimum height $U_A=580E_r$, at point A of Fig. 2, occurs at the same z as the bottom of the main well [Fig. 1(b)]. The internal barrier has a channel structure, with the lowest pass at point B (Fig. 2), at a height of $U_B=200E_r$, between two successive longitudinal sites.

The number of atoms that we should be able to put in each site of this lattice depends of course on the density of the cloud of cold atoms used to load the lattice, but also on the spatial overlap between the cloud and the lattice. In particular, when the atoms are loaded from a MOT, the capture

volume of the lattice is decisive for its filling rate. In the present case, the capture volume is determined by the hollow beam diameter, which may be chosen as several hundreds of micrometers. For example, with $r=100$ μm (Fig. 2) and an initial cloud of radius 1 mm, 1.5% of the initial atoms are inside the hollow beam. Thus, if the lattice is loaded with a cloud of 10^8 atoms in 4 mm^3, which are the typical characteristics obtained from a MOT, 1.5×10^6 atoms are loaded in 2000 sites, leading to a filling rate much larger than 1.

To test the feasibility of this lattice, we have implemented an experiment with the characteristics described above. Cesium atoms are initially cooled in a standard MOT with a -3Γ detuning from resonance. At time $t=-40$ ms, the magnetic field is turned off, while at time $t=-30$ ms, the detuning is increased to -5Γ and the trap beam intensity is decreased: this sequence allows us to obtain at time $t=0$ a 40 μK molasses, corresponding to an energy of $200E_r$, with 10^8 atoms in typically 4 mm^3.

The hollow and Gaussian beams are produced by two laser diodes injected by a single master laser diode in an extended cavity, which ensures the same frequency for both beams. For this demonstration, the beams are tuned 70 GHz above the atomic transition. In these conditions, the power of the Gaussian and hollow beams, respectively, 11.5 and 14 mW, is sufficient to reach the needed potential depth of $200E_r$. The Gaussian beam has a minimum waist of 140 μm, located at the level of the MOT. The axicon setup is mounted on an optical rail, to guarantee good stability of the beam. The incident beam is collimated with a waist equal to 645 μm. The two conical lenses, with a vertex angle of 2°, are separated by a distance of about 10 cm, adjusted to obtain $r=1$ mm. The L focal length of 500 mm leads to $\Delta r=100$ μm. A telescope located just before the trap reduces these values to $r\simeq100$ μm and $\Delta r\simeq10$ μm. We obtain in the MOT a transverse distribution of the hollow beam which is in excellent agreement with the theoretical one.

To load the cold atoms inside the lattice, the latter is turned on at a time $t<0$, so that, when the molasses is switched off, the atoms are already distributed inside the wells. At time $t=0$, the atoms start to fall under the effect of gravity, except for those that are trapped in the lattice. The free atoms need typically 25 ms to quit the camera field of view, so that for $t>25$ ms, only atoms interacting with the optical lattice remain. To observe the atoms, we switch on during 1 ms the trap laser beams near resonance, and we used a low-noise cooled charge-couple device camera to detect the fluorescence emitted by the atoms. A typical picture is shown in Fig. 3. As the resolution of the imaging setup is about 10 μm, individual rings separated by $\lambda/2$ cannot be distinguished. On the contrary, the picture resolves the transverse distribution characterized by two maxima resulting from the side view of the rings. The dashed line is the theoretical distribution obtained when the potential is approximated by a double Gaussian curve. Thus the experimental distribution is less contrasted because the inner walls of the actual wells are flatter than the outer ones.

Figure 4 shows the evolution of the population of the lattice as a function of the time, for the above parameters. The points are obtained by integrating the experimental pictures along the z axis. In order to test the robustness of the

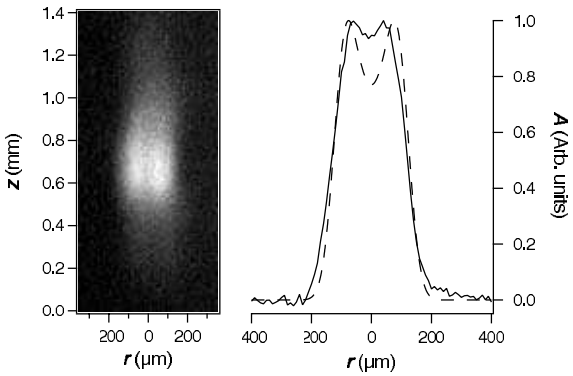

FIG. 3. Left, side view of the lattice obtained by taking a snapshot of the fluorescence of the atoms in the lattice at time $t=40$ ms. Right, the corresponding transverse distribution (solid line) and a rough estimate of the theoretical distribution (dashed line). The two-bump structure reveals the annular structure of the traps.

procedure, eight measurements have been done for each point on the abscissa. Figure 4 shows that the number of atoms decreases exponentially with time. The fit to an exponential (solid line in Fig. 4) gives a lifetime of 30 ms. This value is in good agreement with the theoretical lifetime of the atoms resulting from collisions and spontaneous emission. The number of atoms in the lattice is also in good agreement with the theoretical one: after 40 ms, there are still 30 000 atoms. Assuming that these atoms are localized in about 700 lattice sites, we reach a filling rate of 40 atoms per site. Note that, actually, we have no direct proof of the localization of the atoms, but only the periodic optical potential can prevent the atoms from falling. However, only a direct observation of atom localization, through, e.g., Bragg diffraction, would demonstrate unambiguously that atoms are trapped in the lattice.

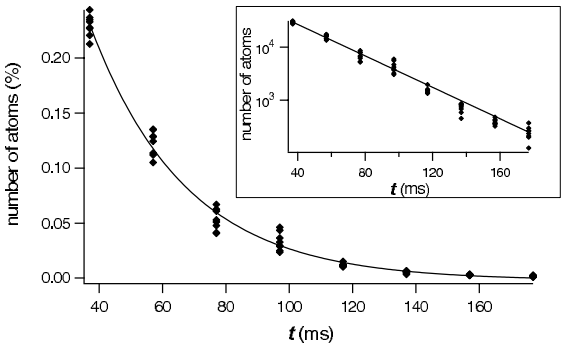

FIG. 4. Number of atoms in the lattice versus time. The main plot is on a linear scale, and the number of atoms is given as a percentage of the molasses population. The solid line corresponds to the fit by an exponential with a decay time $\tau=30$ ms. In the inset, the same results are shown on a logarithmic scale, with the absolute number of atoms. In both cases, points are experimental.

In conclusion, we propose here a lattice geometry consisting of a 1D stack of ring traps, and show its experimental feasibility. The experimental setup remains relatively simple, because the lattice is created from only one pair of beams and it does not need any cavity, contrary to the propositions in, respectively, [14,17]. The other characteristics of this lattice are high confinement of the atoms due to the stiff walls of the trapping sites; large capture volume and filling rate, due to the independence of the torus radius and thickness; and weak interaction between light and atoms, as the traps are dark. We implemented such a lattice experimentally, and loaded it directly from a MOT. We measure the lifetime of the atoms in the lattice of 30 ms. Although we have no direct evidence of the localization of the atoms in the lattice sites, this demonstrates the feasibility of this system. The lifetime should be improved by changing some parameters which were not optimized for this feasibility demonstration. For example, a decrease of the initial temperature of the atoms in the molasses by an adequate cooling sequence leads to relatively deeper traps. An increase of the detuning Δ of the lattice, which requires more intense laser sources, reduces the spontaneous emission. Finally, a decrease of the pressure of the thermal atoms, through, e.g., the use of a double cell, improves the collision rate. Each of these enhancements will contribute to lengthening the lifetime of the atoms in the lattice. If better filling rates are necessary, it would also be possible to increase it. Indeed, when the lattice is switched on, many atoms are heated on the lattice axis, because this axis corresponds to a maximum of the potential. To avoid these extra losses, we plan to switch on the lattice in two steps. First, the hollow beam is switched on just after the trap beams are switched off, so that the atoms inside the beam are trapped and remain in the cylinder. Then, the Gaussian beam is switched on progressively, so that the atoms are adiabatically pushed into the ring traps. This precaution prevents the atoms from being heated by a sudden increase of the potential.

Finally, it would be interesting to study the dynamics of the atoms in this lattice geometry. Moreover, this lattice could be used in systems where interactions between atoms in the same or neighboring sites are required, or when periodic limit conditions are necessary.

The Laboratoire de Physique des Lasers, Atomes et Molécules is Unité Mixte de Recherche de l'Université de Lille 1 et du CNRS (UMR 8523). The Centre d'Études et de Recherches Lasers et Applications (CERLA) is supported by the Ministère chargé de la Recherche, the Région Nord-Pas de Calais and the Fonds Européen de Développement Économique des Régions. The group is supported by the Institut de Recherche sur les Composants logiciels et matériels pour l'Information et la Communication Avancée (IRCICA).

[1] P. Douglas, S. Bergamini, and F. Renzoni, Phys. Rev. Lett. **96**, 110601 (2006).
[2] M. Greiner, O. Mandel, T. Esslinger, T. W. Hänsch, and I. Bloch, Nature (London) **415**, 39 (2002).
[3] B. Paredes, A. Widera, V. Murg, O. Mandel, S. Fölling, I. Cirac, G. V. Shlyapnikov, T. W. Hänsch, and I. Bloch, Nature (London) **429**, 277 (2004).
[4] A. V. Ponomarev, J. Madroñero, A. R. Kolovsky, and A. Buchleitner, Phys. Rev. Lett. **96**, 050404 (2006).
[5] D. Jaksch and P. Zoller, Ann. Phys. **315**, 52 (2005).
[6] O. Mandel, M. Greiner, A. Widera, T. Rom, T. W. Hänsch, and I. Bloch, Nature (London) **425**, 937 (2003); K. G. H. Vollbrecht, E. Solano, and J. I . Cirac, Phys. Rev. Lett. **93**, 220502 (2004).
[7] M. Kramer, C. Menotti, L. Pitaevskii, and S. Stringari, Eur. Phys. J. D **27**, 247 (2003); T. Stöferle, H. Moritz, C. Shori, M. Khöl, and T. Esslinger, Phys. Rev. Lett. **92**, 130403 (2004); M. Cristiani, N. Malossi, M. Jona-Lasinio, M. Anderlini, E. Courtade, and E. Arimondo, Opt. Express **12**, 4 (2004).
[8] C. L. Pando L and E. J. Doedel, Phys. Rev. E **71**, 056201 (2005); D. W. Hallwood, K. Burnett, and J. Dunningham, e-print quant-ph/0602025.
[9] L. Amico, A. Osterloh, and F. Cataliotti, Phys. Rev. Lett. **95**, 063201 (2005).
[10] R. Kanamoto, K. Saito, and M. Ueda, Phys. Rev. A **73**, 033611 (2006).
[11] B. P. Anderson, K. Dholakia, and E. M. Wright, Phys. Rev. A **67**, 033601 (2003).
[12] S. Gupta, K. W. Murch, K. L. Moore, T. P. Purdy, and D. Stamper-Kurn, Phys. Rev. Lett. **95**, 143201 (2005).
[13] A. S. Arnold, C. S. Garvie, and E. Riis, Phys. Rev. A **73**, 041606(R) (2006).
[14] A. R. Carter, M. Babiker, M. Al-Amri, and D. L. Andrews, Phys. Rev. A **73**, 021401(R) (2006).
[15] N. Friedman, A. Kaplan, and N. Davidson, Adv. At., Mol., Opt. Phys. **48**, 99 (2002).
[16] A. Kay, J. K. Pachos, and C. S. Adams, Phys. Rev. A **73**, 022310 (2006).
[17] T. Freegarde and K. Dholakia, Opt. Commun. **201**, 99 (2002).
[18] B. Dépret, Ph. Verkerk, and D. Hennequin, Opt. Commun. **211**, 31 (2002).
[19] K. Bongs, S. Burger, S. Dettmer, D. Hellweg, J. Arlt, W. Ertmer, and K. Sengstock, Phys. Rev. A **63**, 031602(R) (2001).
[20] R. M. Herman and T. A. Wiggins, J. Opt. Soc. Am. A **8**, 932 (1991); J. Arlt and K. Dholakia, Opt. Commun. **177**, 297 (2000).
[21] P.-A. Bélanger, Appl. Opt. **17**, 1080 (1978).
[22] I. Manek, Yu. B. Ovchinnikov, and R. Grimm, Opt. Commun. **147**, 67 (1998); L. Cacciapuoti, M. de Angelis, G. Pierattini, and G. M. Tino, Eur. Phys. J. D **14**, 373 (2001).

Publications stress oxydant

Nanoscale

RSC Publishing

PAPER

View Article Online
View Journal

Hypericin-loaded lipid nanocapsules for photodynamic cancer therapy *in vitro*†

Cite this: DOI: 10.1039/c3nr02724d

Alexandre Barras,[a] Luc Boussekey,[b] Emmanuel Courtade[c] and Rabah Boukherroub*[a]

Hypericin (Hy), a naturally occurring photosensitizer (PS), is extracted from *Hypericum perforatum* plants, commonly known as St. John's wort. The discovery of the *in vitro* and *in vivo* photodynamic activities of hypericin as a photosensitizer generated great interest, mainly to induce a very potent antitumoral effect. However, this compound belongs to the family of naphthodianthrones which are known to be poorly soluble in physiological solutions and produce non-fluorescent aggregates (A. Wirz *et al.*, *Pharmazie*, 2002, **57**, 543; A. Kubin *et al.*, *Pharmazie*, 2008, **63**, 263). These phenomena can reduce its efficiency as a photosensitizer for the clinical application. In the present contribution, we have prepared, characterized, and studied the photochemical properties of Hy-loaded lipid nanocapsule (LNC) formulations. The amount of singlet oxygen ($^1O_2$) generated was measured by the use of *p*-nitroso-dimethylaniline (RNO) as a selective scavenger under visible light irradiation. Our results showed that Hy-loaded LNCs suppressed aggregation of Hy in aqueous media, increased its apparent solubility, and enhanced the production of singlet oxygen in comparison with free drug. Indeed, encapsulation of Hy in LNCs led to an increase of $^1O_2$ quantum yield to 0.29–0.44, as compared to 0.02 reported for free Hy in water. Additionally, we studied the photodynamic activity of Hy-loaded LNCs on human cervical carcinoma (HeLa) and Human Embryonic Kidney (HEK) cells. The cell viability decreased radically to 10–20% at 1 μM, reflecting Hy-loaded LNC25 phototoxicity.

Received 25th May 2013
Accepted 20th August 2013

DOI: 10.1039/c3nr02724d

www.rsc.org/nanoscale

Introduction

Photodynamic therapy (PDT) has emerged in recent years as a non-invasive therapeutic modality for the treatment of various cancers and particularly for the treatment of superficial tumours (*e.g.* oesophagus, bladder, and melanoma).[3] PDT is based on the combined use of a photosensitizer (PS), oxygen and suitable light radiation penetrating many tissues. Taken separately, these three elements are harmless. The photosensitizing substance is designed to concentrate selectively in the tissue to be treated. The radiation then triggers a reaction that will cause a sufficient photodynamic oxidative stress leading to cell death, resulting from necrosis or apoptosis. Indeed, the reaction produces reactive oxygen species (ROS), such as highly reactive singlet oxygen ($^1O_2$) and other free radicals with cytotoxic effects. Other effects observed on blood vessels and the immune response involved in the destruction of the injury enhance the efficacy of PDT *in vivo* and contribute to the long-term control.[4] PDT has many advantages and is an alternative to conventional therapies for cancer treatment.[5–8]

Photosensitizers are most frequently classified as porphyrin-based or nonporphyrin-based molecules.[9] Hematoporphyrin derivatives are among the first generation PS and have been successfully used as PDT agents in the area of oncology. Many other photosensitizers, chemically pure and more efficient, have been designed to overcome the problems of the first generation PS agents.[9] An ideal PS should be stable in its pure form with minimal toxicity in the absence of light exposure. Absorption of light in the red region (>600 nm) with high singlet oxygen quantum yield is required to buck for maximum light penetration and production of ROS. Moreover, selective accumulation of the sensitizer in tumor tissue is essential for targeted therapeutic efficiency.[9–11]

Hypericin (Hy, Fig. 1), St. John's wort extract natural PS, has many advantages. Hy displays strong fluorescence (important for imaging), has a large quantum yield and does not induce toxicity without irradiation (no side effects up to 2 mg per day). Moreover, Hy can be activated at a wavelength around 600 nm, which penetrates more deeply without damaging the tissue constituents such as DNA or proteins. As most photosensitizers, Hy is highly hydrophobic and can easily aggregate in aqueous media.[1,2] The strong interactions between photosensitizer molecules through hydrophobic interactions can affect their photophysical (decrease of $^1O_2$ formation), chemical (decrease

[a]*Institut de Recherche Interdisciplinaire (IRI), USR CNRS 3078, Université Lille 1, Parc de la Haute Borne, 50 Avenue de Halley, BP 70478, 59658 Villeneuve d'Ascq, France. E-mail: rabah.boukherroub@iri.univ-lille1.fr; Fax: +33 3 62 53 17 01; Tel: +33 3 62 53 17 24*

[b]*Laboratoire de Spectrochimie Infrarouge et Raman, UMR CNRS 8516, Université Lille 1, 59655 Villeneuve d'Ascq, France*

[c]*Laboratoire de Physique des Lasers, Atomes et Molécules, UMR CNRS 8523, Université Lille 1, 59655 Villeneuve d'Ascq, France*

† Electronic supplementary information (ESI) available. See DOI: 10.1039/c3nr02724d

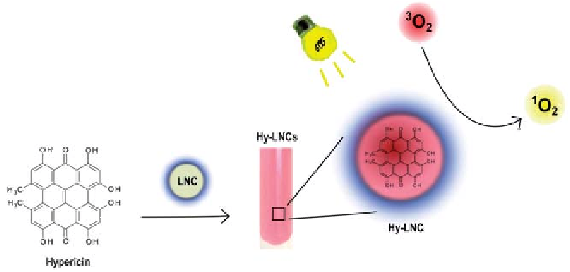

Fig. 1 Chemical structure of hypericin (Hy) and its encapsulation in lipid nanocapsules (LNCs).

of the solubility) and biological properties. It is thus mandatory to use delivery systems to overcome most of the short-comings associated with the classical photosensitizers. Therefore, in recent years, there has been huge progress in the development of new delivery systems.[12,13] The use of biodegradable or non-biodegradable nanocarriers for photosensitizers is a very attractive pathway because these delivery systems can overcome limitations of PS agents like poor aqueous solubility and selectivity.[10,14–16] Hypericin incorporation into nanoparticles allows the systemic administration of this hydrophobic and insoluble molecule under acceptable physiological conditions and may be assessed for photodiagnostic and photodynamic therapy.

Although several delivery systems have been reported for Hy and other photosensitizers,[12] to the best of our knowledge there is no investigation on the encapsulation of photosensitizers reported in lipid nanocapsules (LNCs). LNCs belong to this generation of stealth colloidal carriers.[17] These nanocapsules are obtained without organic solvents and with pharmaceutically acceptable excipients. Such nanocapsules present a stable monodisperse size distribution and their mean diameter can be well-controlled in the range of 20–95 nm.[18] They are made up of an oily liquid triglyceride core surrounded by a hydrophilic surfactant, Solutol® HS15, which exposes a medium PEG chain containing an average of 15 ethylene glycol units conferring long-circulating properties[19] and inhibiting the P-glycoprotein efflux pump (P-gp).[20,21] The rationale behind this approach is to improve the aqueous solubility and delivery, and to increase phototoxicity efficacy by nanoencapsulation of Hy. Indeed, Hy-loaded polylactic acid (PLA) nanoparticles (NPs) induced a higher photoactivity than free drug *in vitro* on the NuTu-19 ovarian cancer cell model derived from Fischer 344 rats.[22] Moreover, nanoencapsulation of Hy in PLA allowed the *in vivo* fluorescence photodetection of ovarian metastases in Fischer 344 rats bearing ovarian tumors and the results showed an improved selective accumulation of Hy in malignant ovarian tissues when NPs were used.[23] Therefore, LNCs seem to be an alternative and attractive approach for controlled delivery of Hy.

In this work, we report on Hy encapsulation in lipid nanocapsules. Hy-loaded LNCs were prepared by a phase inversion process in a size range of 25–100 nm. The resulting nanocapsules were characterized in terms of size, charge and drug loading. Finally, the influence of lipid nanocapsules' size and Hy loading on the production of singlet oxygen and the *in vitro* phototoxicity of the encapsulated Hy in comparison with free drug were evaluated on human cervical carcinoma (HeLa) and Human Embryonic Kidney (HEK) cells.

Experimental section

Materials

Hypericin (Hy, purity >99%) was provided by Planta Natural Products (Wien, Austria). A stock solution of Hy was prepared in dimethylsulfoxide at 10 mM and stored at −20 °C in the dark. Labrafac™ Lipophile WL 1349 (caprylic/capric triglyceride), Phospholipon® 90G (soybean lecithin at 97.1% of phosphatidylcholine), and Solutol® HS15 (a mixture of free polyethylene glycol 660 and polyethylene glycol 660 hydroxystearate) were generously provided by Gattefosse S.A.S. (Saint-Priest, France), Phospholipid GmbH (Köln, Germany), and Laserson (Etampes, France), respectively. Deionized water was obtained from a Milli-Q plus system (Millipore, Paris, France). ER-Tracker™ Blue-White DPX and MitoSOX™ Red were purchased from Life Technologies (Grand Island, USA). Methylene Blue (MB) and all other chemical reagents and solvents were obtained from Sigma-Aldrich (Saint-Quentin Fallavier, France).

Lipid nanocapsule preparation

Hy was mixed with Labrafac prior to all the preparation steps. Thereafter, LNCs were formulated at nominal sizes of 25, 50, and 100 nm using a phase inversion method of an oil–water system, as described by Heurtault.[17] Briefly, the oil phase was mixed with appropriate amounts of Solutol, Phospholipon 90G, NaCl and distilled water, and heated under magnetic stirring up to 85 °C. The mixture was subjected to 3 temperature cycles from 70 to 90 °C under magnetic stirring. Then it was cooled to 78 °C and 3.3 mL of distilled cold water (0 °C) were added. The resulting suspension was stirred at room temperature for another 10 min before further use. The different compositions of the formulations are displayed in Table 1. The percentage composition of Hy is just the total initial mass percentage of the components for the lipid nanocapsules (1.26 g).

Particle size, zeta potential, UV-Vis and fluorescence measurements

LNCs were characterized in terms of size, charge and drug loading. The average diameter and polydispersity index (PI) were determined by dynamic light scattering using a Zetasizer® Nano ZS (Malvern Instruments S.A., Worcestershire, UK). The

Table 1 Composition of the components for the lipid nanocapsule preparation for a total initial mass of 1.26 g. 25, 50 and 100 stand for the average diameter in nm

	Labrafac (%)	Solutol (%)	Phospholipon 90G (%)	NaCl (%)	Water (%)
LNC25	20.0	32.4	3.0	1.7	42.9
LNC50	33.3	19.1	3.0	1.7	42.9
LNC100	40.0	12.4	3.0	1.7	42.9

View Article Online
Paper Nanoscale

zeta potential was measured using the electrophoretic mode with the Zetasizer®. All the batches were diluted at 1/100 (v/v) in distilled water (filtered over 0.22 μm) prior to the analysis and analyzed in triplicate. UV-Vis spectroscopic measurements were carried out on a Perkin Elmer Lambda 950 dual beam spectrophotometer operating at a resolution of 1 nm in a 1 cm spectrometric cuvette. Fluorescence spectra were recorded using a HORIBA Jobin Yvon IHR 320 spectrometer coupled with a microscope upon excitation of the 480 nm line of an argon laser (10 mW) for 10 s at room temperature. The laser beam was focused onto the liquid with a 10× microscope objective, which produces a beam waist of ~1.5 μm on a lens filled with solutions (400 μL).

Drug loading and encapsulation efficiency

The drug loading was directly determined by reversed phase-high performance liquid chromatography (RP-HPLC). RP-HPLC analyses were realized on a Shimadzu LC2010-HT (Shimadzu, Tokyo, Japan). A 5 μm C_4 QS Uptisphere® 300 Å, 250 × 4.6 mm column (Interchim, Montluçon, France) was used as the analytical column. The column was heated to 40 °C. The mobile phase was a mixture of eluent A (trifluoroacetic acid 0.05% in H_2O) and eluent B (trifluoroacetic acid 0.05% in CH_3CN) at a flow rate of 1 mL min^{-1}. The linear gradient was 0% to 80% of eluent B in 30 min and detection was performed at 590 nm. A 10 mM stock solution of Hy was prepared in dimethylsulfoxide for the calibration curve. Concentrations of 5–50 μM of Hy in dimethylsulfoxide were prepared from this stock. Each sample was injected (40 μL) into the RP-HPLC column. Calibration curves were obtained by linear regression of drug concentration (μM) *versus* the peak area and are shown in Table 2.

For the determination of Hy encapsulation rates, LNCs were separated from the supernatant using disposable PD-10 desalting columns (Sephadex® G-25 for gel filtration as the stationary phase, Amersham Biosciences). The column was stabilized with 25 mL of distilled water. Then 1 mL of the LNC suspension was deposited on the column and 1.5 mL of water were added to fill in the dead volume of the column. Finally, the LNCs were collected with 4 mL of distilled water as eluent. We measured Hy concentrations by RP-HPLC before and after filtration to determine the encapsulation efficiency (EE) using eqn (1).

$$\mathrm{EE}(\%) = \frac{[\mathrm{Hy}]_{\mathrm{LNC}}}{[\mathrm{Hy}]_{\mathrm{TOTAL}}} \times 4 \times 100\% \quad (1)$$

where $[Hy]_{LNC}$: amount of Hy loaded in the LNCs; $[Hy]_{TOTAL}$: total Hy amount in LNC suspension; dilution factor of gel filtration = 4.

Table 2 Calibration curves and linear regression of Hy

Compounds	Retention time	Regression equation[a]	k_{drug}	Linear range	r^{2b}
Hy	26.6 min	$Y = 75\,034X$	75 034	5–50 μM	0.999

[a] Equation, where Y is the peak area and X is the concentration of compounds. [b] Correlation coefficient ($n = 5$).

Drug leakage and stability

The drug leakage and stability experiments were performed by placing filtered LNCs at 4 °C in the dark for one month. Samples were evaluated for their drug content as well as any changes in their physical appearance. After gel filtration, the amount of Hy was determined by RP-HPLC similar to the encapsulation efficiency as described above. For the physical stability, we measured the mean diameter and polydispersity by DLS. All measurements were performed in triplicate.

Detection of singlet oxygen

The *p*-nitroso-dimethylaniline (RNO)-bleaching method was used to measure the relative $^1O_2$ generation efficiency of Hy-loaded LNCs.[24,25] The $^1O_2$ generation efficiency was followed by the bleaching of RNO at 440 nm with the transannular peroxide intermediate formed as a result of the reaction between singlet oxygen and imidazole. The solution containing the medium alone as a negative control, blank LNCs, MB, Hy alone or Hy-loaded LNCs was prepared in the presence of imidazole (8 mM) and RNO (12.5 μM) in a 50 mM phosphate buffer (pH = 7.4). Samples in a 1 cm spectrometric cuvette, placed at a distance of 1.8 cm, were irradiated at room temperature in air through a long pass filter ($\lambda = 420$ nm, to suppress the light with wavelength shorter than 420 nm) for 60 min using a visible lamp (Spot Light Source 400–700 nm, L9566-03, Hamamatsu, Japan). The intensity of the light was measured using a PM600™ Laser Fiber Power Meter (Coherent Inc., USA) and was determined to be 0.59 W. The decrease of the absorbance caused by RNO bleaching was monitored spectrophotometrically on a Perkin Elmer Lambda 950 dual beam spectrophotometer operating at a resolution of 1 nm in the region of 350–550 nm. All measurements were performed in duplicate. In order to estimate the $^1O_2$ quantum yield of Hy-loaded LNC aqueous formulations, the natural logarithm values ($\ln A/A_0$) of RNO at 440 nm were plotted *vs.* the photoirradiation time and fitted with a pseudo-first-order kinetic model. The $^1O_2$ quantum yield of Hy-loaded LNCs in aqueous solution can be estimated using methylene blue (MB) as a standard ($\Phi_{MB} = 0.52$ in aqueous solution)[26] using eqn (2).[27]

$$\Phi_{\mathrm{LNC}} = \Phi_{\mathrm{MB}} \frac{k_{\mathrm{LNC}}}{I_{\mathrm{LNC}}} \frac{I_{\mathrm{MB}}}{k_{\mathrm{MB}}} \quad (2)$$

where Φ_{MB}: the $^1O_2$ quantum yield of MB in aqueous solution as a standard; k_{LNC} and k_{MB}: the rate constants for photoreaction of RNO with Hy-loaded LNCs and MB, respectively; I_{LNC} and I_{MB}: light absorbed by Hy-loaded LNCs and MB in aqueous solution, respectively, which are estimated by integration of the absorption bands in the region of 420–700 nm.

Cellular localization

The HeLa (cervix carcinoma, human) cells were maintained in DMEM supplemented with 10% (v/v) fetal-calf serum (FCS) and penicillin/streptomycin in a 5% CO_2 atmosphere at 37 °C. Cells were seeded on round glass coverslips into 12-well plates (2×10^5 cells per 1 mL media per well) 48 h before experiments. Cells

were washed with PBS, maintained in serum-free medium and incubated for 5 h in a CO_2 atmosphere at 37 °C in the presence of 1 μM Hy in PBS–DMSO (<1%) or 1 μM 0.04% Hy-loaded LNC25. After incubation, the cells were washed three times with PBS and then maintained in DMEM supplemented with 10% FBS with 1 μM of ER-Tracker Blue-White DPX for 20 min or 5 μM of MitoSOX Red for 10 min at 37 °C. After incubation, the stained cells were washed three times with PBS, and fixed with 4% paraformaldehyde at room temperature for 15 min. The fixed cells were then washed three times with PBS, mounted and observed using a Nikon A1-R (Nikon Instruments, Tempe, AZ) laser confocal microscope (Nikon 60× Oil) excited at 561 nm and 404 nm, respectively.

Cell culture and *in vitro* phototoxicity

The HeLa (cervix carcinoma, human) and HEK (Human Embryonic Kidney) cells were maintained in DMEM supplemented with 10% (v/v) fetal-calf serum (FCS) and penicillin/streptomycin in a 5% CO_2 atmosphere at 37 °C. Cells were seeded into 96-well plates (1×10^4 cells/100 μL media per well) 48 h before experiments. Prior to incubation, cells were washed with PBS. The medium was replaced with 100 μL of serum-free medium containing blank LNC25, free Hy at 0.25, 0.5, and 1 μM in PBS–DMSO (<1%), and 0.04% Hy-loaded LNC25 at 0.25, 0.5, and 1 μM. After 8 h incubation, cells were washed three times with PBS and then maintained in DMEM supplemented with 10% FCS. Cells were irradiated through a long pass filter ($\lambda =$ 420 nm, to suppress the light with wavelength shorter than 420 nm) for 12 min using a visible lamp (Spot Light Source 400–700 nm, L9566-03, Hamamatsu, Japan). The intensity of the light was measured using a PM600™ Laser Fiber Power Meter (Coherent Inc., USA) and was determined to be 10 mW. Light positive controls (with blank LNCs or without Hy) and dark controls (with and without Hy) were included. After 18 h at 37 °C, cell viability was colorimetrically measured by performing MTT assays. After removing the medium and washing by PBS, 100 μL of MTT solution (1 : 10 dilution of the 5 mg mL^{-1} fresh MTT stock solution in PBS) were added. After incubation for another 3 h, the resulting formazan dye was dissolved in dimethylsulfoxide (50 μL) and the absorbance intensity was measured by a microplate reader (PHERAstar FS, BMG LABTECH GmbH, Germany) at 570 nm with background subtraction at 650 nm. The cell viability was determined as the percentage of live cells per total non-treated cells.

Live cell irradiation and imaging by video-microscopy

The HeLa and HEK cells were maintained in DMEM supplemented with 10% (v/v) fetal-calf serum (FCS) and penicillin/streptomycin in a 5% CO_2 atmosphere at 37 °C. Cells were seeded into a 35 × 10 mm cell culture dish (1×10^5 cells per 2 mL per well) 48 h before experiments. Prior to incubation, cells were washed with PBS. The medium was replaced with 2 mL of serum-free medium containing 0.04% Hy-loaded LNC25 at 1 μM. After 2.5 and 5 h incubation, cells were washed three times with PBS and then maintained in DMEM supplemented with 10% FCS. For video-microscopy experiments, cells were kept under normal physiological conditions. For this purpose, a temperature-controlled and atmosphere (CO_2, N_2 and O_2)-regulated incubator was designed. The cells were irradiated by using a mercury lamp with a 580 nm bandpass filter (10 nm full width at half maximum) in order to match the absorption spectrum of Hy. All experiments were performed with a 10× phase-contrast objective. The size of the image (568 × 758 mm^2) permits the observation of more than 200 cells. One hundred cells were typically irradiated within the light spot (320 μm FWHM) with a power of 9 μW (at 580 nm) for 15 min. The whole field image was detected using a CCD camera and the time-lapse lasted for 14 h with an image taken every 15 min. Cells lying outside the mercury lamp spot provided a control sample. In order to characterize the cell death during video-microscopy experiments, cells were incubated with Annexin-V-Fluorescein in a Hepes buffer containing PI (propidium iodide) (Annexin-V-FLUOS Staining Kit, Roche). Annexin-V binds in a Ca^{2+} dependent manner to negatively charged phospholipid surfaces, and shows high specificity for phosphatidylserine. Therefore, it stains apoptotic and necrotic cells. Propidium iodide stains only the DNA of leaky necrotic cells and allows for a distinction between apoptotic and necrotic cells.

Results and discussion

Preparation and characterization of Hy-loaded LNCs

Hy, a natural photosensitizer (PS) extracted from *Hypericum perforatum*, displays a complex chemical structure as depicted in Fig. 1. Hy formulation was achieved by mixing with excipients at optimized concentrations using the phase inversion method as described above.[17] This method offers a good control over the nanocapsules' size (25, 50 and 100 nm) with monodisperse size characteristics (PI < 0.20) (Table 3). Hy was entrapped in the LNCs with high encapsulation efficiency (>93%) due to the poor solubility of Hy in water. Moreover, its stability was confirmed through the heat cycles required to produce Hy-loaded LNCs with 99% remaining intact at the end of the cycling process. The physicochemical properties of Hy-LNCs are quasi-identical to the blank LNCs, and the presence of the Hy had no effect on the mean diameter and the polydispersity index. However, the zeta potential values of Hy-loaded LNCs were more negative (0.02% Hy-loaded LNCs: −14.6 to −15.0 mV; 0.04% Hy-loaded LNCs: −21.3 to −29.1 mV) as compared to blank LNCs (−4 to −0.5 mV). The net negative charge of blank LNCs seems to be in agreement with the negatively charged phospholipids incorporated into the surface of LNCs. Zeta potential values of Hy-loaded LNCs decreased with increasing Hy loading. In spite of the high hydrophobicity of Hy, the amphiphilic molecules were preferentially located in the layers near the membrane/water interface.[28,29] In view of the results, it seems probable that Hy is arranged at the interface between the oil phase and the hydrophilic polyethylene glycol moieties of the surfactant as shown previously with amiodarone-[30] and quercetin loaded LNCs.[31]

The absorption spectrum of Hy is solvent dependent.[32–34] As observed in Fig. 2, the UV/Vis absorption spectrum of Hy dissolved in DMSO shows an intense band at 599.5 nm and a less intense band at 555.0 nm. The shape of the absorption spectra

View Article Online
Paper Nanoscale

Table 3 Characterization of Hy-loaded lipid nanocapsules

	Hy (%)	Mean diameter (nm)	PI[a]	Zeta potential (mV)	EE (%)
LNC25	0	23.9 ± 0.8	0.054 ± 0.012	−4.0 ± 3.6	0
	0.02	32.6 ± 1.0	0.062 ± 0.011	−14.6 ± 1.9	99 ± 2.7
	0.04	23.6 ± 0.7	0.210 ± 0.010	−24.5 ± 2.1	100 ± 1.0
LNC50	0	53.1 ± 1.2	0.088 ± 0.012	−0.5 ± 0.1	0
	0.02	56.7 ± 1.0	0.091 ± 0.003	−15.0 ± 0.8	98 ± 1.8
	0.04	51.2 ± 0.6	0.055 ± 0.002	−21.3 ± 1.5	98 ± 0.4
LNC100	0	91.8 ± 8.5	0.123 ± 0.006	−1.4 ± 0.1	0
	0.02	76.0 ± 4.3	0.181 ± 0.016	−8.9 ± 0.6	99 ± 0.4
	0.04	109.6 ± 14.4	0.162 ± 0.022	−29.1 ± 0.2	93 ± 7.6

[a] Polydispersity index, mean ± SD, $n = 3$.

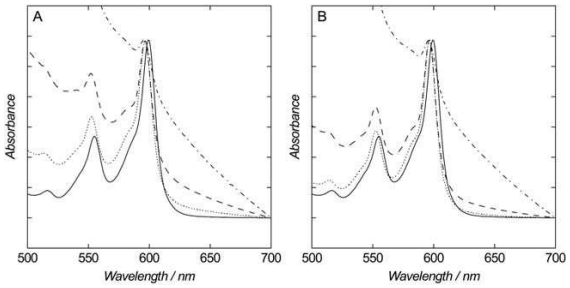

Fig. 2 Absorption spectra between 500 and 700 nm of Hy dissolved in DMSO (continuous line), Hy-loaded LNC25 (dotted line), Hy-loaded LNC50 (dashed line) and Hy-loaded LNC100 (dash-dotted line) at 0.02% (A) and 0.04% (B).

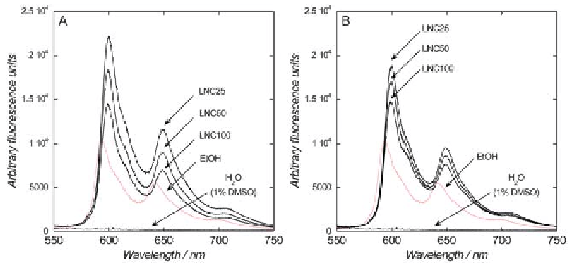

Fig. 3 Fluorescence emission spectra between 550 and 750 nm of 25 μM free Hy dissolved (1% DMSO/water) and ethanol, and Hy-loaded LNC25, Hy-loaded LNC50 and Hy-loaded LNC100 at 0.02% (A) and 0.04% (B) in water. The emission spectra were obtained using an excitation wavelength at 480 nm.

of Hy-loaded LNCs is identical to that of free Hy in DMSO with the exception of a small hypsochromic shift (3 nm) due to the different molecular environments surrounding the Hy molecule. A major influence of the UV/Vis absorption measurements is turbidity due to suspended LNCs that cause light scattering. Thus, it is interesting to note that turbidity increased with increasing the LNC size and affected significantly the UV/Vis spectra of Hy-loaded LNC100.

The effect of encapsulation on the solubility and aggregation of Hy was investigated by fluorescence spectroscopy using an argon laser ($\lambda_{exc} = 480$ nm, 10 mW, $t = 10$ s). Hy is soluble in polar solvents, whereas it is insoluble in non-polar solvents. The fluorescence emission spectra of 25 μM free Hy solutions in different solvents at room temperature are displayed in Fig. 3. When 1% DMSO/water was used as the solvent, no fluorescence was observed. This is most likely due to self-quenching of aggregated Hy. In pure ethanol, Hy displays two emission bands located at 594 and 642 nm, in accordance with previously reported data.[34] Compared to ethanolic solution of free Hy, the fluorescence bands are 6 nm red shifted when the molecules are encapsulated in the lipidic environment of LNCs. This result is in accordance with the entrapment of Hy in liposomes.[35] Interestingly, Hy-loaded LNCs exhibits higher fluorescence intensity for both 0.02 and 0.04% Hy-loaded LNCs at the same concentration compared to ethanol solution of free Hy. However, increasing the size of LNCs from 25 to 100 nm or the loading from 0.02 to 0.04% induced a slight decrease of the emission intensity. The results suggest that Hy encapsulation in the lipidic nanocapsules enhances its solubilisation and the fluorescence emission is predominated by the monomeric form of Hy molecules inside the nanocapsules.

The bar diagram in Fig. 4 depicts the percentage of Hy leakage from 0.02% and 0.04% Hy-loaded LNCs over one month at 4 °C. The 25 nm Hy-loaded LNCs showed a negligible loss (<1%) and ~4% for the 0.04 and 0.02% Hy-loaded LNCs, respectively. The most important loss (~12%) was observed for

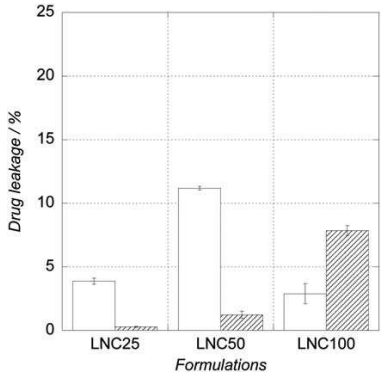

Fig. 4 Drug leakage rates of 0.02% (white) and 0.04% Hy-loaded LNCs (diagonal lines) in the dark after one month storage at 4 °C.

50 nm diameter Hy-loaded LNCs at 0.02% loading. Nevertheless, after these low initial burst releases, the formulations remain physically and chemically stable at 4 °C in the dark up to 18 months with quantitative drug loading (data not shown).

Generation of singlet oxygen

The detection of singlet oxygen was evaluated by spectrophotometric measurement of *p*-nitroso-dimethylaniline (RNO) bleaching by monitoring the absorbance decrease at 440 nm. In a control experiment where blank LNCs were irradiated for 60 min at $\lambda > 420$ nm, no generation of singlet oxygen was detected with concentrations up to 0.72 mg mL^{-1} (data not shown).

Influence of LNC size and Hy loading on singlet oxygen generation

To evaluate the effect of the LNC size on the singlet oxygen generation efficiency, three batches of 0.04% Hy-loaded LNCs with various average diameters (LNC25, LNC50 and LNC100) were tested with the RNO-bleaching method and were compared to free Hy. The nanocarriers containing Hy at 0.5 and 1 μM were irradiated as a function of time. For all tested formulations, the amount of singlet oxygen produced (*i.e.* Δ-absorbance at 440 nm) by 0.04% Hy-loaded LNCs after 60 min irradiation is displayed in Fig. 5.

As shown in Fig. 5A and B, the amount of singlet oxygen increased with illumination time for all investigated formulations. 0.04% Hy-loaded LNC25 exhibited the highest production yield of singlet oxygen compared to LNC50 and LNC100 even though the difference is not very significant. At a Hy concentration of 1 μM, 0.04% Hy-loaded LNCs exhibited a 1.25 fold higher production yield of singlet oxygen than 0.5 μM. The amount of singlet oxygen produced by 0.04% Hy-loaded LNCs and different concentrations of free Hy after 60 min irradiation is displayed in Fig. 6A and B, respectively. One clearly sees that encapsulated Hy is more efficient (10–40 fold) for singlet oxygen generation than free Hy.

In the LNCs, the hydrophobic molecular environment of Hy most likely limited or suppressed its aggregation and water-induced quenching of singlet oxygen. Thus, singlet oxygen is generated without release of Hy directly from the nanocapsules and the level of active singlet oxygen is higher than free Hy. To evaluate the influence of drug loading on singlet oxygen generation, batches of 0.02% Hy-loaded LNCs were tested using the RNO-bleaching method. As shown in Fig. S1,† modulation of LNC drug loading did not influence the amount of singlet oxygen produced. 0.02% Hy-loaded LNCs exhibited a comparable production yield of singlet oxygen than 0.04% Hy-loaded LNCs whatever the size of the nanocapsules. This suggests that Hy was perfectly dissolved in the oily core of LNCs.

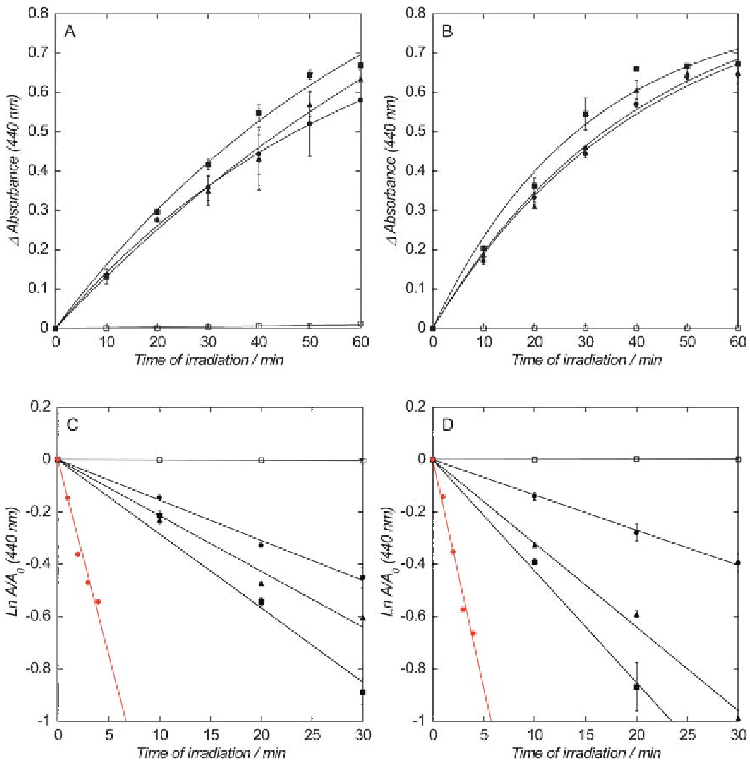

Fig. 5 Generation of singlet oxygen (Δ*A* at 440 nm) (A and B) and pseudo-first order plots of $\ln(A/A_0)$ (C and D) from photo-irradiated free Hy (DMSO 1%), MB and 0.04% Hy-loaded LNCs at 0.5 μM (A and C) and 1 μM (B and D) in a 50 mM phosphate buffer (pH = 7.4) as a function of irradiation time. Open squares, free Hy; black squares, LNC25; black triangles, LNC50; black circles, LNC100; red circles, MB.

View Article Online
Paper Nanoscale

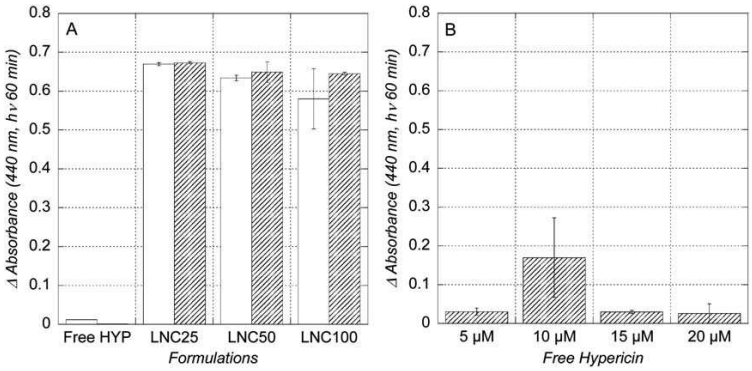

Fig. 6 Generation of singlet oxygen (ΔA at 440 nm, irradiation time: 60 min) from photo-irradiated free Hy (DMSO 1%) and 0.04% Hy-loaded LNCs at 0.5 μM (white) and 1 μM (diagonal lines) in a 50 mM phosphate buffer (pH = 7.4) (A) in comparison with photo-irradiated free Hy (DMSO 1%) at 5, 10, 15 and 20 μM (B) in a 50 mM phosphate buffer (pH = 7.4).

Singlet oxygen quantum yield of Hy-loaded LNCs

The quantum yield of singlet oxygen generation of Hy-loaded LNCs was estimated using the comparative method where MB was used as a standard photosensitizer reference ($\Phi_{MB} = 0.52$).[26] As described above, the depletion of RNO by $^1O_2$ was monitored at 440 nm and plots of $\ln(A/A_0)$ as a function of irradiation time can be fitted with a pseudo-first order reaction (Fig. 5C and D). The rate of singlet oxygen generation was obtained from the slope of the pseudo-first-order plots. A similar plot was obtained for MB as a standard photosensitizer reference and the $^1O_2$ quantum yields of Hy-loaded LNCs in aqueous solution were estimated using eqn (2).[27] The results are summarized in Table 4.

The quantitative estimation of $^1O_2$ generation varies in the range of 0.29–0.44 by comparing the first-order reaction rate constants of RNO bleaching with Hy-loaded LNCs and MB. The quantum yields of Hy-loaded LNCs at 1 μM are nearly similar (0.3–0.6). The values are much higher than $\Phi = 0.02$ reported for free Hy in water,[36] and compare well with the quantum yields of 0.35–0.43 reported for $^1O_2$ generation by Hy entrapped in liposomes.[37–39] Thus, the lipid nanocapsules seem to be a good alternative to solubilize Hy.

Photobleaching of Hy-loaded LNCs

The photobleaching phenomenon refers to a decrease of absorbance and/or fluorescence of the sensitizer exposed to light without the emergence of new peaks. On the one hand, the sensitizer should not be deteriorated too quickly to obtain an efficient elimination of the tumor. On the other hand, the interest in controlled photodegradation is the destruction of the remaining photosensitizer after treatment in order to limit the photosensitivity of the patients following PDT treatment.[40] The kinetics of photobleaching of 0.04% Hy-loaded LNCs in phosphate buffer was followed by spectrophotometric analysis. The results of photobleaching of Hy by irradiation of 0.04% Hy-loaded LNC25 at 10 μM in 50 mM phosphate buffer as a function of time are displayed in Fig. 7A. They indicate a continuous decrease in absorbance of the bands at around 386, 479, 553 and 596 nm without the appearance of new bands. These modifications in absorbance suggest phototransformation and photodestruction of Hy under irradiation over time. The results were compared to those obtained upon illumination of 0.04% Hy-loaded LNC50 and free Hy in DMSO. As shown in Fig. 7B, the rate of Hy photobleaching is faster when it is encapsulated in LNCs. Moreover, the photodegradation of Hy is faster when encapsulated in the smaller LNCs.

The photodegradation of the remaining Hy inside LNCs is beneficial during PDT treatment to reduce the photosensibility of the patients. Thus, the modification of the LNC size can be used to modulate the efficiency of tumor destruction *versus* photosensibility.

Table 4 Pseudo-first-order kinetic parameters and quantum yields of $^1O_2$ determined at 0.5 μM for Hy-LNCs

	Hy (%)	Rate constant k_{obs} (min $^{-1}$)	Quantum yield Φ^b
LNC25	0.02	−0.0245 ± 0.0035	0.29 ± 0.04
	0.04	−0.0300 ± 0.0011	0.41 ± 0.01
LNC50	0.02	−0.0228 ± 0.0030	0.44 ± 0.06
	0.04	−0.0193 ± 0.0009	0.37 ± 0.02
LNC100	0.02	−0.0125 ± 0.0013	0.30 ± 0.03
	0.04	−0.0145 ± 0.0033	0.35 ± 0.08
MB	—	−0.1411	0.52[a]

[a] Literature value[26] [b] mean ± SD, $n = 2$.

Cellular localization

To ascertain the intracellular localization of free Hy and 0.04% Hy-loaded LNCs, confocal microscopy was performed using dual staining methods. As shown in Fig. 8, free Hy (1 μM) following 5 h incubation exhibited partial co-localization with the endoplasmic reticulum (ER) and mitochondria. For a long incubation period as tested here, the mitochondria accumulation appeared diminished.[41] Furthermore, free Hy appears accumulated in cell membranes. The hydrophobic nature of the free molecule allows preferential diffusion across the plasma membrane and accumulation in other intracellular membranes.[42] Co-staining images of HeLa cells with 0.04%

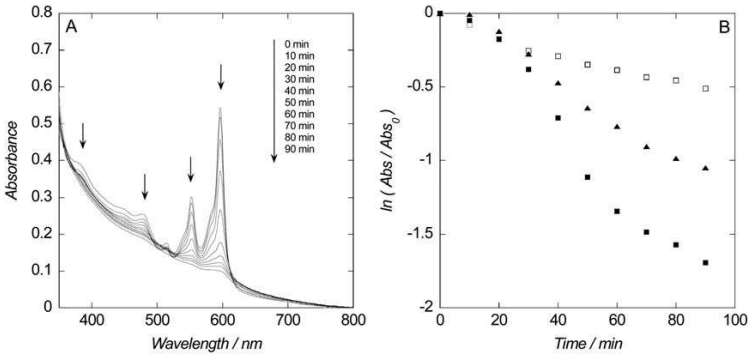

Fig. 7 Effect of photoillumination on the absorption spectrum of 0.04% Hy-loaded LNC25 at 10 μM in 50 mM phosphate buffer as a function of irradiation time (A). Rate of change of maximum absorbance of Hy dissolved at 10 μM in DMSO and 0.04% Hy-loaded LNCs at 10 μM in 50 mM phosphate buffer as a function of irradiation time (B). Open squares, free Hy; black squares, LNC25; black triangles, LNC50.

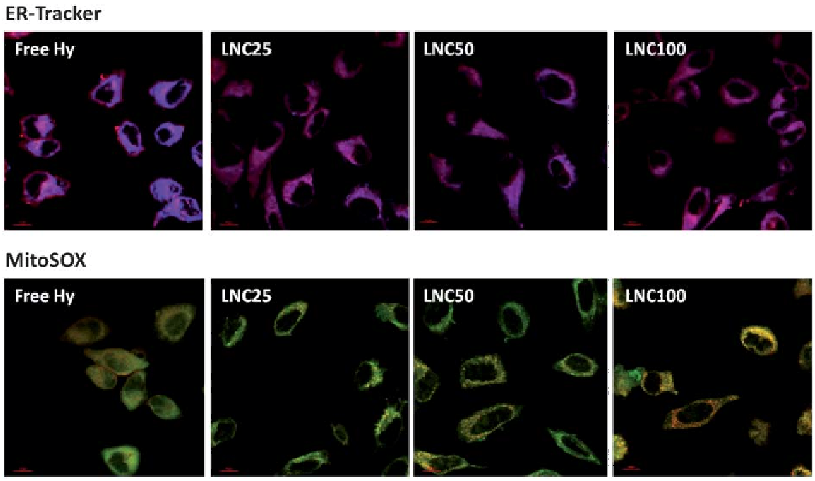

Fig. 8 Intracellular localization of free Hy and 0.04% Hy-loaded LNCs in HeLa cells. Confocal laser scanning microscopy images of HeLa cells double-stained with 1 μM Hy excited at 561 nm, 1 μM ER-Tracker excited at 404 nm and 5 μM excited at 488 nm. Objective magnitude is ×60. The scale bar represents 10 μm.

Hy-loaded LNCs (1 μM) and an endoplasmic reticulum-specific dye (ER-Tracker) revealed an identical overlap, indicating that all LNC formulations localized well in endoplasmic reticulum. This seems different for mitochondria where LNCs are less accumulated. However, a balance between passive diffusion and active transport pathway (such as endocytosis) appears to be preferential for free Hy and Hy-loaded LNCs, respectively, since images showed the vesicular localization. These results are in accordance with previous studies, which showed that LNCs were predominantly internalized by endocytosis.[43,44]

In vitro phototoxicity

The phototoxicity of Hy-loaded LNCs has been studied on human cervical carcinoma (HeLa) and Human Embryonic Kidney (HEK) cells. The cells were incubated in the presence of blank LNC25, 0.04% Hy-loaded LNC25, and free Hy in PBS–DMSO 1% (at 0.25, 0.5 and 1 μM in free-serum medium) and then irradiated using a visible fiber lamp at 420–700 nm for 12 min. Effects of photoillumination are shown in Fig. 9. After 1 day post-irradiation, the phototoxicity was determined by the MTT assay.

Dark controls (LNC25 with and without Hy) and positive controls (blank LNCs with irradiation) reveal a normal cell culture with a slight loss of cell viability due to cell detachment during washing, especially for HEK cells. It is important to note that, when cells are treated with Hy-loaded LNC25 without irradiation, there is no cell toxicity. The results indicate a relationship between the dose of Hy and the *in vitro* phototoxicity. The results showed that after 12 min visible light irradiation, both Hy-loaded LNC25 and free Hy can cause a significant loss of cell viability. The cell viability decreased radically to 50–60% and 10–20% (depending on the cell type) at 0.5 μM and 1 μM, respectively, reflecting Hy-loaded LNC25 phototoxicity. Tumor cells treated *in vitro* with free Hy showed the greatest loss of cell viability at 0.5 and 1 μM. Comparative studies with free and

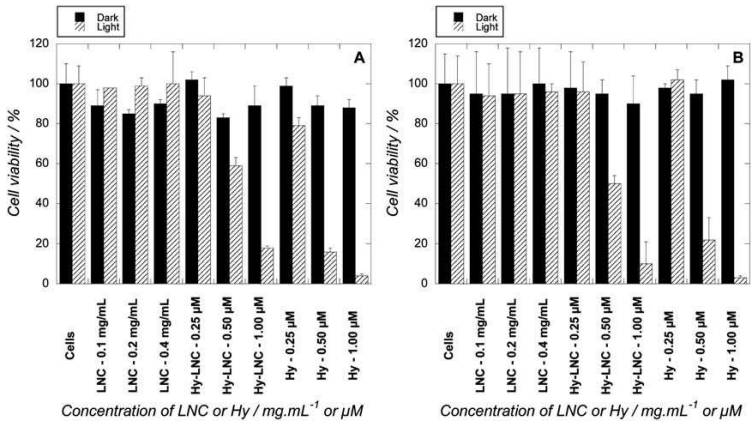

Fig. 9 *In vitro* phototoxicity of Hy and Hy-loaded LNC25. MTT assay data for cells, blank LNC25, 0.04% Hy-loaded LNC25 and free Hy at different concentrations in the dark or upon visible light irradiation (12 min at 10 mW cm^{-1}) on the HeLa cell culture (A) and on the HEK cell culture (B).

encapsulated Hy demonstrated that the photodynamic activity of free Hy was slightly higher than that of encapsulated Hy under the same conditions, which is possibly due to the difference in Hy internalization. It is likely that both diffusion and endocytosis participate in the uptake of Hy even if the more predominant mechanism seems to be the diffusion.[12] In contrast, for LNC uptake, endocytosis is the common pathway into the cell. This might explain the slightly lower activity of Hy-loaded LNCs as compared to free Hy. Since the primary mechanism of the PDT effect might be *via* tumor vasculature damage for Hy, it is more important to improve the circulation time of Hy *in vivo* in the protective delivery system. The results showed that Hy-loaded LNC25 would potentially be therapeutically active for *in vivo* PDT.

Live cell irradiation

In order to confirm the MTT assays, live cell irradiation was performed in order to characterize cell death with both HEK and HeLa cells incubated with 0.04% Hy-loaded LNC25 at 1 µM. In all these experiments, cells were irradiated at 580 nm with a power of ~9 µW for 15 min. The time-lapse lasted for ~14 h with an image taken every 15 min. Photos are shown in Fig. 10, and movies are provided in ESI Movies S1 and S2.† In order to evaluate the phototoxicity of 580 nm light, cells were irradiated without Hy for 15 min with a power of 9 µW. No cell death was detected up to 4.5 h post-irradiation (data not shown).

The first cell death appeared with both HEK and HeLa cells around 2.5 h post-irradiation and can be easily detected through morphological criteria. The cells first became rounder and appear luminous. When cells were dead, they did not move anymore, then cringe and become darker (see Fig. 10 and videos in the ESI†). The adherence of HEK cells was affected after the activation of Hy. In order to correlate those morphological criteria, HeLa cells were incubated with an Annexin-V-Fluorescein/PI assay (Fig. 11). The local intensity *I* of the 580 nm light spot can be precisely determined because its Gaussian intensity

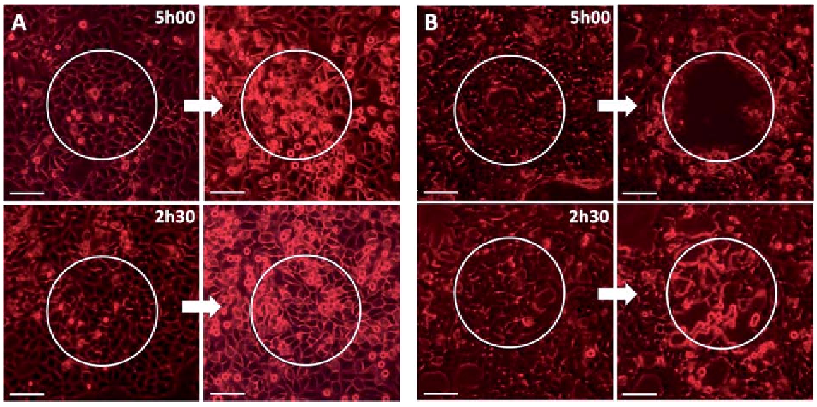

Fig. 10 Live cell irradiation and imaging by video-microscopy. Images of HeLa cell culture (A) and HEK cell culture (B) after incubation with 0.04% Hy-loaded LNC25 (2.5 h or 5 h) at 1 µM irradiated for 15 min at 580 nm (~9 µW) with a 320 µm FWHM light spot (represented with a white circle); before irradiation (left) and after 13.5 h post-irradiation (right). The scale bar represents 100 µm.

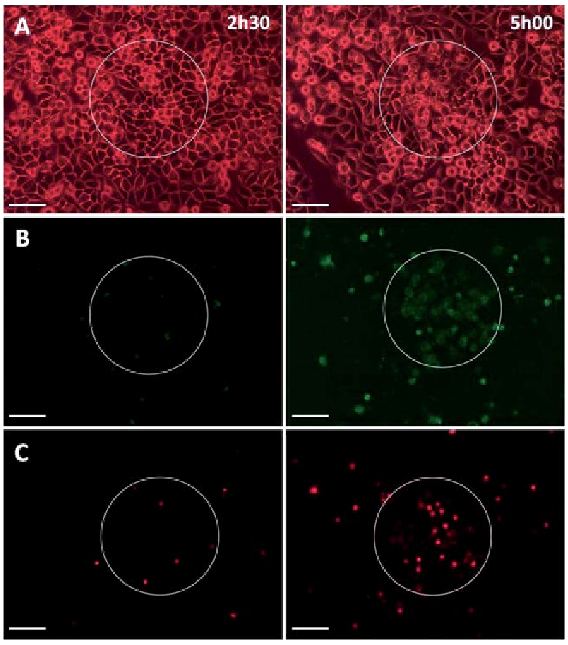

Fig. 11 Cell death analysis (apoptosis/necrosis) on HeLa cells. HeLa cells are irradiated at 580 nm ($P = 9$ μW, $t_{irr} = 15$ min) and analyzed 14 h post-irradiation. The cell death analysis is performed for $I = 11.2$ mW cm^{-2} represented with a black circle. The images are taken with a 10× phase contrast objective providing an image size of 568 × 758 mm^2; (A) cells imaged with white light, (B) Annexin-V fluorescence images, and (C) PI fluorescence images. From the Annexin-V staining (apoptotic and necrotic cells), one can evaluate the ratio of cell death counting cells in (A) and (B) providing the ratio of apoptotic/necrotic from (B) and (C) for 2.5 h incubation (left) and 5 h incubation (right). The cell death is strongly enhanced (up to ~50%) when cells are incubated for 5 h. Scale bar represents 100 μm.

profile is well known (320 μm FWHM). This means that one can evaluate the correlations between the light fluence $F = I \times T_{irr}$ (where T_{irr} is the irradiation time) and the cell death. For instance, for $F = 0.7$ mW cm^{-2} min^{-1} at 580 nm ($P = 9$ μW, 320 μm FWHM and $T_{irr} = 15$ min), one can estimate for HeLa cells incubated for 2.5 h, 8.4% of cell death, a little bit higher than the standard cell death culture (a few%). From Annexin-V/PI staining, one can evaluate 45% of apoptosis and 55% of necrosis. The cell death is strongly enhanced after 5 h incubation, reaching 48% of cell death with 70% of apoptosis and 30% of necrosis (Fig. 11).

In order to compare these results with the MTT assays (Fig. 9A), one has to take into account the spectral characteristics of the light excitation of Hy. In the MTT experiments, cells were irradiated with a 420–700 nm visible lamp matching the entire absorption spectrum of Hy (see Fig. 2). In the live cell irradiation, the excitation of Hy was performed at 580 nm leading to ~40% absorption (see Fig. 2). Taking the fluence of each experiment corrected with the efficiency of Hy excitation, one has to consider 20.1 mW cm^{-2} in order to compare both experiments. By analyzing the cell death on HeLa cells (Fig. 11) for such an intensity, one can find 68% of cell death (65% of apoptosis and 35% of necrosis) in good agreement with the MTT assay results.

Conclusion

We have demonstrated that lipid nanocapsules loaded with hypericin can be successfully used in photodynamic therapy experiments *in vitro*. The formulation method used provided hypericin-loaded LNCs in a size range from 25 to 100 nm with high entrapment yield and very low particle size polydispersity index. Hypericin incorporation into LNCs suppressed aggregation of Hy in aqueous media and increased its apparent solubility. The quantitative estimation of the $^1O_2$ quantum yield varies in the range of 0.29–0.44 which is much higher than 0.02 reported for free Hy in water,[36] suggesting that encapsulation in lipid nanocapsules is a good alternative to solubilize Hy. The photodynamic activity of Hy-loaded LNCs on human cervical carcinoma (HeLa) and Human Embryonic Kidney (HEK) cells showed a decrease of the cell viability to 50–60% and 10–20% at 0.5 μM and 1 μM, respectively. This study provides an *in vitro* proof of concept for using Hy-loaded lipid nanocapsules for PDT and holds promise for potential application of this system for *in vivo* PDT for cancer treatment due to a prolonged circulation time and accumulation in tumor-bearing mice.[45]

Acknowledgements

We gratefully acknowledge financial support from the Centre National de Recherche Scientifique (CNRS), the Université Lille 1 and the Nord Pas de Calais region.

References

1 A. Wirz, B. Meier and O. Sticher, *Pharmazie*, 2002, **57**, 543.
2 A. Kubin, H. G. Loew, U. Burner, G. Jessner, H. Kolbabek and F. Wierrani, *Pharmazie*, 2008, **63**, 263.
3 M. Triesscheijn, P. Baas, J. H. Schellens and F. A. Stewart, *Oncologist*, 2006, **11**, 1034.
4 R. D. Almeida, B. J. Manadas, A. P. Carvalho and C. B. Duarte, *Biochim. Biophys. Acta*, 2004, **1704**, 59.
5 I. J. Macdonald and T. J. Dougherty, *J. Porphyrins Phthalocyanines*, 2001, **5**, 105.
6 S. B. Brown, E. A. Brown and I. Walker, *Lancet Oncol.*, 2004, **5**, 497.
7 J. J. Schuitmaker, P. Baas, H. L. van Leengoed, F. W. van der Meulen, W. M. Star and N. van Zandwijk, *J. Photochem. Photobiol., B*, 1996, **34**, 3.
8 D. E. J. G. J. Dolmans, D. Fukumura and R. K. Jain, *Nat. Rev. Cancer*, 2003, **3**, 380.
9 A. E. O'Connor, W. M. Gallagher and A. T. Byrne, *Photochem. Photobiol.*, 2009, **85**, 1053.
10 D. Bechet, P. Couleaud, C. Frochot, M. L. Viriot, F. Guillemin and M. Barberi-Heyob, *Trends Biotechnol.*, 2008, **26**, 612.
11 R. R. Allison, G. H. Downie, R. Cuenca, X.-H. Hu, C. J. H. Childs and C. H. Sibata, *Photodiagn. Photodyn. Ther.*, 2004, **1**, 27.
12 C. L. Saw, M. Olivo, K. C. Soo and P. W. Heng, *Cancer Lett.*, 2006, **241**, 23.
13 I. Tatischeff and A. Alfsen, *J. Biomater. Nanobiotechnol.*, 2011, **2**, 494.

14 D. K. Chatterjee, L. S. Fong and Y. Zhang, *Adv. Drug Delivery Rev.*, 2008, **60**, 1627.
15 Y. N. Konan, R. Gurny and E. Allemann, *J. Photochem. Photobiol., B*, 2002, **66**, 89.
16 R. Chouikrat, A. Seve, R. Vanderesse, H. Benachour, M. Barberi-Heyob, S. Richeter, L. Raehm, J. O. Durand, M. Verelst and C. Frochot, *Curr. Med. Chem.*, 2012, **19**, 781.
17 B. Heurtault, P. Saulnier, B. Pech, J. E. Proust and J. P. Benoit, *Pharm. Res.*, 2002, **19**, 875.
18 B. Heurtault, P. Saulnier, B. Pech, M. C. Venier-Julienne, J. E. Proust, R. Phan-Tan-Luu and J. P. Benoit, *Eur. J. Pharm. Sci.*, 2003, **18**, 55.
19 S. Ballot, N. Noiret, F. Hindre, B. Denizot, E. Garin, H. Rajerison and J. P. Benoit, *Eur. J. Nucl. Med. Mol. Imaging*, 2006, **33**, 602.
20 E. Garcion, A. Lamprecht, B. Heurtault, A. Paillard, A. Aubert-Pouessel, B. Denizot, P. Menei and J. P. Benoit, *Mol. Cancer Ther.*, 2006, **5**, 1710.
21 A. Lamprecht and J. P. Benoit, *J. Controlled Release*, 2006, **112**, 208.
22 M. Zeisser-Labouebe, N. Lange, R. Gurny and F. Delie, *Int. J. Pharm.*, 2006, **326**, 174.
23 M. Zeisser-Labouebe, F. Delie, R. Gurny and N. Lange, *Eur. J. Pharm. Biopharm.*, 2009, **71**, 207.
24 I. Kraljic and S. El Mohsni, *Photochem. Photobiol.*, 1978, **28**, 577.
25 F. Liu, X. Zhou, Z. Chen, P. Huang, X. Wang and Y. Zhou, *Mater. Lett.*, 2008, **62**, 2844.
26 Y. Usui, *Chem. Lett.*, 1973, 743.
27 M. Hoebeke and X. Damoiseau, *Photochem. Photobiol. Sci.*, 2002, **1**, 283.
28 H. Weitman, M. Roslaniec, A. A. Frimer, M. Afri, D. Freeman, Y. Mazur and B. Ehrenberg, *Photochem. Photobiol.*, 2001, **73**, 110.
29 Y.-F. Ho, M.-H. Wu, B.-H. Cheng, Y.-W. Chen and M.-C. Shih, *Biochim. Biophys. Acta, Biomembr.*, 2009, **1788**, 1287.
30 A. Lamprecht, Y. Bouligand and J. P. Benoit, *J. Controlled Release*, 2002, **84**, 59.
31 A. Barras, A. Mezzetti, A. Richard, S. Lazzaroni, S. Roux, P. Melnyk, D. Betbeder and N. Monfilliette-Dupont, *Int. J. Pharm.*, 2009, **379**, 270.
32 E. I. Kapinus, H. Falk and H. T. N. Tran, *Monatsh. Chem.*, 1999, **130**, 623.
33 F. Gai, M. J. Fehr and J. W. Petrich, *J. Phys. Chem.*, 1994, **98**, 5784.
34 T. Yamazaki, N. Ohta, I. Yamazaki and P. S. Song, *J. Phys. Chem.*, 1993, **97**, 7870.
35 K. Iwanaga, S. Ono, K. Narioka, M. Kakemi, K. Morimoto, S. Yamashita, Y. Namba and N. Oku, *J. Pharm. Sci.*, 1999, **88**, 248.
36 A. P. B. Darmanyan, L. Burel, D. Eloy and P. Jardon, *J. Chim. Phys. Phys.-Chim. Biol.*, 1994, **91**, 1774.
37 H. E. Bouirig, D. Eloy and P. Jardon, *J. Chim. Phys. Phys.-Chim. Biol.*, 1993, **90**, 2021.
38 B. Ehrenberg, J. L. Anderson and C. S. Foote, *Photochem. Photobiol.*, 1998, **68**, 135.
39 M. Roslaniec, H. Weitman, D. Freeman, Y. Mazur and B. Ehrenberg, *J. Photochem. Photobiol., B*, 2000, **57**, 149.
40 J. D. Spikes, *Photochem. Photobiol.*, 1992, **55**, 797.
41 M. C. Galanou, T. A. Theodossiou, D. Tsiourvas, Z. Sideratou and C. M. Paleos, *Photochem. Photobiol.*, 2008, **84**, 1073.
42 C. Thomas and R. S. Pardini, *Photochem. Photobiol.*, 1992, **55**, 831.
43 E. Roger, F. Lagarce, E. Garcion and J. P. Benoit, *J. Controlled Release*, 2009, **140**, 174.
44 A. Paillard, F. Hindre, C. Vignes-Colombeix, J. P. Benoit and E. Garcion, *Biomaterials*, 2010, **31**, 7542.
45 S. Hirsjarvi, S. Dufort, J. Gravier, I. Texier, Q. Yan, J. Bibette, L. Sancey, V. Josserand, C. Passirani, J. P. Benoit and J. L. Coll, *Nanomedicine*, 2013, **9**, 375.

Photochemistry and Photobiology, 2012, 88: 167–174

Cancerous Cell Death from Sensitizer Free Photoactivation of Singlet Oxygen

François Anquez[1], Ikram El Yazidi-Belkoura[2], Stéphane Randoux[1], Pierre Suret[1] and Emmanuel Courtade*[1]

[1]Laboratoire de Physique des Lasers, Atomes et Molécules, UMR 8523 Université Lille 1-CNRS, Villeneuve-d'Ascq Cedex, France
[2]Unité de Glycobiologie Structurale et Fonctionnelle, UMR 8576 Université Lille 1-CNRS, Villeneuve-d'Ascq Cedex, France

Received 25 May 2011, accepted 18 October 2011, DOI: 10.1111/j.1751-1097.2011.01028.x

ABSTRACT

Singlet oxygen ($^1O_2$) is an electronic state of molecular oxygen which plays a major role in many chemical and biological photo-oxidation processes. It has a high chemical reactivity which is commonly harnessed for therapeutic issues. Indeed, $^1O_2$ is believed to be the major cytotoxic agent in photodynamic therapy. In this treatment of cancer, $^1O_2$ is created, among other reactive species, by an indirect transfer of energy from light to molecular oxygen *via* excitation of a photosensitizer (PS). This PS is believed to be necessary to obtain an efficient $^1O_2$ production. In this paper, we demonstrate that production of $^1O_2$ is achieved in living cells from PS-*free* 1270 nm laser excitation of molecular oxygen. The quantity of $^1O_2$ produced in this way is sufficient to induce an oxidative stress leading to cell death. Other effects such as thermal stress are discriminated and we conclude that cell death is only due to $^1O_2$ creation. This new simplified scheme of $^1O_2$ activation can be seen as a breakthrough for phototherapies of malignant diseases and/or as a noninvasive possibility to generate reactive oxygen species in a tightly controlled manner.

INTRODUCTION

Reactive oxygen species (ROS) are chemically active molecules naturally present in living cells. These species are involved in many biological processes such as photosynthesis, mitochondrial respiration, signal transduction or immune response (1–5). At high doses, ROS become toxic and induce an oxidative stress which is observed in several human disorders like Alzheimer's or Parkinson's diseases (6,7).

The cytotoxic effects of ROS are exploited in medicine to remove undesired cells or tissues. In this respect, photodynamic therapy (PDT) uses a photosensitive molecule, the photosensitizer (PS), which is activated by visible light in a tissue targeted for destruction (Fig. 1a). This process leads to primary ROS generation responsible for oxidative stress, cell death and a variety of cytotoxic effects (8). Damages are known to be mediated by two main molecular pathways (Fig. 1a). In the type I pathway, the PS excited state reacts with surrounding molecular targets leading to ROS generation and chain reactions (8). The type II pathway involves the so-called singlet oxygen ($^1O_2$), the first electronic excited state of molecular oxygen, which is recognized as the main initiating agent of PDT phototoxic effects (9,10).

PDT is a routinely used treatment of various forms of cancers (9,11–16) and of age-related macular degeneration (17–19). The PS is a key component in the PDT efficiency. Indeed, the pathway leading to cytotoxic effect in PDT, depicted on Fig. 1a, is an indirect energy transfer involving three components: the PS, light and $^1O_2$. Consequently, PDT exhibits an inherently complex dynamic at several scales relevant for treatments (9,21–24). This crucially depends on many parameters such as the PS dosage and pharmacokinetics or the tumor localization within the human body (20). Moreover, at the cellular level, $^1O_2$ has been shown to be sensitive to intracellular inhomogeneity (25). At the level of the cell, the PS localizes in specified cellular compartments depending on the nature of the PS itself and the cellular type. The spatial distribution of the PS then defines specifically where $^1O_2$ is generated and thus determines a spatial response to the oxidative stress (26).

In this context, it is clear that, despite its high production yield, the indirect $^1O_2$ generation *via* a PS molecule drives to a complex picture from which it can be difficult to learn both from clinical and fundamental points of view. Motivated by a potentially less invasive and less expensive therapy and by the possibility of a simplified generation of $^1O_2$ in cells, we have investigated the PS-free excitation of molecular oxygen into its singlet state ($^1O_2$) through the $^3O_2 \rightarrow {}^1O_2$ optical 1270 nm transition (Fig. 1b).

For the free unperturbed molecule, the optical transition from $^3O_2$ to $^1O_2$ is forbidden by electric dipolar selection rules (27–29). Although the transition is enhanced for the perturbed molecule (i.e. solvated in a dense phase), direct 1270 nm excitation of $^1O_2$ remains a low efficiency process. However, detection of $^1O_2$ 1270 nm phosphorescence has been achieved in biological cells using sensitive detector (30). Thus, direct absorption of 1270 nm laser light might be possible in biological media if sufficiently high laser power is used.

*Corresponding author e-mail: courtade@phlam.univ-lille1.fr (Emmanuel Courtade)

Photochemistry and Photobiology © 2011 The American Society of Photobiology 0031-8655/12

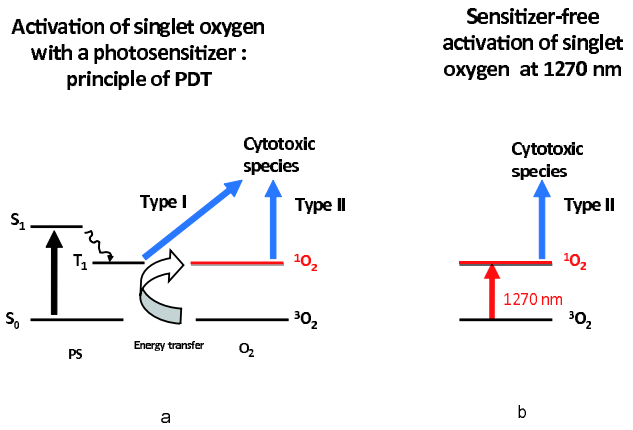

Figure 1. Photophysical mechanisms of singlet oxygen production. Photosensitized production of singlet oxygen requires three elements: light, a photosensitizer (PS) and dioxygen (O_2) (scheme [a]). The PS in its excited triplet state (T_1) can undergo two kinds of reactions. In type I reaction, it can react directly with the cell membrane or a molecule to form a radical anion or cation. These radicals may further react with O_2 to produce reactive oxygen species. In type II reaction, the triplet state of PS can transfer its energy to the molecular ground state of oxygen $^3O_2$ to form singlet oxygen $^1O_2$. The ratio between type I and type II reactions depends on the PS and the local molecular oxygen concentration. At the molecular level, photosensitized production of singlet oxygen exhibits an inherently complex dynamic due to the PS properties (photobleaching with light, reaction with the produced singlet oxygen). This renders difficult a predictive and quantitative dosimetry in photodynamic therapy (PDT). We propose a simplified scheme of PS-free activation of singlet oxygen at 1270 nm (sketched in [b]), overcoming the PS biodistribution within the cell. This scheme produces a lethal stress analogous to the one obtained in PDT.

In solvents, direct PS-free $^1O_2$ production has been reported for the first time by Matheson and Lee in the 1970s (31). These experiments have been performed in high pressure gas phase and are thus quite far from biological conditions. More recently, Krasnovsky *et al.* have shown that $^1O_2$ can be produced in liquids at room temperature and normal pressure *via* the $^3O_2 \rightarrow {}^1O_2$ 1270 nm transition (32–34). These experiments provide estimation of the absorption cross section the $^3O_2 \rightarrow {}^1O_2$ 1270 nm transition in several liquid solvents including water and they open the way for future investigations of intracellular biochemistry of $^1O_2$. Let us emphasize that these previous works have shown that the absorption cross section of the $^3O_2 \rightarrow {}^1O_2$ 1270 nm transition is five orders of magnitude weaker than the one of a typical PS in liquids (32,35).

Only a few investigations about cytotoxic effects arising from 1270 nm irradiation have been undertaken in biological systems. Zakharov *et al.* have discussed the plausible role of $^1O_2$ in reversible changes of cellular membranes and in growth inhibition of rat tumors upon 1264 nm irradiation (36). However, although promising results showing the eradication of human basaliomas *in vivo* upon PS-free 1270 nm irradiation have been recently reported (37), there is no clear evidence of $^1O_2$ creation in all these experiments. Furthermore, an intense laser irradiation induces a thermal stress which can by itself lead to cell death without the implication of any significant oxidative stress. Until now, no attempt has been made to discriminate the various cytotoxic effects arising from a PS-free 1270 nm laser irradiation of living cells.

In this article, we demonstrate that a 1270 nm laser irradiation without a PS leads to the creation of an amount of $^1O_2$ sufficient enough to induce cell death. We demonstrate that the process of cell death is strongly correlated to singlet molecular oxygen creation by showing that the light action spectrum is similar to the spectrum of the molecular oxygen transition $^3O_2 \rightarrow {}^1O_2$. We have carefully measured the temperature increase induced by the laser and conclude that these lethal effects induced by 1270 nm irradiation can be obtained without any hyperthermic stress. Finally we calculate a minimal $^1O_2$ dose to induce cell death that is found to be in close agreement with data previously reported in traditional PDT.

MATERIALS AND METHODS

Cell culture. Breast cancer cell line, MCF-7, is obtained from the American Type Culture Collection and routinely grown as monolayer cultures. Cells are cultured at 37°C in a humidified atmosphere of 5% CO_2 in a Minimal Essential Medium Eagle-Earle's BBS, supplemented with 10% fetal calf serum (FCS), 2 mM L-glutamine and 40 U mL^{-1} penicillin–streptomycin.

In order to show that the phenomenon evidenced in this paper does not depend on the cell type, we have also used rat pheochromocytoma cells (PC12) as an alternate species submitted to laser irradiation. They are grown in Dulbecco's modified Eagle's medium (4.5 g L^{-1} glucose) with 10% FCS and 5% horse serum, L-glutamine and antibiotics.

Live cell irradiation and imaging by video-microscopy. The experimental setup is schematically shown in Fig. 2. For video-microscopy experiments, cells are kept under normal physiological conditions. For this purpose, a temperature-controlled and atmosphere (CO_2, N_2 and O_2)-regulated incubator was designed. With this set-up, the global temperature of the incubator and the concentration of O_2 dissolved in the cell medium are precisely controlled. This custom-made chamber has two optical accesses that allow imaging under a microscope. The cells are irradiated by using a specially designed Raman fiber laser that is tunable around 1270 nm (38) and that is injected in the microscope through a dichroic mirror.

All experiments are performed with a 4× phase-contrast objective. The size of the image (1.665 × 1.249 mm^2) permits the observation of more than 500 cells. One hundred cells are typically irradiated within the laser spot (300 μm FWHM). The whole field image is detected by a CCD camera. Cells lying outside the laser spot provide a control sample.

Noninvasive cell death analysis. Some dyes commonly used in biology have a chemical structure that may lead to $^1O_2$ creation upon light exposure *via* the pathway depicted on Fig. 1a. In order to avoid any doubt on the way through which $^1O_2$ is produced in our experiments, cell death is assessed from the use of morphological criteria without the introduction of any chemical dye. These morphological criteria have been previously correlated in a careful way with a widely accepted cell death assays: the Trypan blue exclusion test (39,40). In all our experiments, the morphological changes evidenced in Fig. 3 are observed as a result of the 1270 nm irradiation. Normal cells are shown in Fig. 3a using a 10× phase-contrast objective. As a result of 1270 nm laser irradiation, the cells first become rounder and appear luminous (Fig. 3b). When cells are dead, they do not move anymore, then cringe and become darker (Fig. 3c).

The morphological criteria defined in Fig. 3c are well correlated with a positive Trypan blue assay. Indeed, Fig. 4 shows cells after 1270 nm irradiation observed with a 4× phase-contrast objective (Fig. 4a) and with a 20× objective (Fig. 4c). For 96% of the cells positive to the Trypan blue test, a morphology identical to Fig. 3c is observed and reciprocally 99% of cells which exhibit such morphology are positively stained with Trypan blue.

Noninvasive and in situ temperature measurements. As observed in optical trapping experiments, the use of high power IR-laser can induce a local temperature increase around the laser spot (41). The

Photochemistry and Photobiology, 2012, 88 169

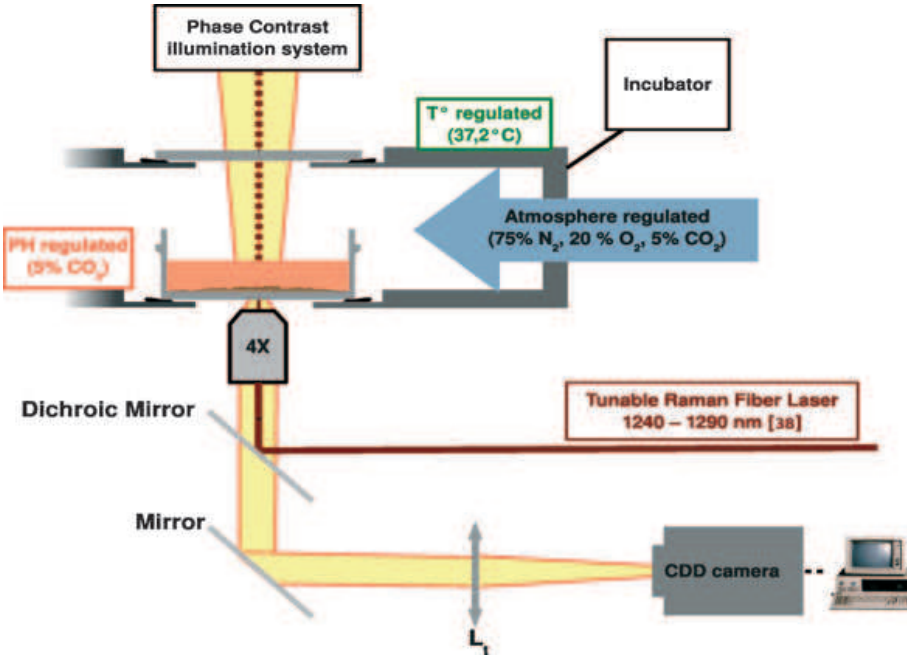

Figure 2. Scheme of the experimental apparatus. In order to perform video-microscopy over 3 days, cells are placed in a temperature- and atmosphere (CO_2, N_2 and O_2)-regulated and controlled humidified incubator. Cells are irradiated using a specially designed high power Raman fiber laser tunable around 1270 nm (38). The laser beam is injected in the microscope through a dichroic mirror. An ensemble of about 500 cells is imaged with a CCD camera through a 4× phase-contrast microscope objective.

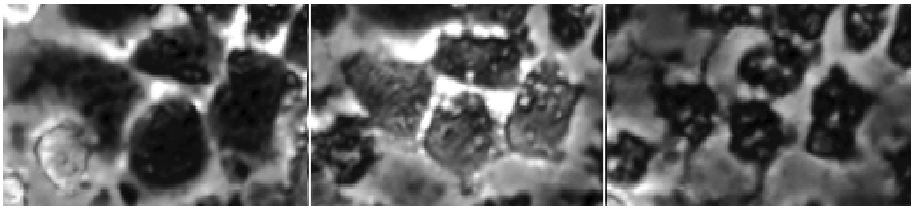

Figure 3. Cell death analysis with Trypan blue assay after a 1270 nm irradiation. (a) Irradiated cells observed using a 4× phase-contrast objective (image size is 0.50×0.52 mm^2), (b) the same cells stained with Trypan blue: one can correlate the morphological changes with Trypan blue exclusion test. In (c) are the cells of image (b) observed with a 20× objective (the image size is 0.44×0.33 mm^2).

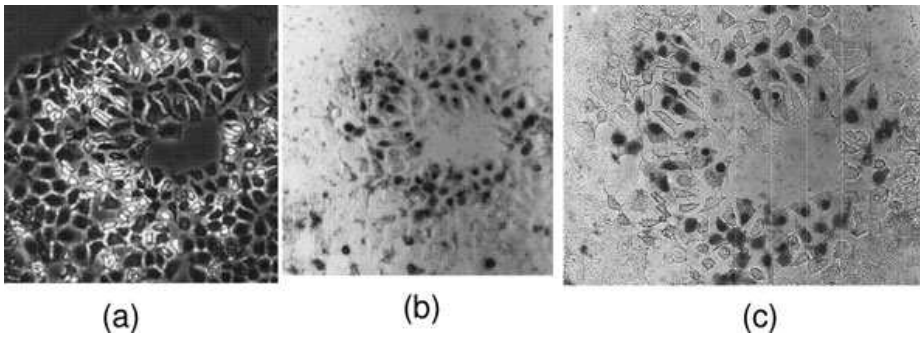

Figure 4. Change in the morphology of cells as a result of the 1270 nm irradiation using a 10× phase-contrast objective. The size of the image is 63×38 μm^2. (a) Living cells before irradiation, (b) cells after irradiation and (c) dead cells.

absorption of the IR-light by the culture medium and the culture dish leads to a temperature increase which can possibly induce cytotoxic effects or cell death. In order to determine this temperature increase, we performed both temperature measurements by fluorescence microscopy and *ab initio* numerical simulations of the heat equation.

Considering the dimensions of the laser spot (300 μm FWHM), a simple thermal sensor may perturb the system and cannot be used for temperature measurements. As proposed by Peterman *et al.*, fluorescent dyes can be used as a temperature indicator (41). We have determined the laser-induced temperature increase from the

ratio of fluorescence intensities of a temperature-dependent dye (Rhodamine B) and a temperature-independent dye (Rhodamine 110) (41–43).

The ratio of fluorescence intensities of Rhodamine B solution (0.3 mM) and Rhodamine 110 solution (0.03 mM) is preliminarily calibrated using the custom-made temperature incubator described previously and the measurements in the presence of the 1270 nm Gaussian laser beam are performed in this home-made incubator. For fluorescence microscopy, the excitation wavelength is 470 nm for both dyes and the emission wavelength is 580 nm for Rhodamine B and 520 nm for Rhodamine 110.

The temperature increase due to laser irradiation has also been determined from numerical simulations. In our model we consider that 1270 nm laser intensity absorbed by the culture medium and the bottom face of the culture dish is fully converted into heat. The stationary heat equation with a term source having the Gaussian profile of the laser beam has been solved using finite element methods with the Freefem++ language (44). Boundary conditions are chosen to take into account convection (approximated by a linear law [45]) with the cold air under the culture dish.

Figure 5a shows numerical and experimental temperature profiles. Numerical calculations agree well with the experimental results. The Gaussian laser beam induces a bell-shaped temperature profile with a maximum which coincides with the center of the 1270 laser spot. As shown in Fig. 5b, one can plot this maximum temperature as a function of the laser power. A 60 K W^{-1} temperature rise is found in our experimental conditions.

Let us emphasize that the temperature increase can be compensated by decreasing the incubator temperature down to 21°C. In these conditions, the temperature of the cell medium does not exceed 42°C for a laser power around 350 mW.

Irradiations in presence of $^1O_2$ quenchers. 1270 nm irradiations have been performed in presence of efficient $^1O_2$ quenchers: bovine serum albumin (BSA) and sodium azide (NaN_3). Cells are first incubated with a quencher 2 h before a 1.5 h – 200 mW irradiation. The quencher is then removed just after the irradiation, and cells are placed in a standard culture medium.

Preliminary experiments have been performed without 1270 nm irradiation in order to evaluate the toxicity of these compounds with a 4 h incubation of the cells. No cell death is observed consecutively to the addition of BSA at concentrations up to 5 mM. From these preliminary experiments, we have also found that NaN_3 is a quencher exhibiting a toxic effect inducing cell death. When the concentration NaN_3 of exceeds 10 mM, cell death is observed 15 h postincubation, whereas at 10 mM no cell death is observed until 48 h.

RESULTS AND DISCUSSION

Cell death induced by 1270 nm laser irradiation

MCF-7 cells are irradiated at several wavelengths around 1270 nm with a 300 μm FWHM Gaussian laser spot. Approximately 100 cells are irradiated and an ensemble of about 500 cells is observed. This provides good statistics on cell death together with a control of the population of non irradiated cells lying outside of the laser spot.

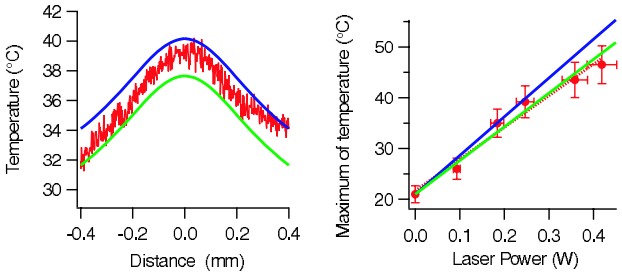

Figure 5. In (a) and (b), experimental data are plotted in red and numerical simulations corresponding to different boundary conditions are plotted in blue and green. (a) Temperature profiles induced by a 265 mW 1270 nm laser irradiation with a 300 m FWHM beam. (b) Maximum temperature increase at the center of the laser spot as a function of the 1270 nm laser power.

As shown in Fig. 6, the consequences of the light irradiation strongly depend on the wavelength of the laser. A 1270 nm laser irradiation induces cell death: 100% of cells lying in a circular region with a radius of *ca* 200 μm (which coincide with the laser spot) are killed. On the other hand, no death is observed from a laser irradiation performed under the same fluence conditions but at a wavelength of 1247 nm which is outside the $^3O_2 \rightarrow {}^1O_2$ absorption band. In experiments of Fig. 6, cells begin to die 15 h after the beginning of laser irradiation. Videos of time lapse corresponding to the experiments described above are accessible in Supporting Information (Movie S1 and Movie S2 corresponding, respectively, to 1270 nm and 1247 nm irradiations).

The same wavelength dependence of the cell death phenomenon has also been observed with PC12 neuronal phenotype rat cells generated from a transplantable rat adrenal pheochromocytoma line.

Death action spectrum around 1270 nm and central role of $^1O_2$

Tuning the laser wavelength across the $^3O_2 \rightarrow {}^1O_2$ transition and determining the fraction of dead cells from a statistical analysis, we have constructed an action spectrum showing the fraction of dead cells as a function of the irradiation wavelength. As shown in Fig. 7, this action spectrum has its maximum at 1270 nm and a width of *ca* 15 nm which strongly match the absorption spectrum of the $^3O_2 \rightarrow {}^1O_2$ transition of

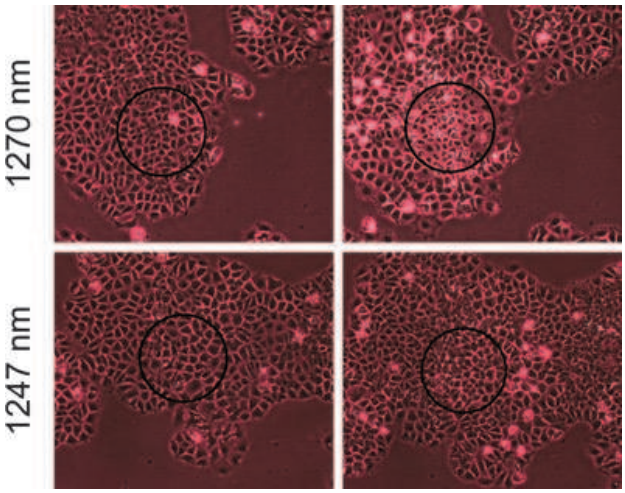

Figure 6. Photos of MCF-7 cells irradiated (*ca* 100 W cm^{-2} – 3 h) at different laser wavelengths. Top and bottom rows show cells which have been irradiated at 1270 nm and 1247 nm, respectively. The image size is 407 × 345 μm^2. Left and right columns show cells before light irradiation and 27 h after light irradiation, respectively. The laser spot (300 μm FWHM) is represented by a black circle on all photos. Approximately 27 h after irradiation at 1270 nm, 100% of cells are dead in a circular region having a radius of 200 μm and centered around the laser spot. On the other hand, no death phenomenon is observed at 1247 nm. The viability is assessed using morphological criteria correlated with commonly accepted cell death assay (Trypan blue exclusion tests).

molecular oxygen measured independently in air saturated solutions (32,38).

To confirm the central role taken by oxygen in the death phenomenon, experiments have been performed putting cells either in hypoxia (saturation in N_2) or in hyperoxia (saturation in O_2). As shown in Fig. 8, a 1270 nm laser irradiation does not induce the death of cells placed under hypoxia. Moreover, the kinetics of the death process and the number of dead cells are strongly enhanced when cells are placed under hyperoxia.

Several authors have reported $^1O_2$ creation *via* mechanisms that may compete with direct 1270 nm excitation of molecular oxygen. On one hand, Singh *et al.* have described a mechanism of $^1O_2$ creation arising from IR illumination due to energy transfer from vibration of water molecules (46). This effect is several orders of magnitude more efficient at wavelength resonant with a vibration of water molecule than for light far-detuned from resonance. There is, to our knowledge, no vibrational mode of water molecules that is resonant at 1270 nm (47). Thus, the resonant effect evidenced in Fig. 7 does not support the implication of a mechanism such as the one described in Ref. (46).

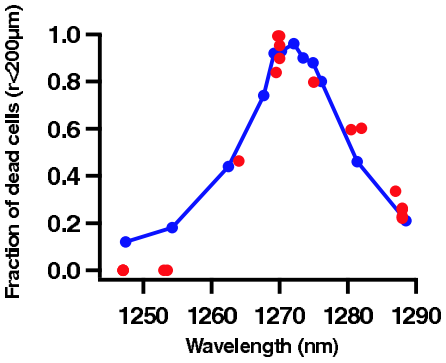

Figure 7. Light action spectrum (red dots) showing the fraction of dead cells in a circular region having a radius of 200 μm centered around the laser spot. The death action spectrum is strongly correlated with the $^3O_2 \rightarrow {}^1O_2$ absorption spectrum of O_2 in ethanol (solid blue line) (40). Three hours long irradiations have been realized in a video-microscopy experiment with an average intensity of 100 W cm^{-2}. The cell death is diagnosed 30 h after the end of the laser irradiation.

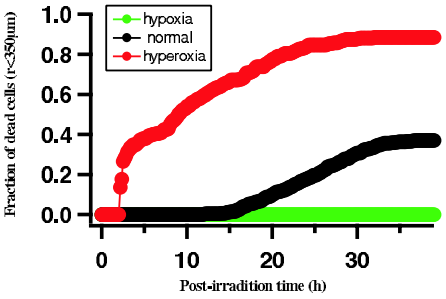

Figure 8. Influence of dissolved oxygen concentration on cell death induced by 1270 nm laser irradiation. 1270 nm irradiations (*ca* 200 W cm^{-2} – 1 h30 min) are performed for different concentrations of oxygen dissolved in the culture medium: normal (black dots), hypoxia (green dots) and hyperoxia (red dots). No cell death is observed under hypoxia whereas the kinetics of the death process and the number of dead cells is strongly enhanced under hyperoxia.

On the other hand, cytotoxic effects observed in optical trapping experiments often arise from 1064 nm irradiations (48). At this wavelength, ROS creation has been reported (49). This wavelength closely corresponds to direct transition to the first vibrational mode of $^1O_2$ which is achieved around 1070 nm. Despite this fact, Landry *et al.* have proposed a mechanism of $^1O_2$ creation which implies a PDT-like energy transfer from the polystyrene beads (used for trapping) to molecular oxygen (48). In order to check that the polystyrene Petri dishes used in our experiments are not responsible for such a mechanism, we have performed irradiation of MCF7 cells cultured in glass Petri dishes. The same wavelength dependent effect is observed for cells cultured on glass.

Control of the thermal stress induced by the laser

As previously mentioned, the laser induces a temperature increase by light absorption of the cell medium. This generates a thermal stress that can possibly lead to cell death. However, the absorption of the cell medium (including culture dish), *ca* 12×10^{-2} mm^{-1}, is constant over the 1250–1290 nm range (data not shown). Therefore, the temperature increase does not depend on the laser wavelength but only on its intensity. The pronounced wavelength dependence evidenced on the action spectrum plotted in Fig. 7 proves that the thermal effects alone cannot induce the death process in our experiments.

To confirm that the cell death is not due to cumulative influence of thermal and oxidative stress, we have evaluated the local temperature increase induced by the laser. In Fig. 6, the maximum temperature within the laser spot, T_{max} is *ca* 43°C for an average laser intensity of 100 W cm^{-2} and an incubator temperature regulated at T_{inc} = 37°C. With the same average intensity, the light-induced death phenomenon is not changed when T_{inc} is decreased to 30°C which corresponds to T_{max} *ca* 36°C. Note that, using the incubator without any laser, we have also additionally checked that MCF-7 cells do not die after a 3 h-long pure-thermal stress at 43°C.

Influence of $^1O_2$ quenchers

In order to (1) confirm that $^1O_2$ is really produced in our experiments and to (2) determine whether $^1O_2$ is produced inside or outside the cell, we have studied the influence of strong $^1O_2$ quenchers. BSA and NaN_3 are known to be efficient quenchers of $^1O_2$ (50). BSA is a relatively large protein (*ca* 70 kDa) which was shown to quench mostly extracellular $^1O_2$ (51). On the other side, NaN_3 is known to penetrate the cells (25) and may thus be present either inside or outside the cells. In order to discriminate the intra and extra cellular contribution of $^1O_2$ in the 1270 nm-induced cell death, we performed a complementary experiment taking advantage that the quenching rate constant for BSA and NaN_3 are similar (50).

First of all, simultaneous use of both quenchers leads to the inhibition of the light-induced cell death phenomenon. Then, the use of BSA alone at a concentration of 1 mM reduces the fraction of cell death to 57% (compared to 100% of cells that die from an irradiation performed in the same conditions but without any quencher). This fraction is decreased down 38% when the concentration of BSA is increased to 5 mM. With a 10 mM concentration of NaN_3 the fraction of cell death is

reduced by 18%. Cell death could only be totally avoided by adding high concentration of both quenchers ([NaN_3] = 10 mM and [BSA] = 5 mM).

On one hand, the influence of these two quenchers strongly confirms the implication of $^1O_2$ in our experiments. On the other hand, inhibition of cell death by BSA shows that part of the damages is due to extracellular $^1O_2$. But, increasing the BSA concentration, we were unable to completely inhibit the process of cell death while the effect of 1270 nm irradiation is also inhibited by addition of NaN_3. As it has been noticed before, BSA quenches mostly extracellular $^1O_2$ (51). This has been shown for Hela cells but it is possible that, in the MCF-7 cells, part of BSA can be integrated inside the cell *via* endocytosis. Thus, BSA may not be exclusively an extracellular quencher. Moreover, the cell density is quite high in our experiments. Indeed, the extracellular volume from which $^1O_2$ could diffuse toward the cell membrane in one lifetime is more than one hundred times smaller than the volume of the cell itself. These last observations suggest that $^1O_2$ could be, in our experiments, activated both within and outside the cells.

Light fluence threshold to induce cell death

We now examine the influence of the laser intensity I and of the irradiation duration Δt on the 1270 nm light-induced cell death. In all the experiments, the local intensity can be precisely determined because the laser Gaussian intensity profile is well known. Compiling data from various experiments, we plot in Fig. 9 the threshold (minimum) intensity I_{TH} which is required to induce the death of cells as a function of Δt. For irradiation parameters which are in regions (I, Δt) lying above the points plotted in Fig. 9, 100% of the cells systematically die as a result of 1270 nm laser irradiation. On the other hand, irradiations made for parameters (I, Δt) lying below points plotted in Fig. 9 do not induce cell death.

In order to establish in an unambiguous way the central role taken by the oxidative stress in those experiments, we have performed other control irradiations with a laser wavelength of 1247 nm that is not resonant with the $^3O_2 \rightarrow {}^1O_2$ transition. Cells have been irradiated at 1247 nm with intensities I and durations Δt identical to those plotted in Fig. 9. In all those experiments, no cell death has been observed at 1247 nm. Let us remind that absorption coefficients of the Petri dish and culture medium are equal at 1247 nm and 1270 nm so that those two wavelengths produce an identical thermal stress for a given value of (I, Δt).

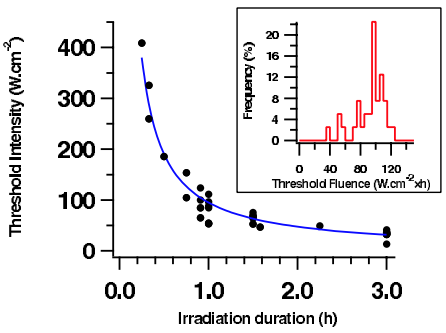

Figure 9. Threshold intensity I_{TH} (dots) required to observe 1270 nm-induced cell death as a function of the irradiation duration Δt. Both the 1270 nm laser intensity I (50–500 W cm^{-2}) and the irradiation duration Δt (15–180 min) have been varied with an incubator temperature down to 21°C. Dots plotted can be fitted (blue line) by the function $I_{TH} = F_{TH}/\Delta t$ with F_{TH} = 95 W cm^{-2} h. The inset shows the histogram of the statistics of the measured threshold fluence. The mean value of F_{TH} is *ca* 93 W cm^{-2} h in good agreement with the previously fitted value.

Oxidative stress induced by irradiations at 1270 nm always triggers the death process when the light fluence $F = I \times \Delta t$ exceeds a threshold fluence F_{TH}. Data plotted in Fig. 9 can indeed be fitted by the function $I_{TH} = F_{TH}/\Delta t$ with F_{TH} = 95 W cm^{-2} h. This threshold fluence F_{TH} is associated to a cumulative $^1O_2$ concentration (defined as the integral over the irradiation time of the $^1O_2$ production rate) already introduced in conventional PDT (52). From the value of F_{TH} and of the cross section of $^3O_2 \rightarrow {}^1O_2$ transition (*ca* 10^{-23} cm^2 [31]), we have determined a minimum cumulative $^1O_2$ concentration of *ca* 4.6 mM. It is very interesting to note that this value is comparable with the minimum cumulative $^1O_2$ concentration found in standard PDT experiments (53–56).

CONCLUSION

We have demonstrated that PS-free 1270 nm irradiation of living cells leads to cytotoxic effects *in vitro* through $^1O_2$ creation. The quantity of $^1O_2$ produced from direct laser irradiation is sufficient to induce an oxidative stress leading to the death of cells. Other effects such as thermal stress have been discriminated and we conclude that cell death is only due to $^1O_2$ creation. We have been able to derive a minimum value for the cumulated $^1O_2$ concentration that is necessary to induce the death of cell. This value has been found to be in agreement with the ones extracted from *in vitro* PDT treatment.

It is interesting to compare the fluence used in this work with the one reported by Zakharov *et al.* for *in vivo* tumor eradication upon 1270 nm irradiation (36). To induce cell death, we irradiate cells with a fluence that is three orders of magnitude greater than the one used in Ref. (37). Such a difference does not imply that cytotoxic effects reported *in vivo* are not due to $^1O_2$ creation (37). This suggests that, in this treatment, tumor removal may not arise from direct cell death. *In vivo*, other effects, such as $^1O_2$-triggered immune response can be expected. Furthermore, thermal effects have to be considered *in vivo*. Even if temperature measurements are more difficult *in vivo* than *in vitro*, a tunable laser could help to discriminate cytotoxic effects due to thermal effects from cytotoxic effects due to oxidative stress.

Experiments in which strong $^1O_2$ quenchers are added in the cellular medium also represent another important aspect of our work. These experiments suggest that $^1O_2$ is produced both within and outside the cell. The possibility of creating $^1O_2$ inside the cell without a PS has interesting application to study the influence of $^1O_2$ in biological systems from both fundamental and therapeutic points of view. It would be possible, for example, to produce $^1O_2$ in a specific cellular compartment by using a focused 1270 nm laser.

However, we have not been able to determine what is the exact fraction of $^1O_2$ produced within the cell. Moreover, it is necessary to determine $^1O_2$ primary targets to get deeper insights on the cellular response leading to cell death in our experiments. Our experiments do not permit us to clearly state

whether $^1O_2$ is homogeneously produced inside the cell or near a specific organelle. A mechanism of absorption enhancement by hydrophobic structures has been proposed (33). This suggests that 1270 nm $^1O_2$ photoactivation rate could be for example higher near the cell membrane than in the cytoplasm. In order to clarify these questions one could use chemical $^1O_2$ traps or probes that localize in different regions of the cell.

Acknowledgements—This work has been supported by French Ministry of Higher Education and Research, Nord-Pas de Calais Regional Council and FEDER through the "Contrat de Projets Etat Region (CPER) 2007-2013," the RNTS-ANR "TLAI," and the Osyris company. We thank the technical staff of the PhLAM laboratory for its participation in this work and N. Peyrieras, J. Piette and F. Lenci for fruitful discussions. We also thank Jaouad Zemmouri for its significant contribution to the initiation of this research project and for stimulating discussions. [This article was published online on 22 November 2011. An error was subsequently identified. This notice is included in the online and print versions to indicate that both have been corrected on 23 November 2011.]

SUPPORTING INFORMATION

Additional Supporting Information may be found in the online version of this article:

Movie S1. Thirty hours long time lapse corresponding to a 3 h – 100 mW irradiation at 1270 nm. The movie lasts 30 h (image taken every 10 min with 10 frames per second for the video). The image size is 407×345 μm^2. A black circle is drawn on the images corresponding to the 300 μm FWHM laser spot. The thicker circle corresponds to the 3 h irradiation. The temperature control incubator is set to 37.2°C during the all experiment. The controlled and regulated atmosphere in the incubator is set to 74% of N_2, 21% of O_2 and 5% of CO_2. The death of the MCF-7 cells are observed 15 h after the beginning of the 1270 nm laser irradiation and 100% of cells lying in a circular region with a radius of *ca* 200 μm centered on the laser spot are killed.

Movie S2. Thirty hours long time lapse with a 3 h – 100 mW irradiation at 1247 nm. The movie lasts 30 h (image taken every 10 min with 10 frames per second for the video). The image size is 407×345 μm^2. A black circle is drawn on the images corresponding to the 300 μm FWHM laser spot. The thicker circle corresponds to the 3 h irradiation. The temperature control incubator is set to 37.2°C during the whole experiment. The controlled and regulated atmosphere in the incubator is set to 74% of N_2, 21% of O_2 and 5% of CO_2. No death is observed from a 1247 nm laser irradiation.

Please note: Wiley-Blackwell is not responsible for the content or functionality of any supporting information supplied by the authors. Any queries (other than missing material) should be directed to the corresponding author for the article.

REFERENCES

1. Apel, K. and H. Hirt (2004) Reactive oxygen species: Oxidative stress, and signal transduction. *Annu. Rev. Plant Biol.* **55**, 373–399.
2. Pitzschke, A., C. Forzani and H. Hirt (2006) Reactive oxygen species signaling in plants. *Antioxid. Redox Signal.* **8**, 1757–1764.
3. Ginn-Pease, M. E. and R. L. Whisler (1998) Redox signals and NF-κB activation in T cells. *Free Radic. Biol. Med.* **25**, 346–361.
4. Schoonbroodt, S. and J. Piette (2000) Oxidative stress interference with the nuclear factor-κB activation pathways. *Biochem. Pharmacol.* **60**, 1075–1083.
5. Chandel, N. S., D. S. McClintock, C. E. Feliciano, T. M. Wood, J. A. Melendez, A. M. Rodriguez and P. T. Schumacker (2000) Reactive oxygen species generated at mitochondrial complex III stabilize hypoxia-inducible factor-1alpha during hypoxia: A mechanism of O_2 sensing. *J. Biol. Chem.* **275**, 25130–25138.
6. Maguire-Zeiss, K. A., D. W. Short and H. J. Federoff (2005) Synuclein, dopamine and oxidative stress: Co-conspirators in Parkinson's disease? *Mol. Brain Res.* **134**, 18–23.
7. Higgins, G. C., P. M. Beart, Y. S. Shin, M. J. Chen, N. S. Cheung and P. Nagley (2010) Oxidative stress: Emerging mitochondrial and cellular themes and variations in neuronal injury. *J. Alzheimers Dis.* **20**, S453–S473.
8. Girotti, A. W. (2001) Photosensitized oxidation of membrane lipids: Reaction pathways, cytotoxic effects, and cytoprotective mechanisms. *J. Photochem. Photobiol. B, Biol.* **63**, 103–113.
9. Dougherty, T. J., C. J. Gomer, B. W. Henderson, G. Jori, D. Kessel, M. Korbelik, J. Moan and Q. Peng (1998) Photodynamic therapy. *J. Natl Cancer Inst.* **90**, 889–905.
10. Foote, C. S. (1968) Mechanisms of photosensitized oxidation. *Science* **162**, 963–970.
11. Dougherty, T. J. (2002) An update on photodynamic therapy applications. *J. Clin. Laser Med. Surg.* **20**(1), 3–7.
12. Dolmans, D. E. J. G. J., D. Fukumura and R. K. Jain (2003) Photodynamic therapy for cancer. *Nat. Rev. Cancer* **3**, 380–387.
13. Moore, C. M., D. Pendse and M. Emberton (2009) Photodynamic therapy for prostate cancer – A review of current status and future promise. *Nat. Clin. Pract. Urol.* **6**, 18–30.
14. Brown, S. B., E. A. Brown and I. Walker (2004) The present and future of photodynamic therapy in cancer treatment. *Lancet Oncol.* **5**, 497–508.
15. Hopper, C. (2000) Photodynamic therapy: A clinical reality in the treatment of cancer. *Lancet Oncol.* **1**, 212–219.
16. Allison, R. R., R. E. Cuenca, G. H. Downie, P. Camnitz, B. Brodish and C. H. Sibata (2005) Clinical photodynamic therapy of head and neck cancers – A review of applications and outcomes. *Photodiagn. Photodyn. Ther.* **2**, 205–222.
17. Beatty, S., H. H. Koh, D. Henson and M. Boulton (2000) The role of oxidative stress in the pathogenesis of age-related macular degeneration. *Surv. Ophthalmol.* **45**, 115–134.
18. Schmidt-Erfurth, U., J. W. Miller, M. Sickenberg, H. Laqua, I. Barbazetto, E. S. Graoudas, L. Zografos, B. Piguet, C. J. Pournaras, G. Donati, A. M. Lane, R. Birngruber, H. Van Den Berg, H. A. Strong, U. Manjuris, T. Gray, M. Fsadni and N. M. Bressler (1999) Photodynamic therapy with verteporfin for choroidal neovascularization caused by age-related macular degeneration: Results of a single treatment in a phase 1 and 2 study. *Arch. Ophthalmol.* **117**, 1177–1187.
19. Messmer, K. J. and S. R. Abel (2001) Verteporfin for age-related macular degeneration. *Ann. Pharmacother.* **35**, 1593–1598.
20. Dysart, J. S., G. Singh and M. S. Patterson (2005) Calculation of singlet oxygen dose from photosensitizer fluorescence and photobleaching during mTHPC photodynamic therapy of MLL cells. *Photochem. Photobiol.* **81**, 196–205.
21. Robertson, C. A., D. Hawkins and H. Abrahamse (2009) Photodynamic therapy (PDT): A short review on cellular mechanisms and cancer research applications for PDT. *J. Photochem. Photobiol. B, Biol.* **96**, 1–8.
22. Castano, A. P., T. N. Demidova and M. R. Hamblin (2004) Mechanisms in photodynamic therapy: Part one – Photosensitizers, photochemistry and cellular localization. *Photodiagn. Photodyn. Ther.* **1**, 279–293.
23. Castano, A. P., T. N. Demidova and M. R. Hamblin (2005) Mechanisms in photodynamic therapy: Part two – Cellular signalling, cell metabolism and modes of cell death. *Photodiagn. Photodyn. Ther.* **2**, 1–23.
24. Castano, A. P., T. N. Demidova and M. R. Hamblin (2005) Mechanisms in photodynamic therapy: Part three – Photosensitizer pharmacokinetics, biodistribution, tumor localization and modes of tumor destruction. *Photodiagn. Photodyn. Ther.* **2**, 91–106.

IOP PUBLISHING LASER PHYSICS
Laser Phys. **23** (2013) 025601 (8pp) doi:10.1088/1054-660X/23/2/025601

Cell death induced by direct laser activation of singlet oxygen at 1270 nm

F Anquez[1], I El Yazidi Belkoura[2], P Suret[1], S Randoux[1] and E Courtade[1]

[1] Laboratoire de Physique des Lasers, Atomes et Molécules, UMR CNRS 8523, Université Lille 1, 59655 Villeneuve-d'Ascq, France
[2] Unité de Glycobiologie Structurale et Fonctionnelle, UMR CNRS 8576, Université Lille 1, 59655 Villeneuve-d'Ascq Cedex, France

E-mail: emmanuel.courtade@univ-lille1.fr

Received 4 November 2011, in final form 12 November 2011
Published 14 December 2012
Online at stacks.iop.org/LP/23/025601

Abstract
Singlet oxygen plays a major role in many chemical and biological photo-oxidation processes. It has a high chemical reactivity, which is commonly harnessed for therapeutic issues. Indeed, singlet oxygen is recognized as the major cytotoxic agent in photodynamic therapy. In this treatment of cancer, singlet oxygen is created, among other reactive species, by an indirect transfer of energy from light to molecular oxygen via excitation of a photosensitizer. In this paper, we show that the conventional singlet oxygen production scheme can be simplified. Production of singlet oxygen is achieved in living cells from photosensitizer-free 1270 nm laser excitation of the electronic ground state of molecular oxygen. The quantity of singlet oxygen produced in this way is sufficient to induce an oxidative stress leading to cell death. Other effects such as thermal stress are discriminated, and we conclude that cell death is only due to singlet oxygen creation. This new simplified scheme of singlet oxygen activation can be seen as a breakthrough for phototherapies of malignant diseases and/or as a non-invasive possibility to generate reactive oxygen species in a tightly controlled manner.

(Some figures may appear in colour only in the online journal)

1. Introduction

Singlet oxygen ($^1O_2$) is the first electronically excited state of molecular oxygen ($^1O_2$). Because of its high chemical reactivity, it plays a central role in many chemical and biological photo-oxidation processes [1–3]. Indeed, singlet oxygen reactivity is harnessed in photodynamic therapy (PDT), which is now a widely used treatment of cancer and age related macular degeneration [2]. As shown in figure 1(a), PDT uses a photosensitive molecule, the photosensitizer (PS). Upon irradiation with light at appropriate wavelength, the PS is activated in the tissue targeted for destruction. This process leads to generation of primary reactive oxygen species (ROSs) responsible for oxidative stress, cell death and a variety of cytotoxic effects [1, 2, 4]. Damage is known to be mediated by two main molecular pathways as shown in figure 1(a). In the type I pathway, the PS excited state reacts with surrounding molecular targets leading to ROS generation and chain reactions [1, 5]. In the type II process, energy transfer from the PS to the ground state of molecular oxygen ($^3O_2$) leads to activation of $^1O_2$ [5, 6]. The second pathway is recognized as the most dominant one in PDT [1, 2].

In PDT, $^1O_2$ generation is achieved through an indirect energy transfer from light to molecular oxygen. From the therapeutic point of view, the PDT efficiency is determined by the PS distribution within the tumor or within the cell, its concentration, its photophysical properties and also the illumination parameters. Indeed, $^1O_2$ production in PDT exhibits an inherently complex dynamic at several scales relevant for treatment [5, 7–9]. At the cellular level, the PS can localize in different compartments so that $^1O_2$ is produced in the neighborhood of different organelles. Thus $^1O_2$ might trigger a wide variety of cellular responses [4, 10]. Moreover, $^1O_2$ has been shown to be sensitive to cellular inhomogeneity [11–13], and its cytotoxicity can depend on its location inside the cell.

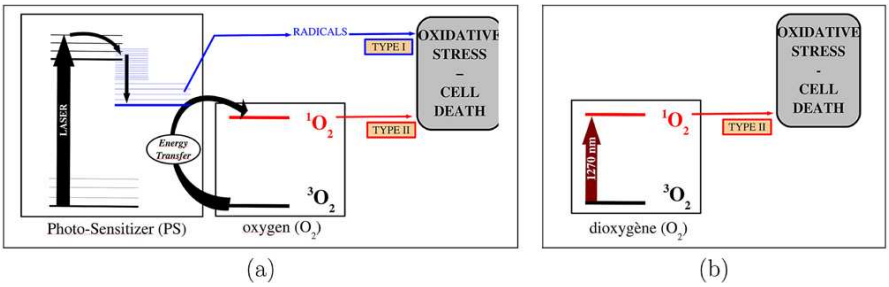

Figure 1. (a) Schematic diagram of PDT mechanisms: the type I process leads to radical formation and the type II leads to singlet oxygen generation. (b) Diagram of direct excitation of singlet oxygen at 1270 nm.

In this context, it is clear that, despite an efficient $^1O_2$ production yield, the indirect singlet oxygen generation via a PS molecule leads to a complex picture with difficult interpretations from both the clinical and the fundamental points of view. Motivated by a potentially less invasive and less expensive therapy and by the possibility of a simplified generation of singlet oxygen in cells, we have investigated the PS-free excitation of molecular oxygen into its singlet state ($^1O_2$) through the $^3O_2 \longrightarrow {}^1O_2$ optical 1270 nm transition (figure 1(b)).

Unlike many other common molecules, the molecular oxygen ground state ($^3O_2$) is a spin triplet. For the free unperturbed molecule, the optical transition from $^3O_2$ to $^1O_2$ is forbidden according to electric dipolar selection rules [14, 15]. Even if the transition is enhanced for the perturbed molecule [16–18] (i.e. solvated in a dense phase), direct 1270 nm excitation of $^1O_2$ remains a low efficiency process. Using high power 1270 nm lasers, Krasnovsky *et al* have nevertheless recently shown that direct excitation of $^1O_2$ can be achieved in liquids at room temperature [19–21]. Their work provides an estimation of the oxygen absorption cross section in liquids including water. They have found that it is five orders of magnitude weaker than the yield of a typical PS [22].

As a result of this poor efficiency, only a few investigations of cytotoxic effects arising from 1270 nm irradiation have been undertaken in biological systems [23–26]. Although promising works have recently reported the eradication of human basalioma *in vivo* upon PS-free 1270 nm irradiation [25], there is no evidence of $^1O_2$ creation in these experiments. In particular, it should be emphasized that an intense laser irradiation may induce a thermal stress, which can by itself lead to cell death [27–29] without the implication of any significant oxidative stress. No attempt has been made to discriminate the various cytotoxic effects arising from a PS-free 1270 nm laser irradiation.

In this paper, we demonstrate that a 1270 nm laser irradiation without a photosensitizer leads to the creation of an amount of singlet oxygen sufficient to induce cell death *in vivo*. We have designed a temperature-controlled experiment in which we can observe the cells over a duration greater than 48 h consecutive to a 1270 nm irradiation. We have made *in situ* measurements of the temperature increase due to laser irradiation. We demonstrate that the observed lethal effects can be obtained without any hyperthermic stress. Irradiations are performed using an especially designed Raman fiber laser tunable across the 1270 nm transition of molecular oxygen [30]. A light action spectrum showing the fraction of cells dead as a function of wavelength has been obtained. This action spectrum is found to be strongly correlated to the oxygen absorption spectrum in solvents around 1270 nm. Additional experiments in which the concentration of molecular oxygen in cells is varied are varied out to confirm the central role taken by oxygen in the death phenomenon observed in our experiments. The use of $^1O_2$ quenchers also supports $^1O_2$ creation and we have finally determined a minimal $^1O_2$ dose to induce cell death. This dose is found to be in good agreement with conventional PDT experiments.

2. Experiments

2.1. Cell culture and video-microscopy

In our experiments, we have used a breast cancer cell line of type MCF-7. It is obtained from the American Type Culture Collection and routinely grown as monolayer cultures. Cells were cultured in minimal essential medium Eagle–Earle's BBS, supplemented with 10% fetal calf serum (FCS), 2 mM L-glutamine and 40 U ml^{-1} penicillin–streptomycin at 37 °C in a humidified atmosphere of 5% CO_2. We have also used pheochromocytoma cells, PC12, as alternate species and different cell type in order to show that the observed effects do not depend on the cellular type. PC12 cells were grown in Dulbecco's modified Eagle's medium (5 g l^{-1} glucose) with 10% FCS, 5% horse serum, L-glutamine and antibiotics.

In order to keep the cells in normal physiological condition for 48 h after the irradiation, we have designed an atmosphere-regulated and temperature-controlled humidified incubator. For normal conditions an atmosphere of 5% CO_2, 20% O_2 and 75% N_2 was constantly flowed through the chamber. The temperature is maintained constant at 37 °C for normal conditions. With no laser irradiation, 5% of the cell population dies, which corresponds to a standard basal percentage of dying cells.

The experimental setup is schematically represented in figure 2. The incubator has two optical accesses that permit the observation of the cells by using phase contrast microscopy.

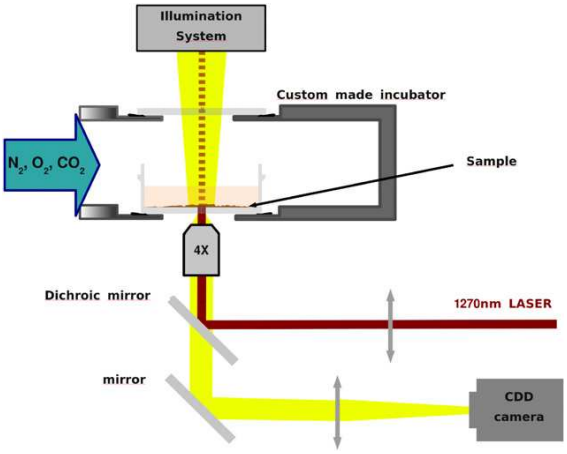

Figure 2. Optical setup for 1270 nm irradiation of living cells. The cells are imaged with a 4× phase contrast objective (Olympus). The 1270 nm laser light irradiates the cells through the objective. A custom made incubator allows observation of the cultured cells for more than 48 h.

All experiments are performed with a 4× phase contrast objective in order to have a large field with about 500 cells. The whole field image is detected by a CCD camera. Video-microscopy movies are constructed with an image taken every 10 min with an exposure duration of 100 ms. Laser irradiation was performed by using an especially designed Raman fiber laser tunable around 1270 nm [30]. The laser is focused at the back focal plane of the objective. The beam irradiating the cells is nearly collimated and its FWHM radius is 300 μm on the cells. One obtains a good statistics on the cell death phenomenon (∼100 cells within the laser spot) together with a control of the population of non-irradiated cells lying outside of the irradiated region.

2.2. *Cell death analysis*

In order to avoid any doubt regarding the way in which $^1O_2$ is produced in our experiments, we do not introduce any perturbing dye inside the Petri dish. Cell death is assessed by using morphological criteria. In all our experiments, cells exhibit morphological changes evidenced in figure 3 consecutive to a 1270 nm irradiation. Using a 4× phase contrast microscope objective, the irradiated cells first become rounder (figure 3(b)) then finally shrink and become darker (figure 3(c)). After observation of the last morphology (figure 3(c)), cells do not move anymore and they are considered as dead.

Those morphological criteria have been correlated to widely accepted cell death assays such as the Trypan blue exclusion test [31]. The Trypan blue dye allows the determination of membrane permeability inherent to any cell death [32]. Trypan blue solution (0.4 % w/v) is obtained from Sigma. After the 1270 nm irradiation, the medium is removed and cells are washed with PBS, before being incubated (5 min) in a mix of one part of 0.4% Trypan blue and one part of PBS. Finally, cells are observed with a bright field transmission microscope (4× or 20× objectives). It is found that the morphological criterion defined in figure 3(c) is well correlated with a positive Trypan blue assay. Indeed, figure 3(d) shows cells after 1270 nm irradiation observed with a 4× phase contrast objective. Figure 3(e) shows the same cells with 20× objective after Trypan blue staining. For 96% of the cells positive to Trypan blue a morphology identical to figure 3(c) is observed, and reciprocally 99% of cells which exhibit such a morphology are positively stained with the Trypan blue test.

2.3. *Non-invasive and in situ measurements of laser induced heating*

As mentioned above, an intense laser irradiation may induce a thermal stress leading to cell death [27–29]. Considering the size of the laser spot (300 μm FWHM), a simple temperature probe may perturb the system and it cannot be employed for *in situ* temperature measurements. As proposed by Sakakibara *et al*, fluorescent dyes can be used as a temperature indicator [33]. The ratio of the fluorescence intensities of a temperature-dependent dye and a temperature-independent dye allows the determination of the whole laser induced temperature field [33–35]. Rhodamine B and rhodamine 110 can be used in fluorescence microscopy for this purpose [33].

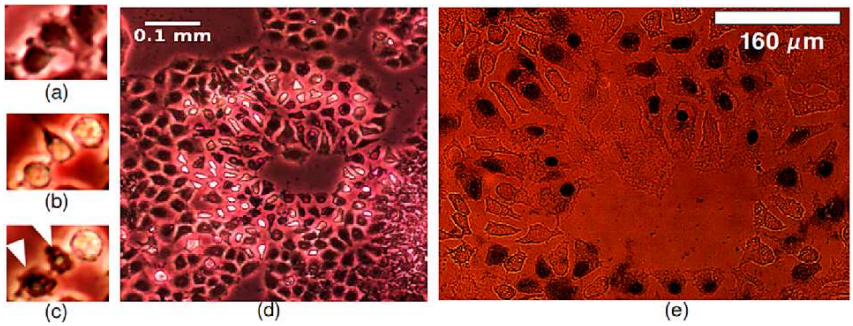

Figure 3. (a)–(c) Morphological changes experienced by cells after 1270 nm irradiation observed by phase contrast microscopy. (a) cells before irradiation, (b) cells ∼5 h after irradiation and (c) dead cells. (d) Cells observed ∼6 h after 1270 nm irradiation with a 4× phase contrast objective. (e) The same cells as in (d) observed with a 20× objective after Trypan blue incubation: a good correlation is found between morphological criteria of cell death and the Trypan blue exclusion test.

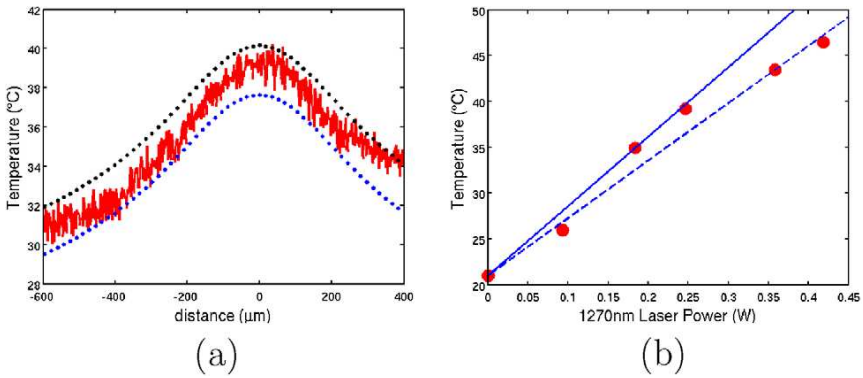

Figure 4. (a) Experimental (red line) and calculated (blue and black dots) temperature profiles at the sample plane in the presence of the 1270 nm laser. The laser power was 265 mW and the incubator temperature is maintained at 21 °C. The black dots are calculated for a transfer coefficient of 5 W m^{-2} K^{-1} and the black dots for an infinite convection coefficient. (b) Experimental (red dots) and calculated (blue lines) variation of the maximum of the temperature profile with laser power. For the simulations, the continuous line corresponds to infinite convection coefficient and the dashed line was calculated with h = 5 W m^{-2} K^{-1}.

As the cell culture medium is mainly composed of water, aqueous solutions of rhodamine are used. The ratio of fluorescence intensities of rhodamine B solution (0.30 mM) and rhodamine 110 solution (0.030 mM) is calibrated using the temperature incubator described previously and the measurements in the presence of the 1270 nm Gaussian laser beam are performed in this home-made incubator. The excitation wavelength is 470 nm for both dyes and the emission wavelength is 580 nm for rhodamine B and 520 nm for rhodamine 110.

In order to confirm experimental measurements of the laser induced temperature increase, we have also performed *ab initio* numerical simulation of the heat equation. Laser induced heating is due to laser light absorption of the culture medium and the Petri dish. In our model we have considered that all the energy absorbed by the media is converted into heat. The stationary heat equation with a term source having a Gaussian shape of the laser beam in the radial direction has been solved by using finite element methods with the Freefem++ language [36].

Far from the laser spot (at the top of the culture medium and on the lateral side of the Petri dish), the temperature is imposed. At the bottom, boundary conditions are chosen to take into account convection with cold air under the Petri dish. Energy transfer by convection from the bottom of the Petri dish to the cold air out of the incubator can be approximated by a linearized law: $-\lambda\frac{\partial T}{\partial z} = h(T - T_e)$, where T is the temperature, z is the longitudinal coordinate parallel to the beam propagation direction, $-\lambda\frac{\partial T}{\partial z}$ is the heat flux, T_e is the temperature of the cold air outside the incubator and h is a transfer coefficient [37]. Two limiting cases of convection efficiencies have been considered. On one hand, if the transfer coefficient is high, the boundary conditions are simplified and the temperature is imposed at the bottom of the side of the Petri dish. On the other hand, the transfer coefficient, h, can be calculated for this geometry [37]: a solid plane in contact with air at the bottom. From data reported in [37] we found $h \sim 5$ W m^{-2} K^{-1}.

Numerical and experimental temperature profiles are shown in figure 4(a). The experimental results are in good agreement with theoretical calculations. The Gaussian laser beam induced a bell-shaped temperature profile with a maximum that coincides with the center of the 1270 nm laser spot. As shown in figure 4, one can plot this maximum temperature as a function of the laser power. A 60 K W^{-1} slope is found in our experimental conditions. Let us emphasize that the laser induced temperature increase can be compensated by decreasing the incubator's temperature (21 °C). This allows us to avoid any thermal stress due to the laser irradiation at a power up to 300 mW.

3. Results and discussion

3.1. Cell death induced by 1270 nm laser irradiation

As shown in figure 5, the consequences of the light irradiation strongly depend on the wavelength of the laser. A 1270 nm laser irradiation induces cell death: 100% of the cells lying in a circular region with a radius of ∼200 μm centered on the laser spot are killed. On the other hand, no death is observed from a laser irradiation performed under the same fluence conditions but at a wavelength of 1247 nm, which is outside the $^3O_2 \longrightarrow {}^1O_2$ absorption band. Cells shown in figure 5 were irradiated for 3 h with an average light intensity of ∼100 W cm^{-2}. A normal atmosphere was maintained (5% CO_2, 20% O_2, 75% N_2) at 37 °C. The death of the MCF7 cells occurs 15 h after the beginning of laser irradiation.

The same wavelength dependence for the cell death phenomenon has also been observed with PC12 neuronal phenotype rat cells generated from a transplantable rat adrenal pheochromocytoma line.

3.2. Death action spectrum and influence of dissolved oxygen: evidence of singlet oxygen creation

Tuning the laser wavelength across the $^3O_2 \longrightarrow {}^1O_2$ transition and determining the fraction of dead cells from a statistical

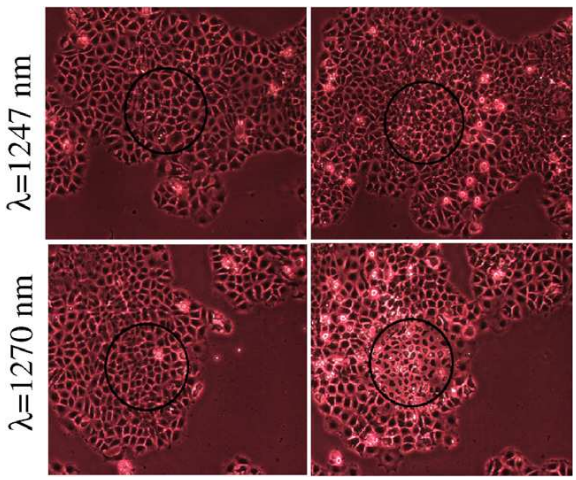

Figure 5. Images of the MCF7 cells before (left column) and after (right column) laser irradiation. Irradiation was performed at 1270 nm (bottom) and 1247 nm (top). The laser intensity was ∼100 W cm^{-2} and the irradiation duration was 3 h. The black circle represents the position of the laser spot (300 μm FWHM). At 1270 nm 100% of the cells die within the laser spot whereas no cell death is observed at 1247 nm. Cells lying outside the laser spot provide a control.

analysis, we have constructed an action spectrum showing the fraction of dead cells as a function of the irradiation wavelength. As shown in figure 6(a), this action spectrum centered around 1270 nm with a width of approximately 15 nm does strongly match the absorption spectrum of the $^3O_2 \longrightarrow {}^1O_2$ transition of molecular oxygen measured independently in air saturated solutions [19, 30].

In order to confirm the central role taken by oxygen in the death phenomenon, experiments have been performed putting cells either in hypoxia (saturation in N_2) or in hyperoxia (saturation in O_2). As shown in figure 6(b), a 1270 nm laser irradiation does not induce the death of cells placed under hypoxia. On the other hand, the kinetics of the death process and the number of dead cells are strongly enhanced when cells are placed under hyperoxia. From all these experiments we conclude that cell death arises from $^1O_2$ creation.

As previously mentioned, the laser induces a temperature (caused by light absorption of the cell medium) that could have generated a thermal stress and cell death. However, the absorption of the cell medium (including the culture dish) is constant over the 1250–1290 nm range (data not shown). Therefore, the temperature increase depends not on the laser wavelength but only on its intensity. The pronounced wavelength dependence evidenced in the action spectrum plotted in figure 6(a) proves that thermal effects alone cannot induce the death process in our experiments.

Moreover, as described in the previous section, we have performed *ab initio* numerical simulations and *in situ* temperature measurements that allow prediction of the temperature increase. For the experiments presented in figure 6(a), the maximum temperature within the laser spot is $T_{max} \sim 43\,°C$ for an average laser intensity of ∼100 W cm^{-2} and an incubator temperature regulated at $T_{inc} = 37\,°C$. With the same average intensity, the light-induced death phenomenon is not changed when T_{inc} is decreased to 30 °C, which corresponds to $T_{max} \sim 36\,°C$. Note that, using the incubator without any laser, we have also additionally checked that MCF-7 cells do not die after a 3 h long pure-thermal stress at 43 °C. Therefore we conclude that 1270 nm irradiation can induce cell death from $^1O_2$ production without the implication of any thermal effect.

3.3. *Effect of strong singlet oxygen quenchers*

1270 nm irradiation has been performed in the presence of strong $^1O_2$ quenchers. On one hand, bovine serum albumin (BSA), which has been shown to preferentially quench $^1O_2$ outside the cell [11], has been used as an intracellular quencher. On the other hand, sodium azide (NaN_3), known to readily penetrate the cells [38], is used as an intracellular quencher. For these experiments, cells have been incubated

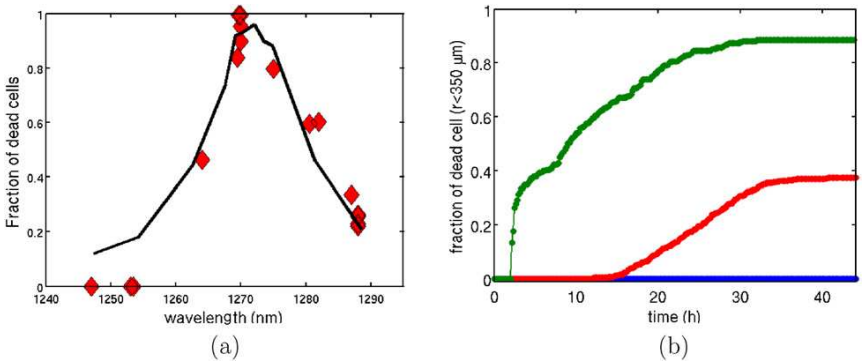

Figure 6. (a) Death action spectrum of laser irradiation around 1270 nm. For these experiments, the laser intensity was 100 W cm^{-2} and the irradiation duration was 3 h. (b) Influence of dissolved oxygen on cell death induced by 1270 nm irradiation. The red curve corresponds to standard oxygen conditions (20% O_2, 5% CO_2, 75% N_2), the green curve to hypoxia (0% O_2, 5% CO_2, 5% N_2) and the blue curve to hyperoxia (100% O_2).

Table 1. Effect of singlet oxygen quencher on 1270 nm induced cell death. The fraction of dead is counted within a radius of $r = 250$ μm around the laser spot. For all experiments the 1270 nm laser intensity was $\sim$200 W cm^{-2} and the duration of the irradiation was 1.5 h.

NaN_3 concentration —	BSA concentration —	Fraction of dead cells ($r < 250$ μm) (%)
0	0	100
10 mM	0	19
0	1 mM	75
0	5 mM	37
10 mM	5 mM	0

two hours before a 200 mW–1 h 30 min irradiation and the quencher is then removed just before the irradiation. Combined use of both quenchers completely inhibits cell death, and both BSA and NaN_3 quenchers lead independently to a strong inhibition of 1270 nm induced cell death. Results for different quencher concentrations are reported in table 1.

The drastic effect of known $^1O_2$ quenchers supports our above conclusions on $^1O_2$ production. Moreover, it is interesting to notice that, in our experiments, the effect of $^1O_2$ is partially inhibited by extracellular quencher. This suggests that part of the $^1O_2$ is generated outside the cell. However, the cell density is quite high in our experiments. The extracellular volume from which $^1O_2$ could diffuse toward the cell membrane in one lifetime is more than 100 times smaller than the volume of the cell itself. This suggests that $^1O_2$ is also produced outside the cell. Indeed, increasing BSA concentration, we were able to totally inhibit cell death.

3.4. Minimal singlet oxygen dose upon 1270 nm irradiation

We now examine the influence of the laser intensity and of the irradiation duration Δt on the 1270 nm light-induced cell death. In all the experiments, the local intensity I can be precisely determined because the laser Gaussian intensity profile is well known. Compiling data from various and multiple experiments, we plot in figure 7 the threshold (minimum) intensity I_{TH} which is required to induce the death of cells as a function of Δt. For irradiation parameters which are in regions (I_{TH}, Δt) lying above the points plotted in figure 7, 100% of the cells systematically die as a result of 1270 nm laser irradiation. On the other hand, irradiations made for parameters (I, Δt) lying below points plotted in figure 7 do not induce cell death.

In order to establish in an unambiguous way the central role taken by the oxidative stress in these experiments, we have performed other control irradiations with a laser wavelength of 1247 nm that is not resonant with the $^3O_2 \longrightarrow {}^1O_2$ transition. Cells have been irradiated at 1247 nm with intensities I and durations Δt identical to those plotted in figure 7. In all these experiments, no cell death has been observed at 1247 nm.

Oxidative stress induced by irradiations at 1270 nm always triggers the death process when the light fluence $F = I \times \Delta t$ exceeds a threshold fluence F_{TH}. Data plotted in

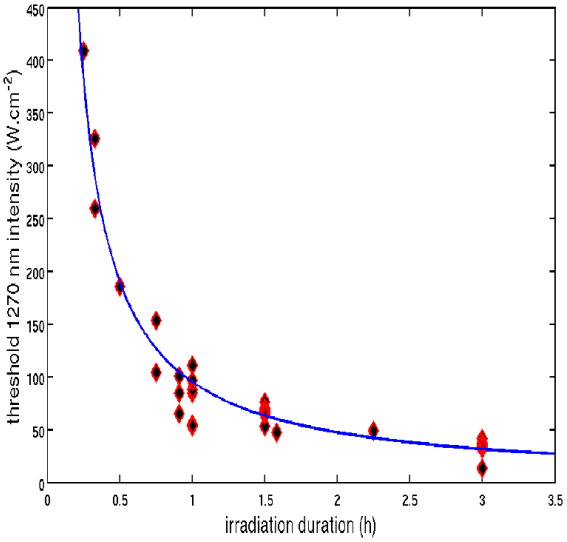

Figure 7. Threshold (minimum) 1270 nm laser intensity required to kill cells versus the irradiation time.

figure 7 can indeed be fitted by the function $I_{TH} = F_{TH}/\Delta t$, with $F_{TH} = 95$ W cm^{-2} h. This threshold fluence F_{TH} is associated with a cumulative $^1O_2$ concentration (defined as the integral over the irradiation time of the $^1O_2$ production rate) already introduced in conventional PDT [39]. From the value of F_{TH} and of the cross section of the $^3O_2 \longrightarrow {}^1O_2$ transition ($\sim 10^{-23}$ cm^2 [21]), we have determined a minimum cumulative $^1O_2$ concentration of $\sim$4.6 mM. It is very interesting to note that this value is comparable with those found in standard PDT experiments [7, 39–42].

4. Conclusions

We have designed temperature-controlled experiments to discriminate various forms of stress imposed on biological cells by laser irradiation. We have studied the effect of a 1270 nm radiation, which is resonant with the electronic transition from the ground state of molecular oxygen to its singlet state, so called singlet oxygen. We have shown that the 1270 nm laser irradiation does induce cell death and that the lethal effect strongly depends on the laser wavelength. We have obtained a death action spectrum which is strongly correlated to the absorption spectrum of molecular oxygen. The fraction of dead cells depends on the quantity of oxygen dissolved in the culture media, and experiments made with strong singlet oxygen quenchers also inhibit the laser induced death phenomenon. From all these experiments we conclude that 1270 nm laser irradiation induces cell death via activation of $^1O_2$. By measuring *in situ* the laser induced temperature increase, we have shown that cell death can be obtained without the implication of any thermal stress. Finally, we have determined a minimal dose of singlet oxygen that is required to induce cell death. This dose is comparable to the one found in conventional PDT experiments.

First, it is interesting to compare the fluence used in this work with that reported by Yusupov *et al* for *in vivo* tumor

eradication upon 1270 nm [25]. The minimal dose necessary to induce cell death in our experiments is three orders of magnitude greater than the one used *in vivo* for the removal of human basalioma. Such a difference does not imply that the cytotoxic effects reported *in vivo* are not due to $^1O_2$ creation. This suggests that tumor removal may not arise from direct cell death. On one hand, very interesting secondary effects triggered by $^1O_2$ creation, such as an immune response, may have induced tumor removal. On the other hand, thermal stress has to be considered also *in vivo*. Even if temperature measurements might not be trivial *in vivo*, the use of a control 1250 nm radiation may help to discriminate the various cytotoxic effects arising from 1270 nm illumination.

Finally, this new way to create singlet oxygen in biological media, from light irradiation alone, without a PS, has implications for phototherapy but it also represents a key tool for a tightly controlled creation of reactive oxygen species. For example, it can be used to study oxidative stress in specific cellular compartments [4, 10] in order to probe molecular events such as secondary ROS generation [4, 5] or other cellular stress response.

References

[1] Dougherty T J, Gomer C J, Henderson B W, Jori G, Kessel D, Koberlik M, Moan J and Peng Q 1998 Photodynamic therapy *J. Natl Cancer Inst.* **90** 889–905

[2] Dolmans D E J G J, Fukumura D and Jain R K 2003 Photodynamic therapy for cancer *Nature Rev.* **3** 380–7

[3] Ogilby P R 2010 Singlet oxygen: there is indeed something new under the sun *Chem. Soc. Rev.* **39** 3181–209

[4] Castano A P, Demidova T N and Hamblin M R 2005 Mechanisms in photodynamic therapy: part two—cellular signalling, cell metabolism and modes of cell death *Photodiagn. Photodyn. Ther.* **2** 1–23

[5] Castano A P, Demidova T N and Hamblin M R 2004 Mechanisms in photodynamic therapy: part one—photosensitizers, photochemistry, and cellular localization *Photodiagn. Photodyn. Ther.* **1** 279–93

[6] Foote C S 1968 Mechanisms of photosensitized oxidations *Science* **162** 963–70

[7] Georgakoudi I, Nochols M G and Foster T H 1997 The mechanism of photofrin© photobleaching and its consequences for photodynamic dosimetry *Photochem. Photobiol.* **65** 135–44

[8] Georgakoudi I and Foster T H 1998 Singlet oxygen *versus* non-singlet oxygen-mediated mechanisms of sensitizer phobleaching and their effects on photodynamic dosimetry *Photochem. Photobiol.* **67** 612–25

[9] Castano A P, Demidova T N and Hamblin M R 2005 Mechanisms in photodynamic therapy: part three—photosensitizer pharmacokinetics, biodistribution, tumor localization and modes of tumor destruction *Photodiagn. Photodyn. Ther.* **2** 91–106

[10] Redmond R W and Kochevar I E 2006 Spatially resolved cellular responses to singlet oxygen *Photochem. Photobiol.* **82** 1178–86

[11] Snyder J W, Skovsen E, Lambert J D C, Poulsen L and Ogilby P R 2006 Optical detection of singlet oxygen from single cells *Phys. Chem. Chem. Phys.* **8** 4280–93

[12] Kuimova M K, Yahioglu G and Ogilby P R 2009 Singlet oxygen in a cell: spatially dependent lifetimes and quenching rate constants *J. Am. Chem. Soc.* **131** 332–40

[13] Skovsen E, Snyder J W, Lambert J D C and Ogilby P R 2005 Lifetime and diffusion of singlet oxygen in a cell *J. Phys. Chem.* B **109** 8570–3

[14] Mulliken R S 1928 Interpretation of the atmospheric oxygen bands; electronic levels of the oxygen molecule *Nature* **122** 505

[15] Schweitzer C and Schmidt R 2003 Physical mechanisms of generation and deactivation of singlet oxygen *Chem. Rev.* **103** 1685–757

[16] Long C and Kearns D R 1973 Selection rules for the intermolecular enhancement of spin forbidden transitions in molecular oxygen *J. Chem. Phys.* **59** 5729–36

[17] Ogilby P R 1999 Solvent effects on the radiative transitions of singlet oxygen *Acc. Chem. Res.* **32** 512–9

[18] Losev A P, Nichiporovich I N, Byteva I M, Drozdov N N and Jghgami I F 1991 The perturbing effect of solvents on the luminescence rate constant of singlet molecular oxygen *Chem. Phys. Lett.* **181** 45–50

[19] Krasnovsky A A Jr and Ambartzumian R V 2004 Tetracene oxygenation caused by infrared excitation of molecular oxygen in air-saturated solutions: the photoreaction action spectrum and spectroscopic parameters of the $^1\Delta_g \longleftarrow {}^3\Sigma_g^-$ transition in oxygen molecules *Chem. Phys. Lett.* **400** 531–5

[20] Krasnovsky A A, Roumbal Ya V, Ivanov A V and Ambartzumian R V 2006 Solvent dependance of the steady-state rate of $^1O_2$ generation upon excitation of dissolved oxygen by cw 1267 nm laser radiation in air-saturated solutions: estimates of the absorbance and molar absorption coefficients of oxygen at the excitation wavelength *Chem. Phys. Lett.* **430** 260–4

[21] Krasnovsky A A, Roumbal Ya V and Strizhakov A A 2008 Rates of $^1O_2$ ($^1\Delta_g$) production upon direct excitation of molecular oxygen by 1270 nm laser radiation in air-saturated alcohols and micellar aqueous dispersions *Chem. Phys. Lett.* **458** 195–9

[22] Krasnovsky J A A, Drozdova N N, Roumbal Ya V, Ivanov A V and Ambartzumian R V 2005 Biophotonics of molecular oxygen: activation efficiencies upon direct and photosensitized excitation *Chin. Opt. Lett.* **3** S1–4

[23] Zakharov S D and Ivanov A V 1999 Light-oxygen effect in cells and its potential applications in tumour therapy (review) *Quantum Electron.* **29** 1031–53

[24] Ivanov A V, Zkharov S D and Mashalov A A 2005 The light oxygen effect as the analogue of photodynamic effect and its possibility in tumour therapy *Prog. Biomed. Opt. Imaging* **6** 59730U

[25] Yusupov A S, Goncharov S E, Zalevski I D, Paramonov V M and Kurkov A S 2010 Raman fiber laser for the drug-free photodynamic therapy *Laser Phys.* **20** 357–9

[26] Anquez F, El Yazidi Belkoura I, Randoux S, Suret P and Courtade E 2011 Cancerous cell death from sensitizer free photo-activation of singlet oxygen *Photochem. Photobiol.* **88** 167–74

[27] Palzer R J and Heidelberger C 1973 Studies on the quantitative biology of hyperthermic killing of HeLa cells *Cancer Res.* **33** 415–21

[28] Lepock J R 2003 Cellular effects of hyperthermia : relevance to the minimum dose for thermal damage *Int. J. Hyperthermia* **19** 252–6

[29] Lepock J R 2005 How do cells respond to their thermal environment? *Int. J. Hyperthermia* **8** 681–7

[30] Anquez F, Courtade E, Sivery A, Suret P and Randoux S 2010 A high-power tunable Raman fiber ring laser for the investigation of singlet oxygen production from direct laser excitation around 1270 nm *Opt. Express* **18** 22928–36

[31] Kroemer G *et al* 2005 Calssification of cell death: recommandations of the nomenclature committe on cell death *Cell Death Differ.* **12** 1463–7

[32] Jauregui H O, Hayner N T, Driscoll J L, Williams-Holland R, Lipsky M H and Galletti P M 1981 Trypan blue dye uptake and lactate dehydrogenase in adult rat hepatocytes-freshly isolated cells, cell suspensions, and primary monolayer cultures *In vitro* **17** 1100–10

[33] Sakakibara J and Adrian R J 1999 Whole field measurement of temperature in water using two-color laser induced fluorescence *Exp. Fluids* **26** 7–15

[34] Peterman E J G, Gittes F and Schmidt C F 2003 Laser-induced heating in optical traps *Biophys. J.* **84** 1308–16

[35] Ebert S, Travis K, Lincoln B and Gluck J 2007 Fluorescence ratio thermometry in a microfluidic dual-beam laser trap *Opt. Express* **15** 15493–9

[36] Hetch F, Pironneau O, Le Hyaric A and Ohtsua K 2010 *Freefem++ manual* Laboratoire Jacques Louis Lions, Paris www.freefem.org/ff++/

[37] Holman J P 2001 *Heat Transfert: Eighth SI Metric Edition* (New York: Mcgraw-Hill)

[38] Leary S C, Hill B C, Lyons C N, Carlson C G, Michaud D, Kraft C S, Ko K, Glerum D M and Moyes C D 2002 Chronic treatment with azide *in situ* leads to an irreversible loss of cytochrome c oxidase activity via holoenzyme dissociation *J. Biol. Chem.* **277** 11321

[39] Dysart J S, Singh G and Patterson M S 2005 Calculation of singlet oxygen dose from photosensitizer fluorescence and photobleaching during mTHPC photodynamic therapy of MLL Cells *Photochem. Photobiol.* **81** 196–205

[40] Niedre M J, Secord A J, Patterson M S and Wilson B C 2003 *In vitro* tests of the validity of singlet oxygen luminescence measurements as a dose metric in photodynamic therapy *Cancer Res.* **63** 7986–94

[41] Weishaupt K R, Dougherty T J and Gomer C J 1976 Identification of singlet oxygen as the cytotoxic agent in photo-inactivation of a murine tumor *Cancer Res.* **36** 2326–9

[42] Coutier S, Mitra S, Bezdetnaya L N, Parache R M, Georgakoudi I, Foster T H and Guillemin F 2001 Effects of fluence rate on cell survival and photobleaching in meta-tetra-(hydroxyphenyl) chlorin-photosensitized Colo 26 multicell tumor spheroids *Photochem. Photobiol.* **73** 297–303

Publications photochimie

A high-power tunable Raman fiber ring laser for the investigation of singlet oxygen production from direct laser excitation around 1270 nm

Francois Anquez, Emmanuel Courtade, Aude Sivéry, Pierre Suret and Stéphane Randoux

Laboratoire de Physique des Lasers, Atomes et Molécules, UMR CNRS 8523, Université Lille 1, Sciences et Technologies, F-59655 Villeneuve d'Ascq, France

pierre.suret@univ-lille1.fr

Abstract: We report on the development of a tunable Raman fiber ring laser especially designed for the investigation of the $^3\Sigma_g^- \rightarrow {}^1\Delta_g$ transition of molecular oxygen. Singlet oxygen ($^1\Delta_g$) is a reactive species of importance in the fields of biology, photochemistry, and phototherapy. Tunability of the Raman fiber ring laser is achieved without the use of an intracavity tunable bandpass filter and the laser thus achieves a slope efficiency only obtained up to now in Perot-Fabry cavities. A measurement of the action spectrum of a singlet oxygen trap is made in air-saturated ethanol and acetone to demonstrate the practical application of the tunable Raman fiber ring laser for the investigation of the $^3\Sigma_g^- \rightarrow {}^1\Delta_g$ transition of molecular oxygen.

OCIS codes: (140.3510) Laser, fiber; (140.3550) Laser, Raman; (260.5130) Photochemistry

References and links

1. M. D. Mermelstein, C. Headley, J.-C. Bouteiller, P. Steinvurzel, C. Horn, K. Feder, and B. J Eggleton, "Configurable three-wavelength Raman fiber laser for Raman amplification and dynamic gain flattening," IEEE Photon. Technol. Lett. **13,** 1286-1288 (2001).
2. B. A. Cumberland, S. V. Popov, J. R. Taylor, O. I. Medvedkov, S. A. Vasiliev, and E. M. Dianov, "2.1 μm continuous-wave Raman laser in GeO_2 fiber," Opt. Lett. **32,** 1848–1850 (2007).
3. A. S. Kurkov, E. M. Dianov, V. M. Paramonov, A. N. Gur'yanov, A. Yu. Laptev, V. F. Khopin, A. A. Umnikov, N. I. Vechkanov, O. I. Medvedkov, S. A. Vasil'ev, M. M. Bubnov, O. N. Egorova, S. L. Semenov, and E. V. Pershina, "High-power fibre Raman lasers emiting in the 1.24-1.34μm range," Quantum Elec. **30,** 791–793 (2000).
4. D. A. Chestnut and J. R. Taylor, "Wavelength-versatile subpicosecond pulsed lasers using Raman gain in figure-of-eight fiber geometries," Opt. Lett. **30,** 2982–2984 (2005).
5. Claude Aguergaray, David Mchin, Vladimir Kruglov et John D. Harvey, "Experimental realization of a Mode-locked parabolic Raman fiber oscillator," Opt. Express **18,** 8680 (2010).
6. E. Bélanger, M. Bernier, D. Faucher, D. Côté, and R. Vallée, "High-power and widely tunable all-fiber Raman laser," IEEE J. Lightwave Technol. **26,** 1696–1701 (2008).
7. A. S. Kurkov, V. M. Paramonov, O. I. Medvedkov, I. D. Zalevskii, and S. E. Goncharov, "Fiber Raman laser at 1450 nm for medical applications," Laser Physics **18,** 1234–1237 (2008).
8. A. S. Yusupov, S. E. Goncharov, I. D. Zalevskii, V. M. Paramonov, and A. S. Kurkov, "Raman fiber laser for the drug-free photodynamic therapy," Laser Physics **20,** 357–359 (2010).
9. P. C. Reeves-Hall and J. R. Taylor, "Wavelength tunable CW Raman fibre ring laser operating at 1486-1551 nm," Electron. Lett. **37,** 491–492 (2001).
10. D. Georgiev, V. P. Gapontsev, A. G. Dronov, M. Y. Vyatkin, A. B. Rulkov, S. V. Popov, and J. R. Taylor, "Watts-level frequency doubling of a narrow line linearly polarized Raman fiber laser to 589 nm," Opt. Express **13,** 6772–6776 (2005).

#132404 - $15.00 USD Received 27 Jul 2010; revised 24 Sep 2010; accepted 25 Sep 2010; published 14 Oct 2010

11. S. A. Babin, D. V. Churkin, S. I. Kablukov, M. A. Rybakov and A. A. Vlasov, "All-fiber widely tunable Raman fiber laser with controlled output spectrum," Opt. Express **15,** 8438–8443 (2007).
12. T. J. Dougherty, C. J. Gomer, B. W. Henderson, G. Jori, D. Kessel, M. Korbelik, J. Moan and Q. Peng, "Photodynamic Therapy", J. Nat. Canc. Inst. **90,** 889–905 (1998).
13. D. E.J.G.J. Dolmans, D. Fukumura and R. K. Jain, "Photodynamic therapy for cancer", Nature **3,** 380–387 (2003).
14. A. G. Griesbeck, A. Bartoschek, J. Neudrfl and C. Miara, "Stereoselectivity in Ene Reactions with $^1O_2$:Matrix Effects in Polymer Supports, Photo-oxygenation of Organic Salts and Asymetric Synthesis", Photochem. Photobiol. **82,** 1233–1240 (2006).
15. C. Long and D. R. Kearns, "Selection rules for the intermolecular enhancement of spin forbidden transitions in molecular oxygen, "J. Chem. Phys. **59,** 5729–5736 (1973).
16. A.P. Losev, I.N. Nichiporovich, I.M. Byteva, N.N. Drozdov and I.F.Al Jghgami, "The perturbing effect of solvents on the luminescence rate constant of singlet molecular oxygen," Chem. Phys. Lett. **181** 45–50 (1991).
17. P. R. Ogilby, "Solvent Effects on the radiative transitions of singlet oxygen ," Acc. Chem. Res. **32,** 512–519 (1999).
18. A. A. Krasnovsky, Jr., N. N. Drozdova, V. Ivanov, and R. V. Ambartzumian, "Activation of Molecular Oxygen by Infrared Laser Radiation in Pigment-Free Aerobic Systems," Biochemistry (Moscow) **68,** 963-966 (2003).
19. A.A. Krasnovsky, Jr. and R. V. Ambartzumian, "Tetracene oxygenation caused by infrared excitation of molecular oxygen in air-saturated solutions : the photoreaction action spectrum and spectroscopic parameter of the $^1\Delta_g \leftarrow\!\!- ^3\Sigma_g$ transition in oxygen molecules" Chem. Phys. Lett. **400,** 531-535 (2004).
20. A. A. Krasnovsky, Jr., N. N. Drozdova, Ya. V. Roumbal, A. V. Ivanov, and R. V. Ambartzumian, "Biophotonics of molecular oxygen: activation efficiencies upon direct and photosensitized excitation," Chinese Opt. Lett. **3,** S1–S4 (2005).
21. A. A. Krasnovsky, Jr., Ya. V. Roumbal, A. V. Ivanov, and R. V. Ambartzumian, "Solvent dependence of the steady-state rate of $^1O_2$ generation upon excitation of dissolved oxygen by cw 1267 nm laser radiation in air-saturated solutions: Estimates of the absorbance and molar absorption coefficients of oxygen at the excitation wavelength," Chem. Phys. Lett. **430,** 260–264 (2006).
22. A. A. Krasnovsky, Jr., Ya. V. Roumbal, and A. A. Strizhakov, "Rates of $^1O_2$ ($^1\Delta_g$) production upon direct laser excitation of molecular oxygen by 1270 nm laser radiation in air-saturated alcohols and micellar aqueous dispersions," Chem. Phys. Lett. **458,** 195–199 (2008).
23. R. K. Jain, C. Lin, R. H. Stolen, W. Pleibel, and P. Kaiser, "A high-efficiency tunable CW Raman oscillator," Appl. Phys. Lett. **30,** 162–164 (1977).
24. C. Lin, R. H. Stolen, W. G. French, and T. G. Malone, "A cw tunable near-infrared (1.085-1.175-μm) Raman oscillator," Opt. Lett. **30,** 96–97 (1977).
25. G. Qin, M. Liao, T. Suzuki, A. Mori, and Y. Ohishi, "Widely tunable ring-cavity tellurite fiber Raman laser," Opt. Lett. **33,** 2014–2016 (2008).
26. Y. Han, C. Kim, J. U. Kang, U. Paek, and Y. Chung, "Multiwavelength Raman fiber-ring laser based on tunable cascaded long-period fiber gratings," IEEE Photon. Technol. Lett. **15,** 383–385 (2003).
27. Y. Han, S. B. Lee, C. Kim, and M. Y. Jeong, "Voltage-tuned multiwavelength Raman ring laser with high tunability based on a single fiber Bragg grating," Appl. Opt. **47,** 6099–6102 (2008).
28. S. V. Chernikov, N. S. Platonov, D. V. Gapontsev, D. Chang, M. J. Guy, and J. R. Taylor, "Raman fibre ring laser operating at 1.24 μm," Electronics Lett. **34,** 680–681 (1998).

1. Introduction

Compared with traditional solid-state lasers, fiber lasers nowadays available present many significant advantages in terms of compactness, reliability and flexibility. In particular continuous-wave pumped all-fiber Raman lasers are versatile light sources which are virtually able to deliver high-power radiation at any wavelength across the $1-2.1$ μm spectral region [1, 2, 3]. Raman fiber lasers (RFLs) have also been shown to exhibit many attractive capabilities such as multiwavelength operation, pulsed emission or tunability [4, 5, 6]. Nowadays RFLs have many applications in various fields such as fiber sensing, fiber telecommunications, material processing but also in surgery and in the treatment of some oncological diseases [7, 8].

Tunable RFLs have been initially developed with the first objective to provide tunable Raman gain in telecommunication fiber amplifiers [9] but they have also been used for fiber device testing and for fiber sensor systems. With the recent development of frequency-doubled RFLs generating visible light, it has been additionally argued that a combination of frequency doubling and tuning in RFLs may provide new sources replacing dye or Ti:Sa lasers [10, 11].

#132404 - $15.00 USD Received 27 Jul 2010; revised 24 Sep 2010; accepted 25 Sep 2010; published 14 Oct 2010

In this paper, we report on the development of a tunable RFL especially designed for the investigation of the $^3\Sigma_g^- \rightarrow ^1\Delta_g$ transition of molecular oxygen. The singlet $^1\Delta_g$-state ($^1O_2$), commonly called singlet oxygen, is the first electronic excited state of the oxygen molecule. It is a metastable state in which molecular oxygen is highly reactive. The singlet state $^1O_2$ of molecular oxygen has been extensively studied for its chemical affinity with biomolecules in photodynamic therapy of cancers [12, 13] and for chemical synthesis [14].

The transition $^3\Sigma_g^- \rightarrow ^1\Delta_g$ of molecular oxygen is forbidden at electric dipolar approximation. In practice, this means that both absorption and emission probabilities are very low for the isolated molecule (gas phase). Nevertheless, interactions in dense phase of molecular oxygen with surrounding molecules of inorganic solvents may enhance the radiative process [15, 16, 17] whose efficiency may be increased by three orders of magnitude compared with gas phase[16].

The mechanisms through which solvents modify the properties of $^3\Sigma_g^- \rightarrow ^1\Delta_g$ molecular oxygen's transition are not fully understood. Although several models have been developed to investigate this question, experimental data are difficult to obtain because of (*i*) weakness of absorption and emission of the considered transition, (*ii*) low efficiency of detectors in this spectral region [22] and (*iii*) poor availability of high power reliable laser sources around 1270 nm.

In this context, Yusupov *et al.* have recently demonstrated a RFL delivering a power of 5.5 Watt at a wavelength of 1262 nm. From direct optical excitation of oxygen, they have successfully employed this source for the treatment of oncological diseases [8]. Although oxygen-dependent effects are presumably coupled to thermal effects in the experiments of Ref. [8], the results obtained by Yusupov *et al.* open promising perspectives for the use of RFLs in the field of cancer therapy. From a more fundamental point of view, Krasnovsky *et al.* have demonstrated that it is possible to obtain the spectrum of the $^3\Sigma_g^- \rightarrow ^1\Delta_g$ transition together with an estimation of molar absorption coefficients in various air saturated organic solvents [18, 19, 20, 21, 22]. With the goal of mimicking the mechanisms of the biological effects arising from laser irradiation, they have used the photooxygenation reaction of $^1O_2$ with a specific trap, 1,3−diphenylisobenzofuran (DPIBF), which leads to colorless endoperoxydes. The variation of absorbance of the trap around 410 nm provides the photooxygenation rate which is linked to the absorption coefficient of molecular oxygen.

A high power narrow-linewidth laser tunable around 1270 nm is of great interest for the investigation of direct creation of singlet oxygen both for medical applications and for more fundamental studies of the transition $^3\Sigma_g^- \rightarrow ^1\Delta_g$ of oxygen molecules in various solvents. From the latter point of view, such a laser would permit to measure the action spectra of the $^1O_2$ traps around 1270 nm with a good resolution. Up to now, most of the measurements of photooxygenation rates of DPIBF have been performed by using either diode lasers or a wavelength-tunable forsterite laser delivering 200 − 250 ns pulses [20, 21, 22]. The wavelength of the diode lasers used cannot be tuned and the peak of their output power spectrum did not necessarily coincide with the maximum of the photooxygenation action spectrum. Moreover their output power did not exceed 700 mW. Although the forsterite laser previously used can be tuned between 1200 nm and 1290 nm, its linewidth of 3 nm was relatively high and its mean power cannot be increased above 120 mW [21].

In this paper we demonstrate a high-power tunable RFL operating in a simple geometry and constructed only from commercially-available fiber components. The RFL linewidth is around 1 nm and its wavelength can be continuously tuned from 1240 nm to 1289 nm to precisely measure the action spectra of $^1O_2$ traps. The RFL delivers a total Stokes power of $\sim$ 2.5 Watt at the maximum available pump power of $\sim$ 7 Watt. Its output power is almost constant at tuning in the 1240 − 1289 nm tuning range. The configuration of the laser cavity is presented in Sec. 2 and it is compared with other configurations previously reported. Laser performances in terms

#132404 - $15.00 USD Received 27 Jul 2010; revised 24 Sep 2010; accepted 25 Sep 2010; published 14 Oct 2010

of output power and tunability are described in Sec. 3. In Sec. 4, a measurement of the action spectrum of a singlet oxygen trap is made in air-saturated ethanol and acetone to demonstrate the practical application of the tunable laser for the investigation of the $^3\Sigma_g^- \rightarrow ^1\Delta_g$ transition of molecular oxygen.

2. Laser design

Tunability is a property of RFLs which has been investigated from the early developments of these lasers in the 1970s [23, 24]. From this date, several techniques to tune RFLs have been proposed. Various cavity geometries have been studied and several types of fibers have been made to increase tunability ranges and output powers. A recent review about the history of development of tunable RFLs can be found in Section 1 of Ref. [6]. Here we will only provide a brief summary of the principles of operation and of the performances currently reached by tunable RFLs operating both in Fabry-Perot and in ring geometries.

RFLs oscillating inside Perot-Fabry cavities can be tuned over several tens of nanometers by using two main techniques. The beam bending technique consists in gluing the fiber Bragg grating (FBG) mirrors of the laser cavity on a plexiglas beam which may be bent thus providing a mechanical tuning of the RFL [11]. Another technique consists in applying a purely axial compression on the FBGs which are embedded in a highly deformable polymer[6]. Using a tunable Ytterbium-doped fiber laser and a phosphosilicate fiber as Raman active medium, a RFL tunable in the range $1258-1300$ nm has been demonstrated with the beam bending technique [11]. Using a 1064-nm Ytterbium-doped fiber laser and a germanosilicate fiber as Raman active medium, a RFL tunable in the range $1075-1135$ nm has been demonstrated by using the axial compression technique of FBGs [6]. Both RFLs are able to deliver Stokes output powers of a few Watt with slope efficiencies around 70%.

In ring cavities, the RFL tunability is commonly achieved from the insertion of a tunable optical bandpass filter inside the laser cavity. The tuning ranges of tunable Raman fiber ring lasers (TRFRLs) which have been demonstrated so far can be wider than tuning ranges of RFLs oscillating in Perot-Fabry cavities. In particular a tuning range of ~ 100 nm (from 1495 nm to 1600 nm) has been recently reported in a Raman laser made with a tellurite fiber [25]. A tuning range in excess of 65 nm from 1486 to 1551 nm has been demonstrated in a TRFRL made with a germanosilicate fiber [9]. However the germanosilicate and the tellurite TRFRLs have maximum Stokes output powers of 420 mW and ~ 500 mW, respectively. TRFRLs demonstrated up to now have typical efficiencies around $\sim 25\%$ and their output powers is lower than tunable RFLs constructed from Perot-Fabry cavities. Note that this point is not necessarily detrimental for telecommunication applications and that several low-power multiwavelength TRFRLs have been designed for wavelength-division-multiplexing systems [26, 27].

Wavelength dense multiplexers (WDMs), circulators or fiber couplers are often used to build ring lasers. As these fiber components do not have pronounced wavelength-dependent losses, ring geometries easily favor multiwavelength Stokes emission [28]. Tunable bandpass filters are therefore used to introduce wavelength-dependent losses inside the laser cavity thus providing single-wavelength emission with a tunability which is often limited by the performances of the optical filter itself. Here we propose a simple ring configuration in which the only narrow-bandwidth of the Raman gain curve of a phosphosilicate fiber (see Fig. 1 of Ref. [7]) is used to restrict the RFL Stokes emission to a single wavelength. With this configuration the use of an intracavity bandpass filter is not required and the RFL is simply tuned by tuning the wavelength of the pump laser.

Our TRFRL is schematically shown in Fig. 1. The pump laser is a commercially-available Ytterbium-doped fiber laser (Manlight ML10-CW-R-OEM-TUNE-1080) which is tunable between 1060 nm and 1100 nm. It delivers a randomly-polarized output beam with a maximum

#132404 - $15.00 USD Received 27 Jul 2010; revised 24 Sep 2010; accepted 25 Sep 2010; published 14 Oct 2010

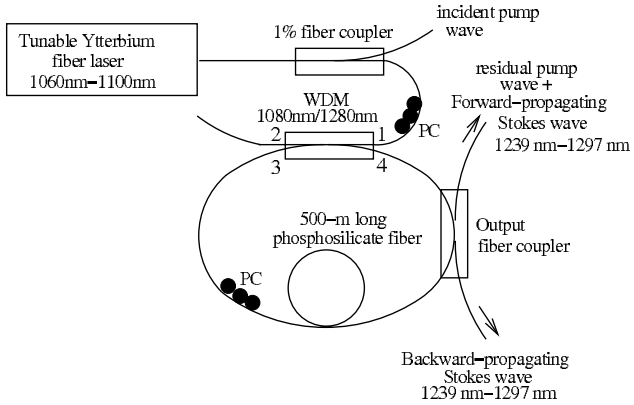

Fig. 1. Schematic representation of the tunable Raman fiber ring laser. PC: Polarization Controller

output power of 7 Watt. The pump light is launched inside the fiber cavity from port 1 to port 3 of a 1080 nm /1280 nm WDM coupler. As in Ref. [3, 11], we have used a phosphosilicate fiber having a large P_2O_5 shift of ~ 40 THz as compared to the Stokes shift of ~ 13.3 THz in germanosilicate fibers. With this phosphosilicate fiber the Stokes wavelength is shifted from only one Stokes cascade in the wavelength region of interest for the investigation of the formation of singlet oxygen (i.e., around 1280 nm).

The TFRFL oscillates in a ring cavity which is formed by recoupling the output end of the 500–m long phosphosilicate fiber at port 4 of the WDM. With the ring cavity arranged in this way, cavity losses vary according to a sine function of wavelength which is maximum around 1080 nm and minimum around 1280 nm. As the P_2O_5-related gain peak of the phosphosilicate fiber is also around 1280 nm, one could first imagine that Stokes emission will simply build up only in this wavelength region. However a SiO_2-related Raman gain bandwidth grows around 1350 nm concomitantly with the emergence of the 1280 nm Stokes component. As the cavity losses are relatively weak around 1350 nm, the RFL can easily deliver two Stokes lines and the radiation around 1350 nm can become much more intense than the radiation around 1280 nm at high pump power. To eliminate this dual-wavelength operation, we have chosen to increase cavity losses in order to push the power threshold of the Stokes component at 1350 nm above the maximum pump power available (i.e., 7 Watt in our setup). As shown in Fig. 1, this has been achieved from the insertion of a 80/20 (manufacturer data) fiber coupler inside the laser cavity. With this intracavity coupler, the power threshold for Stokes emission around 1280 nm is increased around 4 Watt but the fraction of Stokes power extracted from the laser cavity is as high as $\sim 80\%$, which gives a high slope efficiency.

3. Laser performances

In the TRFRL presented in Fig. 1, a forward-propagating pump wave and a forward-propagating Stokes wave copropagate in the counterclockwise direction whereas only a backward-propagating Stokes wave circulates in the clockwise direction. The power carried by the backward-propagating Stokes wave has been simply measured by using a power-meter. Measuring the spectral power density of forward-propagating light over a wavelength span ranging from 1050 nm to 1300 nm by using an optical spectrum analyzer (OSA), we have computed the ratio between the powers carried by the pump wave and by the forward-propagating Stokes wave. From an additional measurement of the total power carried by forward-propagating light, we have simply obtained the power carried by the forward-

#132404 - $15.00 USD Received 27 Jul 2010; revised 24 Sep 2010; accepted 25 Sep 2010; published 14 Oct 2010

propagating Stokes wave and by the pump wave.

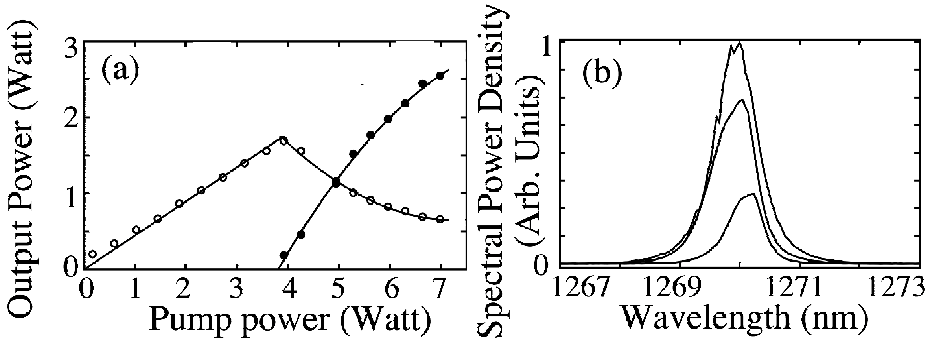

Fig. 2. (a) Power characteristics of the tunable Raman fiber ring laser measured at the output fiber coupler. The pump wavelength is 1085 nm and the Stokes wavelength is 1268 nm. Filled circles : total Stokes power, empty circles : transmitted pump power. (b) Power spectra of the forward-propagating Stokes wave at incident pump powers of 4.9 W, 5.6 W and 7 W. The pump wavelength is 1087 nm and the Stokes wavelength is $\sim$ 1270 nm.

Figure 2(a) shows the power characteristics of our TRFRL measured for a pump wavelength of 1085 nm which produces Stokes emission around $\sim$ 1268 nm. The total Stokes power plotted in Fig. 2(a) is the sum of powers carried by the forward- and the backward-propagating Stokes waves which are extracted from the cavity at the output fiber coupler (see Fig. 1). The laser power threshold is around $\sim$ 3.7 Watt and the Stokes power delivered at the maximum available pump power of 7 Watt is around $\sim$ 2.5 Watt. The corresponding slope efficiency of $\sim$ 75% is close to the efficiency of tunable RFLs oscillating in Perot-Fabry cavities [6, 11].

In the TRFRL shown in Fig. 1, the ratio between the powers carried by the forward- and backward-propagating Stokes waves can be adjusted by using the two fiber polarization controllers (PCs) schematically represented in Fig. 1. Adjusting the PCs, we have found that it is possible to reduce the power of backward-propagating Stokes wave down to a negligible level thus maximizing the power of the forward-propagating Stokes wave. However this kind of operating regime does not correspond to a situation in which the *total* Stokes power is maximized. We have found that the total Stokes power is maximized when the Stokes powers carried by forward- and backward-propagating Stokes waves are roughly comparable. The power characteristics presented in Fig. 2(a) have been obtained by incrementing the incident pump power by steps of $\sim$ 0.3 Watt and by slightly readjusting the PCs at each step in order to get the maximum Stokes power. Let us emphasize that the TRFL is placed into a environment-isolated box and as far as the pump power and the PCs are fixed, the fluctuations of the powers carried by forward- and backward-propagating Stokes waves do not exceed a few percent over several hours.

Figure 2(b) shows the optical power spectra of the forward-propagating Stokes wave. These spectra have been recorded at three different pumping levels and for a pump wavelength of 1087 nm. The full-width at half-maximum (FWHM) of the Stokes spectra approximately increases from $\sim$ 0.5 nm to $\sim$ 1 nm when the pump power is increased from 4.9 W to 7 W. The TFRFL output power spectrum presents a bell-shaped profile which does not vary much with the incident pump power. This feature is very different from the one found in RFLs oscillating in Perot-Fabry cavities which have spectra taking a double-peak structure at high incident pump power [11].

Figure 3(a) shows that the wavelength of Stokes emission linearly varies with the wavelength of the tunable pump laser. Our TRFRL laser can be tuned over 49 nm from 1240 nm to 1289

#132404 - $15.00 USD Received 27 Jul 2010; revised 24 Sep 2010; accepted 25 Sep 2010; published 14 Oct 2010

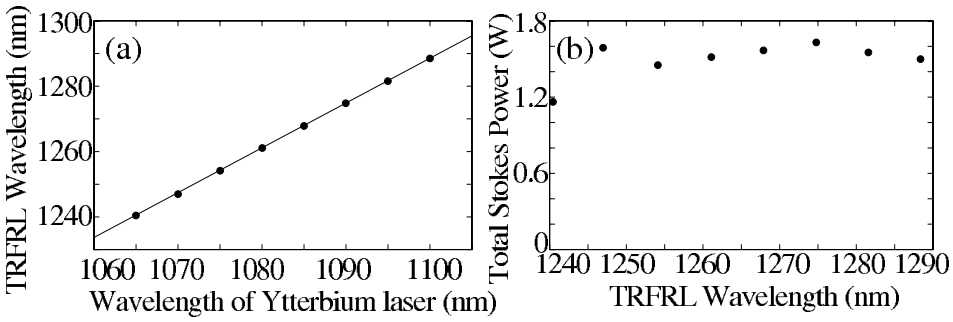

Fig. 3. (a) TRFRL generation wavelength as a function of the wavelength of the pump laser. (b) TRFRL output power as a function of its wavelength for an incident pump power of ~ 5.3 Watt.

nm by tuning the pump laser between 1065 nm and 1100 nm. The tuning range is not limited by any bandpass filter but only by the tuning range of the pump laser. As shown Fig. 3(b), approximately 1.6 Watt of total Stokes power is delivered over the whole tuning range at an incident pump power of ~ 5.3 Watt. This power is more than three times greater than the maximum power previously measured in TRFRLs made with intracavity bandpass filters [9, 25]. In our setup the Stokes power could be increased to ~ 2.5 Watt over the whole tuning range but a significant amount of Stokes light may then be fed back towards the pump laser. To avoid a subsequent damage of the Ytterbium fiber laser, the level of optical feedback towards the pump source has been continually monitored. Using the maximum pump power of 7 Watt, we have been able to tune our TRFRL from ~ 1250 nm to ~ 1280 nm at its maximum output Stokes power of ~ 2.5 Watt without the risk of damaging the pump source. The tuning range at high power will be extended in the near future by inserting a fiber isolator between the Ytterbium fiber laser and the TRFRL.

4. Measurement of the action spectrum of DPIBF in air-saturated ethanol and acetone

In this section, our TRFRL is used to measure the absorption spectrum of the $^3\Sigma_g^- \rightarrow ^1\Delta_g$ transition of molecular oxygen into two distinct solvents. As shown by Krasnovsky *et al.*, measurement of photoxygenation rate of chemical traps can be used for this purpose [18, 19, 20, 21, 22]. Krasnovsky *et al.* have demonstrated that 1270 nm irradiation causes degradation of DPIBF dissolved in air saturated solutions. This degradation is due to directly-excited singlet oxygen ($^1\Delta_g$) which reacts with DPIBF leading to colorless endoperoxydes. The decrease of the concentration of DPIBF is monitored through a decrease in the absorbance of the solution at a wavelength of 410 nm which coincides with an absorption band of DPIBF. The $^1O_2$ production rate is directly proportional to the concentration of DPFIB which is known from the variation of absorbance at 410 nm according to Beer-Lambert's law.

Figure 4 shows the normalized action spectra of DPIBF photooxygenation in air-saturated ethanol and acetone upon irradiation of the TRFRL. The spectra are normalized to the maximum photoxoygenation rate for each solvent. In these experiments, the concentration of DPIBF is $\sim 50\ \mu$ mol.L^{-1} both in ethanol and acetone. The solutions which are placed into a cubic quartz cell of 1 cm long and 1 cm large are illuminated around 1270 nm over a duration of 10 min. The volume of the solutions is 1.4 mL. The solutions are shaken during all the irradiation to prevent any sedimentation of the trap. The diameter of the infrared beam irradiating the quartz cell is ~ 1.6 mm and its power was ~ 0.35 W.

The variation of absorption of DPIBF is monitored by a 405 nm laser beam, simply by measuring the laser power transmitted before and after irradiation. The diameter of the blue

#132404 - $15.00 USD Received 27 Jul 2010; revised 24 Sep 2010; accepted 25 Sep 2010; published 14 Oct 2010

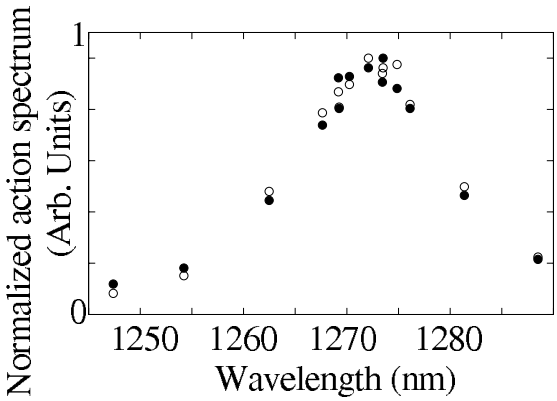

Fig. 4. Normalized action spectra on DPIBF dissolved in air-saturated ethanol (filled circles) and in acetone (empty circles) upon irradiation of the TRFRL between 1247 nm and 1289 nm.

laser beam is 8 mm and its power was $\sim 2\ \mu$W. The relation between the measured laser power and the trap concentration reads

$$ln(\frac{P_0}{P_f}) = -\varepsilon\,([T]_0 - [T]).L \tag{1}$$

where P_0 and P_f are the powers of the blue laser before and after irradiation, respectively. $[T]_0$ and $[T]$ are the DPIBF concentrations (in mol.L^{-1}) before and after irradiation, respectively. L is the path length of the blue light and ε is the molar absorption coefficient of DPIBF. Using the value of $\varepsilon = 2.35 \times 10^4$ M^{-1}cm^{-1} in ethanol [21] and $L = 1$ cm, the photooxygenation rate can be easily obtained from

$$V_r = \frac{[T]_0 - [T]}{\Delta t} \tag{2}$$

where V_r is the photooxygenation rate and Δt is the time of irradiation.

Our results confirm that the maximum of absorption the spectrum of the $^3\Sigma_g^- \rightarrow {}^1\Delta_g$ molecular oxygen band is located at 1273 ± 1 nm, as in previous studies by Krasnovsky *et al.* [21]. The width of the action spectra is ~ 15 nm FWHM both for acetone and ethanol. It is comparable with values previously reported by Losev [16]. Furthermore the relative photooxygenation rates in acetone and ethanol coincide with the values reported by Kransovsky *et al.* [21].

5. Conclusion

In this paper we have demonstrated a high-power RFL which can be continuously tuned between 1240 nm and 1289 nm. The laser design is simple and the cavity is constructed only from commercially-available fiber components. Contrary to ring lasers previously demonstrated, the laser wavelength is not tuned from an intracavity tunable bandpass filter but by tuning the wavelength of the pump laser, the narrow bandwidth of the phosphosilicate gain curve being exploited to restrict the laser emission to a single wavelength component. The RFL tuning range is thus only limited by the tuning range of the pump laser. The TRFRL presents a slope efficiency of $\sim 75\%$ which is comparable to the slope efficiency of RFLs oscillating in Perot-Fabry cavities. It delivers a total Stokes power of ~ 2.5 Watt at the maximum available pump power of ~ 7 Watt.

We estimate that the TRFRL demonstrated in the present paper can be of a specific interest for the investigation of direct creation of singlet oxygen both for medical applications and

#132404 - $15.00 USD Received 27 Jul 2010; revised 24 Sep 2010; accepted 25 Sep 2010; published 14 Oct 2010

for more fundamental studies of the $^3\Sigma_g^- \rightarrow ^1\Delta_g$ transition of oxygen molecules in various solvents. In water, some questions concerning the determination of the 1,3-diphenylbenzofuran photooxidation rate remain open [22]. In this solvent, the quantity of dissolved oxygen is about ten times less than in acetone and ethanol. We have demonstrated that the TRFRL can be used for the reliable measurement of action spectrum of DPIBF in air-saturated ethanol and acetone with only 300 mW of 1270 nm light. With a maximum output power greater than 2 Watt, the TRFRL presented here could thus overcome the weak absorption of molecular oxygen in water. Moreover the designed TRFRL is only limited in terms of accordability and delivered output power by the pump laser. The tunable TRFRL thus opens the possibility to investigate in photochemistry the excitation band of singlet oxygen in solution phases where shifts in the absorption can be important [16].

#132404 - $15.00 USD Received 27 Jul 2010; revised 24 Sep 2010; accepted 25 Sep 2010; published 14 Oct 2010

Chemical Physics Letters 555 (2013) 252–257

Contents lists available at SciVerse ScienceDirect

Chemical Physics Letters

journal homepage: www.elsevier.com/locate/cplett

Singlet oxygen ($^1O_2$) generation upon 1270 nm laser irradiation of ground state oxygen ($^3O_2$) dissolved in organic solvents: Simultaneous and independent determination of $^1O_2$ production rate and reactivity with chemical traps

A. Sivéry [a,1], F. Anquez [a,1], C. Pierlot [b], J.M. Aubry [b], E. Courtade [a,*]

[a] Université de Lille Nord de France, Laboratoire de Physique des Lasers, Atomes et Molécules, UMR 8523 – Université Lille 1, 59655 Villeneuve d'Ascq, France
[b] Université de Lille Nord de France, Laboratoire de Chimie Moléculaire et Formulation, EA-CMF 4478 – ENSCL et Université Lille 1, 59655 Villeneuve d'Ascq, France

ARTICLE INFO

Article history:
Received 12 April 2012
In final form 22 October 2012
Available online 12 November 2012

ABSTRACT

Direct photo-production of singlet oxygen, *via* 1270 nm laser excitation of molecular oxygen, has been the focus of recent articles. The chemical traps 1,3-diphenylisobenzofuran and rubrene are used to monitor singlet oxygen production in organic solvents through the $O_2[^3\Sigma_g^-] \rightarrow O_2[^1\Delta_g]$ transition. In this Letter evolution of the trap concentration is monitored continuously and we propose a new and simple method to measure singlet oxygen production rate. We derive an analytical expression for the trap disappearance rate that allows simultaneous and independent determination of the 1270 nm absorption cross section and the half quenching concentration with the chemical trap.

1. Introduction

Singlet oxygen ($^1O_2[^1\Delta_g]$) is the lowest electronic excited state of molecular oxygen (O_2). Its high chemical reactivity confers it a central role in many chemical and biological photo-oxidation processes [1–3]. In liquids, efficient $^1O_2$ photo-production is commonly achieved *via* activation by visible light of a photo-sensitising molecule (PS). The excited triplet state of the PS transfers its energy to molecular oxygen leading to various reactive oxygen species and, in particular, singlet oxygen ($^1O_2$) [4,5].

This type of process makes $^1O_2$ a key intermediate in several fields from polymer science to biology [3]. In biochemistry, it is indeed involved in plants photosynthesis [6] as well as used clinically in photodynamic therapy for the eradication of cancer cells [1,2]. There is thus a need for water soluble probes in order to characterise $^1O_2$ properties in biochemical system. Such molecular probes have been synthesised to trap or detect this species specifically [7–9]. For example one can mention Singlet Oxygen Sensor Green© which has been designed for optical microscopy [10]. However, quantitative analysis of the data using this probe can be biased [3,11] and, moreover, $^1O_2$ production *via* a PS is a complex dynamic system from which it might be difficult to learn.

In this context, the simplified scheme of direct photosensitiser-free $^1O_2$ photo-production, despite its poor efficiency, naturally appears as a powerful tool for the understanding of $^1O_2$ chemistry. Since $^1O_2$ has been highlighted as a key intermediate in photo-oxidation processes [12], direct excitation of $^1O_2$ has been the focus of several papers in gas phase or liquids [13–18] and in biology [19–22]. For the isolated molecule, this optical transition of molecular oxygen (Eq. 1) is strongly forbidden [5,23]. It is thus poorly efficient and very sensitive to the perturbing effects of the surrounding environment of the oxygen molecule [5,13,24]. Indeed, the absorption cross section or spontaneous emission rate of dissolved oxygen molecules is always enhanced by collisions with solvents [5,13,25,26].

More recently, Krasnovsky et al. have found that 1270 nm high power irradiation causes photo-oxidation of photosensitiser-free solutions of tetracene and 1,3-diphenylisobenzofuran (DPIBF) at normal temperature and pressure in organic solvents [15]. They have shown that this photo-oxidation process occurs through the reaction of DPIBF with $^1O_2$ produced *via* the $^3O_2[^3\Sigma_g^-] \rightarrow {}^1O_2[^1\Delta_g]$ 1270 nm transition [15–18] as described by reactions 1–4:

$$^3O_2 + h\nu_{1270} \rightarrow {}^1O_2 \quad (1)$$

$$^1O_2 \xrightarrow{k_d} {}^3O_2 \quad (2)$$

$$^1O_2 + T \xrightarrow{k_q} {}^3O_2 + T \quad (3)$$

$$^1O_2 + T \xrightarrow{k_r} TO_2 \quad (4)$$

Singlet oxygen is produced *via* the transition $^3O_2[^3\Sigma_g^-] \rightarrow {}^1O_2[^1\Delta_g]$ at 1270 nm (reaction 1). k_d is the pseudo first order kinetic rate

* Corresponding author.
E-mail address: emmanuel.courtade@univ-lille1.fr (E. Courtade).
[1] These authors contributed equally to this work.

0009-2614/$ - see front matter © 2012 Elsevier B.V. All rights reserved.
http://dx.doi.org/10.1016/j.cplett.2012.10.063

constant of singlet oxygen deactivation in the solvent, defined as: $k_d = 1/\tau_\Delta$ where τ_Δ is the lifetime of singlet oxygen in the absence of trap. T is either the DPIBF or rubrene chemical trap, k_q and k_r are the rate constants of singlet oxygen physical and chemical quenching by T respectively. TO_2 is the primary oxidation product of reaction 4.

The use of a high power 1270 nm laser for direct photosensitiser-free creation of $^1O_2$ opens new opportunities for, on the one hand, fundamental studies of the $^3O_2[^3\Sigma_g^-] \rightarrow {}^1O_2[^1\Delta_g]$ transition and, on the other hand, quantitative characterisation of $^1O_2$ fluorescent chemical probes.

In this Letter, following the work of Krasnovsky and co-workers, we aim to provide quantitative insights on (i) $^1O_2$ production rate following direct excitation and (ii) interactions of this species in liquid solvents. We use an specially designed high power laser tunable around 1270 nm [27] to study the reaction kinetics of two chemical traps (DPIBF and rubrene) with $^1O_2$. We set up an experiment that allows real time measurement of the trap concentration and derive a simple analytical expression for its consumption rate. This reaction rate depends only on two parameters which can be expressed in terms of basic physical constants: the half quenching concentration β("reactivity index" [28,29]) and the absorption cross section of the $^3O_2[^3\Sigma_g^-] \rightarrow {}^1O_2[^1\Delta_g]$ transition (σ_{1270}). Studying reaction kinetics of T, both σ_{1270} and β can be determined simultaneously and independently.

2. Theory

The two traps used in this Letter (DPIBF and rubrene) are very reactive towards $^1O_2$: k_r is closed to the so-called diffusion limit [3]. Physical quenching is negligible compared to chemical quenching ($k_q \ll k_r$) [30]. Thus the kinetics of reaction of the species in a solution containing a $^1O_2$ chemical trap upon 1270 nm irradiations (as depicted by reactions 1–4) can be described by the two following equations:

$$\frac{d[^1O_2]}{dt} = \Gamma - k_d[^1O_2] - k_r[^1O_2][T] \tag{5}$$

$$\frac{d[T]}{dt} = -k_r[^1O_2][T] \tag{6}$$

where $\Gamma = \sigma_{1270} I[O_2]$ is the $^1O_2$ production rate (mol L $^{-1}$ s $^{-1}$). This production rate depends on the 1270 nm photon flux I (photon s $^{-1}$ cm $^{-2}$), on the concentration of dissolved oxygen, $[O_2]$ (mol L $^{-1}$), and on the absorption cross section σ_{1270} (cm^2).

In our experiments, the solution is stirred in a quartz cell in contact with air, and oxygen is continuously renewed in the liquid phase. Estimating the consumption of dissolved oxygen during the duration of a full experiment of irradiation, one can expect a decrease of ~6% in the concentration of $^3O_2$ which has a negligible effect on the kinetics of $^1O_2$ production and reactivity (see Supplementary materials for numerical calculations and simulations). Therefore, the concentration of dissolved oxygen may be considered as constant during the trap photodegradation experiment. In this condition, Γ is a constant depending only on the 1270 nm laser power.

Evolution of the amount of the two different species occurs at two well separated time scales. A lower value for the time scale of $^1O_2$ variation can be expressed as follows: $\tau_{^1O_2} = (k_d + k_r[T]_0)^{-1}$. For DPIBF, an upper value for the time scale variation is determined when $[^1O_2]$ is maximum: $\tau_T = (k_r[^1O_2]_\infty)^{-1}$, where $[^1O_2]_\infty = \Gamma/k_d$. For an initial DPIBF concentration of $[T]_0 \sim 10^{-4}$ mol L $^{-1}$, using the values of k_d and k_r in acetone [30] and a value of $\sigma_{1270} \sim 10^{-23}$ cm^2 [15–17]: $\tau_{^1O_2} \sim 10^{-5}$ s $\ll \tau_T \sim 10^4$ s. It is thus clear that quasi-steady-state approximation can be applied to $^1O_2$ and Eq. 5 and 6 can be simplified as follow:

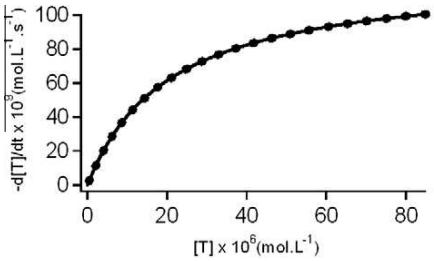

Figure 1. Comparison of Eq. 8 and numerical simulations of the full non-linear system (Eqs. 5 and 6). Both curves are evaluated with values of parameters determined in Section 4 ($\beta = k_d/k_r = 1.7 \times 10^{-5}$ mol L^{-1} and $\Gamma = 1.25 \times 10^{-7}$ mol L^{-1} s^{-1}). Eq. 8 (solid line) and numerical simulations (black dots) show a near perfect agreement for a wide range of parameters. Indeed the relative mean square error is smaller than 10^{-5} for a set of parameters in the ranges: $10^{-6} < \beta < 10^{-4}$ and $10^{-8} < \Gamma < 10^{-6}$.

$$[^1O_2] = \frac{\Gamma}{k_d + k_r[T]} \tag{7}$$

$$\frac{d[T]}{dt} = -\frac{\Gamma}{1 + \beta[T]^{-1}} \tag{8}$$

where $\beta = k_d/k_r$ is the reactivity index. It represents the trap concentration at which the quenching of $^1O_2$ by solvent molecules (k_d) equals the decay due to the total quenching by T ($k_r[T]$).

In order to confirm the validity of Eq. 8 one can simulate the full non-linear system (Eqs. 5 and 6). Figure 1 shows a comparison of numerical simulations and analytical expressions for a typical experiment in acetone. A near perfect agreement between numerical calculations of the full non-linear system and analytical solution (Eq. 7 and 8) is found over several decades for each parameters (Γ, β).

Two limiting cases can be found for the kinetics of the trap disappearance. At the beginning of the experiment, T is in excess ($[T] \gg \beta$), then $-d[T]/dt \approx \Gamma$ is only limited by $^1O_2$ production rate. When $[T]$ becomes smaller ($[T] \ll \beta$), one can approximate $-d[T]/dt \approx \Gamma[T]/\beta$. In the next section, we show that our experimental set up allows the simultaneous and independent determination of both Γ and β.

3. Experimental

We set up an experiment to perform kinetics measurement of the trap concentration in a solution irradiated with a 1270 nm laser. DPIBF (1,3-diphenylisobenzofuran, 97%, Aldrich) and rubrene are used as traps in experiments performed in several organic solvent: acetone (99.5%, Sigma Aldrich), acetone d_6 (99.9%, Sigma Aldrich), ethanol (99.8%, Sigma Aldrich) and in toluene (99.5%, Acros Organics).

Reaction of $^1O_2$ with DPIBF leads to colourless oxidation products. Thus the trap concentration can be monitored *via* the 410 nm band of DPIBF by measuring the absorbance of the solution [15–17]. Using a spectrometer (Perkin Elmer, lambda 19) we verify that normalised absorption spectra of DPIBF before and after 1270 nm irradiation superimpose almost perfectly in the visible range (data not shown). This means that the oxidised products of the reaction does not induce any shift or distortion in the visible part of the spectrum. This allows us to use a single laser, whose wavelength matches the DPIBF absorption spectrum (405 ± 1 nm, Roithner Laser), to measure DPIBF concentration in the solution. A value of $\epsilon_{405} \approx 2.27 \times 10^4$ L mol^{-1} cm^{-1} is taken for the molar absorption coefficient of DPIBF in all solvents to take into account the relative absorbance between 405 and 410 nm ($\epsilon_{410} \approx 2.35 \times 10^4$ L mol^{-1} cm^{-1}) used in [15–17]. Measurements of ϵ_{405} using either

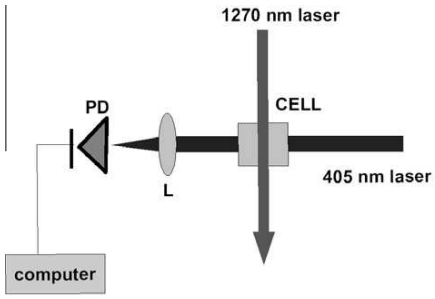

Figure 2. Scheme of the experimental set-up for measurement of DPIBF consumption rate upon 1270 nm excitation of $^3O_2$ [27]. The trap concentration is monitored by a 405 nm laser beam focused on a photodiode (PD) by a lens (L). The 1270 nm and the 405 nm lasers intersect in the quartz cell containing DPIBF solutions saturated with air. For rubrene solutions, the 405 nm laser is replaced by a 532 nm laser.

the 405 nm laser or the spectrometer give consistent results. DPIBF is a reference compound for $^1O_2$ trapping in organic solvents due to its high reactivity [31]. However the primary oxidation product is an unstable ozonide which cleaves into the dibenzoylbenzene plus an unknown oxygenated product [32,33]. In order to check that the ozonide and its degradation products do not change the kinetics, we confirm our results by using rubrene which gives a stable endoperoxide with $^1O_2$. The same set-up is used to study the kinetic reaction of $^1O_2$ with rubrene. The rubrene concentration is monitored *via* its 525 nm absorption band with a 532 nm laser, using a molar absorption coefficient of $\epsilon_{532} \approx 9.5 \times 10^3$ L mol $^{-1}$ cm $^{-1}$.

A scheme of the experimental set-up is represented in Figure 2. Solutions of DPIBF ($\sim$100 μmol L $^{-1}$) are placed in a quartz cell of $1 \times 1 \times 5$ cm^3 (Hellma). The volume of the solutions is 1,4 ml. Fresh DPIBF solutions are stocked in the dark, at room temperature and in contact with air at least several hours before irradiation. Solutions are gently shaken with a small magnetic bar and kept in contact with air during all experiment.

Two lasers are used: a Raman fiber ring laser operating at 1270 nm (FWHM $\sim$1 nm) [27] for $^1O_2$ production and a laser emitting at 405 nm (532 nm) for the monitoring of [DPIBF] ([Rubrene]). These two laser beams are perpendicular and intersect in the quartz cell. The diameter of the infrared beam irradiating the quartz cell is $\sim$3 mm with a power $\sim$1 W measured with a power meter (Ophir). The beam diameter of laser which monitor $[T]$ is adjusted to $\sim$8 mm in order to homogeneously cover all the section of the solution (except the magnetic bar). To prevent bleaching of the trap, the laser power is reduced down to a power of $\sim$10 μW and is switched using a mechanical shutter opened $\sim$1 s every 30 s. Irradiations last for 20–90 min, depending on the solvent. DPIBF is known to be very sensitive to daylight [34], so the whole set up is covered. We perform several experiments in DPIBF solutions without 1270 nm irradiation in each solvent: no variation of 405 nm absorbance is detected for time as long as 90 min (data not shown). This confirms that DPIBF disappearance results solely from the 1270 nm irradiation.

4. Results

DPIBF absorbance is monitored and followed during the full duration of an experiment. Figure 3 represents the decay of DPIBF concentration with time in two organic solvents: acetone and acetone d_6, when the solutions are irradiated with the 1270 nm laser. The values found for β (rescaled to the initial DPIBF concentration $[T]_0$) in the two solvents are also represented.

As described in Section 2, variation of the trap consumption rate $(-d[T]/dt)$ with the trap concentration $[T]$ during irradiation

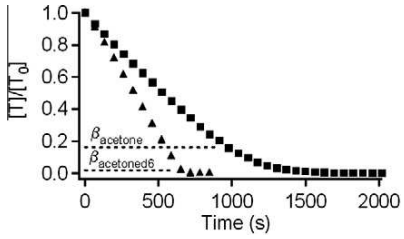

Figure 3. Evolution of DPIBF concentration as a function of time in two air-saturated solvents: acetone (squares) and acetone d_6 (triangles) when the solutions are irradiated by the 1270 nm laser. The experimental values found for β are represented and rescaled to the initial concentration of DPIBF $[T]_0 \sim 110$ μmol L^{-1} in acetone and $[T]_0 \sim 83$ μmol L^{-1} in acetone d_6.

contains information on both parameters: $^1O_2$ production rate, Γ and reactivity index β. Data obtained for each experiment performed in acetone and acetone d_6 upon irradiation at 1270 nm ($P \sim 1.1$ W $\pm$ 1%) are presented in Figure 4.

A reliable fit of the data is obtained using the following expression:

$$-\frac{d[T]}{dt} = \frac{a}{1 + b[T]^{-1}} \tag{9}$$

where $a = \Gamma$ and $b = \beta$.

Singlet oxygen production rate, Γ is unambiguously determined by parameter a. One finds in acetone $\Gamma = 1.29 \times 10^{-7}$ mol L^{-1} s^{-1} $\pm$ 2%. The average 1270 nm photon flux in our experiment is:

$$I = \frac{P_0 L}{h\nu V_{sol}} \times \left(\frac{1 - e^{-\alpha L}}{\alpha L}\right) \times K_{\text{quartz}} \tag{10}$$

in photon cm^{-2} s^{-1}, where $P_0 = 1.1$ W is the laser power and $L = 1$ cm is the length of the quartz curve, $h\nu$ is the energy of 1270 nm photons, $V_{sol} = 1.4$ ml is the volume of the solution in the cell, α is the linear absorption coefficient at 1270 nm of the solvent, due to inactive absorption of laser light which is $\sim$0,04 cm $^{-1}$ in acetone and K_{quartz} ($\sim$0,94) is the absorption of laser light by the first side of the quartz cell. Using the value of $[O_2] = 2.4 \times 10^{-3}$ mol L^{-1} [35] one obtains in acetone $\sigma_{1270} = 11.8 \times 10^{-24}$ cm^2 $\pm$ 3% and $\beta = 1.80 \times 10^{-5}$ mol L^{-1} $\pm$ 4%. In acetone d_6 $\Gamma = 1.38 \times 10^{-7}$ mol L^{-1} s^{-1} $\pm$ 3%, using the same parameters for the analysis one can find $\sigma_{1270} = 12.4 \times 10^{-24}$ cm^2 $\pm$ 4% and $\beta = 1.78 \times 10^{-6}$ mol L^{-1} $\pm$ 21%. The values of the absorption cross section of

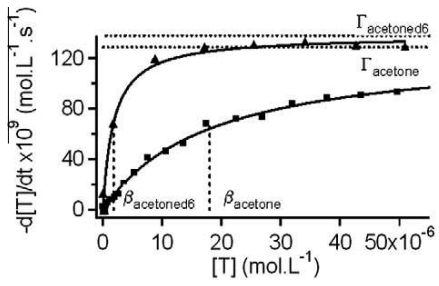

Figure 4. DPIBF consumption rate in acetone (squares) and acetone d_6 (triangles). The 1270 nm laser power is 1.1 $W \pm 1\%$. With a and b as free parameters, one can determine from a fit (solid line) using Eq. 8: $\Gamma = 1.29 \times 10^{-7}$ mol L^{-1} s^{-1} $\pm$ 2% and $\beta = 1.80 \times 10^{-5}$ mol L^{-1} $\pm$ 4% in acetone and $\Gamma = 1.38 \times 10^{-7}$ mol L^{-1} s^{-1} $\pm$ 3% and $\beta = 1.78 \times 10^{-6}$ mol L^{-1} $\pm$ 21% in acetone d_6, where the uncertainties are evaluated from correlation coefficient. The horizontal and vertical dotted lines represent the experimental values found for Γ and β respectively, in protonated and deuterated acetone.

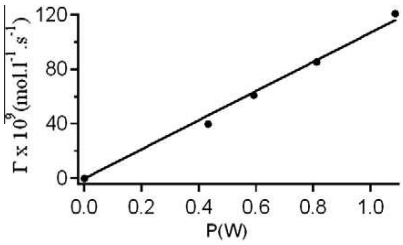

Figure 5. Production rate of singlet oxygen in acetone as a function of the infrared laser power. From a linear fit, one can evaluate $\sigma_{1270} = 10.6 \times 10^{-24}$ cm$^2 \pm 3\%$ using Eq. 10. The obtained value of σ_{1270} is in good agreement with the data reported in Table 1.

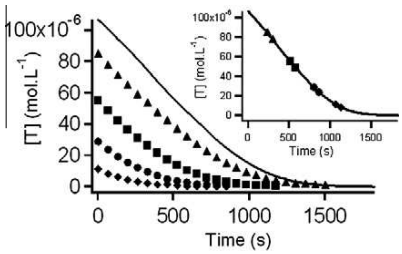

Figure 6. Effect of the degradation products on the kinetic of the trap disappearance rate. Five different concentrations of DPIBF from 100 to 10 μmol L^{-1} in acetone are irradiated at 1270 nm. For small variation of the trap concentration ($\Delta[T] \sim 10\%$), DPIBF degradation is linear in time. The slopes corresponding to small variation in DPIBF concentration (80 μmol L^{-1} in triangles, 50 μmol L^{-1} in squares, 30 μmol L^{-1} in circles and 10 μmol L^{-1} in rhombus) have been reported in the inset of the figure and matches the entire kinetic of the trap degradation (solid line) where $[T_0] \sim 100$ μmol L^{-1}.

molecular oxygen in protonated and deuterated acetone are both in very good agreement.

In order to investigate the influence of potential heating due the infrared laser on the DPIBF photooxygenation rate, experiments at different laser powers up to 1.1 W are performed. A maximum of 5 °C increase of temperature is measured in the quartz cell. Figure 5 represents the rate of $^1O_2$ production as a function of the infrared laser power in acetone. One can indeed estimate σ_{1270}, from the linear dependence of Γ with P_0. A value of $\sigma_{1270} = 10.6 \times 10^{-24}$ cm$^2 \pm 3\%$ is found, which is in very good agreement with the data reported in Table 1. We thus conclude that for the IR laser power used in these experiments, heating (which should increase with laser power) has no effect on the production rate of $^1O_2$.

Dependence of $^1O_2$ production rate with dissolved oxygen concentration has been evaluated (see Supplementary materials) as in [36,37]. The solvent is saturated by bubbling oxygen in the solution for 20 min with a thin capillary. The value of Γ is found to be 4.94 times higher than the one in solution saturated with air ($\Gamma = 6.28 \times 10^{-7}$ mol L^{-1} s^{-1} for the solution saturated with oxygen compared to 1.27×10^{-7} for the other solution). Γ is thus proportional to the dissolved oxygen concentration and the production rate of $^1O_2$ can be greatly enhanced by saturating the solution with $^3O_2$. In oxygen-free solutions (obtained by bubbling ultra pure nitrogen for 1 h) no degradation of the trap is observed upon a 1 h irradiation at 1270 nm.

In order to test if the accumulation of the degradation products (caused by DPIBF degradation) could influence the oxygenation rate of DPIBF, two kinds of experiments have been performed. In the first experiment, a solution of DPIBF in acetone ($[T_0] \sim 100$ μmol L^{-1}) is irradiated at 1270 nm. When all DPIBF has been consumed, fresh DPIBF is dissolved again in the photo degraded solution at ~100 μmol L^{-1} and irradiated again in the same conditions. In these two experiments, the trap kinetics are exactly the same (see Supplementary materials). In order to confirm this result, starting from a solution of DPIBF in acetone at ($[T_0] \sim 100$ μmol L^{-1}), dilutions are realised to obtain four different DPIBF concentrations. All the solutions are completely degraded within the same 1270 nm irradiations (see Figure 6). When small portion of the trap is degraded ($\Delta[T] \sim 10\%$), the trap degradation is linear in time (detailed analysis of the trap kinetics degradation for such conditions have been performed in [15,16,37]). The slopes of DPIBF oxygenation rate for small variation of the trap concentration, are reported in the inset of Figure 6 and matches the entire kinetics of the trap disappearance where $[T_0] \sim 100$ μmol L^{-1}. All these experiments clearly show that the degradation products do not cause any decline of the DPIBF concentration during its photo reaction

Table 1
σ^1_{1270}, and β^a are determined experimentally using DPIBF in different solvents by evaluating parameters a and b of Eq. 9 as described in Section 4. The uncertainties for the estimations are standard deviations upon five experiments. The measured linear absorption coefficient of the solvent and the literature value of dissolved oxygen concentration are reported. The values of τ_Δ take into account the water content [43] of the tested organic solvents using literature values of τ_Δ in pure solvents. For acetone d_6, considering the purity of the solvent (99.9%) and the scattering range of singlet oxygen lifetime, any correction on those lifetime are made. k_r^a is calculated using the estimated values of τ_Δ. The initial concentration of DPIBF is $[T]_0 \approx 100$ μmol L^{-1} and the 1270 nm laser power is set to 1.1 W in all experiments. Minimum and maximum values of β and k_r are reported from [30].

Solvents	τ_Δ (μs)	$[^3O_2]$ (10^{-3} mol L^{-1})	$\alpha_{solvent}$	β (10^{-5} mol L^{-1})	k_r (10^8 L mol^{-1} s^{-1})	σ_{1270} (10^{-24} cm^2)
Acetone	47.5 [5]	2.4 [35]	0.04	$1.8 \pm 10\%^a$ 5 – 9.4 [30]	11.7^a 4.1 – 17 [30]	$11.5 \pm 3\%^a$ $8.0 \pm 10\%$ [37] $6.9 \pm 10\%$ [15] $6.6 \pm 10\%$ [17] $8.8 \pm 15\%$ [18]
Acetone d_6	$690 \pm 3\%$ [38] 992 [5] $410 \pm 5\%$ [39]	2.4	0.04	$0.2 \pm 14\%^a$	7.9^a 5.0^a 13.3^a	$12.6 \pm 3\%^a$
Toluene	$27.8 \pm 10\%$ [40]	1.8 [35]	0.04	$4.2 \pm 7\%^a$ 4 – 12 [30]	8.6^a 4.3 – 8.9 [30]	$34.8 \pm 4\%^a$ 44.4 [41] 15.5 [15]
Ethanol	13.9 [42]	2.1 [35]	0.34	$9.1 \pm 13\%^a$ 6.5 – 20 [30]	7.9^a 4.3 – 13 [30] 11[17] 14[18]	$17.7 \pm 7\%^a$ $12.6 \pm 10\%$ [37] $9.2 \pm 10\%$ [15] $9.9 \pm 10\%$ [17] $8.4 \pm 15\%$ [18]

with singlet oxygen, and thus do not affect the values of σ_{1270} and β.

5. Discussion

Experiments described in the above section have been repeated in different organic solvents. Experimental data and their analysis are reported in the section Supplementary materials.

The mean values of σ_{1270} and β measured from five different experiments in each solvent, are reported in Table 1. For comparison, the literature values of σ_{1270} are also reported. Maximum and minimum values of β and k_r in each solvents are also reported from the review of Wilkinson et al. [30]. In ethanol and toluene, the experimental values found for β are in good agreement with the literature data. In acetone the value for β found in this Letter is not in the range of reported value from [30]. This could be explained by the weak values of τ_Δ used to calculate β in these papers. In all the tested organic solvents, the calculated values of k_r are in the range of the reported value of [30]. As it has been observed in other studies [18,42,44] and this Letter, the values of k_r are solvent dependent.

To our knowledge, estimation of σ_{1270} in liquid solvent have only been reported by Krasnovsky et al. [15–18]. Values reported for acetone in [17,18,37] range from 6.6×10^{-24} to 8.8×10^{-24} cm^2. Our estimation, from Figure 5, is 1.2 to 1.6 higher. In ethanol, σ_{1270} is 17.7×10^{-24} cm^2 compared to published values ranging from 8.4×10^{-24} to 12.6×10^{-24} cm^2 [17,18,37]. Our estimated values of σ_{1270} in acetone and ethanol, are higher than those reported by Krasnovsky et al. while the relative dependence is the same: the ratio between σ_{1270} in ethanol and acetone is approximatively 1.5 (except for the study of [18]).

In order to confirm the value of σ_{1270} found with the DPIBF, same kinetics experiments are performed in acetone d_6 with rubrene. The experimental values found for Γ is 1.43×10^{-7} mol L^{-1} s^{-1} $\pm$ 3% and $\beta = 2.74 \times 10^{-5}$ mol L^{-1} $\pm$ 8%. From Eq. 10, one can estimate the value of $\sigma_{1270} = 11.7 \times 10^{-24}$ cm^2 $\pm$ 4%, which is in very good agreement with the value found with DPIBF.

Let us mention that, using the same analysis described in [15,17,37], *i.e.* calculating the cross section from literature value of β, we also find higher values in acetone and ethanol with several initial DPIBF concentration ($[T]_0 \approx 100$ μmol L^{-1}; 50 μmol L^{-1}) and upon different 1270 nm laser power (1.2 W; 300 mW; 100 mW). From this, one can conclude that such a difference is not due to an experimental artefact and neither to our own analysis of the reaction rate (Eq. 8). We have no explanation for such a difference. However, our data in toluene are close to the value of Losev et al. [41] from high pressure gas phase experiments. In Ref. [16], the authors have mentioned a value two times smaller than the one of [41]. In a more recent paper ([18]), a new method is used to measure the absorption cross section of oxygen in organic solvents and water. σ_{1270} is obtained by comparison of the rates of photooxygenation obtained upon direct excitation of oxygen molecules by IR diodes laser and upon photosensitisation by porphyrins. This new approach gives results consistent with previous works [15–17]. But yet, equal concentrations of DPIBF are required to ensure the acuteness of this new technique and accurate knowledge of singlet oxygen quantum yield generation by the PS is also needed.

6. Conclusion

Summarising our results, we set up an experiment which allows real time measurement of DPIBF concentration $[T]$ upon direct 1270 nm excitation of $^3O_2$. We derive an analytical expression for the trap disappearance rate, $-d[T]/dt$ as a function of the trap concentration during such an experiment. Using this expression, one can determine simultaneously and independently the β, and singlet oxygen production rate Γ. Our approach enables determination of σ_{1270} in a single experiment, *i.e.* without the need of previous knowledge of the reaction rate constant. Comparing the absorption cross section of the $O_2[^3\Sigma_g^-] \rightarrow O_2[^1\Delta_g]$ transition of molecular oxygen found with two different chemical traps, the σ_{1270} values found with DPIBF and rubrene are in very good agreement. Using the kinetics analysis described in this article, one should control the possible effects of the photodegradation products as proposed in part 4.

The fact that singlet oxygen production rate is determined without the need of β knowledge in our Letter, could be useful in experiments where this parameter is unknown or estimated in an indirect way. This is the case for the determination of σ_{1270} in water where DPIBF has to be dissolved using a surfactant (similar experiments are performed in [17,18]). Unfortunately we have not been able to determine unambiguously the value of Γ (and thus σ_{1270}) in water dispersion of surfactant. Indeed, the reader should notice that an initial DPIBF concentration greater than β is necessary for unambiguous determination of Γ. Even by heating the solution, we are not able to dissolve DPIBF in aqueous dispersion at a concentration greater than ~100 μmol L^{-1}. This concentration is not sufficient to observe deviation from the linear regime of the trap disappearance rate. However the method described in this Letter could be of great interest if an efficient water soluble singlet oxygen chemical trap is found or if a more efficient singlet oxygen trap is designed. Furthermore, we believe that the method described in this article provides a simple and reliable tool for singlet oxygen photo-chemistry or photo-physics. For example, it could be used to characterise singlet oxygen fluorescent probes or be combined with time-resolved detection of singlet oxygen phosphorescence which can be difficult to interpret [45].

Acknowledgements

This Letter has been supported by French Ministry of Higher Education and Research. We thank the technical staff of the PhLAM laboratory for its participation in this Letter, D. Leroy (IUT A/Université Lille 1) for the preparation of solutions and S. Randoux and P. Suret for fruitful discussion.

Appendix A. Supplementary data

Supplementary data associated with this article can be found, in the online version, at http://dx.doi.org/10.1016/j.cplett.2012.10.063.

References

[1] T.J. Dougherty et al., J. Natl. Cancer Inst. 90 (1998) 889.
[2] D.E. Dolmans, D. Fukumura, R.K. Jain, Nat. Rev. 3 (2003) 380.
[3] P. Ogilby, Chem. Soc. Rev. 39 (2010) 3181.
[4] C.S. Foote, Science 162 (1968) 963.
[5] C. Schweitzer, R. Schmidt, Chem. Rev. 103 (2003) 1685.
[6] T.G. Owens, Photosynthesis and the Environment, Advance in Photosynthesis and Respiration, vol. 5, Springer, Netherlands, 2004.
[7] V. Nardello, D. Brault, P. Chavalle, J.M. Aubry, J. Photochem. Photobiol. B: Biol. 39 (1997) 146.
[8] V. Nardello, N. Azaroual, I. Cervoise, G. Vermeersch, J.M. Aubry, Tetrahedron Lett. 52 (1996) 2031.
[9] V. Nardello, J.M. Aubry, Tetrahedron Lett. 38 (1997) 7361.
[10] C. Flors et al., J. Exp. Bot. 57 (2006) 1725.
[11] X. Ragàs, A. Jiménez-Banzo, D. Sánchez-García, X. Batllori, S. Nonell, Chem. Commun. 2009 (2009) 2920.
[12] I. Matheson, J. Lee, Chem. Phys. Lett. 7 (1970) 475.
[13] C. Long, D.R. Kearns, J. Chem. Phys. 59 (1973) 5729.
[14] D.R. Kearns, Chem. Rev. 71 (1971) 395.
[15] A.A.J. Krasnovsky, Y.V. Roumbal, A.V. Ivanov, R.V. Ambartzumian, Chem. Phys. Lett. 430 (2006) 260.
[16] A.A.J. Krasnovsky, R.V. Ambartzumian, Chem. Phys. Lett. 400 (2004) 531.
[17] A.A.J. Krasnovsky, Y.V. Roumbal, A.A. Strizhakov, Chem. Phys. Lett. 458 (2008) 195.

Bibliographie

[Abravaya *et al.* 91] K. Abravaya, K. Phillips et R. I. Morimoto. – *Attenuation of the heat shock response in HeLa cells is mediated by the release of bound heat shock transcription factor and is modulated by changes in growth and in heat shock temperatures*. Genes and Development, **5**, 2117–2127 (1991).

[Akerfelt *et al.* 10] M. Akerfelt, R. I. Morimoto et L. Sistonen. – *Heat shock factors : integrators of cell stress, development and lifespan*. Nature Reviews Molecular Cell Biology, **11** (8), 545–555 (2010).

[Anckar et Sistonen 11] J. Anckar et L. Sistonen. – *Regulation of HSF1 Function in the Heat Stress Response : Implications in Aging and Disease. In : Annual Review Of Biochemisrty*, éd. par R. D. Kornberg, C. R. H. Raetz, J. E. Rothman et J. W. Thorner, 1089–1115. – 2011.

[Anquez *et al.* 10] F. Anquez, P. suret, A. Sivery, E. Courtade et S. Randoux. – *A high-power tunable Raman fiber ring laser for the investigation of singlet oxygen production from direct laser excitation around* 1270 *nm*. Optics Express, **18**, 22928 (2010).

[Aubry *et al.* 81] J. M. Aubry, J. Rigaudy et N. K. Cuong. – *Kinetic studies of self-sensitized photo oxygenation in H_2O and D_2O of a water soluble rubrene derivative*. Photochemistry Photobiology, **33**, 155–158 (1981).

[Ballut *et al.* 12] S. Ballut, A. Makky, B. Chauvin, J. P. Michel, A. Kasselouri, P. Maillard et V. Rosilio. – *Tumor targeting in photodynamic therapy. From glycoconjugated photosensitizers to glycodendrimeric one. Concept, design and properties*. Org. Biomol. Chem., **10**, 4485 (2012).

[Bayly *et al.* 63] J. G. Bayly, V. B. Kharta et W. H. Stevens. – *The absorption spectra of liquid phase H_2O, HDO and D_2O from* 0.7 μm *to* 10 μm. Infrared Physics, **3**, 211–223 (1963).

[Bechet *et al.* 10] D. Bechet, P. Couleaud, C. Frochot, M. L. Viriot, F. Guillemin et M. Barberi-Heyob. – *Neuropilin-1 targeting photosensitization-induced early stages of thrombosis via tissue factor release*. Pharm. Research, **27**, 468 (2010).

[Belousov *et al.* 06] V. V. Belousov, A. F. Fradkov, K. A. Lukyanov, D. B. Staroverov, K. S. Shakhbazov, A. V. Terskikh et S. Lukyanov. – *Genetically encoded fluorescent indicator for intracellular hydrogen peroxide*. Nature Methods, **3**, 281 (2006).

[Biamonti et Vourc'h 10] G. Biamonti et C. Vourc'h. – *Nuclear stress bodies*. Cold Spring Harb Perspect Biol., **2**, a000695 (2010).

[Castanoa *et al.* 04] A. P. Castanoa, T. N. Demidova et M. R. Hamblin. – *Mechanisms in photodynamic therapy : part one, photosensitizers, photochemistry and cellular localization.* Photodiagnosis and Photodynamic Therapy, **1**, 279–293 (2004).

[Castanoa *et al.* 05] A. P. Castanoa, T. N. Demidova et M. R. Hamblin. – *Mechanisms in photodynamic therapy : Part three, Photosensitizer pharmacokinetics, biodistribution, tumor localization and modes of tumor destruction.* Photodiagnosis and Photodynamic Therapy, **2**, 91–106 (2005).

[Chiodi *et al.* 04] I. Chiodi, M. Corioni, M. Giordano, R. Valgardsdottir, C. Ghigna, F. Cobianchi, R. M. Xu, S. Riva et G. Biamonti. – *RNA recognition motif 2 directs the recruitment of SF2/ASF to nuclear stress bodies.* Nucleic Acids Res., **32**, 4127 (2004).

[Cotto *et al.* 97] J. J. Cotto, S. Fox et R. I. Morimoto. – *Hsf1 granules : a novel-stress induced nuclear compartments of human cell.* J. Cell Sci., **110**, 2925 (1997).

[Cotto et Morimoto 99] J. J. Cotto et R. I. Morimoto. – Stress-induced activation of the heat-shock response : cell and molecular biology of heat-shock factors. *In : Cellular Responses To Stress*, éd. par CP Downes, CR Wolf et DP Lane, 105–118.

[Coutier *et al.* 01] S. Coutier, S. Mitra, L. N. Bezdetnaya, R. M. Parache, I. Georgakoudi, T. H. Foster et F. Guillemin. – *Effects of Fluence Rate on Cell Survival and Photobleaching in Meta-Tetra-(hydroxyphenyl) chlorin-photosensitized Colo 26 Multicell Tumor Spheroids.* Photochemistry and Photobiology, **73** (3), 297–303 (2001).

[Dahle *et al.* 00] J. Dahle, S. Bagdonas, O. Kaalhus, G. Olsen, H. B. Steen et J. Moan. – *The bystander effect in photodynamic inactivation of cells.* Biochimica et Biophysica Acta, **1475**, 273–280 (2000).

[Derosa et Crutchley 02] M. C. Derosa et R. J. Crutchley. – *Photosensitized singlet oxygen and its applications.* Coordination Chemistry Reviews, **233–234**, 351–371 (2002).

[Dougherty 02] T. J. Dougherty. – *An Update on Photodynamic Therapy Applications.* Journal of Clinical Laser Medicine Surgery, **20**, 3–7 (2002).

[Dougherty *et al.* 76] T. J. Dougherty, C. J. Gomer et K. R. Weishaupt. – *Energetics and efficiency of photoinactivation of murine tumor cells containing hematoporphyrin.* Cancer Research, **36** (7 Part 1), 2330 (1976).

[Dougherty *et al.* 98] T. J. Dougherty, C. J. Gomer, B. W. Henderson, G. Jori, D. Kessel, M. Koberlik, J. Moan et Q. Peng. – *Photodynamic Therapy.* Journal of the National Cancer Institute, **90**, 889–905 (1998).

[Dysart *et al.* 05] J. S. Dysart, G. Singh et M. S. Patterson. – *Calculation of Singlet Oxygen Dose from Photosensitizer Fluorescence and Photobleaching During mTHPC Photodynamic Therapy of MLL Cells.* Photochemistry and Photobiology, **81**, 196 – 205 (2005).

[Elmore 07] S. Elmore. – *Apoptosis : a review of programmed cell-death.* Toxicologic Pathology, **35**, 495–516 (2007).

[Essers *et al.* 04] M. A. Essers, S. Weijzen, A. M. de Vries-Smits, I. Saarloos, N. D. de Ruiter, J. L. Bos et B. M. Burgering. – *FOXO transcription factor activation by oxidative stress mediated by the small GTPase Ral and JNK.* EMBO J., **23**, 4802 (2004).

[Favier 03] A. Favier. – *Le stress oxydant : Intï¿½rï¿½t conceptuel et expï¿½rimental dans la comprï¿½hension des mï¿½canismes des maladies et potentiel thï¿½rapeutique.* L'Actualitï¿½ Chimique, **11**, 108–115 (2003).

[Finikova *et al.* 08] O. S. Finikova, A. Y. Lebedev, A. Aprelev, T. Troxler, F. Gao, C. Garnacho, S. Muro, R. M. Hochstrasser et S. A. Vinogradov. – *Oxygen Microscopy by Two-Photon-Excited Phosphorescence.* ChemPhysChem, **9**, 1673–1679 (2008).

[Foote 68] C. S. Foote. – *Mechanisms of Photosensitized Oxidations.* Science, **162**, 963–970 (1968).

[Fritah *et al.* 09] S. Fritah, E. Col, C. Boyault, J. Govin, K. Sadoul, S. Chiocca, E. Christians, S. Khochbin, C. Jolly et C. Vourch. – *Heat-shock factor 1 controls genome-wide acetylation in heat-shocked cells.* Mol. Biol. Cell, **20**, 4976 (2009).

[Georgakoudi *et al.* 97] I. Georgakoudi, M. G. Nochols et T. H. Foster. – *The mechanism of Photofrin© Photobleaching and its Consequences for Photodynamic Dosimetry.* Photochemistry and Photobiology, **65**, 135–144 (1997).

[Hale et Querry 73] G. M. Hale et M. R. Querry. – *Optical Constants of Water in the 200 nm to 200 µm Wavelength Region.* Applied Optics, **12**, 555–563 (1973).

[Hessling et Buchner 09] M. Hessling et J. Buchner. – *Dissection of the ATP-induced conformational cycle of the molecular chaperone Hsp90.* Nature Struct. and Mol. Biol., **16**, 287–293 (2009).

[Higgins *et al.* 68] R. Higgins, C. S. Foote et H. Cheng. – *Chemistry of Singlet Oxygen. V. Reactivity and Kinetic Characterization.* Advances in Chemistry Series, **77**, 102 (1968).

[Honda *et al.* 00] O. Honda, M. Kuroda, I. Joja, J. Asaumi, Y. Takeda, S. Akaki, I. Togami, S. Kanazawa, S. Kawasaki et Y. Hiraki. – *Assessment of secondary necrosis of Jurkat cells using a new microscopic system and double staining method with annexin V and propidium iodide.* International journal of oncology, **16** (2), 283 (2000).

[Jolly *et al.* 97] C. Jolly, S. Michelland, M. Rocchi, M. Robert-Nicoud et C. Vourc'h. – *Analysis of the transcriptional activity of amplified genes in tumour cells by fluorescence in situ hybridization.* Hum. Genet., **101**, 81 (1997).

[Jolly *et al.* 99] C. Jolly, Y. Usson et R. I. Morimoto. – *Rapid and reversible relocalization of heat shock factor 1 within seconds to nuclear granules.* Proceedings of the National Academy of Sciences USA, **96**, 6769–6774 (1999).

[Jolly *et al.* 02] C. Jolly, L. Konecny, D. L. Grady, Y. A. Kutskova, J. J. Cotto, R. I. Morimoto et C. Vourc'h. – *In vivo binding of active heat shock transcription factor 1 to human chromosome 9 heterochromatin during stress.* J. Cell. Biol., **156**, 775 (2002).

[Jr. *et al.* 03] A. A. Krasnovsky Jr., N. N. Drozdova, A. V. Ivanov et R. V. Ambartzumian. – *Activation of Molecular Oxygen by Infrared Laser Radiation in Pigment-Free Aerobic Systems*. Biochemistry (Moscow), **68**, 1178–1182 (2003).

[Jr. *et al.* 06] A. A. Krasnovsky Jr., Ya. V. Roumbal, A. V. Ivanov et R. V. Ambartzumian. – *Solvent dependance of the steady-state rate of $^1O_2$ generation upon excitation of dissolved oxygen by cw 1267 nm laser radiation in air-saturated solutions : Estimates of the absorbance and molar absorption coefficients of oxygen at the excitation wavelength*. Chemical Physics Letters, **430**, 260–264 (2006).

[Jr. *et al.* 08] A. A. Krasnovsky Jr., Ya. V. Roumbal et A. A. Strizhakov. – *Rates of $^1O_2$ ($^1\Delta_g$) production upon direct excitation of molecular oxygen by 1270 nm laser radiation in air-saturated alcohols and micellar aqueous dispersions*. Chemical Physics Letters, **458**, 195–199 (2008).

[Jr. et Ambartzumian 04] A. A. Krasnovsky Jr. et R. V. Ambartzumian. – *Tetracene oxygenation caused by infrared excitation of molecular oxygen in air-saturated solutions : the photoreaction action spectrum and spectroscopic parameters of the $^1\Delta_g \longleftarrow ^3\Sigma_g^-$ transition in oxygen molecules*. Chemical Physics Letters, **400**, 531–535 (2004).

[Koo *et al.* 04] Y. E. Lee Koo, Y. Cao, R. Kopelman, S. M. Koo, M. Brasuel et M. A. Philbert. – *Real-Time Measurements of Dissolved Oxygen Inside Live Cells by Organically Modified Silicate Fluorescent Nanonsensors*. Analytical Chemistry, **76**, 2498–2505 (2004).

[Kregel 02] K. C. Kregel. – *Heat shock proteins : modifying factors in physiological stress responses and acquired thermotolerance*. Journal of Applied Phisiology, **92**, 2177–2186 (2002).

[Landsberg *et al.* 12] M. Kloster Landsberg, G. Herbomel, I. Wang, J. Derouard, C. Vourc'h, T. Usson, C. Souchier et A. Delon. – *Cellular response to heat shock studied by multiconfocal fluorescence correlation spectroscopy*. Biophys. J., **103**, 1110–1119 (2012).

[Lecoeur *et al.* 01] H. Lecoeur, M. C. Prévost et M. L. Gougeon. – *Oncosis is associated with exposure of phosphatidylserine residues on the outside layer of the plasma membrane : a reconsideration of the specificity of the annexin V/propidium iodide assay*. Cytometry Part A, **44** (1), 65–72 (2001).

[Lide 09] D. R. Lide, editor. – *CRC Handbook of Chemistry an Physics, 89th Edition*. – CRC Press/Taylor and Francis, Boca Raton, FL (2009).

[Linquist et Craig 88] S. Linquist et E. A. Craig. – *The Heat-Shock Proteins*. Annual Review Of Genetics, **22**, 631–677 (1988).

[Maisch *et al.* 07] T. Maisch, J. Baier, B. Franz, M. Maier, M. Landthaler, R. M. Szeimies, et W. Bï¿½umler. – *The role of singlet oxygen and oxygen concentration in photodynamic inactivation of bacteria*. Proceedings of the National Academy of Sciences, **104**, 7223–7228 (2007).

[Mcmillan *et al.* 98] D. R. McMillan, X. Z. Xiao, L. Shao, K. Graves et I. J. Benjamin. – *Targeted disruption of heat shock transcription factor 1 abolishes*

thermotolerance and protection against heat-inducible apoptosis. Journal Of Biological Chemistry, **273** (13), 7523–7528 (1998).

[Metz *et al.* 04] A. Metz, J. Soret, C. Vourc'h, J. Tazi et C. Jolly. – *A key role for stress-induced satellite III transcripts in the relocalization of splicing factors into nuclear stress granules*. J. Cell. Sci., **117**, 4551 (2004).

[Moserova et Kralova 12] I. Moserova et J. Kralova. – *Role of ER Stress Response in Photodynamic Therapy : ROS Generated in Different Subcellular Compartments Trigger Diverse Cell Death Pathways*. PLos One, **7**, e30972 (2012).

[Mulliken 28] R. S. Mulliken. – *Interpretation of the atmospheric oxygen bands ; electronic levels of the oxygen molecule*. Nature, **122** (3075), 505 (1928).

[Ogilby 10] P. R. Ogilby. – *Singlet oxygen : there is indeed something new under the sun*. Chemical Society Reviews, **39** (8), 3181–3209 (2010).

[Petre *et al.* 11] I. Petre, A. Mizera, C. L. Hyder, A. Meinander, A. Mikhailov, R. I. Morimoto, L. Sistonen, J. E. Eriksson et R. J. Back. – *A simple mass-action model for the eukaryotic heat shock response and its mathematical validation*. Natural Computing, **10** (1), 595–612 (2011).

[Pitas et Venetsanopoulos 90] I. Pitas et A. N. Venetsanopoulos. – *Nonlinear Digital Filters : Principles and Applications*. – Springer, *The Kluwer international series in engineering and computer science : VLSI, computer architecture and digital signal processing* (1990).

[Raab 00] O. Raab. – *Ueber die Wirkung fluorescirender Stoffe auf Infusorien*. Z. Biol., **39**, 524 (1900).

[Redmond et Kochevar 06] R. W. Redmond et I. E. Kochevar. – *Spatially resolved cellular responses to singlet oxygen*. Photochemistry and photobiology, **82** (5), 1178–1186 (2006).

[Rieger *et al.* 05] T. R. Rieger, R. I. Morimoto et V. Hatzimanikatis. – *Mathematical modeling of the eukaryotic heat-shock response : Dynamics of the hsp70 promoter*. Biophysical Journal, **88** (3), 1646–1658 (2005).

[Rigaudy et Cuong 62] J. Rigaudy et N. K. Cuong. – *Laddition diï¿½nique anormale en siï¿½rie naphtacï¿½nique- cas du rubrï¿½ne- passage direct ï¿½ un acide rubrï¿½ne dicarboxylique et ï¿½ un acide rubrï¿½ne tï¿½tracarboxylique*. Comptes Rendue Hebdomadaires des Sï¿½ances de l'Acadï¿½mie des Sciences, **254**, 4184 (1962).

[Sakakibara et Adrian 99] J. Sakakibara et R. J. Adrian. – *Whole field measurement of temperature in water using two-color laser induced fluorescence*. Experiments in Fluids, **26**, 7–15 (1999).

[Sarge *et al.* 97] K. D. Sarge, S. P. Murphy et R. I. Morimoto. – *In vivo binding of active heat shock transcription factor 1 to human chromosome 9 heterochromatin during stress*. Mol. Cell. Biol., **13**, 1392 (1997).

[Schweitzer et Schmidt 03] C. Schweitzer et R. Schmidt. – *Physical Mechanisms of Generation and Deactivation of Singlet Oxygen*. Chemical Reviews, **103**, 1685–1757 (2003).

[SE 00] U. Schmidt-Erfurth et T. Hasan. – *Mechanisms of action of photodynamic therapy with verteporfin for the treatment of age-related macular degeneration*. Survey Of Ophtalmology, **45**, 195–214 (2000).

[Singh *et al.* 84] A. Singh, G. W. Korrol et S. A. Antonsen. – *Possible formation of singlet oxygen from vibrationally excited water*. Journal of Photochemistry, **25**, 99–104 (1984).

[Sivery *et al.* 13a] A. Sivery, F. Anquez, A. Barras, C. Pierlot, J. M. Aubry et E. Courtade. – *Singlet oxygen ($^1O_2$) generation upon 1270 nm laser irradiation in water and D_2O : $^1O_2$ production rate and reactivity via chemical quenching with tetrapotassium rubrene-2,3,8,9-tetracarboxylate and DPIBF encapsulated in nanocells*. soumis ï¿½ Phys. Chem. B (2013).

[Sivery *et al.* 13b] A. Sivery, F. Anquez, C. Pierlot, J. M. Aubry et E. Courtade. – *Singlet oxygen ($^1O_2$) generation upon 1270 nm laser irradiation of ground state oxygen ($^3O_2$) dissolved in organic solvents : Simultaneous and independent determination of $^1O_2$ production rate and reactivity with chemical traps*. Chem. Phys. Lett., **555**, 252 (2013).

[SS *et al.* 05] U. Seger-Sauli, M. Panayiotou, S. Schnydrig, M. Jordan et P. Renaud. – *Temperature measurements in microfluidic systems : heat dissipation of negative dielectrophoresis barriers*. Electrophoresis, **26**, 2239–2246 (2005).

[Stewart et Young 04] G. R. Stewart et D. B. Young. – *Heat-shock proteins and the host-pathogen interaction during bacterial infection*. Current Opinion in Immunology, **16** (4), 506–510 (2004).

[Szymanska et Zylicz 09] Z. Szymanska et M. Zylicz. – *Mathematical modeling of heat shock protein synthesis in response to temperature change*. Journal Of Theoretical Biology, **259** (3), 562–569 (2009).

[Tappeiner 09] H. Von Tappeiner. – *Die photodynamische Erscheinung Sensibilisierung durch fluoreszierende Stoffe*. Ergeb. Physiol., **8**, 698–741 (1909).

[Tappeiner et Jodlbauer 04] H. Von Tappeiner et A. Jodlbauer. – *ï¿½ber die Wirkungen der photodynamischen (fluorescierenden) Stoffe auf Protozoen und Enzyme*. Arch. Klin. Med., **80**, 427–487 (1904).

[Vitale *et al.* 93] M. Vitale, L. Zamai, G. Mazzotti, A. Cataldi et E. Falcieri. – *Differential kinetics of propidium iodide uptake in apoptotic and necrotic thymocytes*. Histochemistry and Cell Biology, **100** (3), 223–229 (1993).

[Wang *et al.* 08] S. Wang, W. Xie, M. N. Rylander, P. W. Tucker, S. Aggarwal et K. R. Diller. – *HSP70 Kinetics Study by Continuous Observation of HSP ?GFP Fusion Protein Expression on a Perfusion Heating Stage*. Biotech. Bioengin., **1**, 146 (2008).

[Westerheide *et al.* 09] S. D. Westerheide, J. Anckar, S. M. Stevens, L. Sistonen et R. I. Morimoto. – *Stress-inducible regulation of heat shock factor 1 by the deacetylase SIRT1*. Science, **363**, 1063 (2009).

[Yusupov *et al.* 10] A. S. Yusupov, S. E. Goncharov, I. D. Zalevski, V. M. Paramonov et A. S. Kurkov. – *Raman Fiber Laser for the Drug-Free Photodynamic Therapy*. Laser Physics, **20**, 357–359 (2010).

[Zakharov et Ivanov 99] S. D. Zakharov et A. V. Ivanov. – *Light-oxygen effect in cells and its potential applications in tumour therapy (review).* Quantum Electronic, **29**, 1031–1053 (1999).

[Zhao *et al.* 11] H. Zhao, D. Xing et Q. Chen. – *New insights of mitochondria reactive oxygen species generation and cell apoptosis induced by low dose photodynamic therapy.* Eur. J. Cancer., **47**, 2750–2761 (2011).